# Implementation of a Faraday Effect Based Optical Current Transducer Using Digital Signal Processing Techniques

# Pawel Niewczas MSc

A thesis presented for the Degree of Doctor of Philosophy

Centre for Electrical Power Engineering

Department of Electronic and Electrical Engineering

University of Strathclyde

Glasgow G1 1XW

Scotland, UK

June 2000

The copyright of this thesis belongs to the author under the terms of the United Kingdom Copyright Acts as qualified by University of Strathclyde Regulation 3.49. Due acknowledgement must always be made of the use of any material contained in, or derived from this thesis.

Signed Nicwcras Date 8/6/2000

### **Abstract**

In recent years, the idea of replacing conventional high voltage (HV) current transformers (CTs) with optical current transducers (OCTs) has gained increased attention. This is a direct consequence of a progress in fibre-optic sensing technology which can now provide a means of current measurement with potentially superior performance and functionality over the conventional CTs.

Optical current transducers offer many advantages including inherent high voltage insulation, intrinsically safe failure modes, immunity to electromagnetic interference, enhancement in signal bandwidth and dynamic range, ease of integration into future digital control and protection systems and reduced costs. Additional benefits include reduced size and weight of the transducers compared to the conventional devices providing easier installation and potentially reduced substation land requirements.

The research work presented in this thesis is related specifically to compensation of environmental factors within operation of the Faraday Effect based OCT using digital signal processing (DSP) techniques. The thesis analyses measurement errors within the optical current sensor attributed mainly to thermal influences, vibration induced noise and magnetic cross-talk. It is shown that the use of a fully automatic, real time, processing facility, as developed within this research work, for implementation of software based temperature, vibration and magnetic cross-talk compensation schemes will satisfy the accuracy specifications demanded from the OCT.

It is also demonstrated, that the same DSP system can facilitate the linearisation of the sensor response characteristic in real time operation and increase the maximum modulation level of the measured signal. This allows for use of an extended sensor dynamic range and relaxes some critical design requirements of the photodetector circuit.

## Acknowledgements

I would like to express my sincere gratitude to Professor Jim McDonald for providing me the opportunity to work in his dynamic research group and for his supervision and guidance during the past four years.

I would also like to thank Andy Cruden who introduced me to this research, and tried to express his ideas in Polish (dzień dobry!), and to Craig Michie for his ability to carry on technical discussions which, perhaps, I was able to understand and appreciate! I wish to thank for their significant contributions to the research presented in this thesis and for their constructive criticism.

To all my work colleges I would like to give my thanks for their support and encouragement, in particular:

- Adam Dyśko for being a good friend, lodger and vodka drinker in times of despair and joy (perhaps more despair).
- Keshav & Anjana Dahal, Joel Padulles, Judith Menal and Faina Edwards for being my international support team and great cooks!
- Bob Baird for his ability to make my dreams true in the lab.
- Iain Madden for putting up with his driving duty on the many occasions of our trips to Newcastle.

I would like to express my gratitude to my colleges at the Lublin Technical University for the support I needed in order to be able to stay in Scotland.

I must also thank my parents, Jerzy and Janina, and my sisters Ewa and Dorota for their constant encouragement and support, their many e-mails and telephone calls which I always enjoyed, and for their great hospitality back in Poland.

And last, but by no means least, I would like to thank my dear fiancée Sarah, for her love, support and prayer. God has shown a lot of grace to us darling!

# **Contents**

1. Introduction	1
1.1. Justification for and Introduction to Research	1
1.2. Primary Objectives and Outcomes of the Research	4
1.3. Thesis Outline	6
1.4. Associated Publications	8
1.5. Chapter References	11
2. Conventional Current Measurement Methods	12
2.1. Introduction	12
2.2. Conventional Current Transformer	12
2.2.1. Equivalent Circuit	14
2.2.2. CT Errors	15
2.2.3. Accuracy Limit Current	17
2.2.4. Accuracy Requirements	17
2.2.4.1. Metering CTs	17
2.2.4.2. Protection CTs	18
2.2.5. Transient Behaviour of a CT	19
2.2.6. CT Voltage Withstand	19
2.2.7. Summary Appraisal of Iron-Cored CTs	19
2.3. Competitive Current Measuring Devices	20
2.3.1. Rogowski Coil	20
2.3.2. Hall Effect Device	23
2.3.3. Magnetoresistive Sensors	24
2.4. Summary	25
2.5. Chapter References	25
3. Essential Optics	27
3.1. Introduction	27
3.2. Propagation of Light Waves	28
3.3. Polarisation Properties	31
3.4. Coherence Properties	35
3.5. Interaction of Light with Matter	37
3.5.1. Light Absorption and Scattering	38
3.5.2. Classical Theory of Propagation in Isotropic Dielectrics	41
3.5.3. Propagation in an Anisotropic Media	49
3.5.4. Birefringence	52

3.5.5. Retarders	54
3.5.6. Optical Activity	55
3.5.7. Faraday Rotation in Solids	59
3.5.8. Other Magneto-optic Effects	63
3.5.9. Electrogyration	64
3.5.10. Photoelastic Effect	64
3.5.11. Electro-optic Effects	66
3.6. Summary	66
3.7. Chapter References	67
4. Optical Sensing Techniques - Basic Concepts	68
4.1. Introduction	68
4.2. Optical Fibres - a Technical Overview	69
4.3. Optical Fibre Sensors - Basic Principles and Configurations	76
4.3.1. Intensity Sensors	80
4.3.2. Wavelength and Frequency Modulation Sensors	84
4.3.3. Interferometric Sensors	86
4.4. Multiplexed and Distributed Sensing	94
4.5. Summary	95
4.6. Chapter References	96
5. The Optical Current Transducer	97
5.1. Introduction	97
5.2. Review of Optical Current Transducer Types	98
5.2.1. Conventional CT Addressed by Optical Fibres	98
5.2.2. Magnetostrictive Current Sensor	100
5.2.3. Faraday Effect Based OCTs	103
5.2.3.1. Wound Optical Fibre OCT	106
5.2.3.2. Bulk Optic OCT	114
5.2.3.3. Faraday Cell OCT	116
5.2.3.4. Flux Concentrator OCT	119
5.3. The Design of the Author's Preferred OCT Type	120
5.3.1. OCT Basic Function and Accuracy Requirements	120
5.3.2. OCT Temperature and Vibration Specifications	124
5.3.3. Construction of the Sensor Head	124
5.3.3.1. OCT Polarisation and Collimating Components	125
5.3.3.2. OCT Response Characteristic	126
5.3.3.3. Selection of the Magneto-optic Medium	131

5.3.3.4. Modelling of the Magnetic Field Surrounding the Busbar	133
5.3.3.5. TGG Linear-design	139
5.3.3.6. FR-5 Reflective-design	142
5.4. Summary	148
5.5. Chapter References	149
6. Environmental Factors in the OCT Operation	153
6.1. Introduction	153
6.2. Vibration Induced Noise	153
6.2.1. Transmission Losses within Optical Fibre	154
6.2.2. Optical Connection Losses	156
6.2.2.1. Intrinsic Losses	156
6.2.2.2. Extrinsic Losses	157
6.2.2.3. Losses Associated with Modal Noise Effect	159
6.2.3. Stress Induced Birefringence within Sensing Medium	160
6.3. Vibration Compensation	161
6.3.1. Background	162
6.3.2. The Principle of Compensation	164
6.3.3. Pulsed Operation of the System	168
6.4. Temperature Effect	169
6.5. Temperature Compensation	171
6.5.1. Impact of the Temperature Measurement Precision on OCT Performance	173
6.5.2. Indirect Recovery of Sensor Temperature	175
6.5.3. Direct Recovery of Sensor Temperature	179
6.5.3.1. Bragg Grating Temperature Sensor	180
6.5.3.2. Absorption Glass Temperature Sensor	181
6.6. Magnetic Cross-Talk Effect	183
6.7. Cross-Talk Compensation	190
6.7.1. The Principle of Compensation	191
6.8. Summary	194
6.9. Chapter References	196
7. Digital Signal Processing Unit as an Integrated System for Condition	oning of
the OCT Output	199
7.1. Introduction	199
7.2. DSP Unit Hardware (Single Phase System)	
7.2.1. DSP board	
7.2.1.1. ADSP-2181 processor	203

	7.2.2. Analogue Interface Board	208
	7.2.2.1. A/D Converters	210
	7.2.2.2. D/A Converters	210
	7.3. Analogue Optoelectronic System	211
	7.3.1. Light Source Driver	211
	7.3.2. Photodetectors	213
	7.4. DSP Software Development	213
	7.5. Downloading Software to the DSP Unit	215
	7.6. Software Created for the Use with the DSP Unit	216
	7.6.1. Initialisation	216
	7.6.2. Autocalibration	217
	7.6.3. DC Filtering	217
	7.6.4. Offset Zeroing and Normalisation	221
	7.6.5. Vibration Compensation	221
	7.6.6. Linearisation of the OCT Response Characteristic	221
	7.6.6.1. Direct Lookup Table	222
	7.6.6.2. Lookup Table with Linear Interpolation	223
	7.6.7. Temperature Compensation	225
	7.7. DSP Implementation of the Cross-Talk Compensation Scheme (Three-Phase	se System).226
	7.8. Error Associated with Analogue-to-digital Conversion Process	228
	7.8. Error Associated with Analogue-to-digital Conversion Process	
		229
	7.8.1. Quantisation Error	229
	7.8.1. Quantisation Error	229 231 232
	7.8.1. Quantisation Error	229231232233
	7.8.1. Quantisation Error	229231232233
	7.8.1. Quantisation Error	229231232233235
8.	7.8.1. Quantisation Error	229231232233235237
8.	7.8.1. Quantisation Error 7.8.2. Case Studies 7.8.2.1. Protection Applications 7.8.2.2. Metering Applications 7.8.2.3. Combined Protection and Metering Applications 7.9. Summary 7.10. Chapter References	229231232235237239
8.	7.8.1. Quantisation Error 7.8.2. Case Studies 7.8.2.1. Protection Applications 7.8.2.2. Metering Applications 7.8.2.3. Combined Protection and Metering Applications 7.9. Summary 7.10. Chapter References	229231232233237239
8.	7.8.1. Quantisation Error 7.8.2. Case Studies 7.8.2.1. Protection Applications 7.8.2.2. Metering Applications 7.8.2.3. Combined Protection and Metering Applications 7.9. Summary 7.10. Chapter References 8.1. Introduction	229231232233235237239239
8.	7.8.1. Quantisation Error 7.8.2. Case Studies 7.8.2.1. Protection Applications 7.8.2.2. Metering Applications 7.8.2.3. Combined Protection and Metering Applications 7.9. Summary 7.10. Chapter References 8.1. Introduction 8.2. Low Noise Photodetector Design	
8.	7.8.1. Quantisation Error 7.8.2. Case Studies	
8.	7.8.1. Quantisation Error  7.8.2. Case Studies	
8.	7.8.1. Quantisation Error 7.8.2. Case Studies	
8.	7.8.1. Quantisation Error 7.8.2. Case Studies 7.8.2.1. Protection Applications 7.8.2.2. Metering Applications 7.8.2.3. Combined Protection and Metering Applications 7.9. Summary 7.10. Chapter References 8.1. Introduction 8.2. Low Noise Photodetector Design 8.2.1. Design Criteria 8.2.2. Choice of the Photodiode Circuit Configuration 8.2.2.1. DC Performance and Bandwidth 8.2.2.2. Noise Performance	

8.2.4.2. DC Performance	248
8.2.5. Photodetector with J-FET Input Stage	249
8.2.5.1. Noise Performance	250
8.2.5.2. DC Performance	251
8.2.6. Demand for Input Optical Power	254
8.3. Laboratory Evaluation of the OCT Measurement System	256
8.3.1. Accuracy Tests of the DSP Monitoring Unit	256
8.3.2. Linearisation Routine of OCT Response Characteristic	259
8.3.3. Accuracy of the Monitored TGG 15mm Sensor	261
8.3.4. Accuracy of the Monitored FR-5 Sensor	263
8.4. Vibration Tests	264
8.4.1. Vibration Tests (1997) - Proof of Principle	265
8.4.1.1. Description of the Test System	266
8.4.1.2. Accuracy Tests	268
8.4.1.3. Vibration Tests	270
8.4.2. Vibration Tests (1999) - Utilisation of DSP Unit	273
8.4.2.1. Description of the Test System	273
8.4.2.2. OCT Accuracy Tests with no Vibration Present	274
8.4.2.3. Vibration Tests	276
8.4.2.4. OCT Accuracy Tests (sensor head vibrated)	278
8.4.2.5. Vibration Tests (optical connectors vibrated)	279
8.4.2.6. OCT Accuracy Tests (sensor head and connectors vibrated)	281
8.5. Temperature Tests	282
8.5.1. Description of the Test Set-up	282
8.5.2. Tests with a Thermocouple	284
8.5.3. Temperature Compensation Using FBG Sensor	285
8.5.3.1. Fibre Bragg Grating System	286
8.6. DC Testing	288
8.7. Long Term Engineering Evaluation of the OCT	290
8.7.1. Description of the Field Trial Set-up	290
8.7.2. Initial Tests Results	292
8.7.3. Laboratory Investigations	294
8.8. Summary	297
8.9. Chapter References	298
9. General Conclusions and Future Work	299
9.1. Principal Results and Contributions	299
0.2 February Wests	202

Annendix		
annondiz		
	nnondi:	24 14

# **List of Figures**

Figure 2-1 Medium voltage ring (window), bar and wound type CTs	13
Figure 2-2 High voltage CTs (132kV)	13
Figure 2-3 Equivalent circuit of a current transformer	14
Figure 2-4 Equivalent circuit of a current transformer referred to the secondary	15
Figure 2-5 Equivalent circuit and vector diagram of a current transformer referred to the second	lary 15
Figure 2-6 Basic Rogowski transducer	20
Figure 2-7 Rogowski coil and a basic integrator circuit	21
Figure 2-8 Hall Effect device	23
Figure 2-9 Commercial magnetoresistive sensor	25
Figure 3-1 Polarisation components of the E wave	33
Figure 3-2 Wave train representation of a photon	35
Figure 3-3 Spectral spread of laser emission	36
Figure 3-4 Energy level diagram for absorption and corresponding spectrum	38
Figure 3-5 Energy level diagram for fluorescence and corresponding spectrum	39
Figure 3-6 Energy level diagram for scattering mechanisms	41
Figure 3-7 Index of refraction and extinction index for a hypothetical substance with absorption	1
bands in the infrared, visible and ultraviolet regions of the spectrum	48
Figure 3-8 Principal semi-axes of the index ellipsoid	53
Figure 4-1 Optical fibre	70
Figure 4-2 Light guiding in an optical fibre due to total internal reflection	70
Figure 4-3 The transmission of light ray in a perfect optical fibre due to multiple reflections	71
Figure 4-4 The acceptance angle $\theta_a$ when launching light into an optical fibre	72
Figure 4-5 Optical fibre sensor configuration (extrinsic sensor)	77
Figure 4-6 Generic intensity based sensor	80
Figure 4-7 Pressure diaphragm sensor	81
Figure 4-8 Typical response from pressure diaphragm sensor	81
Figure 4-9 Reflective type temperature sensor	82
Figure 4-10 Recirculating path referencing	83
Figure 4-11 Balanced-intensity referencing	84
Figure 4-12 Spectra produced by various spectral modulation sensors	85
Figure 4-13 Schematic diagram of an interferometer	87
Figure 4-14 Intensity variation with time delay (t)	88
Figure 4-15 (a) Conventional Mach-Zehnder interferometer, (b) Fibre-optic Mach Zehnder	
	90

Figure 4-16 (a) Conventional Michelson interferometer, (b) fibre-optic Michelson interferometer, (c)
Interferometer output as a function of mirror displacement90
Figure 4-17 Fibre-optic Sagnac interferometer
Figure 4-18 Fibre-optic Fabry-Perot interferometer91
Figure 4-19 Basic polarimetric sensor
Figure 5-1 Conventional CT addressed by optical fibre
Figure 5-2 Mach-Zehnder interferometer used to monitor the CT output99
Figure 5-3 Basic components of a magnetostrictive fibre optic current sensor employing a Mach-
Zehnder interferometer
Figure 5-4 Magnetostrictive current sensor in a polarimetric detection scheme103
Figure 5-5 Typical arrangement of optical components and polarisation components in the Faraday
sensor105
Figure 5-6 OCT using single-mode optical fibre
Figure 5-7 The layout architecture of the OCT sensing head
Figure 5-8 Wound optical fibre OCT using a polarimeter
Figure 5-9 Periodic conductor structure for fibre type OCT111
Figure 5-10 Experimental arrangement of a Sagnac interferometer based OCT113
Figure 5-11 OCT employing an orthoconjugate reflector
Figure 5-12 Bulk optic current sensor
Figure 5-13 Bulk optic OCTs without the detrimental reflections problem116
Figure 5-14 Faraday cell OCT
Figure 5-15 Multi-pass Faraday cell OCT
Figure 5-16 Flux concentrator OCT
Figure 5-17 GRIN lens assembly and POLARCOR polarisers
Figure 5-18 Explanation of the OCT linear response region
Figure 5-19 Necessary dynamic limitations in order to comply with the accuracy requirements for
metering and protection class devices
Figure 5-20 Cross-sections of the selected conductors used in the electricity industry
Figure 5-21 Separation distance between the conductor and the sensing element
Figure 5-22 Magnetic field distribution at the level of 'separation distance' for the copper busbar. 136
Figure 5-23 Magnetic field density along the longitudinal section of the sensing element for the
cylindrical conductor137
Figure 5-24 Magnetic field density along a longitudinal section of the sensing element for the hollow
conductor138
Figure 5-25 TGG sensor head141
Figure 5-26 A range of prototype TGG based sensors
Figure 5-27 Multi-pass Faraday cell OCT

Figure 5-28 Sensor normalised output signal at different polariser bias points	. 145
Figure 5-29 Active alignment set-up	. 146
Figure 5-30 FR-5 optical assembly (left) and completed FR-5 sensor (right)	.146
Figure 5-31 FR-5 sensor housing	.147
Figure 6-1 OCT optical transmission system	.154
Figure 6-2 Bending loss mechanism	.156
Figure 6-3 Intrinsic Losses Associated with Fibre Tolerances	.157
Figure 6-4 Extrinsic Losses	.158
Figure 6-5 Modal noise effect	.159
Figure 6-6 Graphical illustration of the nonreciprocal nature of the magneto-optic Faraday effect	.162
Figure 6-7 The configuration of the bidirectional light propagation in the optical system	.164
Figure 6-8 A graphical illustration of the proposed compensation method	.166
Figure 6-9 A graphical illustration of the ac current measurement vibration compensation system	167
Figure 6-10 A block diagram of the basic vibration compensation arrangement	.168
Figure 6-11 Variation in Verdet constants with temperature for TGG and FR5 materials	.172
Figure 6-12 Verdet constant error vs. temperature measurement precision, δT	.174
Figure 6-13 Two-wavelength temperature compensation scheme	.176
Figure 6-14 Precision of indirect temperature recovery process using two wavelengths,	
$\delta\theta$ = 100μdeg	.178
Figure 6-15 Fibre Bragg grating manufacture process	.180
Figure 6-16 Bragg Grating Sensor Operation	.181
Figure 6-17 Basic concept of absorption glass temperature sensor	.183
Figure 6-18 Minimal cross-talk for conductors positioned in one plane	.184
Figure 6-19 Geometrical evaluation of the parallel field component Bx	.185
Figure 6-20 Magnetic cross-talk vs. conductors separation distance for different h factors	.187
Figure 6-21 Simulated Cross-talk error vs. conductors separation for metering OCT	.188
Figure 6-22 Simulated Cross-talk error vs. conductors separation for protection OCT	.189
Figure 6-23 Three-phase, high voltage GIS, current measurement chamber	.190
Figure 6-24 Explanation of the calibration process in phase 1	.192
Figure 7-1 Block schematic of the DSP monitoring system	.202
Figure 7-2 DSP board	.203
Figure 7-3 Functional block diagram of the ADSP-2181	.204
Figure 7-4 ADSP-2181 basic system configuration	.207
Figure 7-5 DSP unit with removed top and front panels	.209
Figure 7-6 Optoelectronic part of the OCT monitoring system	.211
Figure 7-7 Light source driver	.212
Figure 7.8 System dayalonment process overview	214

Figure 7-9 A conceptual representation of a digital filter	218
Figure 7-10 Simulated maximum error of the 256 values sin <sup>-1</sup> (x) direct lookup table	223
Figure 7-11 Simulated maximum error of the 256 values $\sin^{-1}(x)$ lookup table using the linear	
approximation approach	224
Figure 7-12 DSP implementation of magnetic cross-talk compensation scheme	227
Figure 7-13 Quantisation errors vs. A/D resolution at 1000A	233
Figure 7-14 Quantisation errors vs. current for 16 and 18 bit A/D converters compared with me	tering
class specifications	234
Figure 7-15 Performance of the combined metering and protection OCTs	236
Figure 8-1 Transimpedance configuration of the photodiode monitoring op-amp	241
Figure 8-2 Main sources of noise in the photo-receiver circuit	243
Figure 8-3 Experimental set-up	245
Figure 8-4 Photodetector noise vs. output voltage (500kHz bandwidth)	246
Figure 8-5 Electrical S/N ratio vs. photo-receiver output (500kHz bandwidth)	247
Figure 8-6 Photodetector offset drift vs. temperature	248
Figure 8-7 J-FET photodetector circuit	250
Figure 8-8 Comparison of the two photodetectors output noise levels	251
Figure 8-9 Comparison of the two photodetectors S/N ratios	251
Figure 8-10 The dc performance of the J-FET prototype and the conventional photodetector des	ign252
Figure 8-11 The modified source follower in the J-FET photodetector circuit	252
Figure 8-12 Improved dc performance of the J-FET photodetector	253
Figure 8-13 DC offset drifts of the conventional photo-receiver and the improved J-FET	
photodetector	253
Figure 8-14 Improvement in S/N ratio for the circuit with a lower feedback resistance Rf	255
Figure 8-15 J-FET photo-receiver	256
Figure 8-16 Block schematic of the DSP monitoring system	257
Figure 8-17 Accuracy of the measurement equipment and the A/D-D/A channel	258
Figure 8-18 Maximum quantisation error compared with experimental data	258
Figure 8-19 Accuracy of the measured arcsin look-up table using linear interpolation	259
Figure 8-20 Round-off errors of the arcsin look-up table coefficients	260
Figure 8-21 Errors of the OCT measurement system compared with the protection class 5P	
specification	262
Figure 8-22 Current source in the Strathclyde University Laboratory (max. current » 6000A)	263
Figure 8-23 Output errors of the fully compensated FR-5 sensor	264
Figure 8-24 OCT vibration testing.	266
Figure 8-25 Experimental set-up for vibration testing	267
Figure 8-26 Vertical vibration as the most severe case	268

Figure 8-27 OCT current response characteristics and output errors (TGG 25mm pigtailed sensor)268
Figure 8-28 OCT current response characteristics and output errors (TGG 15mm unpigtailed sensor)269
Figure 8-29 Vibration response with and without compensation (unpigtailed sensor)270
Figure 8-30 Unpigtailed sensor output errors (vibration: 26Hz, 6.63g)271
Figure 8-31 Oscilloscope traces of the two OCT outputs during the vibration test (vibration: 26Hz,
6.63g, equivalent current: 230Amps)272
Figure 8-32 Oscilloscope traces of the two OCT outputs during the vibration test (pigtailed sensor,
vibration: 26Hz, 6.63g, no current)272
Figure 8-33 Experimental set-up for vibration testing
Figure 8-34 OCT current response characteristics and output errors
Figure 8-35 OCT vibration response of the compensated and uncompensated channels vs. vibration
frequency (connectors not vibrated)277
Figure 8-36 Oscilloscope traces of the two OCT outputs during the vibration test (vibration: 50Hz,
10g, no current, connectors not vibrated)277
Figure 8-37 OCT current response characteristics and output errors (vibration 5g, 100Hz, connectors
not vibrated)279
Figure 8-38 OCT vibration response of the compensated and uncompensated channels vs. vibration
frequency (connectors vibrated)
Figure 8-39 Oscilloscope traces of the two OCT outputs during the vibration test (vibration: 180Hz,
8g, no current, connectors vibrated)
Figure 8-40 Oscilloscope traces of the two OCT outputs during the vibration test (vibration: 180Hz,
8g, current: 4Amps, connectors vibrated)
Figure 8-41 OCT current response characteristics and output errors (vibration: 180Hz, 10g,
connectors vibrated)
Figure 8-42 Schematic of the temperature test system
Figure 8-43 OCT temperature testing
Figure 8-44 OCT temperature compensation using a thermocouple
Figure 8-45 FBG probe (to the left), and the complete OCT interrogating system (to the right)287
Figure 8-46 OCT temperature compensation using a fibre Bragg grating
Figure 8-47 DC Output errors
Figure 8-48 DC magnetic field modelling
Figure 8-49 OCT single phase installation at the BSTS291
Figure 8-50 User interface of the modified FBG software (to the left), and the data acquisition
window (to the right)292
Figure 8-51 Example of recorded current signals (medium currents)
Figure 8-52 Example of recorded current signals (high currents)
Figure 8-53 Illustration of 'phase lag' of the reference signal

Figure 8-54 Symmetrical and asymmetrical currents generated in the laboratory	295
Figure 8-55 Current broken in non zero-crossing point	296
Figure 8-56 Oscillations in the power amplifier	296

# **List of Tables**

Table 2-1 Limits of current error for accuracy classes 0.1 to 1	17
Table 2-2 Maximum phase displacement specifications for metering current transformers	18
Table 2-3 Limits of error for accuracy Class 3 and Class 5	18
Table 2-4 Limits of current error for accuracy Class 5P and Class 10P	18
Table 2-5 Maximum phase displacement specifications for protection current transducers	19
Table 3-1 Values of the Verdet constant for some selected substances	60
Table 5-1 OCT accuracy specifications for metering applications in relation to the rated current	122
Table 5-2 OCT accuracy specification for protection applications in relation to the rated current	122
Table 5-3 Maximum phase displacement specifications for metering current transducers in relat	ion
to the rated current	122
Table 5-4 Maximum phase displacement specifications for protection current transducers in rela	ation
to the rated current	122
Table 5-5 Some properties of magneto-optic materials	132
Table 5-6 OCT maximum dynamic range for different conductor geometries	139
Table 5-7 Possible applications of TGG based OCT in the electricity industry	140
Table 5-8 Possible applications of FR-5 based OCT in the electricity industry	143
Table 7-1 Comparison of the DSP microprocessors	208

# **Glossary of Terms**

ac Alternating Current

A/D Analogue-to-Digital Converter

ALU Arithmetic/Logic Unit

BEM Boundary Element Method

BSO Bismuth Silicon Oxide

BSTS British Short-circuit Testing Station

CMOS Complementary Metal-Oxide Semiconductor

CT Current Transformer

D/A Digital-to-Analogue Converter

DAG Data Address Generator

dc Direct Current

DMA Direct Memory Access

DSP Digital Signal Processing

emf Electro-Mgnetic Force

EPROM Erasable Programmable Read-Only Memory

FBG Fibre Bragg Grating

FIR Finite Impulse Response

FR-5 Faraday Rotator 5 glass

GRIN Graded Index

Hi-Bi Highly Birefringent

HV High Voltage

HVDC High Voltage Direct Current

IEC International Electrotechnical Commission

IIR Infinite Impulse Response

I/O Input/Output

J-FET Junction Field Effect Transistor

LED Light Emitting Diode

LV Low Voltage

MAC Multiplier/Accumulator

mmf Magnetomotive Force

MFR Mirrored Faraday Rotator

MR Magnetoresistive

MV Medium Voltage

NA Numerical Aperture

NGC National Grid Company

OCT Optical Current Transducer

OCR Orthoconjugate Reflector

PC Personal Computer

pH the measure of a solution's acidity

PTFE Polytetrafluorethylene (Teflon)

RAM Random-Access Memory

R&D Research and Development

rms Root-Mean-Square Value

S/N or SNR Signal-to-Noise Ratio

SOP State of Polarisation

TAG Terbium Aluminium Garnet

TGG Terbium Gallium Gernet

UV Ultra Violet

YIG Yttrium Iron Garnet

## **Definition of Terms**

**Antialiasing** - removing the frequency components greater than a half of the Nyquist frequency in order to accurately reconstruct the original signal from the sampled signal.

**Azimuth** - an angle measured in the clockwise direction between the vertical line and the electrical vector of a linearly polarised light, or the orientation of the major axes of the ellipse of the elliptically polarised light with respect to some convenient axis, i.e. the vertical line.

**Birefringence** - the name given to the phenomena exhibited by optically anisotropic materials for which the refractive index is a function of the state of light polarisation (SOP). In a linearly birefringent material two orthogonal linear SOPs (eigenmodes) propagate at different velocities.

**Demagnetisation** - a residual magnetic field existing in the sample of a highly permeable material due to the response of magnetic moments in the sample to the applied magnetic field in a manner that the external field is partially cancelled or magnified.

Eigenmodes - two orthogonal linear states of light polarisation propagating in the optically transparent medium.

Ellipticity - elliptical polarisation of light (see page 34)

Extinction ratio - the ratio between the transmission of the two orthogonal wave components passing through a polariser, of which one is parallel to the polariser axis.

Magnetostriction - change in the dimensions of a ferromagnetic material, such as iron or nickel, produced by a change in the direction and extent of its magnetisation.

**Nyquist frequency** - the minimum sample rate to retain all of the signal information of bandwidth B, equal to or greater than 2B.

**Quantisation** - the process of conversion of the sampled analogue quantity to a finite-length digital word. Assuming a random input signal the errors associated with the quantisation process are white and uncorellated, and yield a best-case signal to noise ratio of around 6n dB, where n is the number of bits in the output word.

**Sampling** - capture of a continuously varying quantity at a precisely defined instant in time.

# 1. Introduction

## 1.1. Justification for and Introduction to Research

Electric energy is one of the fundamental resources of modern industrial society. Electric power is available to the user instantly, at the correct voltage and frequency, and exactly in the amount that is needed. This remarkable performance is achieved through careful planning, design, installation and operation of a very complex network of generators, transformers, and transmission and distribution lines. The fundamental requirement for safe and efficient operation of this network is the measurement of electric current. This allows utilities to determine the loading of various sections of the network for energy trading or stability purposes, and is used as an input to protection devices to provide automatic disconnection of the network in the event of a fault.

At present, the current measuring and monitoring functions are delivered mostly by instrument current transformers (CTs) which have been widely used for over a 100 years, and provide the most accurate and reliable means of current measurement. Because of decades of experience with conventional CTs, there exists a great deal of confidence in the performance of these devices and the operational principles and issues involved in their exploitation are generally well known and familiar to all power engineers.

However, there are a number of significant problems associated with conventional current transformers which could have been solved altogether if a radical change of concept of current sensing, such as utilisation of fibre-optic technology, had been widely accepted. The problems associated with conventional CTs can be recognised in the three major areas:

#### safety issues

High voltage current transformers require extensive electrical insulation between the secondary windings and the high voltage circuit, which is normally provided by oil impregnated paper insulation, housed in a bath of oil enclosed within a porcelain insulator. During the device operation, if the CT secondary is open-circuited (due to a fault or a human mistake) then potentially lethal voltages can be generated, hazardous both to personnel and possibly causing a serious damage (even an explosion) to the unit.

#### • costs of manufacture, installation and maintenance

The manufacture of high voltage CTs involves a great deal of manual labour which adds to the cost and also results in inconsistent quality of production. Due to the large size and weight of single units, additional space and lifting gear are required during their manufacture, storage, transportation and installation. In addition, maintenance requirements, such as periodic monitoring of oil or SF<sub>6</sub> insulation within the insulator stack and after-service recycling process, amount to significant lifecycle costs for a conventional CT.

#### • limited functionality

Efforts to optimise power system operation and utilisation have resulted in new fast acting control and operational procedures of protection devices which require higher frequency measurements. In addition, increased use of power electronic devices on the power network require improved harmonic and dc measurements to assist in power quality assessment and to monitor system stability<sup>1,2</sup>. These requirements demand higher and wider bandwidths from the current measurement devices, which in many cases cannot be delivered by conventional CTs.

An increasing attention is gained by other competitive current transducer technologies, in particular Rogowski coils and Hall effect devices, which in some cases, may surpass the function and accuracy features of the conventional current transformers. Nevertheless, the lack of inherent electrical insulation in these devices places them in the same league together with conventional CTs. In the author's view, the only genuine alternative to the conventional current sensing technology is an

optical current transducer (OCT) with its inherent electrical insulation facilitated through the use of optical addressing fibres.

Fibre-optic sensors have naturally evolved from the communication industry, following the advances in the production of optical fibres with excellent transmission properties. The maturity of the optical fibre communication technology led to the development of many advanced optoelectronic and fibre optic components, e.g., semiconductor lasers and LEDs, photodetectors, couplers, connectors etc. This has accelerated work on optical fibre sensors and enabled further developments in the field after the definition of specific properties required from the optoelectronic devices for sensing applications. Extensive research and development activity has resulted in the design and realisation of optical fibre sensors for the measurement of many physical and chemical measurands<sup>3-6</sup>.

As a result of these technological advances, also optical methods of current measurement have been proposed<sup>7-9</sup> as alternatives to the conventional CTs. Optical current transducers offer many advantages including inherent high voltage insulation, immunity to electromagnetic interference, enhancement in signal bandwidth and dynamic range, ease of integration into future digital control and protection systems and reduced costs. Additional benefits include reduced size and weight of the transducers compared to the conventional devices providing easier installation and potentially reduced substation land requirements.

The research contained in this thesis centres on the implementation of the magnetooptic effect (discovered by Michael Faraday in 1845) to the construction of an optical current transducer. Although the underlying concept is relatively straight forward, the practical implementation of such a device is far from trivial and requires deriving suitable methods to overcome deficiencies such as vulnerability to vibration, sensitivity to temperature changes and errors associated with the magnetic cross-talk. The techniques to overcome the above environmental effects are proposed in this thesis, and it is believed that this will contribute significantly to the process of commercial utilisation of optical current measurement technology in the near future.

#### 1.2. Primary Objectives and Outcomes of the Research

The research reported in this thesis was undertaken in collaboration with Rolls-Royce T&D, (latterly VATech Reyrolle Ltd.) and its remit was to develop an unlinked optical current transducer and associated interrogation systems delivering current measurement functions suitable for protection and metering applications within the electric power industry.

Building upon the research of A. Cruden<sup>10</sup>, who successfully developed a range of prototype current sensors and basic interrogation opto-electronic units, a number of significant problems associated with the OCT operation have been identified. These problems can be attributed mostly to the deficiencies in the sensor performance with respect to the influence of environmental factors, such as vibration, temperature and magnetic cross-talk effects. In practical implementations of the proposed measurement system, these deficiencies will cause unacceptable increase in output errors and would require compensation to meet stringent accuracy requirements demanded from the current measurement instrument.

In addition, the nature of the polarimetric demodulation technique employed in the proposed optical current sensor design, gives rise to the non-linear response characteristic of the device and is a source of a significant error at the higher modulation levels of the measured signal. It is therefore desirable to facilitate the linearisation function of the device characteristic.

The research work presented in this thesis is related specifically to compensation of environmental factors within operation of the Faraday Effect based Optical Current Transducer (OCT) using digital signal processing techniques. The thesis analyses measurement errors within the optical current sensor attributed mainly to thermal influences, vibration induced noise and magnetic cross-talk. It is proposed that the use of a fully automatic, real time, processing facility, as developed within this research work, for implementation of software based temperature, vibration and magnetic cross-talk compensation schemes will satisfy the accuracy specifications demanded from the OCT.

It is also proposed, that the same DSP system can facilitate the linearisation of the sensor response characteristic in real time operation and increase the maximum modulation level of the measured signal. This will allow for use of an extended sensor dynamic range and relax some design requirements of the photodetector circuit.

The objectives of this work can be summarised as follows:

- to identify the most promising optical current sensing technique on the basis of the immense research work carried out by many researchers since the early 1970s and define function and accuracy requirements of the OCT
- to select the most appropriate optical sensing medium for the OCT designated for the electricity industry applications and revise the methods of the sensor head manufacture
- to investigate and quantify the external factors which limit the OCT performance,
   such as vibration, temperature and magnetic cross-talk effects
- to propose methodologies for vibration, temperature and cross-talk compensation of the sensor
- to implement the developed compensation schemes into an integrated sensor interrogation system based on digital signal processing and facilitate additional functions, such as autocalibration and linearisation of the sensor transfer characteristic

The novelty of the research reported in this thesis lies primarily in the following areas:

- manufacture of a sensor head using multi-pass reflective arrangement of a sensing element with implementation of a novel active alignment method
- development of a robust sensor interrogation unit based on a digital signal processing system and real time software procedures for conditioning of the OCT output signal
- development and real time software implementation of a vibration compensation technique for the OCT, based on the non-reciprocal property of the Faraday effect and bi-directional arrangement of the current sensor interrogation scheme with alternately pulsed light sources and time gated photo-receivers
- development and real time software implementation of a temperature compensation technique with utilisation of a Fibre Bragg Grating (FBG) sensor used to derive the OCT temperature
- real time software implementation of the OCT linearisation routine
- demonstration of both ac and dc current measurement capabilities of the current sensor
- development of a methodology for magnetic cross-talk compensation based on a parallel processing of the information from all three phases to reject the cross-talk components

#### 1.3. Thesis Outline

The thesis is divided into nine major chapters which are described briefly below:

Chapter 2 gives an overview of conventional current measurement techniques, in particular those suitable for the medium to high voltage electricity networks, and discusses the operational features and principles of the conventional current sensing devices, thereby providing an introduction to the application domain in which the research described in this thesis is applied. The advantages and limitations of the conventional technology are presented and the need for an alternative means of

current sensing, namely fibre-optic sensors with inherent electrical insulation, is manifested.

Chapter 3 forms the theoretical basis to the description of optical principles and mechanisms upon which the optical measurement process can be realised in practice. The essential optical phenomena relevant to the operation of many optical fibre sensing systems are explained on the basis of the classical theory of light propagation and interaction of light with matter using Maxwell equations.

Chapter 4 provides an overview of the available optical fibre sensor technology and presents a diversity of solutions which can be applied in the fibre-optic sensor design. A technical overview of optical fibres is given, describing their basic properties, transmission characteristics and birefringence effects. This is followed by a description of the basic techniques and configurations used in optical fibre sensors.

Chapter 5 reviews a diverse range of optical current measurement methods, in particular those with relevance to the high voltage electricity industry. Main issues of environmental effects on the operation of optical current transducers are introduced and various techniques to overcome these effects are presented. Building upon the research by A. Cruden<sup>10</sup>, the author's preferred type of the optical current transducer and the sensor head construction are described in detail along with the novel approaches to the sensor head manufacture.

Chapter 6 concentrates on the external factors responsible for the current sensor performance limitations, i.e., vibration, temperature and magnetic cross-talk effects. The physical grounds behind the above effects are studied in detail and the potential influence of these factors on the OCT performance is quantified. On that basis appropriate active compensation methods are proposed.

Chapter 7 details the development of a flexible digital signal processing (DSP) unit for use with optical current transducers and provides a functional description of the

developed hardware and software modules. The implementation of software solutions for the necessary compensation schemes in the optoelectronic system such as: autocalibration, digital filtering, OCT vibration and temperature compensation, and the sensor response characteristic correction is presented. A potential for DSP implementation of the magnetic cross-talk compensation scheme is investigated and the methodology to implement a 3-phase optical current measurement system into integrated DSP software solution is demonstrated.

This chapter also investigates the issues associated with the analogue-to-digital conversion process and provides recommendations on how to select an OCT for operation with a given analogue-to-digital converter (and vice-versa) in order to meet stringent accuracy requirements for metering and protection class instruments within the power industry.

Chapter 8 reports on the extensive experimental work carried out during the development of the prototype optical current sensors and the associated interrogation systems. The reported testing carried out in the laboratory and field conditions concentrates on the engineering evaluation of the range of prototype current sensors, interrogating optoelecronics, signal processing hardware and the relevant DSP software modules. A relative success of the developed vibration and temperature compensation methods for the OCT is also demonstrated.

Finally, Chapter 9 details the conclusions derived from the research contained in this thesis. Future work, which the author feels may prove particularly beneficial, is also elaborated on.

#### 1.4. Associated Publications

The following publications have arisen from the research detailed in this thesis:

- W. Wójcik, P. Niewczas, A. Kotyra, "Review of Optical Current Measurement Methods", IV Konferencja Naukowa, Technologia i Zastosowanie Œwiat³owodów, Krasnobród 1996, Poland,
- A. Cruden, I. Madden, C. Michie, P. Niewczas, J.R. McDonald and I. Andonovic, "Optical current measurement system for high voltage applications", Measurement: Journal of the International Measurement Confederation, Vol.24, No. 2, pp.97-102, 1998,
- W.C. Michie, A. Cruden, P. Niewczas, W. I. Madden, J.R. McDonald, A. Kinson, "Transient Voltage Instability Investigation Using Optical Voltage Sensor", IEEE Power Engineering Review, Vol.19, No.3, pp.55-56, 1999,
- A. Cruden, W.C. Michie, J.R. McDonald, W.I. Madden, P. Niewczas, and I. Andonovic, "Advanced optical sensors for transmission and distribution applications", Paper 99TD178, IEEE Transmission and Distribution Conference, New Orleans, April 1999,
- P. Niewczas, A. Cruden, W.C. Michie, W.I. Madden, J.R. McDonald, I. Andonovic, "Error analysis of an optical current transducer operating with a digital signal processing system", Proceedings of the 16th IEEE Instrumentation and Measurement Technology Conference, Vols. 1-3, Ch. 349, pp.1160-1165, 1999,
- P. Niewczas, A. Cruden, W.C. Michie, W.I. Madden, J.R. McDonald and I. Andonovic, "A vibration compensation technique for an optical current transducer", Optical Engineering, Vol.38, No.10, pp.1708-1714, Oct. 1999,
- W.I. Madden, W.C. Michie, A. Cruden, P. Niewczas, J.R. McDonald and I. Andonovic, "Temperature compensation for optical current sensors", Optical Engineering, Vol.38, No.10, pp.1699-1707, Oct. 1999,

- P. Niewczas, W.C. Michie, A. Cruden, W.I. Madden and J.R McDonald, "Magnetic cross-talk compensation for an optical current transducer", accepted for presentation at IEEE Instrumentation & Measurement Technology Conference, 01-05 May 2000,
- P. Niewczas, W.C. Michie, W.I. Madden, A. Cruden and J.R. McDonald, "Field evaluation of FR5 glass optical current transducer", accepted for presentation at EOS/SPIE Symposium on Applied Photonics, 22-25 May 2000,
- P. Niewczas, W.I. Madden, W.C. Michie, A. Cruden, J.R. McDonald, I. Andonovic and N. Coe, "Progress towards a protection class optical current sensor", submitted for publication in Power Engineering Letters, June 1999.

Other publications on related topics are:

A. Cruden, Z. Richardson, J.R. McDonald and I. Andonovic, "Current and voltage measurement using optical crystal based devices", IEE Power Division Discussion Meeting on New Methods of Measuring Current and Voltage in Distribution and Transmission Systems, London, June 1995,

A. Cruden, Z. Richardson, J.R. McDonald and I. Andonovic, "Optical crystal based devices for current and voltage measurement", IEEE Transactions on Power Delivery, Vol. 10, No. 3, pp.1217-1223, July 1995,

A. Cruden, Z. Richardson, J.R. McDonald, I. Andonovic, W. Laycock, A. Bennett and K. Brewis, "Novel protection and monitoring functions applying optical current and voltage transducers", Paper 34-104, CIGRE, Paris, 1996,

A. Cruden, Z.J. Richardson, J.R. McDonald, I. Andonovic, W. Laycock and A. Bennett, "Enhanced measurement and quality of supply monitoring utilising optical current and voltage transducers", 6th International Conference on Developments in Power System Protection, Nottingham, Mar. 1997,

A. Cruden, Z.J. Richardson, J.R. McDonald, I. Andonovic, W. Laycock and A. Bennett, "Compact 132 kV combined optical voltage and current measurement system", IEEE Transactions on Instrumentation and Measurement, Vol.47, No.1, pp.219-223, 1998,

## 1.5. Chapter References

- 1) A. Wright and C. Christopoulos, "Electrical power system protection", Chapman & Hall, London, 1993,
- 2) S. H. Horowitz, A. G. Phadke, "Power System Relaying", Research Studies Press Ltd., Taunton, Somerset, England, 1992,
- J. Dakin, B. Culshaw, "Optical fiber sensors: systems and applications", Volume2, Artech House, Inc., 1989,
- 4) J. Dakin, B. Culshaw, "Optical fiber sensors: applications, analysis, and future trends", Volume 4, Artech House, Inc., 1997,
- 5) E. Udd, "Fiber optic sensors: an introduction for engineers and scientists", New York: Wiley, 1991,
- 6) J. Dakin, B. Culshaw, "Optical fiber sensors: principles and components", Volume 1, Artech House, Inc., 1988,
- 7) B. M. Pressmann, "The TRASER system for light coupled current measurement at EHV", Proc. SPIE, 21: pp 93-102, 1975,
- A. Brown, J. Zinkernagel, "Optoelectronic electricity meter for high-voltage lines", IEEE Transaction on Instrumentation and Measurement, IM-22(4), pp. 394-399, 1973,
- 9) A. J. Rogers, "Optical Measurement of Current and Voltage on Power Systems", Electric Power Applications, Vol. 2, No. 4, Aug 1979, pp. 120-124,
- 10) A.Cruden, "Electric Current Measurement using crystal based, magneto-optic point field sensors", PhD Thesis, University of Strathclyde, Department of Electronic and Electrical Engineering, June 1998.

## 2. Conventional Current Measurement Methods

#### 2.1. Introduction

The electricity power network requires constant current monitoring and measuring for protection and energy trading purposes. These functions are delivered mostly by instrument current transformers which have been widely used for over a century, and provide the most accurate and reliable means of current measurement. Due to the number of significant problems associated with conventional current transformers, there is an increasing interest in other competitive current transducer technologies which, in some cases, may surpass the function and accuracy features of the conventional current transformers. This chapter will discuss the main advantages and limitations of instrument current transformers, in particular for use in medium and high voltage power system networks, and will present the main competitive non-optical technologies exploited in current sensing, namely: Rogowski coils, Hall effect devices and magnetoresistive sensors.

#### 2.2. Conventional Current Transformer

The term current transformer (abbreviated as CT) is used to describe a piece of equipment consisting of a pair of mutually-coupled windings mounted around a core, usually of magnetic material. Such transformers are normally used to step down high currents flowing in their primary windings to a lower level suitable for feeding to measuring and protective equipment. Insulation associated with the primary windings provides isolation of the equipment from the primary power system voltage. The standard rating for the secondary current is either 1 A or 5 A.

An iron-cored CT operates as a series transformer, i.e., the primary winding is connected in series with the power circuit of interest. The CT itself can be constructed in a number of different ways: a ring type CT where the conductor is passed through the centre of a core; a bar primary CT where a fixed conductor constituting an integral part of the CT unit passes through the centre of the core and circuit

connections can then be made to either end of the bar; a wound type CT where the primary is in the form of winding around the core. In all cases the CT secondary consists of a winding around the core, with the electrical isolation between primary and secondary provided by a number of means: insulating tape; cast resin; oil; dielectric gas such as sulphur hexaflouride (SF<sub>6</sub>) or any combination of these.

Figure 2-1 illustrates the different types of medium voltage CTs, namely ring (or window), bar and wound types, and Figure 2-2 illustrates high voltage (132kV) CT installation.



Figure 2-1 Medium voltage ring (window), bar and wound type CTs



Figure 2-2 High voltage CTs (132kV)

#### 2.2.1. Equivalent Circuit

In principle, current transformers behave similarly to all two-winding transformers and can therefore be represented by the well-known equivalent circuit shown in Figure 2-3. Because the connected burdens are normally of low impedance, and because of the turns ratio, the voltage drop across the primary winding is negligible. For this reason, primary winding resistance and reactance may normally be omitted in the equivalent circuit which now can be simplified to that shown in Figure 2-4.

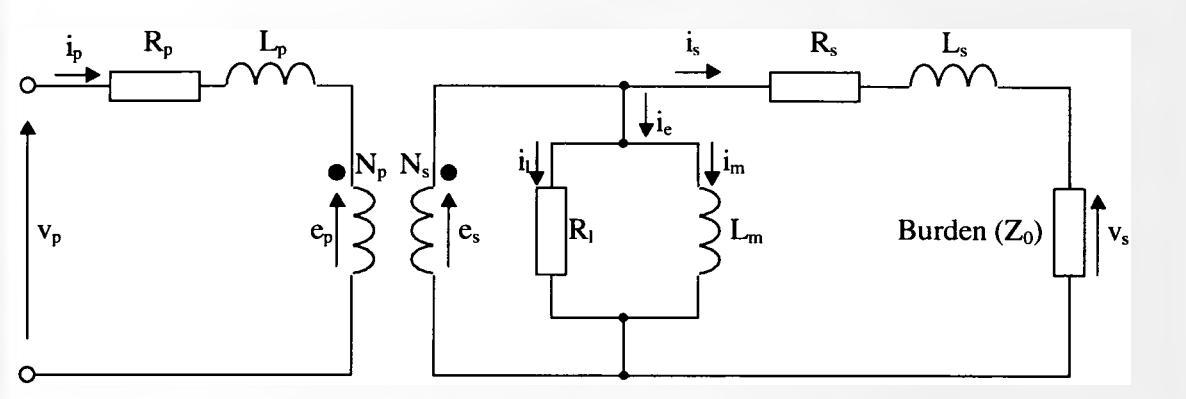


Figure 2-3 Equivalent circuit of a current transformer

#### where:

v<sub>p</sub> - primary voltage

R<sub>p</sub> - primary resistance;

L<sub>p</sub> - primary inductance;

N<sub>p</sub> - primary turns;

N<sub>s</sub> - secondary turns;

Z<sub>0</sub> - burden impedance;

R<sub>1</sub> - loss resistance;

L<sub>m</sub> - magnetising inductance;

e<sub>p</sub> - primary emf;

e<sub>s</sub> - secondary emf;

v<sub>s</sub> - secondary output voltage;

i<sub>p</sub> - primary current;

is - secondary current;

i<sub>e</sub> - exciting current;

R<sub>s</sub> - secondary resistance;

L<sub>s</sub> - secondary inductance.

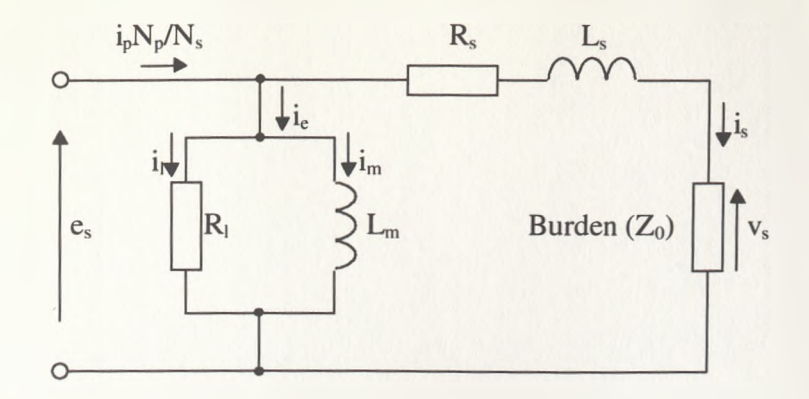


Figure 2-4 Equivalent circuit of a current transformer referred to the secondary

The above simplified equivalent circuit can be used to represent any current transformer operating with any burden and primary current under either steady state or transient conditions.

#### 2.2.2. CT Errors

A CT's main purpose is to scale down the primary current as accurately as possible. However, it is evident from the vector diagram (Figure 2-5) that errors arise because of shunting of the burden by the exciting impedance.

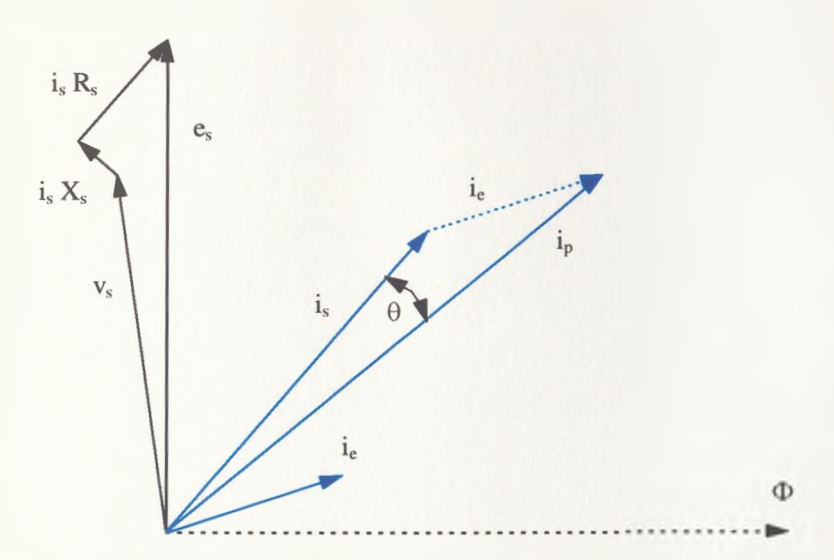


Figure 2-5 Equivalent circuit and vector diagram of a current transformer referred to the secondary

where:

 $\theta$  - phase angle error;

Φ - flux;

i<sub>s</sub>R<sub>s</sub> - secondary resistance voltage drop;

i<sub>s</sub>X<sub>s</sub> - secondary reactance voltage drop;

Two types of errors are introduced:

• Current or ratio error is defined as the amount by which the actual transformation ratio departs from the rated value K<sub>n</sub>.

$$Current error = \frac{\frac{|I_p|}{|I_s|} - K_n}{K_n}$$
 (2-1)

• Phase error is defined as the angle θ between the phasor representing primary current i<sub>p</sub> and the secondary current i<sub>s</sub>. It is regarded as positive when the secondary current leads the primary current.

A reduction of secondary winding by one or two turns is a usual means of compensation for the small current error introduced by the i<sub>e</sub> component. No corresponding correction can be made for phase error, however, for moderately reactive burdens the value of phase error is small.

• Composite error is defined<sup>2</sup> as the rms value of the difference between the ideal secondary current and the actual secondary current. It includes current and phase errors and the effect of harmonics in the exciting current. When the leakage flux can be neglected, composite error corresponds to the rms value of the exciting current, usually expressed as a percentage of the primary current<sup>1</sup>.

Composite error = 
$$\frac{|I_e|}{|I_p|} \times 100\%$$
 (2-2)

## 2.2.3. Accuracy Limit Current

CTs designed to work in conjunction with protective equipment must endure expected fault current levels and extend their expected accuracy beyond the rating value of the current, up to the highest relevant current. This value is termed as an 'accuracy limit current'. It may be expressed as a primary or equivalent secondary value. The ratio of the accuracy limit current to the rated current is known as the 'accuracy limit factor'. Standard accuracy limit factors used in British practise are according to IEC 44-1: 1996 and these are 5, 10, 15, 20 and 30.

#### 2.2.4. Accuracy Requirements

The electricity industry demands clearly specified accuracy from current transformers destined to work on various transmission systems and designed for various purposes. The accuracy specifications for metering and protection CTs are stated in IEC 44-1: 1996 and are briefly discussed in the following paragraphs.

#### 2.2.4.1. Metering CTs

For metering current transformers the accuracy class is designated by the highest permissible percentage current error at rated current prescribed for the accuracy class concerned. The standard accuracy classes for metering CTs are: 0.1, 0.2, 0.5, 1, 3 and 5. For Classes 0.1 to 1 the current error and phase displacement at rated frequency should not exceed the values given in Tables 2-1 and 2-2 when the secondary burden is any value from 50% to 100% of the rated burden. For Class 3 and Class 5, the current error at the rated frequency should not exceed the values given in Table 2-3.

Accuracy class	±Percentage current error at percentage of rated current below			current shown
	5	20	100	120
0.1	0.4	0.2	0.1	0.1
0.2	0.75	0.35	0.2	0.2
0.5	1.5	0.75	0.5	0.5
1.0	3.0	1.5	1.0	1.0

Table 2-1 Limits of current error for accuracy classes 0.1 to 1

	±Phase displacement at percentage of rated current								
			<b> </b>	ıs			Min	utes	·
% of rate current		5%	20%	100%	120%	5%	20%	100%	120%
	0.1	13.9	7.4	4.6	4.6	15	8	5	5
Accuracy	0.2	27.8	13.9	9.3	9.3	30	15	10	10
Class	0.5	83.3	41.7	27.8	27.8	90	45	30	30
	1.0	166.7	83.3	55.6	55.6	180	90	60	60

<u>Table 2-2 Maximum phase displacement specifications for metering current transformers</u>

Accuracy class		entage current error at percentage of rated current shown below	
	50	120	
3	3	3	
5	5	5	

Table 2-3 Limits of error for accuracy Class 3 and Class 5

#### 2.2.4.2. Protection CTs

For protective current transformers the accuracy class is designated by the highest permissible percentage composite error at the rated accuracy limit current prescribed for the accuracy class concerned, following by the letter 'P' (to indicate protection). The standard accuracy classes for protective current transformers are 5P and 10P. At rated frequency and with rated burden connected, the current error, phase displacement and composite error should not exceed the values given in Tables 2-4 and 2-5.

Accuracy class	Current error at rated	Current error at rated accuracy limit
	primary current (%)	(5,10,15,20,30)x primary current (%)
5P	±1	±5
10P	±3	±10

Table 2-4 Limits of current error for accuracy Class 5P and Class 10P

Accuracy class	±Phase displacement at rated primary current		
	μs	Minutes	
5P	55.6	1.8	
10P	-	-	

Table 2-5 Maximum phase displacement specifications for protection current transducers

#### 2.2.5. Transient Behaviour of a CT

Under severe fault conditions or during some transients the CT often cannot be considered as a linear device. For example the current level flowing through the CT may be sufficient to saturate the core material which consequently leads to the distortion of the current waveform. This effect must be taken into consideration when the performance of the current transformer operating with the protection equipment is being studied. The dynamic response of the CT must be known before the protection operation can be properly determined, and often a detailed numerical model of the CT is required when studying dynamic protection performance<sup>3</sup>.

#### 2.2.6. CT Voltage Withstand

Voltage withstand of a CT is an integral part of the decoupling of the measurement/protection circuit from the HV high current primary circuit. Numerous tests have to be carried out to ensure the relevant insulation strength is met for the different fault conditions found in power systems, e.g, power frequency overvoltages tests, dc overvoltage tests, impulse voltage tests and flashover tests in a variety of polluted atmospheres. It is this insulation factor that most affects both the size and cost of HV CTs.

# 2.2.7. Summary Appraisal of Iron-Cored CTs

The iron-cored CT is generally very robust, mechanically simple, and accurate means of achieving a current measurement. For low voltage use, CTs are very cheap instruments, however at medium and particularly high voltage levels (132kV and

above) their design becomes complicated and expensive due to the requirements for extensive electrical insulation.

Current transformers are relatively stable devices over a wide range of temperatures and vibration levels yet do suffer from a number of significant problems in other areas. The main reason for these problems is the iron-core itself, causing ratio and phase errors, being prone to saturation and remanence effects and generating high voltages if the secondary winding is open-circuited. Additionally, the core makes the CT a very heavy instrument and difficult to install due to the large size and linked nature of the core. The CT ultimate performance is restricted to a relatively low frequency range (depending on the core material), and due to its nature, is not suitable for use on HVDC transmission systems or for dc traction systems.

# 2.3. Competitive Current Measuring Devices

#### 2.3.1. Rogowski Coil

A Rogowski coil, also called an air-cored coil, is a closely and evenly wound coil of N turns/m on a non-magnetic, usually plastic, former of constant cross sectional area, as shown in Figure 2-6. Usually, one end of the winding (the 'free' end) is returned to the other end along the central axis of the former to minimise the magnetic cross-talk.

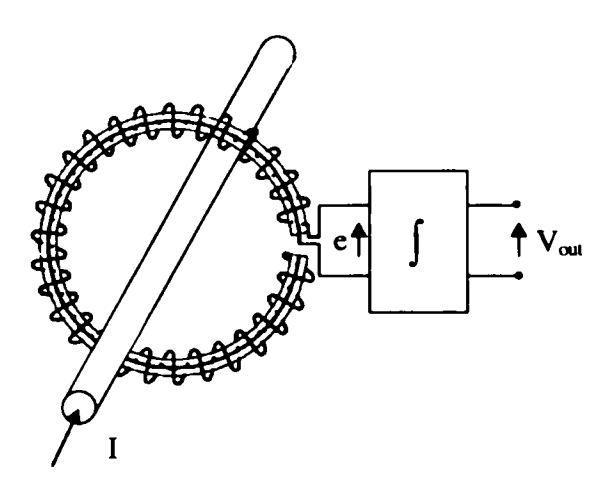


Figure 2-6 Basic Rogowski transducer

Rogowski coil theory is based upon Fraday's Law that states, "The total electromotive force induced in a closed circuit is proportional to the time rate of change of the total magnetic flux linking the circuit". Provided the coil constitutes a closed loop with no discontinuities, a voltage output e is proportional to the time rate of change of the magnetic field produced by the primary current I according to the relationship<sup>4</sup>

$$e = K \frac{dI}{dt}$$
 (2-3)

where, K (Vs/A) is the coil sensitivity and I is the current to be measured encircled by the loop.

The loop does not need to be circular and e (in principle) is independent of the current position in the loop. To reproduce the current waveform as a measurement signal directly proportional to the encircled current, the coil voltage must be accurately integrated.

The op-amp integrator, in its simplest form, with an input resistor R and feedback capacitor C, as shown in Figure 2-7, has a gain  $1/(2\pi fCR)$  at frequency f. The integrator gain increases as frequency is reduced and in theory will become infinite as the frequency approaches zero. This would result in unacceptable dc drift and low frequency noise; hence the integrator frequency has to be limited at low frequencies. This limitation is achieved by placing a low pass filter in parallel with the integrating capacitor as shown in Figure 2-7.

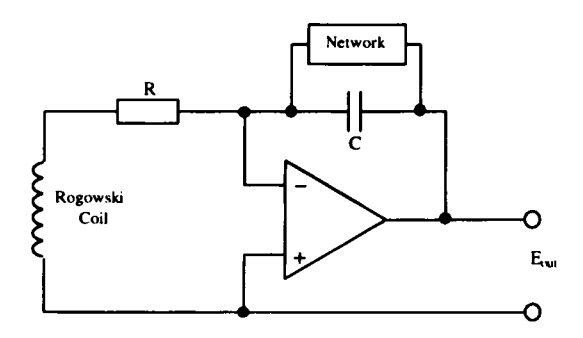


Figure 2-7 Rogowski coil and a basic integrator circuit

Rogowski coils have been in limited use since 1912 but have recently become popular due to advances in integrator design. Advantages of this type of current transducer include: output isolation from the primary circuit, large measurement range, high bandwidth (up to 2.5MHz), good accuracy<sup>5</sup> (<2%). The absence of an iron core virtually eliminates circuit loading and saturation concerns and contributes to an almost unlimited overcurrent tolerance. Modern Rogowski coils have an extremely wide measurement range<sup>5</sup> - from 30A to more than 100kA full scale, with sensitivities ranging from 0.01mV/A to 100mV/A. The most significant feature of a flexible Rogowski coil is its ability to encircle large, awkward geometry conductors.

The maximum current range limitation exists due to the finite gain-bandwidth and output swing of the integrator electronics. Variables such as number of windings, cross sectional area, amplifier gain, zero drift and, in particular, shielding, affect di/dt. The lower limit of di/dt is determined by the integrator design.

Accurate measurement is dependent on a uniform coil cross section. Bending flexible coils into a closed path deforms the circular cross section into an oval, decreasing the turns area. The interruptions in turns at the ends of the coil or "gap" can also cause non-uniformities that contribute to position sensitive errors and the magnetic cross-talk from the adjacent conductors. The Rogowski transducer is also noted for the temperature dependence of its output signal<sup>4</sup>.

Nevertheless, there is a growing interest in these devices for low and medium voltage applications, they are now offered as replacement current measurement units in a number of LV/MV switchgear cubicles<sup>6</sup>. The use of Rogowski coils in high voltage applications is however questionable as there remains a problem of providing suitable insulation for running the signal wires from the HV conductor to earth.

#### 2.3.2. Hall Effect Device

The "Hall Effect" is named after Edwin Hall who discovered the phenomenon in 1879. The Hall Effect principal states that when a current carrying conductor (or semiconductor) is placed in a magnetic field, a voltage will be generated perpendicular to the direction of the field and the flow of current (see Figure 2-8). This is a direct consequence of a Lorentz force interacting with the moving charged particles, i.e., electrons or holes.

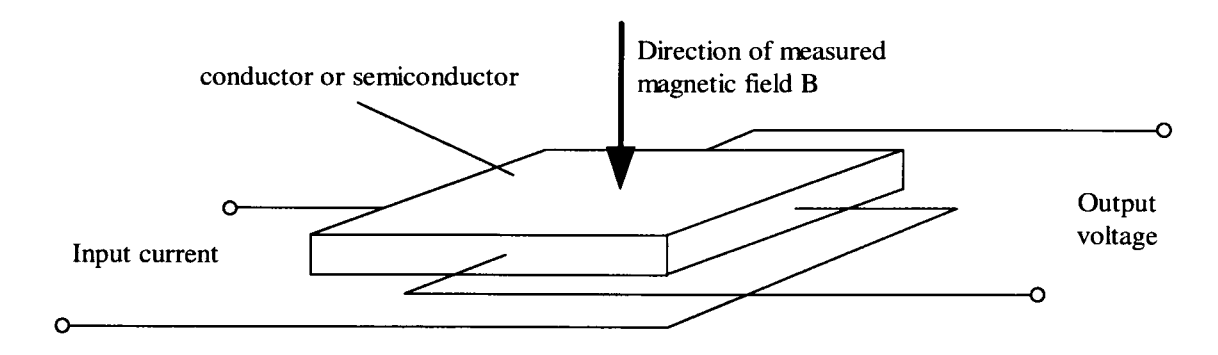


Figure 2-8 Hall Effect device

If the external magnetic field is produced by a current in a separate conductor then the Hall effect device can be used to determine this current. The Hall effect device is capable of measuring static dc currents and offers a measurement bandwidth in excess of conventional iron-core CTs<sup>7</sup> (100kHz). However, most commonly, such a device is placed within the air gap of an iron-core enclosing the conductor. This allows to concentrate the magnetic field in order to increase measurement sensitivity, and to minimise the effect of stray magnetic fields.

Hall sensors can operate in a closed loop configuration using feedback to improve the device performance<sup>5</sup>. In such a configuration the Hall element is placed within the air gap of a flux concentrator onto which is wrapped a feedback coil. The Hall element functions as the input error amplifier and is optimised for sensitivity. Together with a high gain, high current output amplifier, the circuit produces a current which is fed to the feedback coil to null the magnetic circuit and close the magnetic loop. This current

may then be used directly as a current output, directly proportional to the measured current encircled by the flux concentrator.

The main disadvantage of a Hall effect device is the need for electrical wiring to measure the output voltage (similarly to all the conventional current measuring devices) and additionally to deliver an input current to the Hall chip. Furthermore, the Hall probe is sensitive to temperature changes<sup>7</sup> and may require temperature compensation in order to maintain the required accuracy. The use of flux concentrator brings problems similar to those of an iron-core current transformer.

# 2.3.3. Magnetoresistive Sensors

Magnetoresistive (MR) devices, originally designed for sensitive high-speed disk drive heads, measure an induced magnetic field by detecting a change in the sensing material resistance depending on the incident magnetic field. Because the MR element is much more sensitive than a traditional Hall element, these transducers may be compensated in a fashion similar to the closed-loop Hall sensors, but without the need for a flux-concentrating core or multiple compensation windings<sup>5</sup>. The primary's field is detected by a sensor element in the form of a Wheatstone bridge. Using a special layout arrangement, the sensor detects only magnetic field gradients and rejects the ambient field. The current compensation ratio of the device does not depend on a turns ratio, but rather on the ratio of fields impinging on the MR elements from both the primary turn and compensation turn.

Compared to traditional Hall elements, these sensors (Figure 2-9) feature smaller size but a slightly lower bandwidth<sup>8</sup> (20-50kHz) and a limited variety of current ranges. Their coreless design makes them free of both the advantages of a transformer (true current measurement) and its disadvantages (size, weight, limited bandwidth).



Figure 2-9 Commercial magnetoresistive sensor<sup>8</sup>

The absence of a core allows MR devices to be integrated directly into a hybrid module. To provide voltage isolation, the solid primary conductor is mounted on the bottom of the substrate. Their small size, low weight and "wire-free" packaging suit these sensors to many applications requiring the measurement of ac and dc currents.

# 2.4. Summary

In this chapter an overview of conventional current measurement techniques have been presented. The instrument current transformer with its high accuracy and familiar technology still plays the main role in applications concerning the electricity power industry. Although, the other competitive current transducers, in particular the Rogowski coil, are recently gaining an increased attention, their lack of inherent electrical insulation places them in the same league together with conventional CTs. The only true competitor to the conventional current sensing technology is an optical current transducer which does not require the extensive electrical insulation due to the use of non-metallic optical fibres to address the sensor. Next chapters will concentrate on the description of the optical fibre technology relevant to the operation principles of the optical current transducer.

# 2.5. Chapter References

 A. Wright and C. Christopoulos, "Electrical power system protection", Chapman & Hall, London, 1993,

- 2) IEC 44-1 International Standard, "Instrument transformers: Part 1: Current transformers", December 1996.,
- 3) A.Dysko, "A Dynamic Modelling Methodology for Protection System Performance Assessment", PhD Thesis, University of Strathclyde, Department of Electronic and Electrical Engineering, June 1998,
- 4) "Rogowski current transducers", Power Electronic Measurements Ltd, Nottingham, UK,
- 5) Compiled by F. P. Wahl, "Select Current Sensor Performance to Match the Application's Requirements", Power Conversion & Inteligent Motion Magazine, 1998,
- 6) A. W. Yacoub, H. Fink, "ZX1 A switchgear of tomorrow: Medium voltage switchgear with computerised functions", IEE Conference on Trends in Distribution Switchgear, Conf. Pub. pp. 37-43, No. 400, 1994,
- 7) Amploc Hall Effect Current Sensors Energy Science, Product Datasheet, Internet address: www.amploc.com, 1999,
- 8) Bell Technologies Inc., Product Datasheet, Internet address: www.belltechinc.com, 1999.

# 3. Essential Optics

## 3.1. Introduction

This chapter describes the basic optical properties, phenomena and techniques which are exploited in optical fibre sensing systems, in particular those applicable to the optical fibre sensors suitable for the electricity supply industry.

Firstly, the fundamental optical properties of the propagation of the light waves, polarisation and coherence are described. This is followed by a discussion of the interaction of light with matter which is the key to the operating principles of many optical fibre sensors. The phenomenon of birefringence, an important effect exploited in many different optical fibre sensing techniques is described next, together with practical components, e.g., quarter wave plates that are used to control the polarisation state of light. The fundamental property of optical activity in which a range of materials rotate the plane of polarisation of light is then described. Following this, a description is given on the principles on which many of the optical fibre sensors for applications in the power industry are based. These include, the Faraday effect, the magnetically induced optical activity used in magnetic field and current sensors, and the photoelastic effect, i.e., mechanically induced linear birefringence. Following this the electro-optic effect is outlined briefly, the phenomenon of linear birefringence induced by electric field used in electric field and voltage sensors.

The prime objective of this chapter is to provide a background of the basic optical principles upon which the operation of the optical fibre sensors described in the later chapters depends. Additionally, the chapter presents optical phenomena not related directly to the principles of the sensors operation, but which can potentially cause undesirable interference of environmental factors with a measured signal.

# 3.2. Propagation of Light Waves

The terms 'light' and 'optical' are generally used to describe the range of frequencies covering the infrared and visible parts of the electromagnetic spectrum. Maxwell's equations describe the relationships between the electric fields **E** and **D** and magnetic fields **H** and **B** of the electromagnetic light wave, which vary both spatially and temporally. The electromagnetic state of matter at a given point is described by four quantities:

- (i) the volume density of electric charge  $\rho$
- (ii) the volume density of electric dipoles, called the *polarisation* **P**
- (iii) the volume density of magnetic dipoles, called the magnetisation M
- (iv) the electric current per unit area, called the current density J

All of these quantities are considered to be macroscopically averaged in order to smooth out the microscopic variations due to the atomic makeup of all matter. They are related to the macroscopically averaged fields **E** and **H** by the following Maxwell equations<sup>1</sup>:

$$\nabla \times \mathbf{E} = -\mu_0 \frac{\partial \mathbf{H}}{\partial t} - \mu_0 \frac{\partial \mathbf{M}}{\partial t}$$
 (3-1)

$$\nabla \times \mathbf{H} = \varepsilon_0 \frac{\partial \mathbf{E}}{\partial t} + \frac{\partial \mathbf{P}}{\partial t} + \mathbf{J}$$
 (3-2)

$$\nabla \cdot \mathbf{E} = -\frac{1}{\varepsilon_0} \nabla \cdot \mathbf{P} + \frac{\rho}{\varepsilon_0}$$
 (3-3)

$$\nabla \cdot \mathbf{H} = -\nabla \cdot \mathbf{M} \tag{3-4}$$

where the permeability of the vacuum  $\mu_0=4\pi\cdot 10^{-7}\,kg\cdot m\,/\,s^2$  and the permittivity of the vacuum  $\epsilon_0=8.8542\cdot 10^{-12}\,(C\cdot s)^2\,/\,kg\cdot m^3$ .

If one introduces the abbreviation **D** for the quantity  $\varepsilon_0 \mathbf{E} + \mathbf{P}$ , known as the *electric displacement*, and the abbreviation **B** for  $\mu_0(\mathbf{H} + \mathbf{M})$ , called the magnetic induction, then Maxwell's equations assume the more compact forms:

(Faraday's law) 
$$\nabla \times \mathbf{E} = -\frac{\partial \mathbf{B}}{\partial t}$$
 (3-5)

(Ampere's law) 
$$\nabla \times \mathbf{H} = \frac{\partial \mathbf{D}}{\partial t} + \mathbf{j}$$
 (3-6)

(Gauss's law in electrostatic ) 
$$\nabla \cdot \mathbf{D} = \rho$$
 (3-7)

(Gauss's law in magnetostatics) 
$$\nabla \cdot \mathbf{B} = 0$$
 (3-8)

The response of conduction electrons to the electric field is given by the current equation (Ohm's law)

$$\mathbf{J} = \sigma \mathbf{E} \tag{3-9}$$

where  $\sigma$  is the conductivity. The constitutive relation

$$\mathbf{D} = \varepsilon \mathbf{E} \tag{3-10}$$

describes the aggregate response of the bound charges to the electric field. The corresponding magnetic relation is:

$$\mathbf{B} = \mu \mathbf{H} \tag{3-11}$$

where  $\varepsilon = \varepsilon_r \varepsilon_0$  and  $\mu = \mu_r \mu_0$ , and  $\varepsilon_r$  is the relative permittivity and  $\mu_r$  is the relative permeability of the medium.

An alternative way to express the response of the bound charges is

$$\mathbf{P} = (\mathbf{\varepsilon} - \mathbf{\varepsilon}_0) \mathbf{E} = \mathbf{\chi} \mathbf{\varepsilon}_0 \mathbf{E}$$
 (3-12)

which gives the proportionality between the polarisation and the impressed electric field. The proportionality factor

$$\chi = \frac{\varepsilon}{\varepsilon_0} - 1 \tag{3-13}$$

is known as the electric susceptibility. In the case of isotropic media, for example, glass,  $\chi$  is a scalar quantity having the same value for any direction of the applied electric field. For nonisotropic media, such as most crystals, the magnitude of the polarisation varies with the direction of the applied field and, consequently,  $\chi$  must be expressed as a tensor.

In free space  $\mu = \mu_0$ ,  $\varepsilon = \varepsilon_0$ ,  $\rho = 0$  and J = 0, and thus the equations become:

$$\nabla \times \mathbf{E} = -\mu_0 \frac{\partial \mathbf{H}}{\partial t} \tag{3-14}$$

$$\nabla \times \mathbf{H} = \varepsilon_0 \frac{\partial \mathbf{E}}{\partial t} \tag{3-15}$$

$$\nabla \cdot \mathbf{E} = 0 \tag{3-16}$$

$$\nabla \cdot \mathbf{H} = 0 \tag{3-17}$$

Taking the curl of both sides of equation (3-14) and substituting (3-15) results in:

$$\nabla \times (\nabla \times \mathbf{E}) = -\mu_0 \frac{\partial}{\partial t} (\nabla \times \mathbf{H}) = -\mu_0 \varepsilon_0 \frac{\partial^2 \mathbf{E}}{\partial t^2}$$
(3-18)

On expanding  $\nabla \times (\nabla \times \mathbf{E}) = \nabla (\nabla \cdot \mathbf{E}) - \nabla^2 \mathbf{E}$ , equation (3-18) becomes

$$\nabla^2 \mathbf{E} = \varepsilon_0 \mu_0 \frac{\partial^2 \mathbf{E}}{\partial \mathbf{r}^2}.$$
 (3-19)

This is a wave equation for E where the Laplacian operator  $\nabla^2$  describes the spatial variation of the field. A similar equation applies for the magnetic field vector  $\mathbf{H}$ .

The simplest form of solution to the wave equation (3-19) represents a plane wave travelling in the z-direction and may be written as<sup>2</sup>:

$$E_x = E_0 e^{i(\omega t - kz)}$$
 (3-20)

Equation (3-20) describes a wave linearly polarised in the x-direction with an angular frequency  $\omega$  and propagation constant  $k = 2\pi/\lambda$  where  $\lambda$  is the wavelength. The sinusoidal electric field excites a magnetic field in the orthogonal plane (y-direction) producing an electromagnetic field transverse to the direction of propagation TEM wave. The phase velocity of the wave in the free space is given by

$$c = \frac{\omega}{k_0} = \frac{1}{\sqrt{\epsilon_0 \mu_0}} = 2.998 \cdot 10^8 \,\text{m/s}$$
 (3-21)

If the wave propagates through a medium with relative permittivity  $\varepsilon_r$  and relative permeability  $\mu_r$  which are not unity then the phase velocity is now given by:

$$u = \frac{\omega}{k} = \frac{1}{\sqrt{\epsilon_0 \epsilon_r \mu_0 \mu_r}}.$$
 (3-22)

# 3.3. Polarisation Properties

Polarisation plays an important part in a variety of optical techniques and systems, including optical fibre systems and sensors. It is essential therefore to understand the

role of polarisation in such systems and the means by which the polarisation properties may be characterised.

The 'typical' sinusoidal solution of Maxwell's wave equation given by equation (3-19) is, of course, only one of an infinite number of such sinusoidal solutions. The general solution for a sinusoid of angular frequency  $\omega$  is given by:

$$\mathbf{E} = \mathbf{E}_0 e^{i(\mathbf{k} \, \mathbf{r} - \omega \mathbf{t})} \tag{3-23}$$

Here **E** and **E**<sub>0</sub>, are in general complex vectors and  $\mathbf{k} \cdot \mathbf{r} = x k_x + y k_y + z k_z$ , where  $(k_x, k_y, k_z)$  are the components of the propagation direction and (x, y, z) are the components of the point in the space where the field **E** is evaluated.

Considering, for simplicity, only plane monochromatic (single frequency) waves propagating in free space in the direction Oz, the general solution to the wave equation for the electric field can be expressed in the form:

$$E_x = e_x \cos(\omega t - kz + \delta_x)$$
 (3-24)

$$E_{y} = e_{y} \cos(\omega t - kz + \delta_{y})$$
 (3-25)

where  $\delta_x$  and  $\delta_y$  are arbitrary phase angles. Thus it is possible to describe this solution completely by means of two waves: one in which the electric field lies entirely in the xz plane, and the other in which it lies entirely in the yz plane (Figure 3-1). If these waves are observed at a particular value of z, say  $z_0$ , they take the oscillatory form:

$$E_{x} = e_{x} \cos(\omega t + \delta_{x}') \qquad \delta_{x}' = \delta_{x} - kz_{0} \qquad (3-26)$$

$$E_{y} = e_{y} \cos(\omega t + \delta_{y}') \qquad \delta_{y}' = \delta_{y} - kz_{0}$$
 (3-27)

and the tip of each vector appears to oscillate sinusoidally with time along a line.  $E_x$  is said to be linearly polarised in the direction Ox, and  $E_y$  is said to be linearly polarised in the direction Oy.

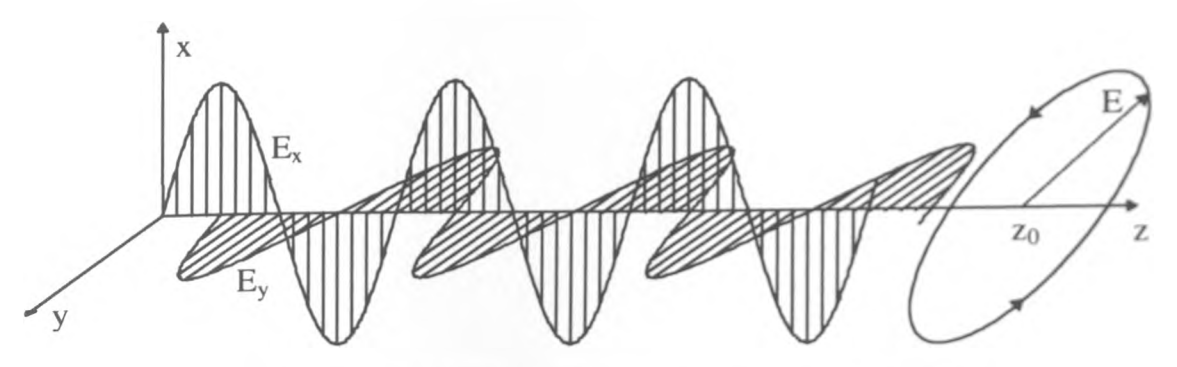


Figure 3-1 Polarisation components of the E wave

The tip of the vector which is the sum of  $E_x$  and  $E_y$  will in general describe an ellipse whose Cartesian equation in the xy plane at the chosen  $z_0$  will be given by

$$\frac{E_{x}^{2}}{e_{x}^{2}} + \frac{E_{y}^{2}}{e_{y}^{2}} + 2\frac{E_{x}E_{y}}{e_{x}e_{y}}\cos\delta = \sin^{2}\delta$$
(3-28)

where  $\delta = \delta_y$ '-  $\delta_x$ '.

Now, the state of polarisation (SOP) of an electromagnetic wave propagating along the z-axis may be ascertained from the path traced by the tip of the electric field vector **E** in the xy plane. Three states of polarisation can be defined:

# (i) Linear Polarisation

The electric field vector oscillates along a straight line in xy plane. Any linear polarised light can be resolved into two orthogonal components along the x and y axes,  $(E_x \text{ and } E_y)$  with a path difference of  $\delta = m\pi$ , where m is an integer. If m is 0 or an even integer, then the two components are in phase. Linear polarisation is specified by its orientation and amplitude.

#### (ii) Circular Polarisation

The tip of the electric field vector rotates in the xy plane. Circular polarisation arises from the superposition along the x and y axes of two linearly polarised waves of equal amplitude but differing in phase by  $\delta = \pm \pi/2$ . A phase difference of  $\delta = -\pi/2 + 2m\pi$ , where  $m = 0, \pm 1, \pm 2...$  gives rise to right circular polarised light, i.e., the electric field vector rotates clockwise when viewed looking towards the source; and a phase difference of  $\delta = \pi/2 + 2m\pi$  gives rise to left circular polarised light. Linearly polarised waves can be synthesised from two opposite polarised circular waves of equal amplitudes. The orientation of the x and y axes is immaterial, and circular polarised light can be specified by its amplitude and whether it is left or right polarised.

#### (iii) Elliptical Polarisation

The tip of the electric field vector rotates, tracing an ellipse in the xy plane, and the electric vector also changes in magnitude. Elliptical polarised light results from the superposition along the x and y axes of two linearly polarised waves of arbitrary (and different) amplitudes and phase difference. Elliptical polarisation is fully specified by its amplitude, ellipticity and the orientation of the major axes of the ellipse with respect to some convenient axes. Linear and circular polarisation can be considered as special cases of elliptically polarised light.

The polarisation properties of light waves are particularly important for propagation within anisotropic media in which the physical properties are dependent on direction. In this case the propagation characteristics for the component  $E_x$  will in general differ from those from  $E_y$ , so that the values of  $e_x$ ,  $e_y$  and  $\delta$  will vary along the propagation path. The polarisation state of the light will now become dependent upon propagation distance and on the state of the medium.

There are several formal ways of representing and handling polarisation and the transmission of polarised light through polarising medium such as birefringent materials. The most important of these are the Jones vectors and matrices<sup>3</sup> and the

Poincare sphere construction<sup>2</sup>. The Jones vectors provide a mathematical treatment of polarised light whilst Poincare sphere creates geometrical representation of polarisation.

# 3.4. Coherence Properties

The coherence of a wave describes the extent to which it can be represented by a pure sine wave. A pure sine wave has infinite extension and hence cannot exist in reality. Perfect coherence is thus unachievable, but it is nevertheless a valuable concept.

A beam of light can be considered as comprising of a discrete collection of photons, each with its own characteristic lifetime. The photon is essentially a wave train where the electric field exists for a short period of time, or propagation distance (see Figure 3-2).

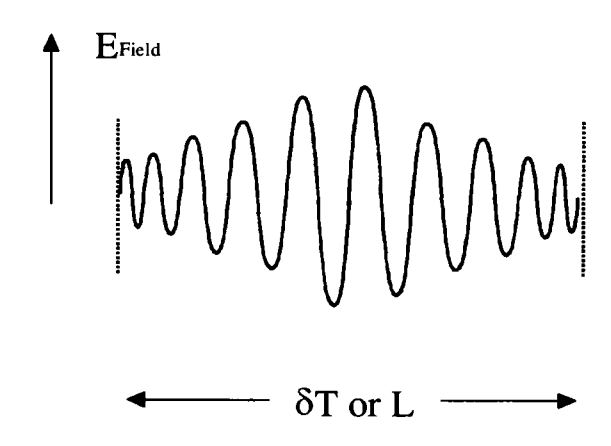


Figure 3-2 Wave train representation of a photon

The optical wave from a conventional light source is a collection of randomly generated photons with arbitrary phase relationships. The maximum distance L over which the phase of a light source can be predicted (the source coherence length) is directly related to the lifetime of the photon and can be expressed as

$$L = c\delta T \tag{3-29}$$

where c is the speed of light and  $\delta T$  is the photon lifetime.

The wave train associated with a single photon is not a pure sinusoid but can be considered as a series of sine waves of different frequencies and amplitudes. The distribution of these frequencies is generally characterised by a near Gaussian distribution, as shown in Figure 3-3, where the Full Width Half Maximum (FWHM) linewidth of the distribution is given by  $\delta v = 1/\delta T$ .

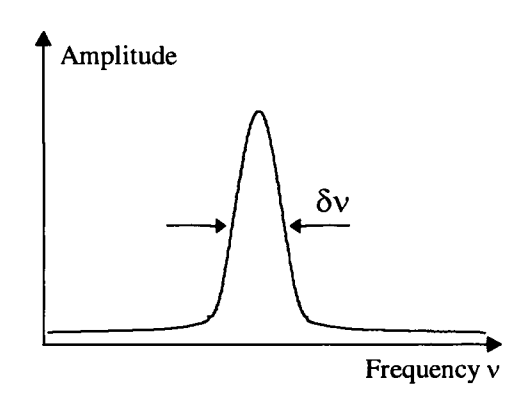


Figure 3-3 Spectral spread of laser emission

The coherence length of a source, the length over which the phase of the light can be related to the spectral spread of the source (its linewidth) can be derived by differentiating the expression  $c = v\lambda$  to give:

$$\delta v = \frac{c}{\lambda^2} \delta \lambda \tag{3-30}$$

As an analogy to Equation (3-29):

$$L = \frac{c}{\delta v} \tag{3-31}$$

and

$$L = \frac{\lambda^2}{\delta \lambda} \tag{3-32}$$

Hence for a Light Emitting Diode with a source wavelength of 850nm and a linewidth of 50nm the coherence length would be approximately 15µm. Laser sources are characterised with much higher values of coherence due to their significantly lower FWHM factors.

# 3.5. Interaction of Light with Matter

There are two different models which can be used to describe the interaction between light and matter; the classical model and the quantum mechanic model<sup>2</sup>. In classical physics the atom is held to possess natural resonant frequencies. These correspond to the electromagnetic wave frequencies which the atom is able to emit when excited into oscillation. Conversely, when light radiation at any of these frequencies falls upon the atom, the atom is able to absorb energy from the radiation in the way of all classical resonant system-driving force interactions.

The propagating electromagnetic wave is specified by its wavelength  $\lambda$  which is related to the oscillation frequency  $\nu$  through propagation velocity c,  $\lambda = c/\nu$ . From the quantum theory of light, the wave is considered to be contained within packets of 'photons', the energy of which is given by  $E = h\nu$ , where h is Planck's constant and  $\nu$  is oscillation frequency. Matter is formed from a collection of atoms and molecules which can exist in specific energy states (electronic, vibrational and rotational energy levels). When an optical signal propagates through a material, an interaction over an energy exchange between the light and the matter occurs. The interaction can manifest itself in two different primary forms, absorption and scattering, each of which is particular to a specific wavelength. Several different parameters of the optical signal can be measured to assess the interaction:

- intensity, represented by the number of photons,
- wavelength, which relates to the energy of the photons,

- polarisation, which is the orientation of the electric field vector,
- time delay, which is often measured as a phase shift with respect to a reference signal.

#### 3.5.1. Light Absorption and Scattering

The interaction of light and matter can occur via several different mechanisms. A photon incident onto a molecule can be *absorbed* by the molecule which is excited from the ground electronic energy state to a higher electronic energy state. Within each electronic state the molecule can occupy different vibrational levels, and rotational levels. The energy is dissipated non-radiatively by degradation into thermal vibrations and the molecule returns to its initial energy state (Figure 3-4). The probability of absorption is grater when the energy of the photon is equal to an energy transition of the molecule, i.e., resonance. Therefore characteristic absorptions for a given material occur at specific wavelengths and the intensity of the propagating light is reduced accordingly.

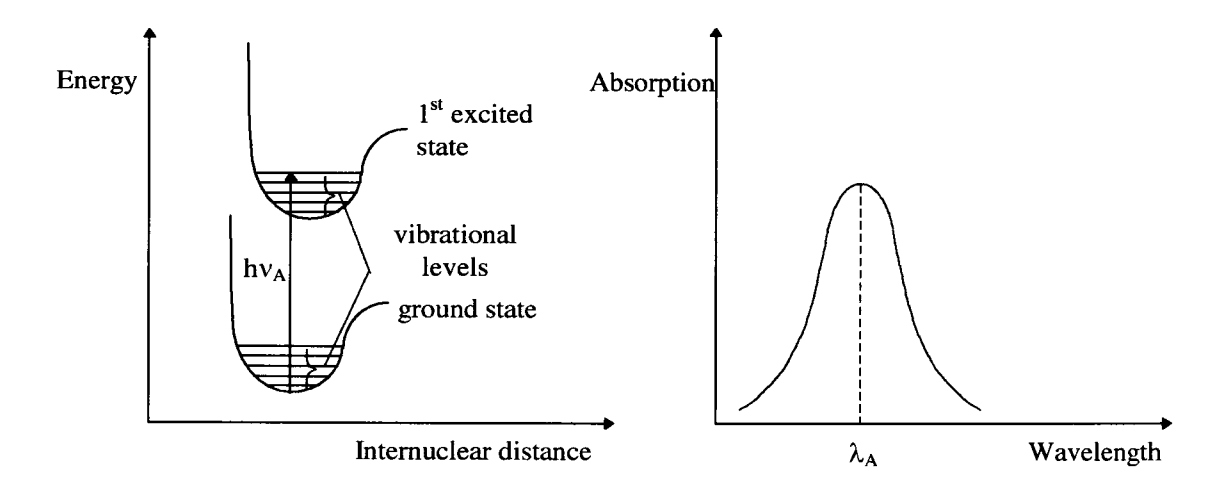


Figure 3-4 Energy level diagram for absorption and corresponding spectrum

It is possible, following the absorption of the photon that the molecule can drop to a lower vibrational state within the excited electronic state by rapid weak collisions with neighbouring molecules<sup>3</sup>. Provided that this excited state has a finite lifetime, the molecule can decay to the ground electronic state radiatively by emitting a photon

(Figure 3-5). The emitted photon will be of a lower energy than that of the incident photon and can occur in any particular direction. This phenomenon is known as *fluorescence* and its intensity depends on the quantum efficiency, the interaction pathlength, the concentration of the emitting molecule (fluor or fluorophore) and the intensity of light detected. A similar phenomena, *phosphorescence* occurs when the photon emission takes place from a triplet state lying close below the excited electronic state (singlet); however phosphorescence has a longer lifetime (msec) then fluorescence (nsec). *Luminescence* is a term used to describe any photon absorption /emission process.

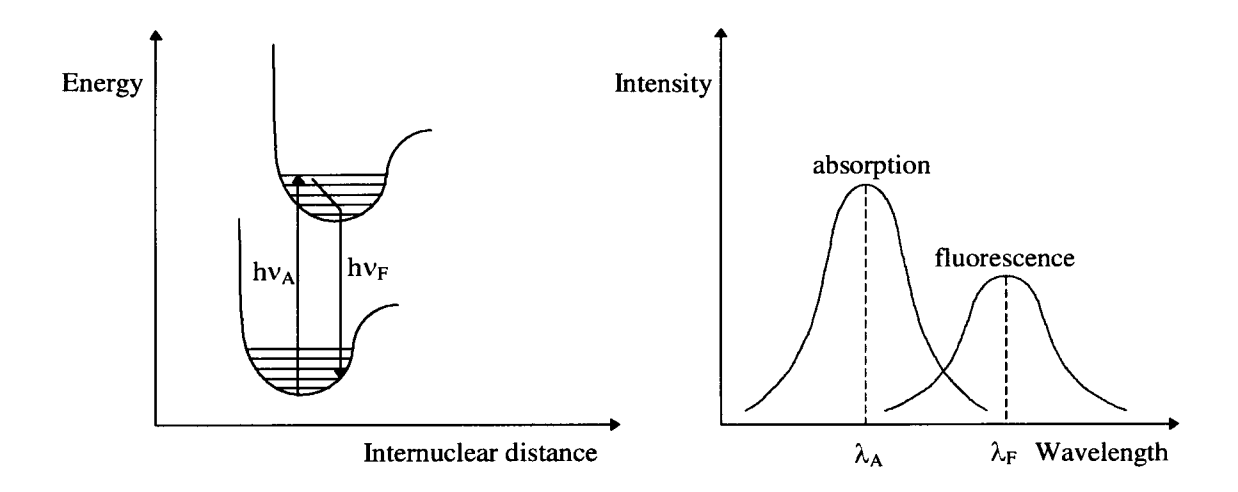


Figure 3-5 Energy level diagram for fluorescence and corresponding spectrum

When the energy of the photon is not coincident with that of the transition of the molecule, scattering will occur. The incident photon is absorbed by the molecule, which is excited to a virtual/intermediate state (not coincident with a stable energy state); and since an excited state of finite lifetime does not exist, the photon immediately emitted with the same energy as that of the incident photon and the molecule returns to its initial energy state. This is known as Rayleigh scattering, which is an elastic process resulting in a photon coherent with the incident photon and of the same wavelength (and energy). The intensity of the scattering is proportional to the fourth power of the frequency  $v^4$  or  $\lambda^{-4}$ .

Raman scattering occurs when the molecule does not return to its initial energy state following the emission of the photon. This effect is an inelastic scattering process producing photons of both lower and higher energy then the incident photons, Stokes and anti-Stokes lines. As for Rayleigh scattering, the non resonant incident photons excite the molecule to a virtual, intermediate state, followed by the immediate radiation of a photon. Stokes scattering produces photons of a lower energy than the incident photons and the molecule returns to an excited vibrational state of the ground electronic state. If, however the molecule is initially in an excited vibrational state (usually in the ground electronic state), the molecule decays to a lower vibrational state (usually ground) resulting in photons of a higher energy than those incident via anti-Stokes scattering. The difference in photon energy corresponds to that of vibrational transition.

Figure 3-6 illustrates the different scattering mechanisms. Anti-Stokes scattering occurs less than Stokes scattering since the probability of a large population of states with a higher energy than the ground state is lower. As for Rayleigh scattering, Raman scattering is instantaneous and not an absorption/emission process with a finite lifetime excited state such as fluorescence. The frequency shift between the Rayleigh line at the incident wavelength and the scattered light at the Stokes or anti-Stokes lines is the frequency corresponding to a particular molecular transition. Each molecular species exhibits a unique Raman spectrum which can be used for identification.

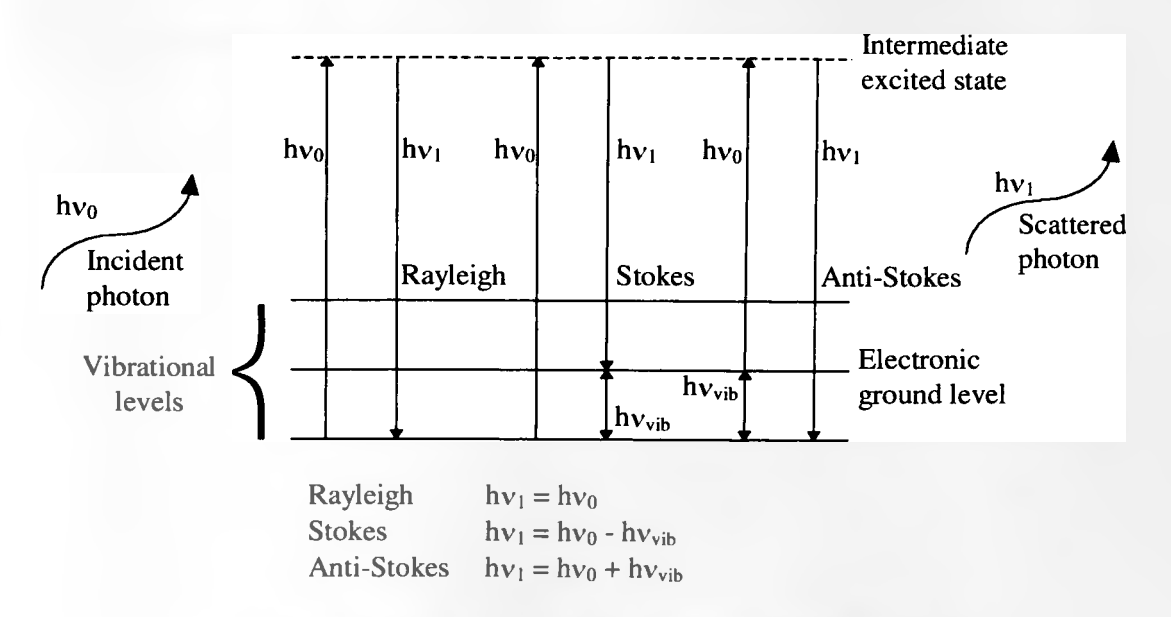


Figure 3-6 Energy level diagram for scattering mechanisms

In some situations, it should be noted that the energy difference between the incident and scattered photons does not correspond to a vibrational transition, but is taken up by an acoustic phonon and Brillouin scattering occurs.

# 3.5.2. Classical Theory of Propagation in Isotropic Dielectrics

In many cases the classical model of interaction between light and matter is sufficient to explain certain optical phenomena which on the other hand would be difficult to explain using the quantum mechanical description. This applies to a relatively long wavelength of the electromagnetic radiation in the visible or infrared range. In this, and in the next sections the classical model will be used to explain such optical phenomena as propagation of light in the medium, optical activity and the Faraday magneto-optic effect.

For a nonmagnetic, electrically neutral media the magnetisation M and the volume density of electric charge  $\rho$  are both zero. Maxwell's equations, in the form expressed by Equations (3-1) to (3-4), then reduce to the following:

$$\nabla \times \mathbf{E} = -\mu_0 \frac{\partial \mathbf{H}}{\partial t} \tag{3-33}$$

$$\nabla \times \mathbf{H} = \varepsilon_0 \frac{\partial \mathbf{E}}{\partial t} + \frac{\partial \mathbf{P}}{\partial t} + \mathbf{J}$$
 (3-34)

$$\nabla \cdot \mathbf{E} = -\frac{1}{\varepsilon_0} \nabla \cdot \mathbf{P} \tag{3-35}$$

$$\nabla \cdot \mathbf{H} = 0 \tag{3-36}$$

The general wave equation for the E field is obtained by taking the curl of Equation (3-33) and eliminating H. The result is

$$\nabla \times (\nabla \times \mathbf{E}) + \frac{1}{c^2} \frac{\partial^2 \mathbf{E}}{\partial t^2} = -\mu_0 \frac{\partial^2 \mathbf{P}}{\partial t^2} - \mu_0 \frac{\partial \mathbf{J}}{\partial t}$$
(3-37)

The two terms on the right-hand side of the above equation are called source terms<sup>1</sup>. They stem from the presence of polarisation charges and conduction charges, respectively, within the medium. The way in which the propagation of light is affected by the sources is revealed by the solution of the wave equation when the source terms are included. In the case of nonconducting media the polarisation term  $-\mu_0 \frac{\partial^2 P}{\partial t^2}$  is of importance. It leads to an explanation of many optical effects, including dispersion, absorption, double refraction, and optical activity. In the case of metals it is the conduction term  $-\mu_0 \frac{\partial J}{\partial t}$  that is important, and the resulting solutions of the wave equation explain the large opacity and high reflectance of metals. Both terms must be taken into account in the case of semiconductors.

In a nonconducting, isotropic medium, the electrons are permanently bound to the atoms comprising the medium and there is no preferential direction in the spatial orientation of the molecules. This is what is meant by a simple isotropic dielectric such as glass. Suppose that each electron, of charge -e, in a dielectric is displaced a

distance r from its equilibrium position. The resulting macroscopic polarisation P of the medium is given by

$$\mathbf{P} = -\text{Ner} \tag{3-38}$$

where N is the number of electrons per unit volume. If the displacement of the electron is the result of the application of a static electric field **E**, and if the electron is elastically bound to its equilibrium position with an elastic force constant f, then the force equation is

$$-e\mathbf{E} = f\mathbf{r} \tag{3-39}$$

The static polarisation is therefore given by

$$\mathbf{P} = \frac{\mathrm{Ne}^2}{\mathrm{f}} \mathbf{E} \tag{3-40}$$

However, if the impressed field **E** varies with time, the above equation is incorrect. In order to find the true polarisation in this case, the actual motion of the electrons must be taken into account. The bound electrons are considered as classical damped harmonic oscillators. The differential equation of motion is

$$m\frac{d^2\mathbf{r}}{dt^2} + m\gamma\frac{d\mathbf{r}}{dt} + f\mathbf{r} = -e\mathbf{E}$$
(3-41)

The term  $m\gamma \frac{d\mathbf{r}}{dt}$  represents a frictional damping force that is proportional to the velocity of the electron, the proportionality constant being written as  $m\gamma$ .

Now suppose that the applied electric field varies harmonically with time according to the usual factor e<sup>-iωt</sup>. Assuming that the motion of the electron has the same harmonic time dependence, it can be found<sup>1</sup> that the equation (3-41) becomes

$$(-m\omega^2 - i\omega m\gamma + f)\mathbf{r} = -e\mathbf{E}$$
 (3-42)

Consequently, the polarisation, from Equation (3-38), is given by

$$\mathbf{P} = \frac{\mathrm{Ne}^2}{-\mathrm{m}\omega^2 - \mathrm{i}\omega\mathrm{m}\gamma + \mathrm{f}}\mathbf{E} \tag{3-43}$$

It reduces to the static value, Equation (3-40), when  $\omega = 0$ . Thus for a given amplitude of the impressed electric field, the amount of the polarisation varies with frequency. The phase of **P**, relative to that of the electric field, also depends on the frequency. This is shown by the presence of the imaginary term in the denominator.

A more significant way of writing Equation (3-43) is

$$\mathbf{P} = \frac{Ne^2/m}{\omega_0^2 - \omega^2 - i\omega\gamma} \mathbf{E}$$
 (3-44)

in which the abbreviation  $\omega_0$  is given by

$$\omega_0 = \sqrt{\frac{f}{m}} \tag{3-45}$$

This is the effective resonance frequency of the bound electrons.

The polarisation formula (3-44) is similar to the amplitude formula for a driven harmonic oscillator since it is the displacement of the elastically bound electrons that actually constitutes the polarisation. It is therefore expected to find an optical resonance phenomenon occurring for light frequencies in the neighbourhood of the resonance frequency  $\omega_0$ . As it will be shown, this resonance phenomenon is

manifested as a large change in the index of refraction of the medium and also by a strong absorption of light at or near the resonance frequency.

To show how the polarisation affects the propagation of light, the general wave equation (3-37) can be presented in a form

$$\nabla \times (\nabla \times \mathbf{E}) + \frac{1}{c^2} \frac{\partial^2 \mathbf{E}}{\partial t^2} = \frac{-\mu_0 N e^2}{m} \left( \frac{1}{\omega_0^2 - \omega^2 - i\gamma \omega} \right) \frac{\partial^2 \mathbf{E}}{\partial t^2}$$
(3-46)

Note, that for a dielectric there is no conduction term and the polarisation is given by Equation (3-44).

Also, from the linear relationship between **P** and **E**, it follows from (3-35) that  $\nabla \cdot \mathbf{E} = 0$ . Consequently,  $\nabla \times (\nabla \times \mathbf{E}) = -\nabla^2 \mathbf{E}$ , and the above wave equation reduces to the simpler one after rearranging terms and using the relation  $1/c^2 = \mu_0 \varepsilon_0$ :

$$\nabla^2 \mathbf{E} = \frac{1}{c^2} \left( 1 + \frac{Ne^2}{m\epsilon_0} \cdot \frac{1}{\omega_0^2 - \omega^2 - i\gamma\omega} \right) \frac{\partial^2 \mathbf{E}}{\partial t^2}$$
 (3-47)

The trial solution of the above equation can be written as follows<sup>1</sup>

$$\mathbf{E} = \mathbf{E}_0 e^{i(\mathbf{K}\mathbf{z} - \omega t)} \tag{3-48}$$

This solution represents homogeneous plane harmonic waves. Direct substitution shows that this is a possible solution provided that

$$K^{2} = \frac{\omega^{2}}{c^{2}} \left( 1 + \frac{Ne^{2}}{m\varepsilon_{0}} \cdot \frac{1}{\omega_{0}^{2} - \omega^{2} - i\gamma\omega} \right)$$
 (3-49)

The presence of the imaginary term in the denominator implies that the wavenumber K must be a complex number. In order to present the physical significance of this, K can be expressed in terms of its real and imaginary parts as

$$K = k + i\alpha \tag{3-50}$$

This is equivalent to a complex index of refraction

$$n = n' + in'' \tag{3-51}$$

where

$$K = \frac{\omega}{c} n \tag{3-52}$$

and n' and n" are respectively real and imaginary components of the refractive index n.

The solution in Equation (3-48) can then be written as

$$\mathbf{E} = \mathbf{E}_0 e^{-\alpha z} e^{i(kz - \omega t)} \tag{3-53}$$

The factor  $e^{-\alpha z}$  indicates that the amplitude of the wave decreases exponentially with distance. This means that as the wave progresses, the energy of the wave is absorbed by the medium. Since the energy in the wave at a given point is proportional to  $|\mathbf{E}|^2$ , then the energy varies with distance as  $e^{-2\alpha z}$ . Hence  $2\alpha$  is the *coefficient of absorption* of the medium. The imaginary part n" of the complex index of refraction is known as *extinction index*. The two numbers  $\alpha$  and n" are related by the equation

$$\alpha = \frac{\omega}{c} \, n'' \tag{3-54}$$

The phase factor  $e^{i(kz-\omega t)}$  indicates that the wave is of a harmonic type in which the phase velocity is

$$u = \frac{\omega}{k} = \frac{c}{n'} \tag{3-55}$$

From Equations (3-49) and (3-52)

$$n^{2} = (n' + in'')^{2} = 1 + \frac{Ne^{2}}{m\varepsilon_{0}} \left( \frac{1}{\omega_{0}^{2} - \omega^{2} - i\gamma\omega} \right)$$
 (3-56)

Equating real and imaginary parts yields the following equations:

$$n'^{2} - n''^{2} = 1 + \frac{Ne^{2}}{m\varepsilon_{0}} \left( \frac{\omega_{0}^{2} - \omega^{2}}{\left(\omega_{0}^{2} - \omega^{2}\right)^{2} + \gamma^{2}\omega^{2}} \right)$$
(3-57)

$$2n'n'' = \frac{Ne^2}{m\varepsilon_0} \left( \frac{\gamma \omega}{\left(\omega_0^2 - \omega^2\right)^2 + \gamma^2 \omega^2} \right)$$
 (3-58)

from which the optical parameters n' and n" may be found.

In the above discussion it has been assumed that all of the electrons were identically bound, and hence all had the same resonance frequencies. In order to take into account the fact that different electrons may be bound differently, it may be assumed that a certain fraction  $f_1$  has an associated resonance frequency  $\omega_1$ , a fraction  $f_2$  has the resonance frequency  $\omega_2$ , and so on. The resulting formula for the square of the complex index of refraction is of the form

$$n^{2} = 1 + \frac{Ne^{2}}{m\varepsilon_{0}} \sum_{j} \left( \frac{f_{j}}{\omega_{j}^{2} - \omega^{2} - i\gamma_{j}\omega} \right)$$
(3-59)

The summation extends over all various kinds of electrons indicated by the subscript j. The fractions  $f_j$  are known as oscillator strengths. The damping constants associated with the various frequencies are denoted by  $\gamma_j$ . Figure 3-7 shows graphically the general dependence of the real and imaginary parts of the complex refraction index n as determined by Equation (3-59). This graph is intended to show qualitatively the case for a substance, such as glass, which is transparent in the visible region and has absorption bands in the infrared and ultraviolet regions of the spectrum.

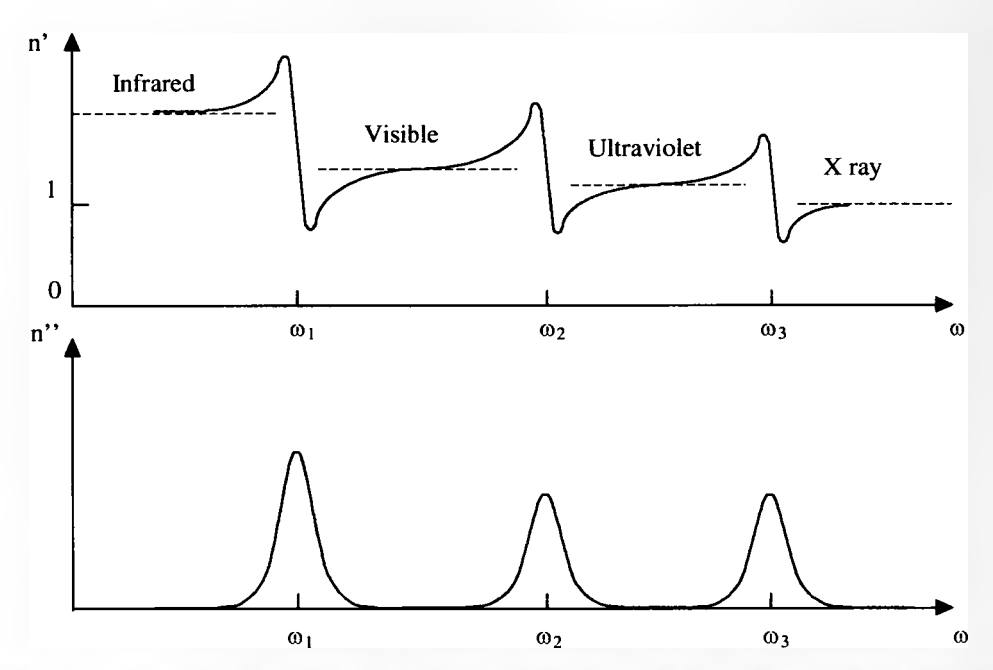


Figure 3-7 Index of refraction and extinction index for a hypothetical substance with absorption bands in the infrared, visible and ultraviolet regions of the spectrum

In the limit of zero frequency, the square of the index approaches the value  $n^2 = 1 + \frac{Ne^2}{m\epsilon_0} \sum_j \left(\frac{f_j}{\omega_j^2}\right).$  This is just the static dielectric constant of the medium.

In the high frequency region, the theory predicts that the index should dip below unity and then approach unity from below as  $\omega$  becomes infinite. This effect is actually seen experimentally<sup>1</sup>.

If the damping constants  $\gamma_j$  are sufficiently small so that the terms  $\gamma_j \omega$  can be neglected in comparison to the quantities  $\omega_j^2 - \omega^2$  in Equation (3-59), then the index of refraction is real and its square is given by

$$n^2 = n'^2 = 1 + \frac{Ne^2}{m\varepsilon_0} \sum_{j} \left( \frac{\mathbf{f}_{j}}{\boldsymbol{\omega}_{j}^2 - \boldsymbol{\omega}^2} \right). \tag{3-60}$$

#### 3.5.3. Propagation in an Anisotropic Media

The propagation of an electromagnetic wave through an isotropic medium has already been discussed. The induced polarisation is parallel to the electric field and related to it by  $\mathbf{P} = \varepsilon_0 \chi \mathbf{E}$ , where  $\chi$  is the linear susceptibility, and in this case a scalar factor which is independent of the direction along the field is applied. In addition the state of polarisation of the lightwave propagating through the isotropic medium remains constant.

However, many materials are anisotropic, i.e., their properties are not the same in all directions within any given sample, for example dielectric and birefringent materials which exhibit a directional variation in refractive index. The propagation of light through such a medium is more complex than that of an isotropic medium. The induced polarisation depends both in its magnitude and direction, on the direction of the applied field. The induced polarisation is now related to the electric field through the susceptibility tensor  $\chi$ :

$$\mathbf{P} = \mathbf{\varepsilon}_0 \mathbf{\chi} \mathbf{E} \tag{3-61}$$

which when expanded gives:

$$\begin{bmatrix} P_{x} \\ P_{y} \\ P_{z} \end{bmatrix} = \varepsilon_{0} \begin{bmatrix} \chi_{11} & \chi_{12} & \chi_{13} \\ \chi_{21} & \chi_{22} & \chi_{23} \\ \chi_{31} & \chi_{32} & \chi_{33} \end{bmatrix} \begin{bmatrix} E_{x} \\ E_{y} \\ E_{z} \end{bmatrix}$$
(3-62)

The magnitude of the  $\chi_{ij}$  coefficients depends on the choice of the x, y, z axes relative to that of the crystal structure. It is possible to choose x, y, z axes in such a way that the off diagonal coefficients disappear and the equation (3-62) reduces to:

$$\begin{bmatrix} P_{x} \\ P_{y} \\ P_{z} \end{bmatrix} = \varepsilon_{0} \begin{bmatrix} \chi_{11} & 0 & 0 \\ 0 & \chi_{22} & 0 \\ 0 & 0 & \chi_{33} \end{bmatrix} \begin{bmatrix} E_{x} \\ E_{y} \\ E_{z} \end{bmatrix}$$
(3-63)

The three  $\chi$ s are known as the principal susceptibilities. Corresponding to these, the quantities  $\varepsilon_{11} = 1 + \chi_{11}$  ..., and so forth are called the principal dielectric constants.

In view of Equation (3-61), the general wave equation (3-37) can be written in the following form:

$$\nabla \times (\nabla \times \mathbf{E}) + \frac{1}{c^2} \frac{\partial^2 \mathbf{E}}{\partial t^2} = -\frac{1}{c^2} \chi \frac{\partial^2 \mathbf{E}}{\partial t^2}$$
(3-64)

It then follows that the crystal can sustain monochromatic plane waves of the usual form  $e^{i(\mathbf{k}\cdot\mathbf{r}-\omega t)}$  provided the propagation vector  $\mathbf{k}$  satisfies the equation

$$\mathbf{k} \times (\mathbf{k} \times \mathbf{E}) + \frac{\omega^2}{c^2} \mathbf{E} = -\frac{\omega^2}{c^2} \chi \mathbf{E}$$
 (3-65)

Written out in terms of components, the above equation is equivalent to the following three equations:

$$\left(-k_{y}^{2}-k_{z}^{2}+\frac{\omega^{2}}{c^{2}}\right)E_{x}+k_{x}k_{y}E_{y}+k_{x}k_{z}E_{z}=-\frac{\omega^{2}}{c^{2}}\chi_{11}E_{x}$$

$$k_{y}k_{x}E_{x}+\left(-k_{x}^{2}-k_{z}^{2}+\frac{\omega^{2}}{c^{2}}\right)E_{y}+k_{y}k_{z}E_{z}=-\frac{\omega^{2}}{c^{2}}\chi_{22}E_{y}$$

$$k_{z}k_{x}E_{x}+k_{z}k_{y}E_{y}+\left(-k_{x}^{2}-k_{y}^{2}+\frac{\omega^{2}}{c^{2}}\right)E_{z}=-\frac{\omega^{2}}{c^{2}}\chi_{33}E_{z}$$
(3-66)

In order to interpret the physical meaning of these equations, a particular case can be considered of a wave propagating in the direction of one of the principal axes, say the x axis. In this case  $k_x = k$ ,  $k_y = k_z = 0$ , and the three equations reduce to

$$\frac{\omega^{2}}{c^{2}}E_{x} = -\frac{\omega^{2}}{c^{2}}\chi_{11}E_{x}$$

$$\left(-k^{2} + \frac{\omega^{2}}{c^{2}}\right)E_{y} = -\frac{\omega^{2}}{c^{2}}\chi_{22}E_{y}$$

$$\left(-k^{2} + \frac{\omega^{2}}{c^{2}}\right)E_{z} = -\frac{\omega^{2}}{c^{2}}\chi_{33}E_{z}$$
(3-67)

The first equation implies that  $E_x = 0$ , because neither  $\omega$  nor  $\chi_{11}$  is zero. This means that the E field is transverse to the x-axis, which is the direction of propagation. Consider next the second equation. If  $E_y \neq 0$ , then

$$k = \frac{\omega}{c} \sqrt{1 + \chi_{22}} = \frac{\omega}{c} \sqrt{\varepsilon_{22}}$$
 (3-68)

The third equation, likewise, implies that if  $E_z \neq 0$ , then

$$k = \frac{\omega}{c} \sqrt{1 + \chi_{33}} = \frac{\omega}{c} \sqrt{\varepsilon_{33}}$$
 (3-69)

Now  $\frac{\omega}{k}$  is the phase velocity of the wave. Thus there are two possible phase velocities, namely,  $\frac{c}{\sqrt{\epsilon_{22}}}$  if the E vector points in the y direction, and  $\frac{c}{\sqrt{\epsilon_{33}}}$  if the E vector is in the z direction.

More generally it can be shown that for any direction of the propagation vector k, there are two possible values of the phase velocity<sup>1</sup>.

#### 3.5.4. Birefringence

One of the consequences of anisotropy is the phenomenon of birefringence in which the phase velocity of an optical wave propagating in the crystal depends on the direction of polarisation of its electric field vector. Therefore, the crystal will also show a directional variation in refractive index

$$n_{1} = \sqrt{1 + \chi_{11}} = \sqrt{\varepsilon_{11}}$$

$$n_{2} = \sqrt{1 + \chi_{22}} = \sqrt{\varepsilon_{22}}$$

$$n_{3} = \sqrt{1 + \chi_{33}} = \sqrt{\varepsilon_{33}}$$
(3-70)

Considering a wave propagating along the x-axis it was shown in the previous section that Maxwell's equations allow two solutions: one with its linear polarisation along z-axis with a phase velocity  $\frac{c}{\sqrt{\epsilon_{33}}}$ , and the second orthogonal, with its linear polarisation along the y-axis with a phase velocity  $\frac{c}{\sqrt{\epsilon_{22}}}$ . If however, the wave is propagating in an arbitrary direction in the crystal, the problem becomes more complicated and a full treatment requires the use of the so-called index ellipsoid to determine the directions of polarisation of the two allowed waves, and their phase velocities.

The index ellipsoid is defined by the ellipsoid equation

$$\frac{x^2}{n_1^2} + \frac{y^2}{n_2^2} + \frac{z^2}{n_3^2} = 1 \tag{3-71}$$

with principal semi-axes  $n_1$ ,  $n_2$ ,  $n_3$  as shown in Figure 3-8.

For wave propagation not coincident with principal axis the index ellipsoid is cut through its centre with a plane, normal to the direction of wave propagation. The intersection of the plane and the ellipsoid is an ellipse. The major and minor semi-axes of the ellipse give the relevant refractive indices for the two linearly polarised wave solutions having their D vectors in the major and minor axis directions respectively.

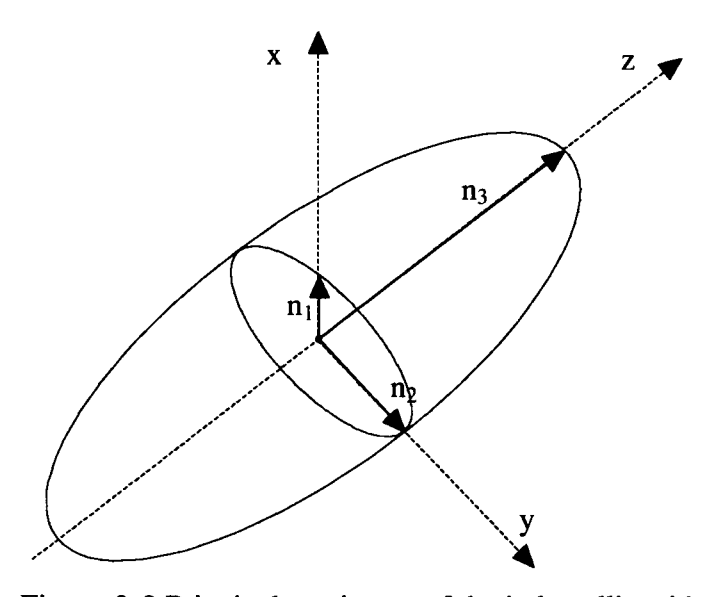


Figure 3-8 Principal semi-axes of the index ellipsoid

The phenomenon of birefringence was first observed in calcite crystal CaO<sub>3</sub> (Iceland spar) and initially known as double refraction, since two linearly polarised orthogonal rays known as the ordinary and extraordinary rays propagate through the crystal. The ordinary rays are spherical and the extraordinary rays are elliptical. Along an optic axis which corresponds to a direction about which atoms are arranged symmetrically,

the two rays propagate with the same velocity, otherwise they exhibit different phase velocities and hence the crystal has two refractive indices and is birefringent.

Crystals are classified into 32 classes grouped within 7 systems<sup>3</sup>. They can also be classified optically:

- biaxial crystals, with principal dielectric constants  $\varepsilon_{11} \neq \varepsilon_{22} \neq \varepsilon_{33}$ ,
- uniaxial crystals, with principal dielectric constants  $\varepsilon_{11} = \varepsilon_{22} \neq \varepsilon_{33}$ ,
- anaxial/isotropic crystals, with principal dielectric constants  $\varepsilon_{11} = \varepsilon_{22} = \varepsilon_{33}$ .

For uniaxial crystals, the principal velocities are  $v_1 = v_2 \neq v_3$ . However, uniaxial crystals are birefringent and ordinary and extraordinary rays are generated with velocities  $v_o = v_1 = v_2$  and  $v_e = v_3$  respectively. It can be seen from the index ellipsoid that no matter what the direction of the incident wave, there is always a wave solution with velocity  $v_o$ . The velocity of the second wave solution depends on the direction of propagation. The birefringence is the difference in refractive index  $\Delta n = \left| n_e - n_o \right|$ . When  $\Delta n$  is positive, i.e.,  $n_e > n_o$  the crystal is a positive uniaxial crystal and  $v_o > v_e$ . When  $\Delta n$  is negative, i.e.,  $n_o > n_e$  the crystal is a negative uniaxial crystal and  $v_e > v_o$ . The axis of the optical crystal are often referred to as the fast and slow axes relating to  $v_o$  and  $v_e$ .

### 3.5.5. Retarders

Retarders are optical elements, made of birefringent materials which are used to change the polarisation state of an incident wave. The retarder operates by causing one of the two constituent coherent polarisation components to lag behind the other by a predetermined amount. On emerging from the retarder, the relative phase of the two components is different from the initial phase, and so therefore, is the state of polarisation.

The relative phase difference or retardance  $\Delta \phi$  between the two constituent components ordinary and extraordinary waves (or components along the fast and slow axes is given by:

$$\Delta \phi = \frac{2\pi}{\lambda} d(|\mathbf{n}_{o} - \mathbf{n}_{e}|) \tag{3-72}$$

where d is the thickness of the birefringent material,  $\lambda$  is the wavelength of the propagating light and  $n_o$  and  $n_e$  are the refractive indices of the ordinary and extraordinary wave components respectively.

The thickness of the birefringent material d is chosen so as to introduce the required relative phase difference between the two components. Some common retarders are half wave plate and quarter wave plate. The half wave plate rotates the plane of linearly polarised light by 90°. A phase difference of  $\pi/2$  is introduced between the light components propagating along fast and slow axes.

The quarter wave plate changes linearly polarised light incident at an angle  $45^{\circ}$  to the optic axis into circularly polarised light. In this case the birefringent material introduces a phase difference of  $\pi/4$  between the two component waves which combine to give circularly polarised light.

## 3.5.6. Optical Activity

Optical activity is an inherent property of many materials, and is the ability of the material (described as optically active) to rotate the plane of polarisation of incident linearly polarised light. The electric field vector of the linearly polarised wave undergoes a continuous rotation as it propagates along the optic axis of the material.

Optical activity can be explained on the basis of the simple assumption that the speed of propagation for right circularly polarised light in the medium is different from that of left circularly polarised light. To show this, it will be convenient to use the Jones vector notation<sup>4</sup>. Let  $n_R$  and  $n_L$  denote, respectively, the indices of refraction of the medium for right and left circularly polarised light. The corresponding wavenumbers are  $k_R = n_R \frac{\omega}{c}$  and  $k_L = n_L \frac{\omega}{c}$ , and the expressions

$$\begin{bmatrix} 1 \\ -i \end{bmatrix} e^{i(k_R z - \omega t)} \tag{3-73}$$

$$\begin{bmatrix} 1 \\ i \end{bmatrix} e^{i(k_L z - \omega t)} \tag{3-74}$$

represent the two kinds of the wave in the medium.

Now suppose that a beam of linearly polarised light travels a distance d through the medium. Let the initial polarisation be in the horizontal direction. The initial Jones vector, separated into right and left circular components, is

$$\begin{bmatrix} 1 \\ 0 \end{bmatrix} = \frac{1}{2} \begin{bmatrix} 1 \\ -i \end{bmatrix} + \frac{1}{2} \begin{bmatrix} 1 \\ i \end{bmatrix} \tag{3-75}$$

The complex amplitude of the light wave, after travelling a distance d through a medium, is

$$\frac{1}{2} \begin{bmatrix} 1 \\ -i \end{bmatrix} e^{ik_R d} + \frac{1}{2} \begin{bmatrix} 1 \\ i \end{bmatrix} e^{ik_L d} = \frac{1}{2} e^{i(k_R + k_L)\frac{d}{2}} \left\{ \begin{bmatrix} 1 \\ -i \end{bmatrix} e^{i(k_R - k_L)\frac{d}{2}} + \begin{bmatrix} 1 \\ i \end{bmatrix} e^{-i(k_R - k_L)\frac{d}{2}} \right\}$$
(3-76)

Upon introducing the quantities  $\psi$  and  $\theta$  where

$$\psi = \frac{1}{2} \left( k_R + k_L \right) d \tag{3-77}$$

$$\theta = \frac{1}{2} \left( k_R - k_L \right) d \tag{3-78}$$

the complex amplitude can be expressed as

$$e^{i\psi} \left\{ \frac{1}{2} \begin{bmatrix} 1 \\ -i \end{bmatrix} e^{i\theta} + \frac{1}{2} \begin{bmatrix} 1 \\ i \end{bmatrix} e^{-i\theta} \right\} = e^{i\psi} \begin{bmatrix} \frac{1}{2} \left( e^{i\theta} + e^{-i\theta} \right) \\ \frac{1}{2} i \left( e^{i\theta} - e^{-i\theta} \right) \end{bmatrix} = e^{i\psi} \begin{bmatrix} \cos \theta \\ \sin \theta \end{bmatrix}$$
(3-79)

This represents a linearly polarised wave in which the direction of polarisation is turned through an angle  $\theta$  with respect to the original direction of polarisation. From Equation (3-78) angle  $\theta$  can be expressed as

$$\theta = (n_R - n_L) \frac{\omega d}{2c} = (n_R - n_L) \frac{\pi d}{\lambda}$$
 (3-80)

where  $\lambda$  is the wavelength in vacuum. It follows that the specific rotatory power  $\delta$ , as a function of wavelength, is given by

$$\delta = \left(n_R - n_L\right) \frac{\pi}{\lambda} \tag{3-81}$$

The indices n<sub>R</sub> and n<sub>L</sub> are also, of course, functions of wavelength.

It is simple matter to show that if the susceptibility tensor has conjugate imaginary off-diagonal elements, namely,

$$\mathbf{\chi} = \begin{bmatrix} \chi_{11} & i\chi_{12} & 0 \\ -i\chi_{12} & \chi_{11} & 0 \\ 0 & 0 & \chi_{33} \end{bmatrix}$$
 (3-82)

where  $\chi_{12}$  is real, then the medium is optically active. To prove this the components of the wave equation (3-65) can be written for the above susceptibility tensor. For simplicity a wave propagating in the z direction is considered:

$$-k^{2}E_{x} + \frac{\omega^{2}}{c^{2}}E_{x} = -\frac{\omega^{2}}{c^{2}}(\chi_{11}E_{x} + i\chi_{12}E_{y})$$
(3-83)

$$-k^{2}E_{y} + \frac{\omega^{2}}{c^{2}}E_{y} = -\frac{\omega^{2}}{c^{2}}\left(-i\chi_{12}E_{x} + \chi_{11}E_{y}\right)$$
(3-84)

$$\frac{\omega^2}{c^2} E_z = -\frac{\omega^2}{c^2} \chi_{33} E_z \tag{3-85}$$

The last equation merely gives  $E_z = 0$ , so the wave is transverse. The determinant of the coefficients of the first two equations must be equal zero for a nontrivial solution, namely,

$$\begin{vmatrix} -k^2 + \frac{\omega^2}{c^2} (1 + \chi_{11}) & i \frac{\omega^2}{c^2} \chi_{12} \\ -i \frac{\omega^2}{c^2} \chi_{12} & -k^2 + \frac{\omega^2}{c^2} (1 + \chi_{11}) \end{vmatrix} = 0$$
 (3-86)

Solving for k,

$$k = \frac{\omega}{c} \sqrt{1 + \chi_{11} \pm \chi_{12}}$$
 (3-87)

Now, by substituting the above expression for k back into either of Equations (3-83) or (3-84) it can be found that

$$E_{x} = \pm iE_{y} \tag{3-88}$$

where the upper sign corresponds to the upper sign in Equation (3-87) and similarly for the lower sign. The above result means that the two values of k given by Equation (3-87) correspond to right and left circularly polarised light. The indices of refraction are, accordingly,

$$n_R = \sqrt{1 + \chi_{11} + \chi_{12}} \tag{3-89}$$

$$n_{L} = \sqrt{1 + \chi_{11} - \chi_{12}} \tag{3-90}$$

for right and left circularly polarised light, respectively. It follows that the difference between  $n_R$  and  $n_L$  is given approximately by

$$n_R - n_L \approx \frac{\chi_{12}}{\sqrt{1 + \chi_{11}}} = \frac{\chi_{12}}{n_o}$$
 (3-91)

where  $n_0$  is the ordinary index of refraction. The specific rotatory power from Equation (3-81) is then

$$\delta = \frac{\chi_{12}\pi}{n_0\lambda} \tag{3-92}$$

The result shows that the specific rotatory power is directly proportional to the imaginary component  $\chi_{12}$  of the susceptibility tensor.

### 3.5.7. Faraday Rotation in Solids

If an isotropic dielectric is placed in a magnetic field and a beam of linearly polarised light is sent through the dielectric in the direction of the field, a rotation of the plane of polarisation of the emerging light is found to occur. In other words the presence of the field causes the dielectric to become optically active. This phenomenon was discovered in 1845 by Michael Faraday. The amount of rotation  $\theta$  of the plane of polarisation of the light is proportional to the magnetic induction B and to the length L of travel in the medium. Thus the relationship can be expressed as

$$\theta = VBL \tag{3-93}$$

where V is a constant of proportionality. This constant is called the Verdet constant.

The Verdet constant for a particular material varies with both wavelength (dropping rapidly as  $\lambda$  increases) and temperature.

Some examples are given<sup>1,5,6</sup> in Table 3-1. The figures given are for yellow light, 589nm and 20°C.

Substance	Verdet constant	
-	min/Oe/cm	$x10^3 \text{ deg/T/m}$
Fluorite	0.0009	0.015
Diamond	0.012	0.200
Crown glass	0.015-0.025	0.250-0.417
Flint glass	0.030-0.050	0.050-0.833
Sodium chloride	0.036	0.600
FR-5	0.29	4.833
TGG	0.45	7.5

Table 3-1 Values of the Verdet constant for some selected substances

By convention a positive Verdet constant corresponds to a material for which the induced activity is l-rotatory when the light moves parallel to the applied magnetic field, and d-rotatory when the light moves antiparallel to the magnetic field.

The Faraday effect is non-reciprocal. If plane polarised light is rotated through angle  $\theta$  in one passage through the medium, then returning the light in the reverse direction will result in a further  $\theta$  rotation, so that on a double passage the total rotation will be  $2\theta$  rather than zero as is the case of optical activity.

The Faraday effect occurs since the atomic electrons can more easily rotate in one direction about the field direction than in the other (Lorentz force), and so field dependent circular birefringence is introduced.

All materials exhibit some Faraday rotation. The effect is weakest for diamagnetics and increasingly stronger for paramagnetics and ferromagnetics. There is a strong

temperature dependence in ferromagnetic and paramagnetic materials, but a negligible temperature dependence in diamagnetics.

In order to explain the Faraday effect, the equation of motion of the bound electrons must be considered in the presence of the static magnetic field **B** and the oscillating electric field **E** of the light wave. The differential equation of motion is

$$m\frac{d^2\mathbf{r}}{dt^2} + f\mathbf{r} = -e\mathbf{E} - e\left(\frac{d\mathbf{r}}{dt}\right) \times \mathbf{B}$$
(3-94)

where, as in the treatment of the theory of dispersion in dielectric media (Section 3.5.2), **r** is the displacement of the electron from its equilibrium position and f is the elastic-force constant. For reasons of simplicity the force due to the magnetic field of the optical wave as well as the damping effect will be neglected. These small effects are not particularly germane to the understanding of the basic theory of the Faraday effect.

It is assumed that the optical field E has the usual harmonic time dependence  $e^{-i\omega t}$ . The particular solution of interest is the steady state condition for which the displacement r has the same harmonic time dependence as the light wave. Hence,

$$-m\omega^2 \mathbf{r} + f\mathbf{r} = -e\mathbf{E} + i\omega e\mathbf{r} \times \mathbf{B}$$
 (3-95)

But the polarisation  $\mathbf{P}$  of the medium is just a constant times  $\mathbf{r}$ , namely, -Ner, hence the above equation implies that

$$(-m\omega^2 + f)\mathbf{P} = Ne^2\mathbf{E} + i\omega e\mathbf{P} \times \mathbf{B}$$
 (3-96)

Now this equation can be solved for  $\mathbf{P}$  by writing the equation in component form and solving for the components of  $\mathbf{P}$ . The result can be expressed in the following way<sup>1</sup>:

$$\mathbf{P} = \varepsilon_0 \mathbf{\chi} \mathbf{E} \tag{3-97}$$

where  $\chi$  is the susceptibility tensor. Its form is precisely that of an optically active medium, namely,

$$\mathbf{\chi} = \begin{bmatrix} \chi_{11} & i\chi_{12} & 0 \\ -i\chi_{12} & \chi_{11} & 0 \\ 0 & 0 & \chi_{33} \end{bmatrix}$$
 (3-98)

where

$$\chi_{11} = \frac{Ne^2}{m\epsilon_0} \left[ \frac{{\omega_0}^2 - {\omega}^2}{({\omega_0}^2 - {\omega}^2)^2 - {\omega}^2 {\omega_c}^2} \right]$$
(3-99)

$$\chi_{33} = \frac{\text{Ne}^2}{\text{m}\varepsilon_0} \left[ \frac{1}{\omega_0^2 - \omega^2} \right] \tag{3-100}$$

$$\chi_{12} = \frac{Ne^2}{m\varepsilon_0} \left[ \frac{\omega\omega_c}{\left(\omega_0^2 - \omega^2\right)^2 - \omega^2\omega_c^2} \right]$$
 (3-101)

In deriving the above result it has been assumed that the magnetic field  $\bf B$  is in the z direction. The following abbreviations are used:

$$\omega_0 = \sqrt{\frac{f}{m}}$$
 (resonance frequency) (3-102)

$$\omega_{c} = \frac{eB}{m}$$
 (cyclotron frequency) (3-103)

Finally, referring to Equation (3-92), the specific rotatory power induced by a magnetic field is given by the approximate equation

$$\delta \approx \frac{\pi N e^2}{n_o \lambda m \varepsilon_0} \left[ \frac{\omega \omega_c}{\left(\omega_0^2 - \omega^2\right)^2} \right] = \frac{\pi N e^3}{n_o \lambda m^2 \varepsilon_0} \left[ \frac{\omega}{\left(\omega_0^2 - \omega^2\right)^2} \right] B$$
 (3-104)

or similarly with Equation (3-93) the rotation  $\theta$  can be expressed as

$$\theta = \frac{\pi N e^3}{n_o \lambda m^2 \varepsilon_0} \left[ \frac{\omega}{\left(\omega_0^2 - \omega^2\right)^2} \right] BL$$
 (3-105)

In the above equations it is assumed that  $\omega \omega_c \ll |\omega_0|^2 - \omega^2$ . Note, that  $\omega = \frac{2c}{\lambda}$ .

Faraday rotation is a particularly useful effect in optical fibre sensor and component systems, for example, it is employed in Optical Current Transducers (OCTs) which allow current measurement by determining the magnetic field near the current carrying conductor. This application forms the basis of this thesis.

The effect is also used in optical modulators, and its non reciprocal property is exploited in optical isolators and circulators as well as in the vibration compensation scheme for the OCT developed by the author (more details in Chapter 6).

### 3.5.8. Other Magneto-optic Effects

There are several other magneto-optic effects. However only two of them will be briefly considered in this work. The Voigt and Cotton-Mouton effects both arise when a constant magnetic field is applied to a transparent medium perpendicular to the direction of propagation of the incident light beam. The former occurs in vapours while the latter, which is stronger, occurs in liquids. In both cases, the medium exhibits a birefringence similar to a uniaxial crystal whose optic axis is in the direction of the constant magnetic field (i.e., normal to the propagating light beam). The two refractive indices correspond to two component waves with linear polarisation parallel

or perpendicular to the magnetic field. The refractive index difference  $\Delta n$  (i.e., birefringence) is proportional to the square of the applied magnetic field. The Cotton-Mouton effect is the magnetic analogue of the Kerr electro-optic effect which will be considered later, and occurs concurrently with the Faraday effect although it is much weaker.

## 3.5.9. Electrogyration

Electrogyration is the electric field analogue of the Faraday magneto-optic effect; circular birefringence is induced in some materials in the presence of an electric field. However, the effect only occurs in a limited number of materials, those which have a spiral crystal structure, and thus an intrinsic circular birefringence. The electric field effectively alters the pitch of the spiral and therefore the magnitude of the circular birefringence. The effect can be used to measure electric fields and voltages.

#### 3.5.10. Photoelastic Effect

The application of a mechanical stress perpendicular to the direction of the propagation of a light wave induces an increase in the refractive index for light polarised along the stress direction. This phenomenon is known as mechanical birefringence, photoelasticity, or stress birefringence, and is a linear birefringence effect with the induced birefringence proportional to the applied stress. The effect occurs in virtually all solids (regardless of crystal symmetry) and isotropic substances thus become optically anisotropic (i.e., exhibit birefringence), whilst in anisotropic materials the effect becomes directional. Under compression or tension the isotropic material will take on the properties of a negative or positive uniaxial crystal, respectively.

In general the elasto-optic coefficients are relatively small so that small stresses may only be detected by integrating the effect over a long path length. However, the effect is commonly exploited in optics via acousto-optics and Bragg cell modulators. Acoustic waves (e.g., surface acoustic waves) produce a sinusoidal density variation,

which generates a refractive index variation through the acousto-optic effect. The refractive index  $\Delta n$  is related to the strain s by<sup>3</sup>:

$$\Delta n = \frac{-n^3 ps}{2} \tag{3-106}$$

where p is the photoelastic constant of the medium, defined by the above equation. The strain s is related to the acoustic intensity  $I_{acoustic}$  by:

$$s = \left(\frac{2I_{\text{acoustic}}}{\rho v_s^3}\right)^{\frac{1}{2}}$$
 (3-107)

where  $\rho$  is the mass density of the medium (kg/m³) and  $v_s$  is the velocity of sound in the material. A figure of merit M is defined as

$$M = \frac{n^6 p^2}{\rho v_s^3}$$
 (3-108)

which gives a direct measure of the efficiency of the interaction of light with an acoustic wave (Bragg diffraction). In many materials (especially crystals) the total photoelastic phase modulation depends on the relative orientation of the input wave polarisation, the crystal axes, and the applied acoustic wave.

It should be noted that in many cases the photoelastic effect can be parasitic and cause unneeded interference of environmental factors (such as vibration or stress) within the optical sensor dedicated to measure other parameters. This will be an issue which will be investigated further in Chapter 6.

## 3.5.11. Electro-optic Effects

Application of an external electric field can cause induced anisotropy. Two types of effect are common. First, many isotropic materials such as glass, and liquids such as nitrobenzene, become uniaxial with their optic axis along the direction of the electric field. The effect is proportional to the square (or polynomial including only even powers) of the applied field E<sub>0</sub>.

$$n_e - n_o \propto E_o^2$$
 (3-109)

where  $n_e$  and  $n_o$  are extraordinary and ordinary indices of refraction respectively. This is called the Kerr effect.

On the other hand, crystals without a centre of symmetry in the atomic arrangement of their unit cell are able to distinguish between positive and negative fields and so the electro-optic effect can depend on any power of the field; in particular, a linear effect is possible known as the Pockels effect. Its magnitude can also be a function of the orientation of the field and so a complete description of the effect, even at a phenomenological level, becomes complicated. The effect is utilised to produce light shutters, modulators and voltage sensors.

# 3.6. Summary

In this chapter the essential optical phenomena relevant to the operation of many optical fibre sensing systems have been described. Most of the optical principles have been explained on the basis of the classical theory of light propagation and interaction of light with matter using Maxwell equations. The concept of light as an electromagnetic wave was sufficient to portray such optical phenomena as birefringence, optical activity and the Faraday effect. The classical model, however, was incapable of explaining phenomena such as light scattering, fluorescence, phosphorescence or luminescence and therefore these optical mechanisms have been described qualitatively using the quantum mechanic concepts of light.

This chapter has formed the theoretical basis to the description of optical principles and mechanisms upon which the optical measurement process can be realised in practice. The practical implementation of these mechanisms to the optical sensor construction will be discussed in the next chapter.

# 3.7. Chapter References

- 1) G. R. Fowles, "Introduction to modern optics", Holt, Rinehart and Winston, 1975,
- 2) J. Dakin, B. Culshaw, "Optical fiber sensors: principles and components", Volume 1, Artech House, Inc., 1988,
- N. G. Dadswell, R. Dean, "Optical sensors for power industry applications", REA Technology Ltd., 1995,
- 4) K. D. Moller, "Optics", University Science Books, 1998,
- 5) Hoya Corporation USA, "FR-5 glass specification data sheet",
- 6) N. P. Barnes, L. B. Petway, "Variation of the Verdet constant with temperature of terbium gallium garnet", J. Opt. Soc. Am. B/Vol. 9, No. 10/October 1992.

# 4. Optical Sensing Techniques - Basic Concepts

## 4.1. Introduction

Following the development of optical fibre as a low-loss, low-dispersion, high bandwidth, low-cost transmission medium for optical communication systems, its additional advantages and potential in the field of optical sensing were investigated. The maturity of the optical fibre communication technology led to the development of many advanced optoelectronic and fibre optic components, e.g., semiconductor lasers and LEDs, photodetectors, couplers, connectors etc. This accelerated work on optical fibre sensors and enabled the definition of specific properties required for sensing applications. Consequently, additional specialised components have been developed for example birefringent optical fibres, demultiplexers and fibre polarisers. Extensive research and development activity has resulted in the design and realisation of optical fibre sensors for the measurement of many physical and chemical measurands.

Optical fibre sensors offer significant potential in a wide range of applications and a substantial investment has been made to demonstrate this potential. Major advantages can be shown when the sensors are operated passively without electrical power, and much of the R&D activity has been focused on this type of sensor. The fact that the modulated signal can be transmitted to and from the sensing region without recourse to electrical connection removes problems associated with ground plane separation, electrical safety regulations and render optical sensors immune from electromagnetic interference. This feature also allows optical fibres to be routed in close proximity to high current carrying cables, high power rf systems and provides a level of instrumentation protection during lightning strikes. The sensor and transmission systems are intrinsically safe because no electrical power is required and when damaged, sparks are not created. Sensors of this type therefore find application in hazardous environments.

Additional advantages of optical fibre sensors include chemical passivity, small size and light weight due to the fibre optic transmission medium, and potentially high sensitivity and the ability to interface with a wide range of measurands. The measurand can be virtually any physical or chemical influence and the range of optical fibre sensors that have been demonstrated is extremely diverse<sup>1,2,3</sup>. The property of the optical signal which can be modulated is also extremely diverse including intensity, phase, Doppler shifts, state of polarisation, subcarrier modulation function or colour.

This chapter is not intended to be a comprehensive description of optical fibres and optical fibre sensors due to the very wide range of the possible devices. This can be found in many textbooks<sup>1,2,3</sup> available on these subjects. Details of the various optical components which are utilised in optical fibre sensors for example optical sources, detectors, couplers etc., can also be found in the textbooks.

The aim of this chapter is to provide an overview of the available optical fibre sensor technology and present a diversity of solutions which can be applied in the fibre-optic sensor design. Initially a technical overview of optical fibres is given, describing their basic properties, transmission characteristics and birefringence effects. This is followed by a description of the basic techniques and configurations used in optical fibre sensors.

# 4.2. Optical Fibres - a Technical Overview

Optical fibres are circular cross section electromagnetic waveguides which consist of a cylindrical rod of dielectric medium concentrically surrounded by another dielectric, Figure 4-1. The inner dielectric is a core of the fibre and has a slightly higher refractive index than the outer dielectric, the cladding of the fibre. Optical fibres for communication applications are made of silica in which the core region has been doped with impurities to raise the refractive index value. Other typical forms of optic waveguides include planar and rectangular.

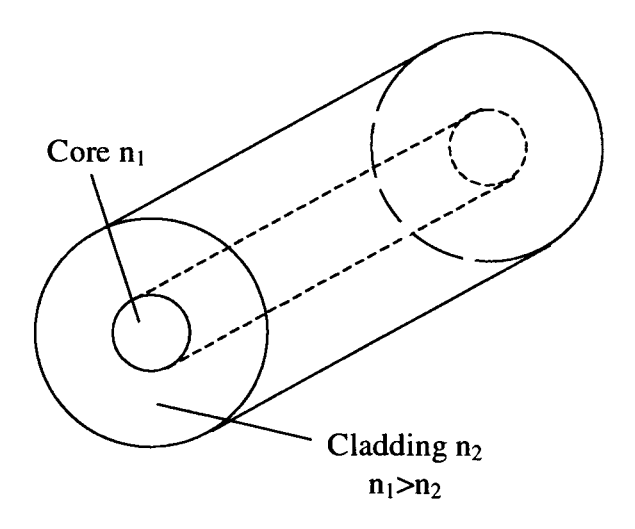


Figure 4-1 Optical fibre

The propagation of light guided in an optical waveguide may be explained by a ray model. Light incident at an angle  $\theta_1$  on the boundary between two dielectric media of refractive indices  $n_1$  and  $n_2$  where  $n_1 > n_2$ , will in general produce a transmitted and a reflected wave. The reflected wave will emerge at an angle  $\theta_r = \theta_1$ , whilst the transmitted wave is bent towards the normal making an angle  $\theta_2$  to the normal given by Snell's Law<sup>4</sup>,  $n_1 \sin \theta_1 = n_2 \sin \theta_2$ , as shown in Figure 4-2.

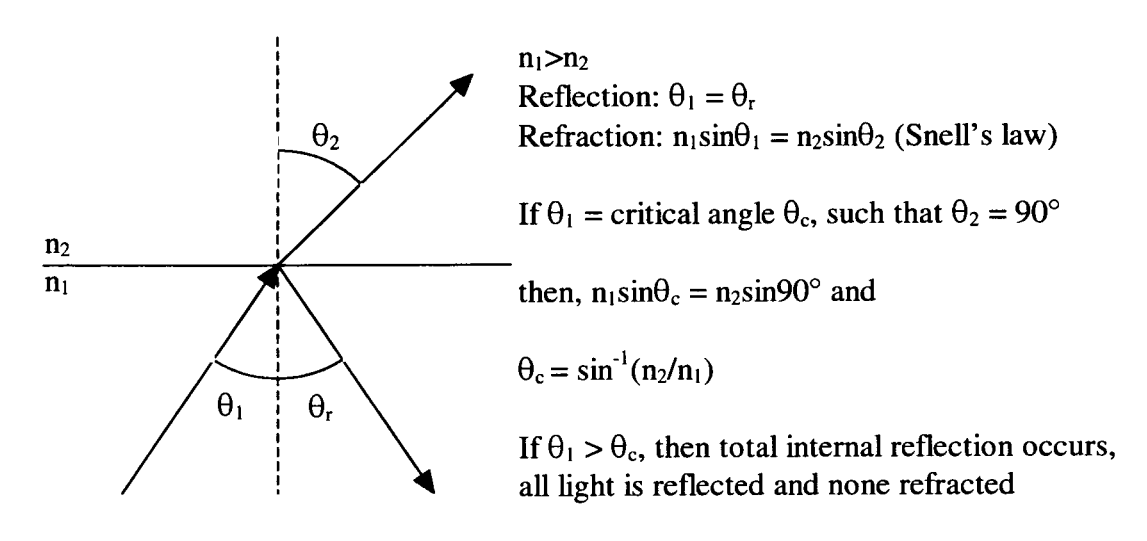


Figure 4-2 Light guiding in an optical fibre due to total internal reflection

If the incident angle  $\theta_1$  is increased to a critical angle  $\theta_c$  such that  $\theta_2 = 90^\circ$ , then:

$$\theta_1 = \theta_c = \sin^{-1} \left( \frac{n_2}{n_1} \right) \tag{4-1}$$

If  $\theta_1 > \theta_c$ , then there is no transmitted light, all the light is reflected and total internal reflection occurs. The principle of total internal reflection is employed in optical waveguides, and light propagates along an optical fibre by multiple reflections from the core-cladding interface as shown schematically in Figure 4-3.

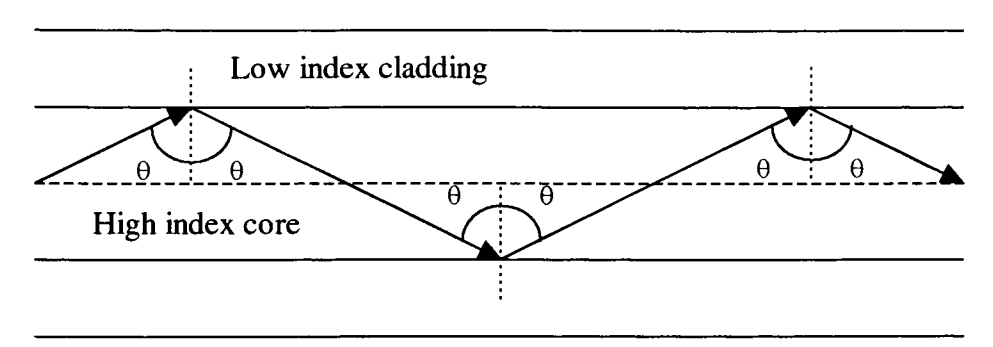


Figure 4-3 The transmission of light ray in a perfect optical fibre due to multiple reflections

The core diameter of the fibre is 2a, the cladding diameter 2b and considered infinite in thickness in that the optical field does not extend beyond the parameter of 2b. The range of incident angles  $\theta_1 > \theta_c$ , over which total internal reflection occurs, defines an input acceptance cone to the optical fibre, within which incident light will propagate along the fibre. The cone is defined by the numerical aperture NA.

$$NA = (n_1^2 - n_2^2)^{\frac{1}{2}} = n \sin \theta_a$$
 (4-2)

where  $\theta_a$  is the acceptance angle, i.e., the limiting case of  $\theta_1$ , and n is the refractive index of the medium surrounding the optical fibre, which is generally air for which n = 1 (Figure 4-4).

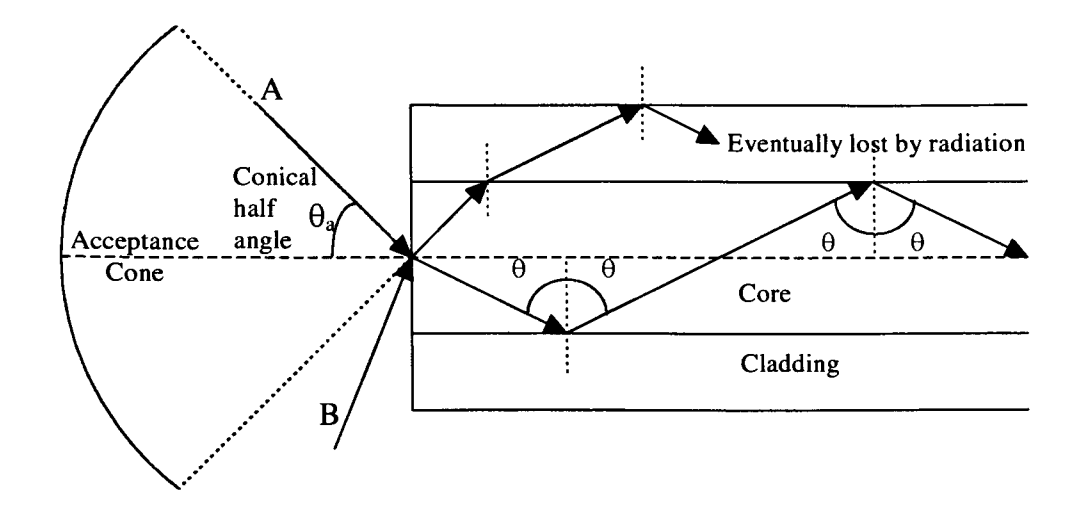


Figure 4-4 The acceptance angle  $\theta_a$  when launching light into an optical fibre

Whilst the ray model explains the essential elements of the propagation phenomena by total internal reflection, for a complete description of propagation of light along an optical waveguide, electromagnetic theory must be used. Electric and magnetic field distributions in the different dielectric materials can be derived and the solution of Maxwell's equations determined by applying the appropriate boundary conditions<sup>4</sup>. Following this, a discrete set of paths (modes) along which the light can propagate is defined. These modes are determined by the fibre and optical wave parameters and defined by the quantity V-number of the optical fibre:

$$V = \frac{2\pi a}{\lambda} (NA) = \frac{2\pi a}{\lambda} (n_1^2 - n_2^2)^{\frac{1}{2}}$$
 (4-3)

Where  $\lambda$  is the wavelength of the propagating light and a is the radius of the core of the fibre.

Each mode propagates along the fibre with a different velocity, therefore there is a differential time delay for information travelling along different modes for a set length of fibre. Two types of fibre are defined, single or mono-mode and multimode; multimode fibre supports propagation of many modes, whilst single mode when V < 2.405, which corresponds to the first zero crossing of the Bessel function describing the electromagnetic modal propagation<sup>4</sup>.

Multi-mode optical fibre is available in a range of sizes and various standard fibres are in use, the more common are:

Core diameter [µm]	Cladding diameter [µm]
50.0	125
62.5	125
100.0	140
200.0	280

However large >1mm polymer fibres are also readily commercially available. Fibres are primary coated with a polymer during fabrication to protect from crack propagation. Many are secondary coated to provide further protection and these coatings vary considerably.

Two main types of multimode optical fibres are in use, step index and graded index. Step index fibre has a sharp change in refractive index at the core-cladding interface and an essentially constant refractive index profile across the core. Graded index fibre has a gradual refractive index change across the core which is maximum in the centre and decreases with radial distance from the centre to match the cladding at the interface. This has the effect of focusing the propagating modes to reduce intermodal dispersion.

Single mode optical fibre has a core diameter dependent upon the operational wavelength on the V-number and is typically between  $4\mu m$  and  $10\mu m$ , with the cladding diameter generally  $125\mu m$ .

The transmission characteristic of optical fibres, in particular attenuation (transmission loss) and bandwidth, are of utmost importance when considering the suitability of optical fibres for specific applications. The signal attenuation of a fibre  $\alpha$  is usually expressed in decibels per unit length (i.e., dB km<sup>-1</sup>) following:

$$\alpha_{dB}L = 10\log\frac{P_i}{P_i} \tag{4-4}$$

where  $\alpha_{dB}$  is the attenuation per unit length, L is the length of fibre,  $P_i$  is the input (transmitted) optical power into the fibre and  $P_o$  is the output (received) optical power from the fibre. Several different mechanisms are responsible for the signal attenuation within an optical fibre, and are influenced by material composition, preparation and purification technique, and waveguide structure. These include: material absorption, Rayleigh and Mie scattering, stimulated Brilouin and Raman scattering and bending losses. All these phenomena are described in more detail in the open literature<sup>4,5</sup>.

Finally, it is important from the point of view of optical fibre sensors based on single-mode fibres to mention the phenomenon of birefringence present along the optical fibre. Any cross sectional variation in the refractive index profile of a single mode fibre gives rise to the birefringence phenomenon due to the difference in effective refractive indices and hence phase velocities for the two orthogonally polarised modes which propagate along the fibre. The two modes have different propagation constants  $\beta_x$  and  $\beta_y$  which are dictated by the anisotropy of the fibre cross-section. The modal birefringence of the fibre  $B_F$  is given by<sup>5</sup>:

$$B_{F} = \frac{\beta_{x} - \beta_{y}}{2\pi / \lambda} \tag{4-5}$$

Due to the difference in phase velocities of the two modes the fibre exhibits a linear retardation  $\phi(z)$  (known as modal retardance) which depends upon the fibre length L in the z direction and is given by:

$$\phi(z) = (\beta_x - \beta_y)L \tag{4-6}$$

The characteristic length  $L_B$ , is the length over which the relative phase of the two modes is retarded by  $2\pi$  and is known as the beat length of the fibre defined by:

$$L_{B} = \frac{2\pi}{\beta_{x} - \beta_{y}} = \frac{\lambda}{B_{F}}$$
 (4-7)

In non perfect fibres, various perturbations along the fibre length such as strain or variations in the fibre geometry and composition lead to coupling between the two orthogonal components. This causes the state of polarisation to vary along the length of the fibre in an unpredictable way. These perturbations are difficult to eradicate since they often occur during manufacture. Indeed optical fibre has birefringence 'frozen in' during manufacture but can be modified by external factors such as changes of temperature, stress or bending. Therefore, the state of polarisation for light propagating through an optical fibre is dependent upon external interaction. In order to stabilise the linear polarisation state it is necessary to reduce the amount of coupling between the two orthogonal polarisation components.

Two types of optical fibre have been developed to preserve the state of polarisation for single mode propagation, low birefringence (lo-bi) and high birefringence (hi-bi) fibre. Low birefringence fibres need a reduction in the possible perturbations within the fibre during the manufacture and extreme care must be taken when jacketing and winding these fibres to reduce bends or twists that may contribute to the birefringence. One technique is to spin the fibre preform during the drawing process to integrate any intrinsic birefringence effects during fabrication. The fibre produced in such a manner has no birefringent properties and produces extremely low variation in the state of polarisation providing there are no external birefringence effects. This type of fibre has been used in current sensor applications, where external effects, e.g., bends and pressure are used to re-introduce the birefringence; the measurement of magnetic fields and electric currents can also be performed by exploiting the Faraday effect.

High birefringence optical fibres are produced by introducing a strong linear birefringence into the fibre which has two preferential axes which propagate essentially two orthogonal, linear polarisation modes. The two axes, known as the fast and slow axes, have different effective refractive indices and consequently different propagation constants. The birefringence is defined by the beat length which is the length of fibre over which the two polarisation modes slip relative phase by  $2\pi$  radians; typically high birefringence fibres exhibit beat lengths < 3mm. A linear polarisation mode launched onto one of the fibre axes will remain in that polarisation mode to the end of the fibre, i.e., the state of polarisation is maintained.

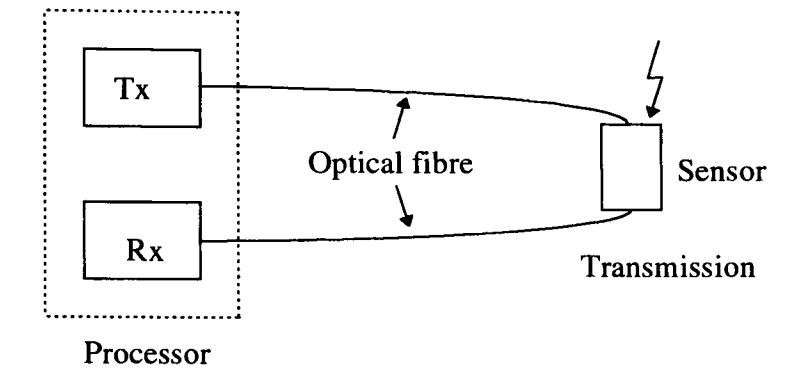
Most of the fibres were initially developed for communication system applications, but all have found application in sensors and several have been refined specifically for sensor applications.

# 4.3. Optical Fibre Sensors - Basic Principles and Configurations

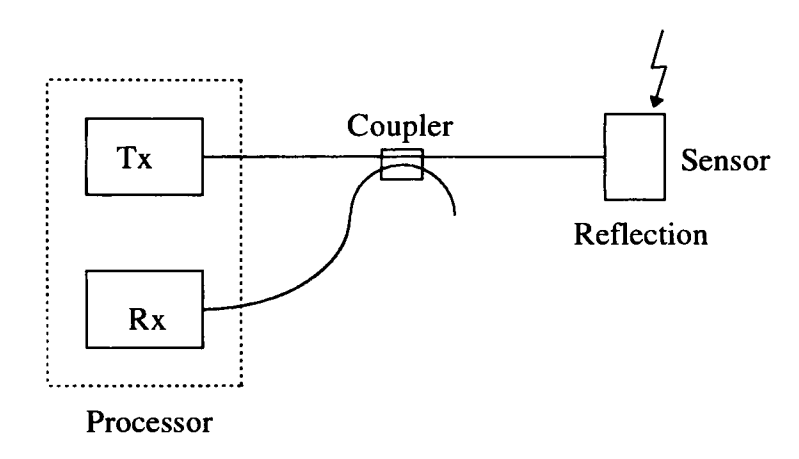
Optical fibre sensors are based on the interaction of the variable of interest with light in the sensor in such a way that modification of one of the properties of the optical signal occurs in proportion to the measurand. The four basic parameters of the optical signal which may be used as a basis of an optical sensor are:

- intensity, represented by the number of photons
- wavelength, which is associated with the energy of the photons
- polarisation state, which is the orientation of the electric field vector
- time delay, which is measured as phase shift with respect to a reference signal

Optical fibre sensor can operate in either transmissive or reflective mode as shown in Figure 4-5.



### (a) Transmission mode



(b) Reflection mode

Figure 4-5 Optical fibre sensor configuration (extrinsic sensor)

An optical detector responds to the number of photons impinging the interaction region, consequently any optical property which is varying in response to the measurand is initially converted to an intensity change before conversion to an electronic signal for further processing.

It should be noted that of the earlier mentioned modulation parameters, the only one which can be measured directly is intensity. Some form of optical signal processing must be employed in order to allow the remaining quantities to be measured. Examples of optical signal processing include the interferometer (which allows phase variations to be transformed in intensity changes), the polariser (which transforms polarisation state information into intensity) and optical colour filters (which provide

similar function for spectral content). Thus the classes of optical fibre sensors are more commonly known as intensity, interferometric, polarimetric and wavelength.

Optical fibre sensors can also be classified into single mode and multi mode sensors since both single-mode and multi-mode fibres can be utilised. In order to retain information on either the phase or state of polarisation of light guided in the optical fibre, the fibre must be either single mode or highly birefringent. If, however, the sensor is based on the modulation of intensity or spectral content (wavelength), then preservation of phase and/or polarisation state is not usually a requirement and multi mode optical fibres can be used, maximising the amount of light reaching the detector and allowing alignment tolerances of the system to be relaxed. Single mode and multi mode optical fibre sensors require different components, e.g., fibres and optical sources. For example, single mode systems usually require optical sources with high coupling efficiency into low NA fibre, of small core diameter (typically 3-10µm) and high coherence properties (for observation of interference effects) and therefore laser sources are necessary. Multimode systems, with fibres of higher NA and core size (typically >50µm) can take advantage of alternative, low cost LEDs.

There are several parameters frequently used to assess sensor performance, assuming the sensor output is an analogue electrical voltage, representing the state of the measurand. All optical communication and telemetry systems finally depend on the detection of optical intensity. The signal-to-noise ratio gives a useful indication of the resolution (smallest discernible change in measurand):

$$SNR = \left(\frac{\eta P}{hvB}\right)^{\frac{1}{2}} \tag{4-8}$$

where, P is optical power incident on the detector,  $\eta$  is quantum efficiency of the detector,  $h\nu$  is photon energy and B is bandwidth of the optical receiver.

It is assumed that the signal in question is the total power, P, received by the detector (i.e., the sensor can provide 100% modulation index). Thus the minimum resolvable increment in the optical signal level is proportional to the square root of the rate of arrival of photons in the time interval 1/B. If the modulation signal from the sensor is a small fraction of the mean level, P, then the signal-to-noise ratio will be reduced by the same factor as the modulation index.

There are several additional noise sources in a sensor system which contribute to the total noise which increases with bandwidth, including noise from connectors, couplers, and electrical noise from optical sources and detectors. In addition, whilst optical fibres are immune to the electrical noise they are susceptible to mechanical noise such as vibration and bending. Finally, it is desirable that the sensitivity of the sensing element (i.e., the constant of proportionality between the output and input) is constant over the range of operation.

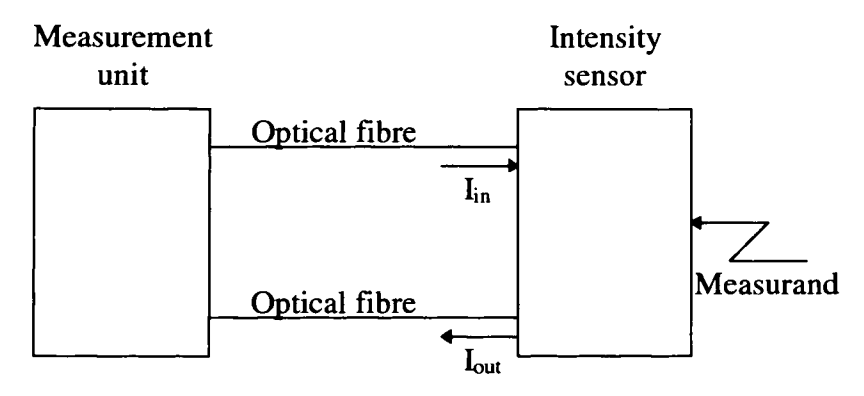
Optical fibre sensors can be divided into two categories, intrinsic and extrinsic sensors. Intrinsic sensors modify the propagation of the light through the optical fibre in the transduction process, and the optical fibre is the sensor in this case. Whereas extrinsic sensors use the optical fibre to transmit the optical signal between the sensor head and the processor unit, but the transducer is external to the fibre. Examples of both types of a sensor are given below.

Optical fibre sensors are further categorised into the techniques upon which they are based, i.e., which parameter undergoes modulation, intensity, wavelength, polarisation or phase. Intensity sensors use a variety of techniques to modify the light intensity as a function of the measurand. This type of sensor typically gives a limited sensitivity and dynamic range but is considered to be simple in structure. Interferometric sensors are based on modifying the phase of the propagating light thus providing a highly sensitive measurement solution. However, such sensors necessitate the use of a reference signal which adds complexity to the design.

## 4.3.1. Intensity Sensors

Intensity based sensors are optically straight forward and are consequently often termed simple sensors. This notation has created considerable misunderstanding and consequential under estimation of system design requirements. In common with all systems design these sensors are a mix of technological development requirements. In the case of intensity based sensors the complexity of the problem has been moved away from the optics.

Intensity based optical sensors modify the optical power transmission as a function of the measurand. A schematic of the generic intensity based optical fibre sensor is shown in Figure 4-6. The output from an optical source is launched into a length of optical fibre and transmitted to the sensor head. The light is then attenuated as a function of the measurand and returned, either via the transmission fibre or through a second fibre.



Output intensity  $(I_{out}) < Input intensity (I_{in})$ 

Figure 4-6 Generic intensity based sensor

This type of sensor is usually extrinsic, but some important intrinsic devices have been developed. There are numerous methods to provide the required attenuation, the simplest being is to move an object through the optical beam, e.g., shutter or part of gratings (one fixed). An example of an extrinsic sensor is the moving diaphragm which has been demonstrated for pressure sensing (Figure 4-7)<sup>1</sup>.

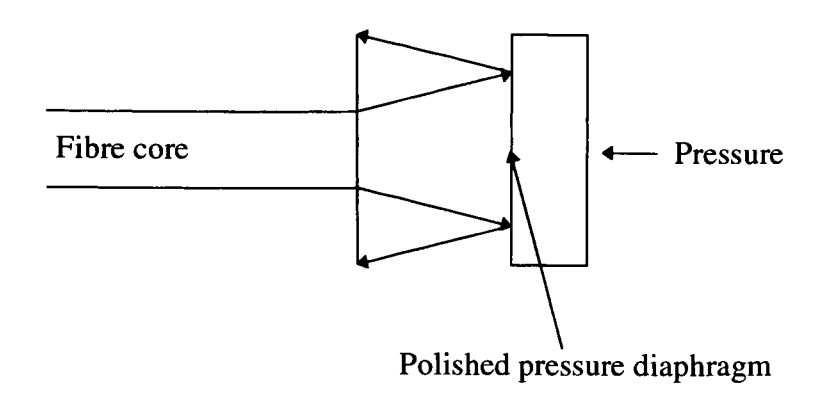


Figure 4-7 Pressure diaphragm sensor

The optical fibre is fixed at a small distance from a reflective diaphragm surface, the light travels out from the fibre in a cone defined by the numerical aperture, is reflected by the diaphragm towards the fibre and a proportion is propagated back to the receiver. The level of light returned to the receiver is dependent upon the distance of the fibre end from the diaphragm. The response of such a sensor is shown in Figure 4-8, the displacement range is a function of the fibre properties. Typically, a 50µm core step index communications fibre will give a 50µm measurement range, the dynamic range is typically 30dB for a device of this type.

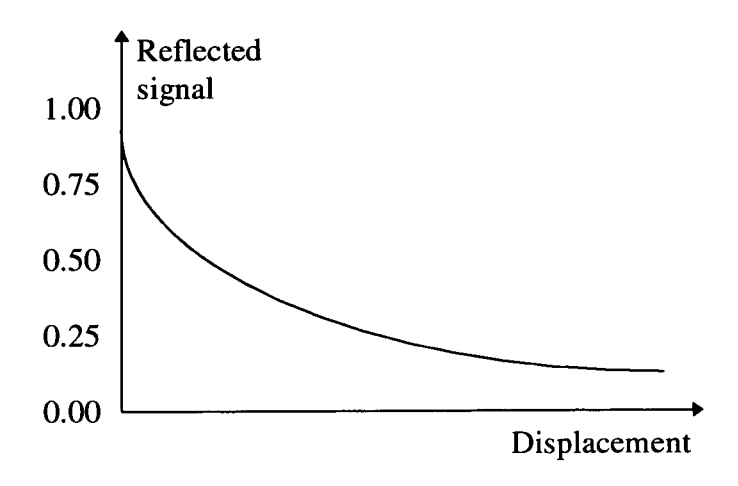


Figure 4-8 Typical response from pressure diaphragm sensor

The same mechanism can be used for temperature measurement<sup>6</sup>. The diaphragm is replaced by a mirror fixed at a known distance from the fibre head. Both the fibre and mirror are located in a cavity formed from material with an appropriate thermal expansion coefficient. As the material heats it expands (conversely it contracts on

cooling) thereby increasing the separation between the fibre and the mirror. The schematic of the sensor is shown in Figure 4-9.

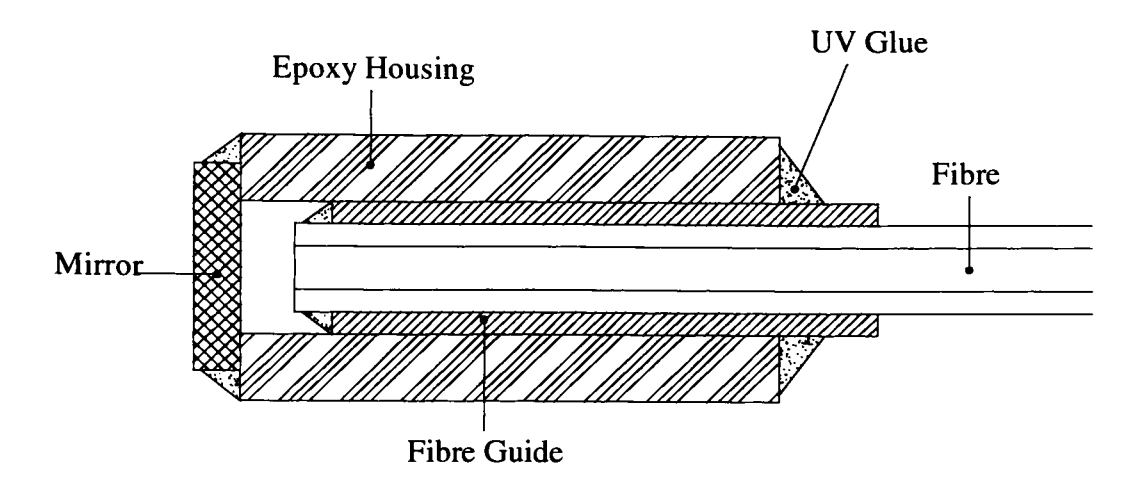


Figure 4-9 Reflective type temperature sensor

The advantages of this sensor type are, that it is simple in concept, easy to implement and requires standard optical components. The complexity is incorporated into the precision mechanical design, stability and repeatability requirements, and electronic processing design.

The main problems associated with intensity based sensors are these of undesirable changes in the transmission characteristics of the system, e.g., coupling losses at connectors and splices, source fluctuations, fibre bending and vibration losses, and system drive. Several referencing techniques have been proposed to compensate for the variable effects whilst retaining the modulation information of the sensor. Differential sensor configurations use two spatially separated channels (different fibres) and ratio the two detector outputs to reduce drift effects. However, the two fibres also exhibit different attenuations. Two distinguishable channels which undergo identical system induced losses except at the sensing mechanism are required. This can be achieved in two ways, either two channels, one of which is the signal channel and one a reference channel unaffected by the modulation; or by two channels which show different effects to the modulation. Possible solutions include dual wavelength techniques incorporating two optical sources and two detectors of different, but close

wavelengths, so the same non-sensor losses are experienced in the two channels; the sensing element attenuates light of one wavelength but not the other. Both optical sources send light along the same optical path through the system via a coupler, and are alternatively pulsed giving an output in the form of a ratio of the sensor-dependent losses. Another solution is the recirculating path as a time domain referencing technique in which light is manipulated, so that successively smaller portions recirculate through the sensing element<sup>1,5</sup>. For a short pulsed input, the ratio of the intensities of successive peaks thus gives an intensity referenced measurement of the sensor-induced attenuation (Figure 4-10).

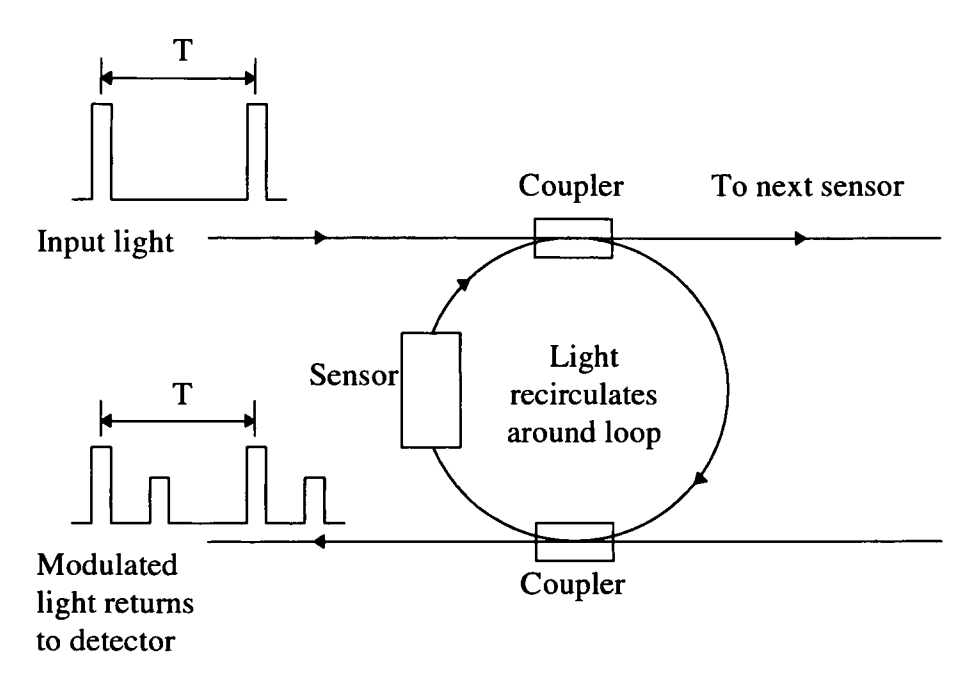


Figure 4-10 Recirculating path referencing

Yet another time domain technique is that of balanced intensity referencing<sup>1</sup> which uses two sources of the same nominal wavelength, two separate fibre paths for the signal and referencing channels and two detectors. In addition, it is necessary for both beams to pass through as shown in Figure 4-11. Its operation is analogous to an electrical Wheatstone bridge arrangement and the output ratio is independent of source intensity variations, fibre and connector losses and detector sensitivity. It is, however, dependent on the coupling losses in the bridge network; it can be assumed

that these are stable and small compared to sensor-induced losses. The construction of the sensor head is complicated, requiring four fibres.

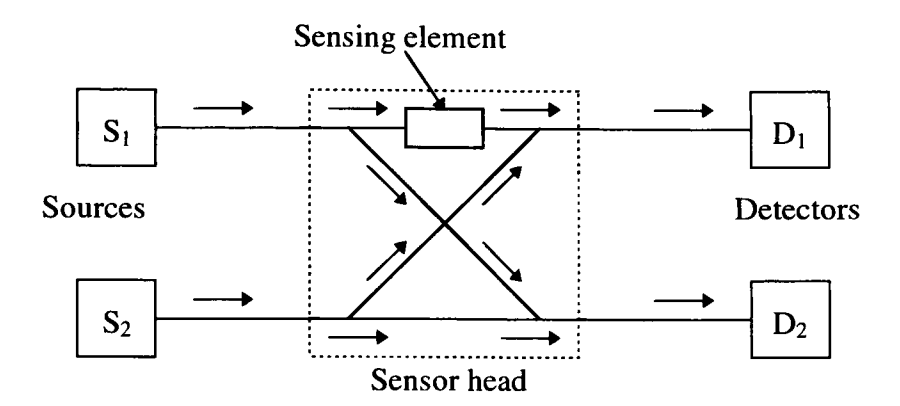


Figure 4-11 Balanced-intensity referencing

It is clear once these simple sensors are examined in detail for many applications, the complexity, size and cost increase for a practical sensor design.

### 4.3.2. Wavelength and Frequency Modulation Sensors

Wavelength modulation sensors operate by measuring changes in the spectrum of the light arriving at the optical receiver. To achieve this, relatively large changes in the transmitted, fluorescent or reflected spectra (due to interaction with the measurand of interest) are desirable. This may be achieved by specially designed sensing heads incorporating spectral filters. Alternatively materials such as fluorescent species or indicator dyes which show a characteristic change in optical emission or transmission spectra may be used, for example the absorption spectra of gases can be used to measure their concentration. Figure 4-12 shows typical spectral characteristics of modulated light.

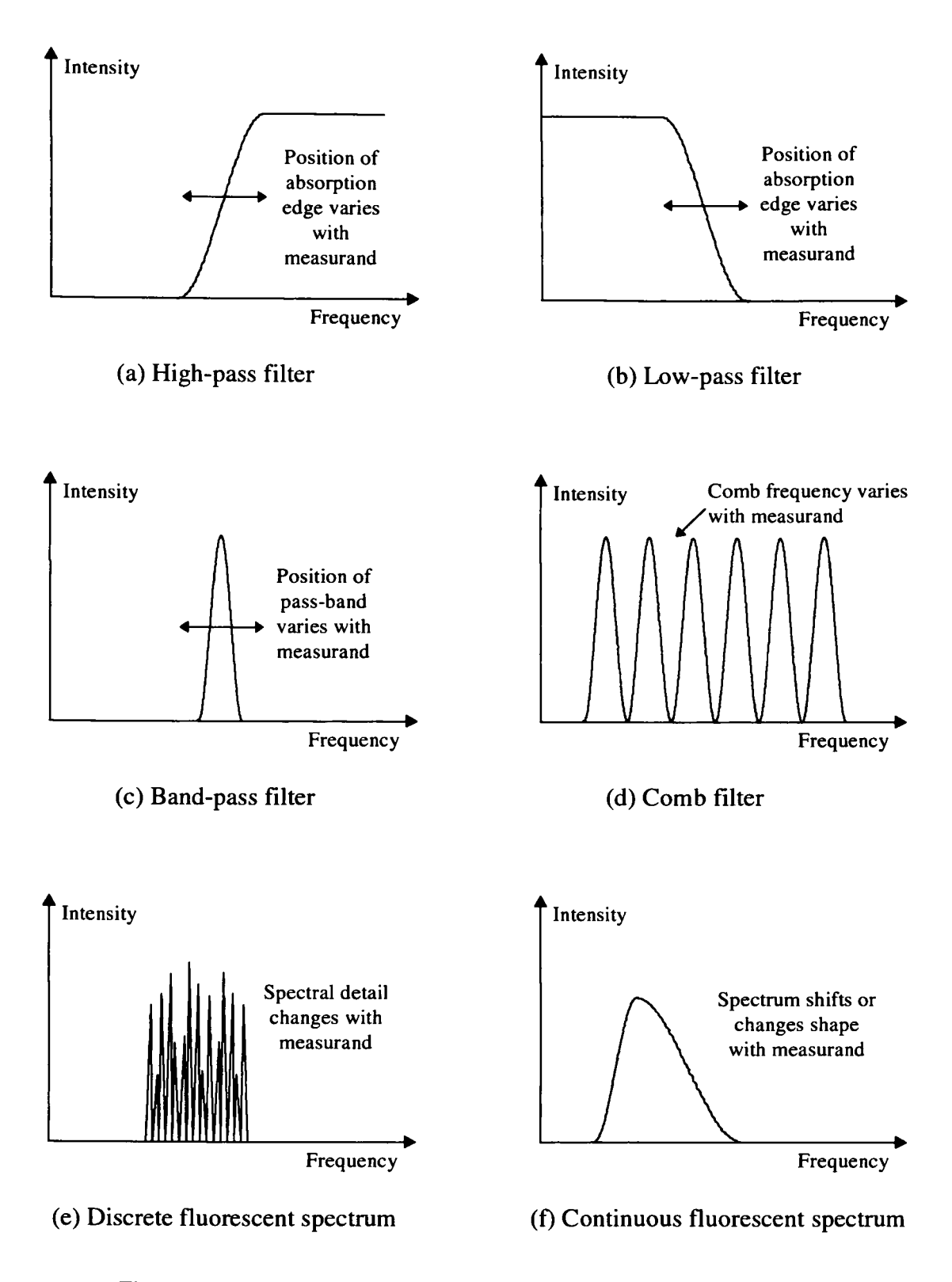


Figure 4-12 Spectra produced by various spectral modulation sensors

Prior to detection, wavelength analysis or filtering is required utilising specialised optical components such as dichroic beamsplitters, optical filters, dispersive elements (prisms, diffraction gratings), special filters (interference, birefringent). The filtering

process may involve ratiometric analysis, in which the signal is split into two channels subjected to different filters and the two detected intensities ratioed; filter matching, using a filter which has a tuneable spectral modulation or white light interferometry to match the sensing element; or high accuracy spectrometers.

Wavelength modulation sensors are less sensitive to overall changes in attenuation characteristics of the system components, e.g., optical sources, than intensity based systems, however the optical receivers are more complex.

Many extrinsic wavelength modulation optical fibre sensors have been developed for the measurement of chemical parameters, e.g., pH and the concentration of analytes (both gas and liquid phase), utilising fluorescent species and indicator dyes. There is a great interest in such sensors for pollution and environmental monitoring applications.

Optical fibre sensors based on wavelength modulation have also been developed for physical parameters, in particular temperature. In one such sensor the fibre tip is coated with a phosphor which when excited by UV light, exhibits an emission spectrum dependent on temperature<sup>1</sup>.

The wavelength changes are sometimes small and difficult to measure directly, however the accompanying frequency changes are larger and can be monitored by mixing the light with a reference beam, observing the beat signal and utilising the heterodyne detection schemes. The most widely implemented frequency modulated sensors are those based on laser Doppler velocimetry where laser light reflected off a moving object undergoes a Doppler frequency shift.

### **4.3.3.** Interferometric Sensors

Interferometric sensors are single mode optical fibre sensors used to measure the vector properties of the optical wave which are modified by the measurand; that is the amplitude and phase. The interferometer operates as an optical signal processor to convert the phase information into intensity modulation which can then be detected.

An interferometer provides a reference which can be compared with the signal. Figure 4-13 shows a schematic of an interferometer in which the input is split into two paths with differential time delay  $\tau$ .

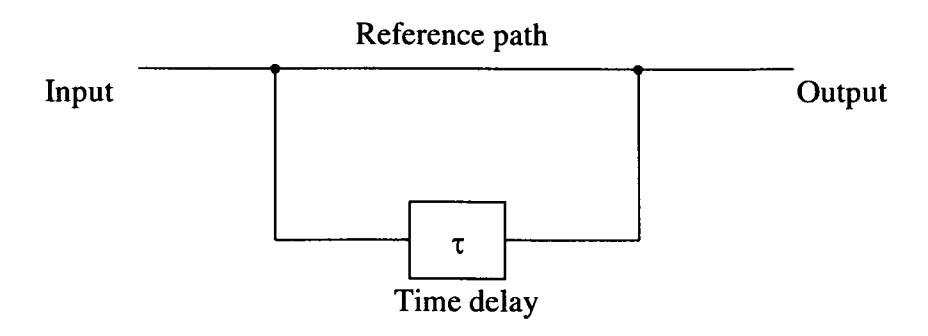


Figure 4-13 Schematic diagram of an interferometer

The two paths are recombined and the resultant intensity detected. The input wave can simply be described by  $E_0 e^{-i\omega t}$ , assuming the reference path experiences time delay  $t_1$  and attenuation  $A_1$  giving an output of  $E_1 e^{-i\omega(t-t_1)}$  and the signal path experiences a time delay  $t_2$  and attenuation  $A_2$  giving an output of  $E_2 e^{-i\omega(t-t_2)}$ . The two amplitudes are added and the result intensity detected, given by:  $E_1^2 + E_2^2 + 2E_1E_2\cos\omega(t_1-t_2)$ .

The response of this is a function of differential time delay or phase as shown in Figure 4-14. Varying the amplitude of either optical signal causes the overall intensity level to change and varying the time delay introduced causes the intensity to vary in a cyclic fashion, these are the interference fringes associated with such interferometers.

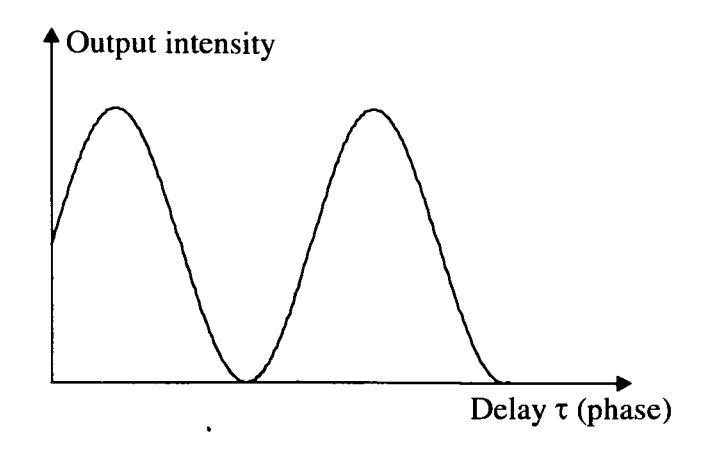


Figure 4-14 Intensity variation with time delay  $(\tau)$ 

Throughout the discussion the signals have been assumed to be coherent. This assumption is valid for many laser sources, but has to be seriously considered in sensor design using semiconductor laser sources. In general all optical sources are partially coherent. If a coherent signal is delayed and recombined the signals add in amplitude, thus preserving the phase information. If the combined signals are incoherent then they add in power and the phase information is lost.

There are four categories of interferometer, all of which have been used in optical fibre sensors:

- two beam interferometers, e.g., Michelson, Mach-Zehnder
- multiple beam, e.g., Fabry-Perot, ring resonator
- differential, e.g., polarimetric
- reciprocal, e.g., Sagnac

Figure 4-15 and Figure 4-16 show both bulk optical and optical fibre versions of the Mach Zehnder and Michelson interferometers. The most common is the Mach Zehnder interferometer which uses two couplers to split and recombine the two optical signals. This type of device operates in the transmission mode, thus avoiding any optical feedback to the laser source which can occur in reflective sensors. The two outputs from the interferometer vary in antiphase and hence simple electronic signal processing can be employed. Many signal processing schemes utilise a piezoelectric modulator to control the phase in one arm of the interferometer with

respect to the other. The Michelson interferometer is essentially a reflective version of the Mach-Zehnder and requires only a single coupler to both split and recombine the optical signal. Although simpler than the Mach-Zehnder, additional considerations are needed to accommodate the scattering effects and spurious reflections from the fibre paths. In addition, polarisation effects can reduce the visibility of the fringes and polarisation controllers of birefringent fibres may be required.

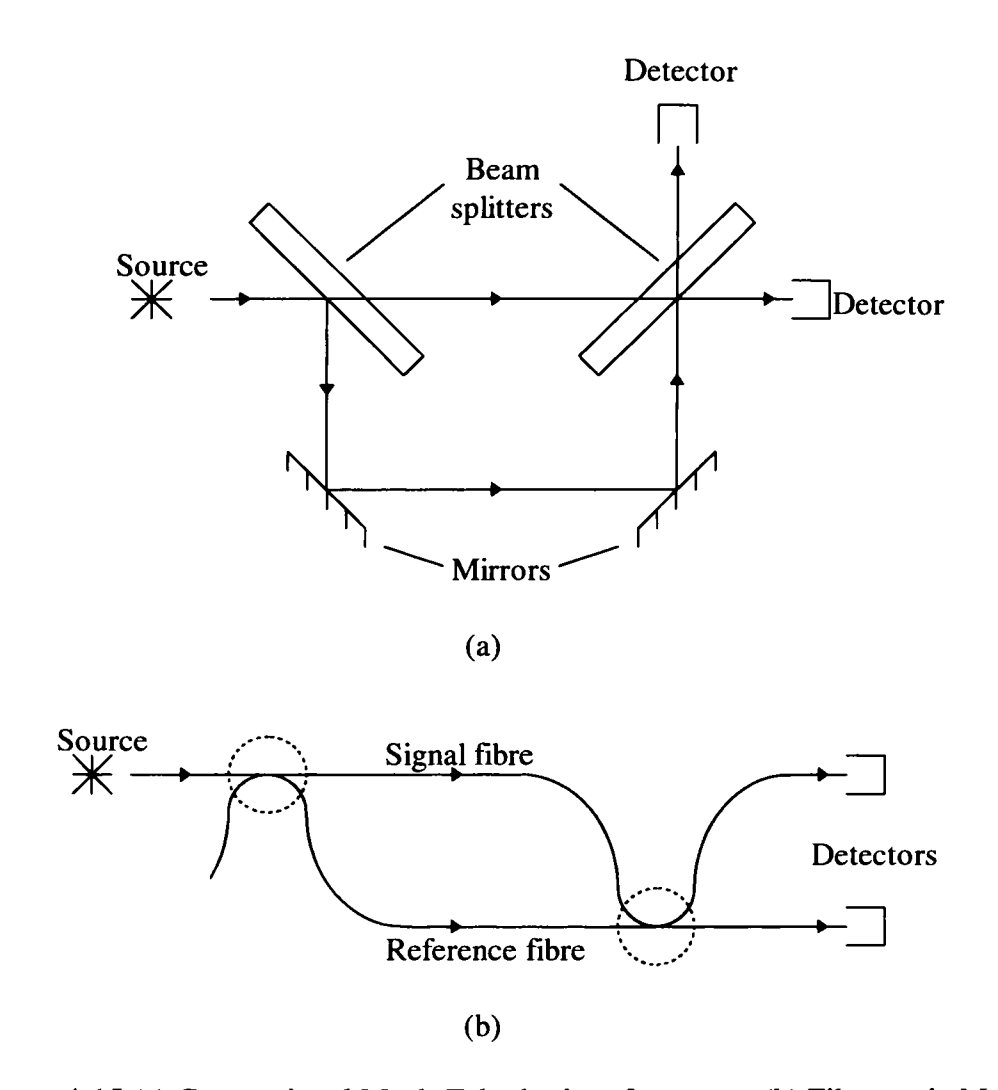


Figure 4-15 (a) Conventional Mach-Zehnder interferometer, (b) Fibre-optic Mach
Zehnder interferometer

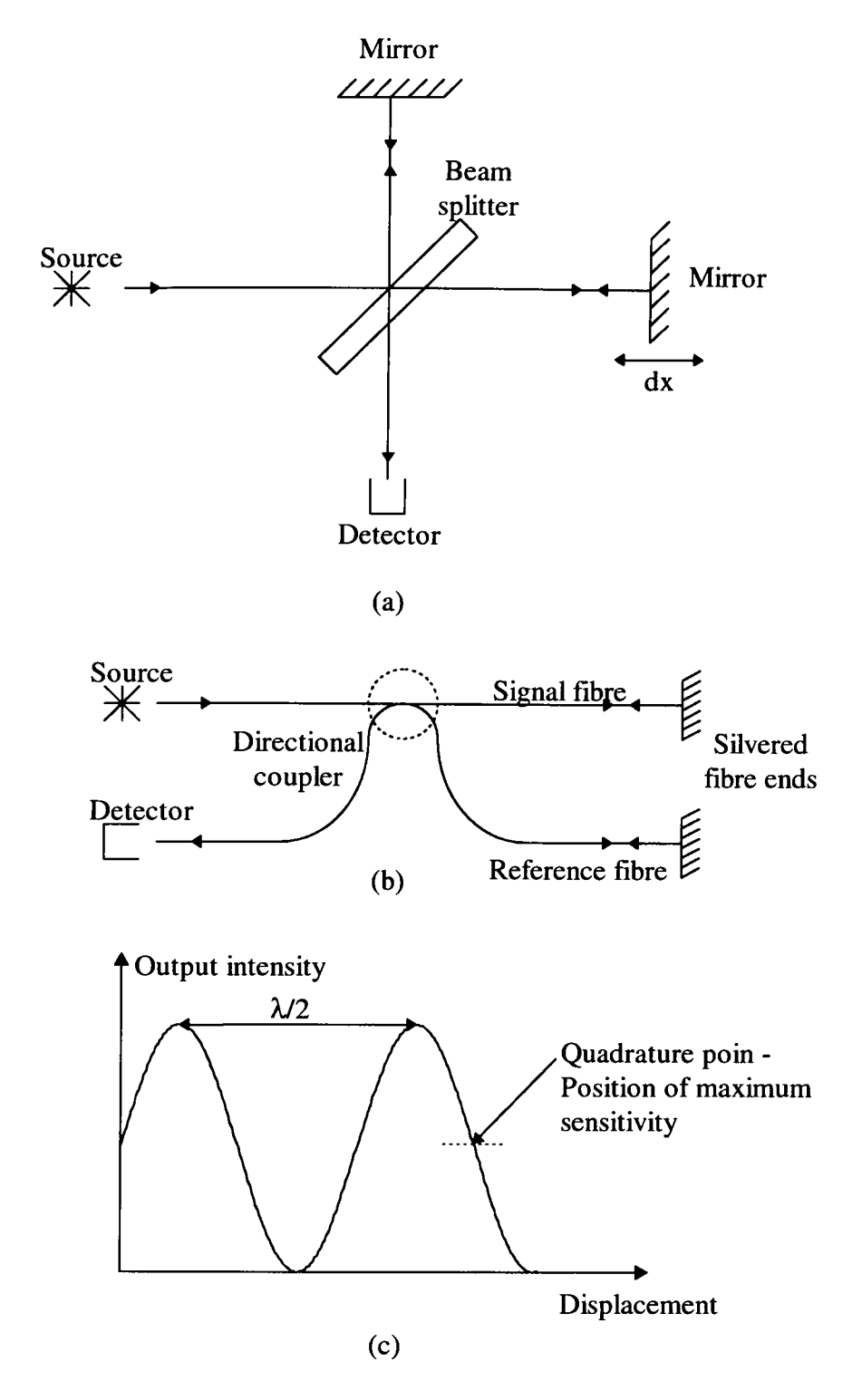


Figure 4-16 (a) Conventional Michelson interferometer, (b) fibre-optic Michelson interferometer, (c) Interferometer output as a function of mirror displacement

The Sagnac interferometer (Figure 4-17) is a closed path device in which the split signals travel identical fibre paths, but in different directions. The additional coupler in the optical fibre version allows truly reciprocal output since the clockwise and

anticlockwise beams undergo the same number of direct transmissions and cross coupling through the coupler. For many path delay changes both signals experience similar phase shift, however, any non-reciprocal effects are detected. This type of interferometer has been used to measure rotation rates (gyroscopes) and current sensors, utilising the Faraday effect.

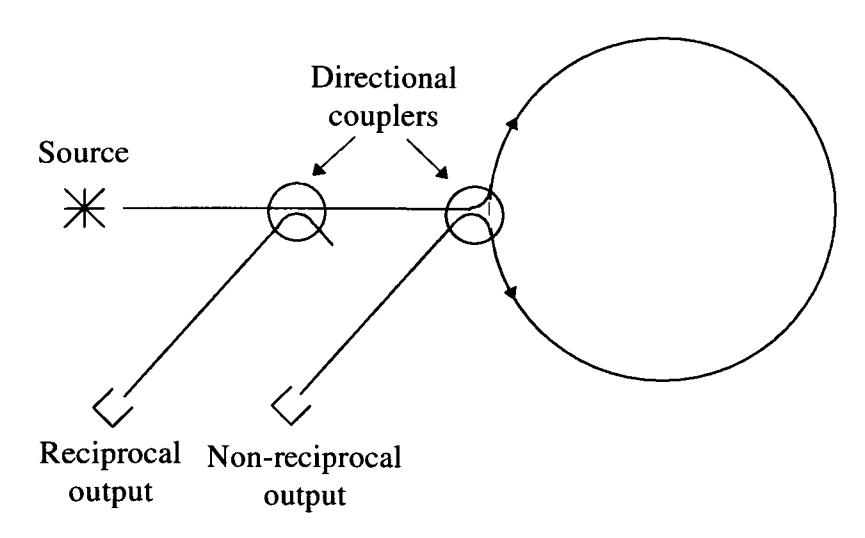


Figure 4-17 Fibre-optic Sagnac interferometer

All the interferometers described above are two beam interferometers, an additional important class are multibeam interferometers, and in particular the Fabry-Perot interferometer. The interferometer is formed by two parallel, highly reflecting surfaces which cause the optical signal to undergo multiple reflections (Figure 4-18), thus giving an effective increase in optical path and thereby increasing sensitivity.

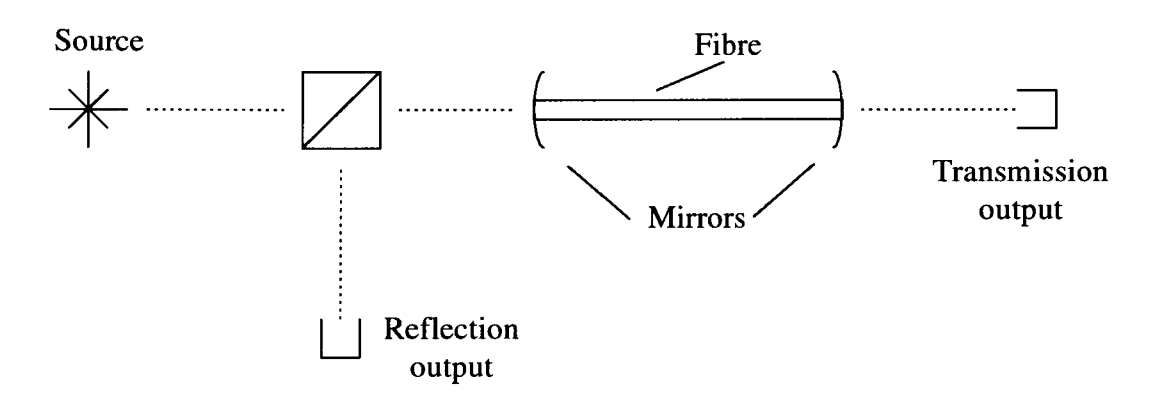


Figure 4-18 Fibre-optic Fabry-Perot interferometer

Interferometric optical fibre sensors have been developed for a range of applications including, strain, acoustic, magnetic field, current, temperature, rotation rate and flow velocity. The measurand is converted into a phase change in one path of the interferometer which is then compared with the unaffected reference path. The typical sensitivity for this type of sensor<sup>5</sup> is  $10^{-6}$  radians phase shift/ $\sqrt{\text{Hz}}$ . Optical fibre interferometric sensors are typically intrinsic and the optical fibre is the transducer.

Another form of interferometric sensors are polarimetric sensors which operate on the principle of modifying the linear birefringence of a material in response to a stimulation from the measurand. The sensor is of a form of differential interferometer which can be produced with a single optical fibre. The two light beams travel in the same fibre but with orthogonal polarisations. Figure 4-19 shows the technique schematically.

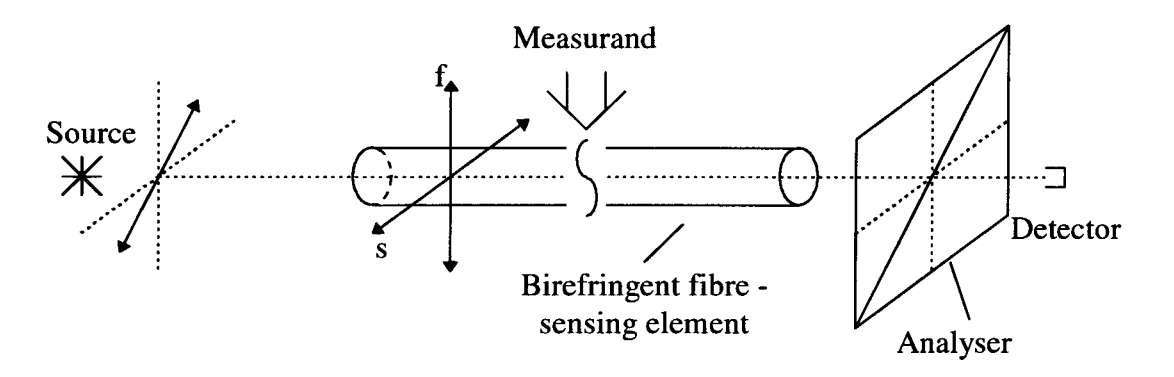


Figure 4-19 Basic polarimetric sensor

The input beam is linearly polarised at 45° to the birefringent axes of the sensing material. Resolved along the axes of the material each component of the polarisation will experience a different phase shift dependent upon the interaction of the measurand and the material (i.e., temperature, applied load or strain), thus modifying the state of polarisation. A second polariser at the output located at 45° samples a component from each of the material orthogonal axes and combines them coherently, so that the output intensity varies as a function of phase shift (exhibiting the same transfer function as the two beam interferometer).

Both extrinsic and intrinsic sensors have been developed using this technique and include the measurement of load, strain and temperature. Using this approach it is possible to produce simple single fibre probe sensors for temperature or pressure which are highly sensitive and very compact.

A fundamental problem with all single mode optical fibre sensors (both interferometric and polarimetric) is that their transfer functions are periodic; and the complementary outputs from a two-beam system are in antiphase. The effect of this periodicity is that the value of the recovered measurand is ambiguous and the sensitivity is variable. The sensitivity is dependent on a phase difference  $\theta_d$  between the two beams arising from environmental drift and noise. When  $\theta_d$  is zero, the sensitivity is also zero and the signal fades completely. Ideally, operation of the sensor should occur, where the sensitivity is a maximum ( $\theta_d = \frac{\pi}{2}$ ); this is called the quadrature condition and is the position halfway between the maximum and minimum of the transfer function. The objective of any signal processing scheme is to produce an output of constant sensitivity which is free from fading, and linear with respect to the measurand.

There are two basic classifications of signal processing schemes: homodyne (active and passive) and heterodyne. Active homodyne signal processing avoids signal fading and maintains constant sensitivity by using feedback to lock the sensor system at the quadrature point. This is achieved by phase control for interferometric systems and polarisation control for polarimetric systems. Phase modulation is achieved by either path length tuning, in which the phase retardance of the beam is controlled by varying the optical path length, e.g., by using piezoelectric transducer to strain the fibre in axial direction or by thermal modulation using electric currents passed through metallic coatings, or finally by wavelength tuning of the laser diode source. Polarisation modulation can be performed by straining or heating birefringent fibre which varies the phase difference between the two eigenmodes and hence controls the polarisation ellipticity. Active homodyne systems exhibit simplicity but need resetting due to the limited phase tracking of the modulator and suffer from noise problems.

Passive homodyne processing produces two outputs from the interferometer bearing a constant phase relationship to each other so that they cannot fade simultaneously; one signal is at quadrature point when the other has faded and vice versa. The generation of the quadrature outputs can be achieved by a 3 x 3 directional coupler<sup>1</sup> (which introduces a phase shift between the transmitted and coupled beams); dual wavelength technique; or polarisation biasing, a quarter wave plate produces a 90° phase shift between the two orthogonal modes. Electronic signal processing can then be implemented, either square and add, or differentiate and multiply the two outputs to obtain a constant linear output.

The heterodyne processing uses a frequency shift imposed onto one of the beams to create a heterodyne carrier signal which is then modulated by the measurand. Several techniques exist for the demodulation of the carrier signal<sup>5</sup>. The frequency offset between the two beams is difficult to achieve directly in optical fibre systems, and so pseudo frequency shifters are used in which the phase is modulated. For example, if the injection current of the laser is modulated by a ramp signal, then ramp modulation of the optical frequency occurs causing a constant rate of change of the phase in the interferometer which is equivalent to a frequency shifter.

Noise is present in signal processing schemes from several sources: environmental and intrinsic drift, shot and terminal noise from detector and electronics, excess laser noise both intensity and frequency which converts to phase noise in unbalanced interferometers. Intensity noise can be compensated for by electronically dividing the output by an intensity reference from the source.

## 4.4. Multiplexed and Distributed Sensing

A very important feature of optical fibre sensors is their multiplexed or distributed sensing capability. For many sensing applications it is necessary to make either several point measurements or a continuous measurement over an area. This can be achieved with optical fibres by two approaches. The first, multiplexing techniques, uses a single

optical fibre highway to address a number of point optical sensors at different locations over an area. The second approach, distributed techniques, uses the intrinsic sensing properties of the fibre itself to make a spatially continuous measurement. In both cases the requirement is to monitor the magnitude of the measurand and to locate its position. This problem is analogous to that in radar systems in which several targets are to be located and information gained such as velocity, direction and size. The analogy extends to the techniques which have been developed for optical sensing. The basic techniques are based on time gating, frequency modulation and spectral slicing. In addition, each of these techniques can be applied through sub-carrier methods whereby the optical signal is modulated by a high frequency signal which is in turn modulated. In this case the optical signal is purely a carrier. Many techniques have been explored in detail<sup>5</sup>, those receiving the major attention are, time division multiplexing, frequency modulated continuos wave, wavelength division multiplexing and coherence domain multiplexing. Each of these has been proposed for both multiplexing and distributed sensing. The diversity of the techniques and methods does not allow to discuss them here in depth. More attention will be dedicated only to the Fibre Brag Grating (FBG) measurement system (more details in Chapter 6), used as a means for optical temperature measurement in the direct temperature compensation scheme for the optical current sensor developed during the research work.

## 4.5. Summary

This chapter has provided an overview of the optical fibre sensor technology. There is an abundance of transduction and processing methods applicable to monitoring measurands using optical fibre based techniques. This vast resource of approaches has led to many alternative sensors being proposed for particular applications. It is perhaps this diversity of the investigation that has restricted the commercialisation of a very valuable approach to many measurement problems. Optical fibre sensors have led the technology edge and whilst creating an enormous background knowledge have had little impact on product development. However, this wealth of knowledge is

available to be utilised and with a correctly identified measurement problem to be addressed, the full benefits of this technology can be realised. Next chapter will concentrate on reviewing optical current measurement methods with the main focus on the particular measurement technique used by the author.

## 4.6. Chapter References

- 1) J. Dakin, B. Culshaw, "Optical fiber sensors: systems and applications", Volume 2, Artech House, Inc., 1989,
- 2) J. Dakin, B. Culshaw, "Optical fiber sensors: applications, analysis, and future trends", Volume 4, Artech House, Inc., 1997,
- 3) E. Udd, "Fiber optic sensors: an introduction for engineers and scientists", New York: Wiley, 1991,
- 4) J. Dakin, B. Culshaw, "Optical fiber sensors: principles and components", Volume 1, Artech House, Inc., 1988,
- 5) N. G. Dadswell, R. Dean, "Optical sensors for power industry applications", REA Technology Ltd., 1995,
- 6) I. Madden, "Report on testing of an optical temperature sensor", CEPE reference number: RR/OPT/TR/1998-001.

# 5. The Optical Current Transducer

### 5.1. Introduction

The electrical power industry requires accurate measurement and monitoring of the electric current which is the most important measurand amongst other parameters, i.e., voltage, temperature, pressure and chemical measurands. The information about current (and voltage) is used for measurement of generated and consumed energy and for protection purposes, i.e., fault detection and location.

The most widely used conventional method of current measurement (as described in Chapter 2) is based on the 'current transformer' (CT) which is deployed around a current carrying conductor (busbar). The busbar is generally at high voltage, e.g., 440kV, and hence appropriate insulation is required making CTs expensive and large. In addition, CTs suffer from saturation and hysteresis effects and have limited bandwidth.

Optical methods of current measurement have been widely investigated as alternatives to the conventional CTs. Optical Current Transducers (OCTs) offer many advantages including inherent high voltage insulation, intrinsically safe failure modes, immunity to electromagnetic interference, enhancement in signal bandwidth and dynamic range, ease of integration into future digital control and protection systems and reduced costs. Additional benefits include reduced size and weight of the transducers compared to the conventional devices providing easier installation and potentially reduced substation land requirements.

In this chapter optical current measurement methods will be reviewed, in particular those applicable for the use in the power industry; then the author's preferred type of the Optical Current Transducer and its construction will be discussed in detail.

## 5.2. Review of Optical Current Transducer Types

## 5.2.1. Conventional CT Addressed by Optical Fibres

Conceptually, one of the simplest means of implementing an OCT is to use a hybrid design. The current measurement device of this type accommodates a conventional current transformer with added an insulated optical information channel to replace the copper wire output (Figure 5-1). The current transformer used in this approach can differ from a design of a normal high voltage CT. Since the CT needs no high voltage insulation, a shorter iron length is possible. The resistive burden connected across the secondary terminals is also constant and consumes very little power. This allows a further reduction in core dimensions, and also a greater freedom to use air-gap cores, ferrite, or an air-cored transformer, to obtain better high frequency performance.

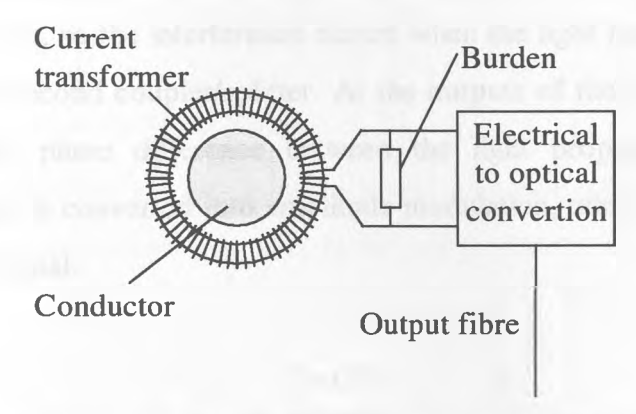


Figure 5-1 Conventional CT addressed by optical fibre

Several methods to convert the current transformer output into optical form can be employed in this type of device. One possible solution is to use electronics to produce optical output in either digital form or by a voltage-to-frequency conversion<sup>1,2,3</sup>. The transmitted optical signal is then detected and decoded to provide a measure of the current flowing in the conductor.

Such conventional type OCTs can suffer from problems associated with power requirements to supply the conversion electronics near the conductor. In some instances a second conventional CT is installed to provide the power for the electronics. Other approaches provide power via a transmitted light signal of sufficient

intensity to be able to re-convert to suitable electrical power levels. Both methods complicate the measurement.

Another method of converting the CT output into a modulated light employs the Mach-Zehnder interferometer<sup>2</sup>. In this approach the voltage across the resistive burden on the CT output is applied to a piezo-electric element onto which is wound optical fibre. The piezo-electric element causes the section of optical fibre to be mechanically strained. The strained section forms the sensing arm of the interferometer.

In the prototype OCT of this type (Figure 5-2), the output of a single-mode coherent optical source is split by a 3-dB coupler/splitter into the two arms of the interferometer. The light in one arm of the interferometer serves as a reference for the light in the other arm, so the interference occurs when the light from the two arms is recombined in the second coupler/splitter. At the outputs of the second coupler any modulation of the phase difference between the light propagating in the two interferometer arms is converted into amplitude modulation, which is then converted into the electrical signal.

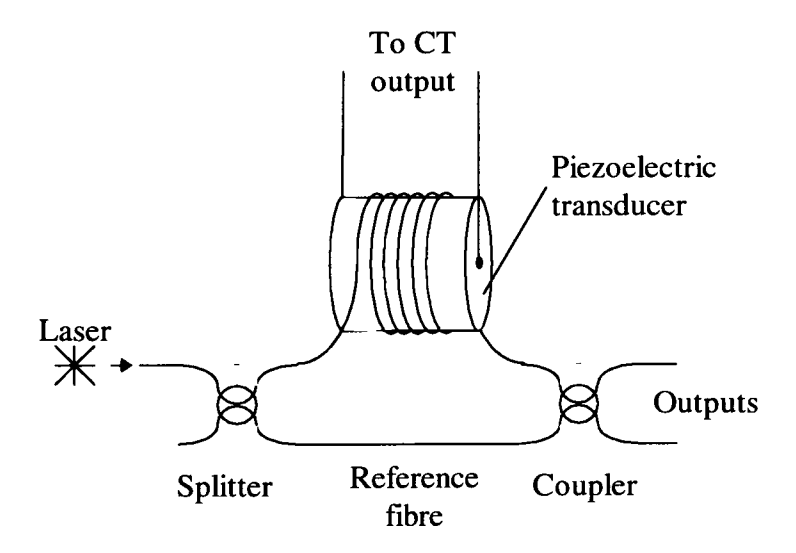


Figure 5-2 Mach-Zehnder interferometer used to monitor the CT output

This type of an OCT uses in fact two transduction mechanisms in order to convert the measured current into the modulated light; this may be the reason that so little commercial devices of this type have been so far developed. Additionally, the above measurement arrangement suffers from temperature changes and mechanical vibration, and its operation is restricted to certain frequencies when the mechanical resonance of the piezo-electric device occurs.

Yet another method of converting the CT output into a modulated light uses the Faraday effect (Faraday effect based OCTs will be discussed later in this chapter). The current from an uninsulated CT is used to create a magnetic field in a separate solenoid containing a Faraday cell used as a transducer from the electrical domain to the optical<sup>3</sup>. The need for a CT and an additional solenoid complicate the physical arrangement of the device.

### **5.2.2.** Magnetostrictive Current Sensor

Magnetostrictive materials exhibit a strain in the presence of an applied external magnetic field; this phenomenon is used in the magnetostrictive fibre optic current sensors which effectively measure the strain induced by the magnetic field.

Following the development of low loss single mode optical fibre and its employment in fibre interferometers for sensing applications, the first proposal was published<sup>4</sup> for the magnetostrictive fibre magnetic sensor utilising a bare optical fibre jacketed with nickel (a magnetostrictive material) and detecting the magnetically induced strain interferometrically. This was subsequently experimentally demonstrated<sup>5</sup>, and further work has involved the investigation of magnetostrictive fibre sensors with various magnetostrictive materials for example nickel and amorphous ferromagnetic metallic glass alloys (e.g., metglass), and different transducers configurations including fibre jackets, cylinders and toroids wrapped with optical fibre. There is a lot of work reported on the investigation of fibre magnetometers using magnetostrictive materials, with the Naval Research Laboratories, in the USA, being a major contributor<sup>6</sup>.

The magnetostrictive strain, when transferred to an optical fibre, will affect the propagating light in the fibre core. The magnetostrictive materials must physically be attached to the fibre. The measurement process is therefore indirect as the transducer consists of the fibre and the magnetostrictive material. If the transducer is introduced into one arm of an interferometer, the magnetic field induced strain of the magnetostrictive material will be coupled to the fibre, which will be observed as a phase shift of the light compared to the reference arm.

The magnetostrictive strain is generally determined interferometrically utilising either Michelson or more commonly Mach-Zehnder fibre optic interferometers (Figure 5-3). Often a piezo-electric fibre stretcher is introduced into the reference arm of the interferometer to actively stabilise the interferometer at the quadrature point of operation.

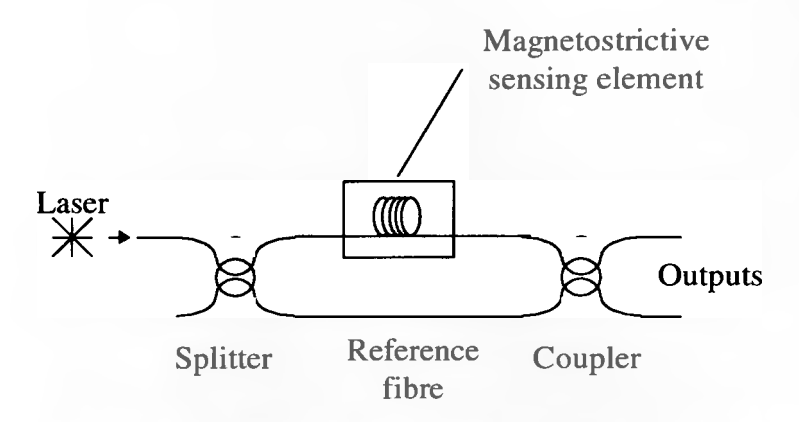


Figure 5-3 Basic components of a magnetostrictive fibre optic current sensor employing a Mach-Zehnder interferometer

In fibre optic current sensors the magnetostrictive strain must be coupled efficiently to an optical fibre. There are two basic types of transducers which achieve this. In the first type, the optical fibre is jacketed with a magnetostrictive materials, either over a bare fibre or over a fibre already jacketed with non-magnetic polymer, thus yielding a continuous length of 'magnetically sensitive' fibre. Alternatively, a length of fibre is bonded to a flat rectangular strip (e.g., ribbon or wire) or cylinder of magnetostrictive material. Epoxy is required to bond the fibre to the material and introduces a

substantial wading effect in the second type of transducer. The use of a jacketed optical fibre eliminates this and exhibits more efficient coupling of the magnetostrictive strain to the fibre. Even though not all of the strain induced in the magnetostrictive material will be coupled to the core of the fibre since the losses occur at the interface between the fibre and the material. The amount of strain transferred to the fibre depends on the type and thickness of the adhesive used for bonding, the type of fibre jacketing material and the frequency of operation.

In practice the magnetostrictive response of the material is modified by the effects of demagnetisation, mechanical loading and mechanical resonance, which must be taken into consideration. Demagnetisation exists since the magnetic field inside a highly permeable material is never equal to the externally applied field. This is due to the response of magnetic moments in the sample to the applied field in a manner that the external field is partially cancelled or magnified. Detrimental mechanical loading introduced when attaching the optical fibre to the magnetostrictive element clamps the material to a certain extent. Strong mechanical resonance have been observed in all magnetostrictive transducers with frequencies dependent on the transducer geometry, boundary conditions and effective mechanical modulus of the entire transducer arrangement (material, fibre, adhesive). The effective response to the magnetic field is degraded due to the demagnetisation, mechanical winding and coupling efficiency, whilst mechanical resonance in the transducer either enhance or diminish the response depending on the frequency of operation.

There is a vast quantity of reported work on magnetostrictive fibre optic magnetometers (current sensors), the majority of it based on the approach of bonding long lengths of fibre onto magnetostrictive glass and using a Mach-Zehnder interferometer as a strain detection instrument. Typical results have been obtained using an annealed  $25\mu m$  thick metaglass cylinder 60mm long by 44.5 mm diameter wrapped with 31m of jacketed single mode fibre<sup>7</sup>. Using low-modulus bonding epoxy the transducer exhibited the effective proportionality coefficient of  $5x10^{-6}$  Oe<sup>-2</sup> and a mechanical resonance at 26kHz. The resolution of the device is  $20pT/\sqrt{Hz}$ .

In most fibre optic magnetostrictive sensors, the change in optical path length introduced as a result of the magnetic field induced strain is measured using interferometric techniques. The external magnetostrictive strain, however, also causes a change in the state of polarisation of light in the fibre which can be detected using a polarimeter and used as a basis for a sensing scheme as shown in Figure 5-4. Using an annealed metallic glass tube wrapped with 20m of high-birefringence fibre, resolution of 2.6nT/ $\sqrt{\text{Hz}}$  has been achieved<sup>8</sup>.

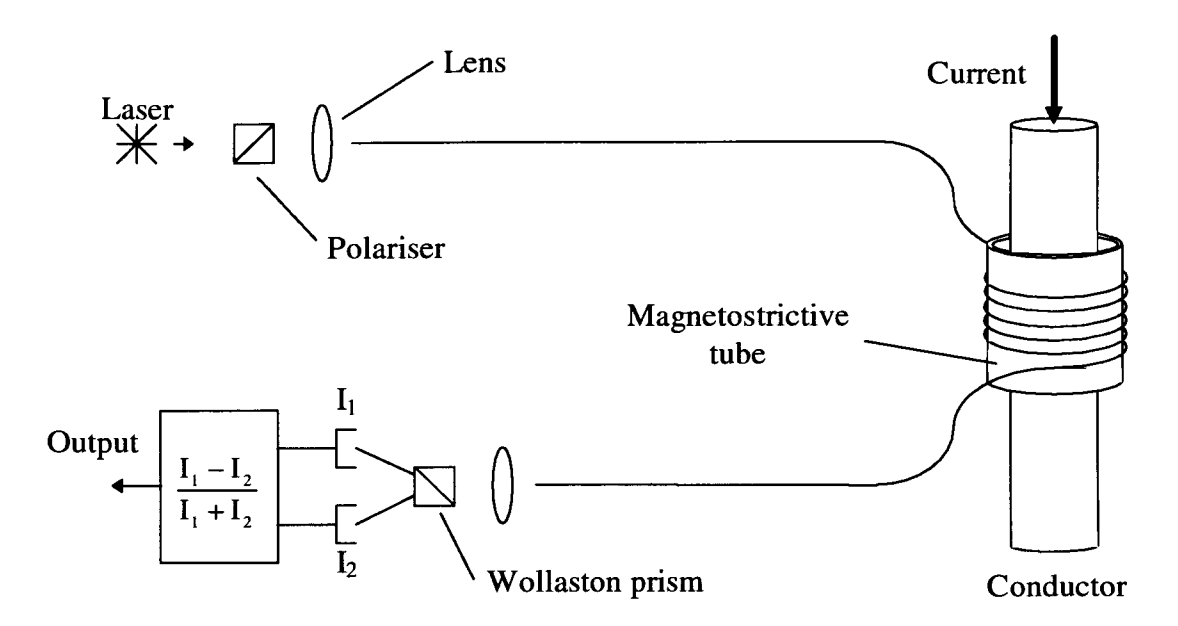


Figure 5-4 Magnetostrictive current sensor in a polarimetric detection scheme

The magnetostrictive devices can provide very sensitive current measurement yet unfortunately remain susceptible to external error sources, such as vibration and temperature, and internal mechanical resonance effects.

## 5.2.3. Faraday Effect Based OCTs

The Faraday magneto-optic effect was described in detail in Section 3.5.8. The effect can be summarised in one sentence; the linearly polarised light passing through a transparent medium in the presence of an applied magnetic field, undergoes a rotation

of the plane of polarisation  $\theta$  proportional to the line integral of the magnetic field, performed over the optical path length L:

$$\theta = \mu V \int_{0}^{L} \mathbf{H} d\mathbf{L} \tag{5-1}$$

where V is the Verdet constant of the material, H the magnetic field and dL the path element. If the magnetic field is uniform over the length then

$$\theta = VBL \tag{5-2}$$

From Ampere's law, the current I is given by the integral of the field around a closed path enclosing the current carrying conductor:

$$I = \oint \mathbf{H} d\mathbf{L} \tag{5-3}$$

The similarity with Equation (5-1) is clear; the current can be simply determined by measurement of the rotation  $\theta$  in the optical path enclosing the conductor. If the linearly polarised light is constrained to travel in a closed optical path N times around the conductor, then

$$\theta = \mu VNI \tag{5-4}$$

The rotation  $\theta$  in this case is independent of the position of the conductor within the closed path; for currents that pass outside the closed path, the integral is zero.

Current and magnetic field sensors can be realised based on the detection of the Faraday rotation  $\theta$ , which is most commonly done by polarimetric techniques (it will be shown that other detection schemes described earlier in Chapter 4 can also be used). The measurement is made by examining the linearly polarised light emerging

from the sensor by a means of a second polariser (termed an analyser). The magnitude of the linearly polarised electric field component of the light wave in any arbitrary direction can be extracted by properly orienting the analyser.

Figure 5-5 shows a typical arrangement of optical components and polarisation components in a Faraday effect based sensor in the basic polarimetric detection configuration. The light delivered from the light source to the sensor via the addressing fibre is polarised by the first polariser. The sensor rotates the plane of the linearly polarised light by an angle  $\theta$  in proportion to the applied magnetic field, and the second polariser (analyser), orientated at an angle  $\alpha$  with respect to the first polariser, converts the rotation  $\theta$  into the intensity modulated light. The modulated light is passed to the photodetector via the output fibre where it is converted into the electrical signal proportional to the measured current.

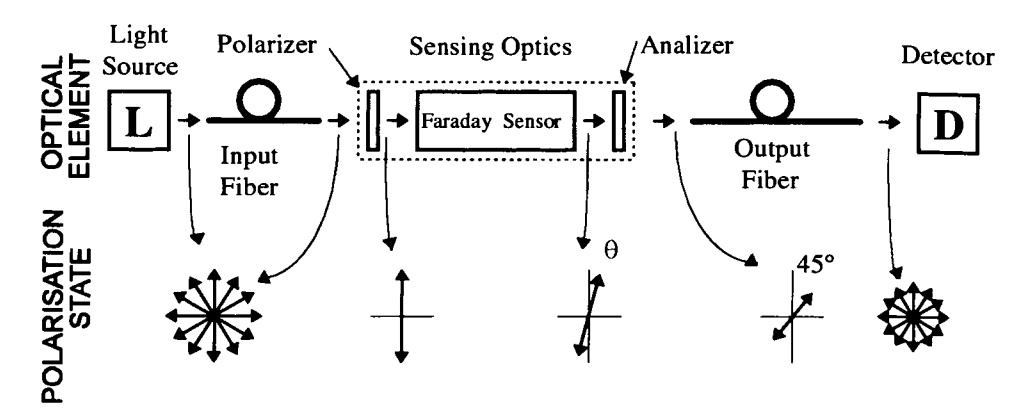


Figure 5-5 Typical arrangement of optical components and polarisation components in the Faraday sensor

In order to quantify the above principles the electrical vector of the input polarised light  $E_0$  is considered, of which only the component parallel to the analyser orientation can be further transmitted. The transmitted component E is given by

$$E = E_0 \cos(\alpha + \theta) \tag{5-5}$$

Consequently, knowing that the optical power is proportional to the square of the E field, and assuming there is no insertion loss, the light power P at the photodetector is given in terms of the input power  $P_0$  by

$$P = P_0 (\cos(\alpha + \theta))^2 = \frac{1}{2} P_0 (1 + \cos 2(\alpha + \theta))$$
 (5-6)

Typically, the polariser and analyser are arranged at an angle  $\alpha$  of 45°, and assuming that there is no linear birefringence, the above equation takes the following form:

$$P = \frac{1}{2} P_0 (1 - \sin(2\theta))$$
 (5-7)

With no applied magnetic field, the optical power input to the photodetector is only half the input power. If the rotation angle  $\theta$  is small, the change in the photodetector output is practically a linear function of the field.

The Faraday effect based current sensors form the largest and the most important group of the optical current transducers. Within this group a vast diversity of optical and processing techniques can be employed to effectively measure the magnetic field and hence the electric current. The following sections review the most successful current sensing approaches based on the magneto-optic Faraday effect.

### 5.2.3.1. Wound Optical Fibre OCT

The wound optical fibre OCT can be regarded as a 'classical' intrinsic fibre optic sensor. The optical fibre itself acts as a current sensing element utilising the magneto-optic Faraday effect. The use of optical fibre as a transducer enables the measurement of a true current to be performed by a means of constraining the optical path around the conductor. The sensitivity of the sensing coil can be easily adjusted by varying the number of turns around the conductor, or by adding dopants to the fibre core to change its Verdet constant.

An early approach of the enclosed path current sensor using monomode fibre as the sensing element was demonstrated as the most straightforward configuration of this type of device<sup>9</sup> (Figure 5-6). Linearly polarised light is launched into the optical fibre which has been wrapped around the current carrying busbar several times. The Faraday rotation is determined using the dual quadrature polarimetric detection scheme by means of an output beam-splitter and two photodetectors; the rotation of the polarisation azimuth causes the output of one detector to rise and the other to fall, which is then converted into a measurement signal using simple processing electronics.

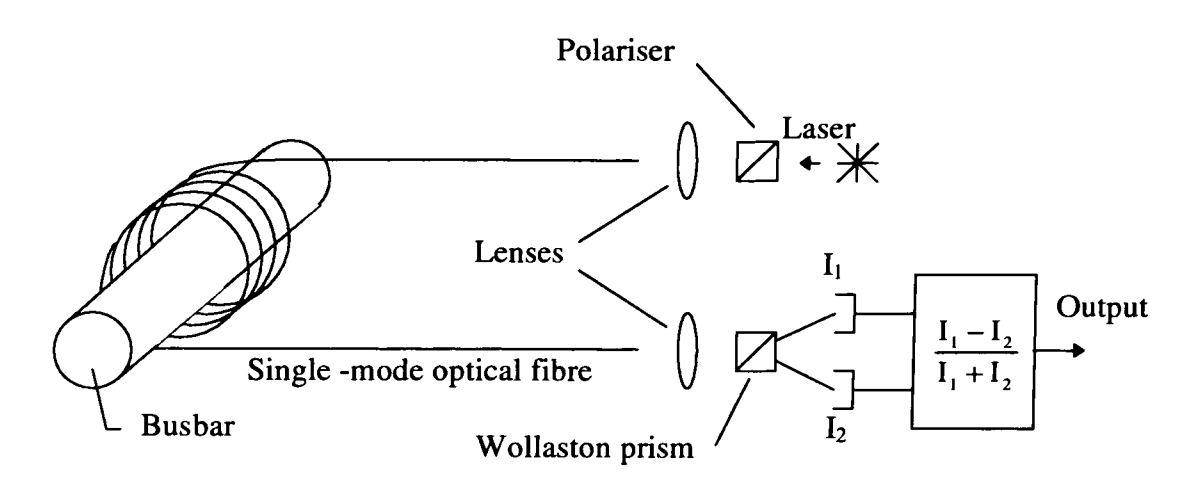


Figure 5-6 OCT using single-mode optical fibre

The condition exists for wound optical fibre OCTs, under which the state of polarisation of linearly polarised light propagating along the optical path is often not preserved due to the presence of intrinsic birefringence induced by core ellipticity and asymmetric stress or the extrinsic birefringence introduced in deploying the fibre sensing element, and hence the sensitivity of this type of device is less than that would be predicted from Equation (5-4). Furthermore, since the birefringence is temperature dependent, the device sensitivity is also subject to environmental temperature perturbations. In order to improve the performance of this type of sensor, it is important to reduce the effects of all extraneous sources of birefringence in designing optical fibre current sensors. On the basis of the results of a number of sensing

schemes which have been reported, some of the possible solutions for dealing with the problem of birefringence may be summarised under the following headings.

### OCT Based on the Optical Fibre with a High Degree of Circular Birefringence

If a large amount of circular birefringence is introduced into the fibre, the bend induced linear birefringence can be suppressed. The Faraday rotation, which is a magnetically induced circular birefringence effect, is superimposed onto this fibre intrinsic circular birefringence, and hence the measuring sensitivity may be retained. A special type of fibre with a large degree of circular birefringence can be obtained by twisting the fibre 10, or by using a spun elliptically birefringent fibre 11.

The main problem of sensors constructed from this type of fibre is that they are temperature dependent, which is largely due to the fact that the circular birefringence is subject to such a temperature variation. However, by employing an active temperature compensation scheme<sup>11</sup>, it has been demonstrated that over 20-70°C temperature range, a fibre current sensor made from spun elliptically birefringent fibre exhibits a 0.05%/°C change in its sensitivity.

### **OCT Employing an Annealed Fibre Coil**

The bend induced linear birefringence can be removed by means of annealing the fibre coil<sup>12</sup>. In this approach, a fibre coil is heated to 800-900°C for about 24 hours and then cooled slowly. Using this technique, an all-fibre current sensor of a few centimetres diameter and more than 100 turns of fibre has been demonstrated<sup>12</sup>. A disadvantage of this approach is that high-temperature annealing removes fibre protective coating and tends to weaken the fibre, hence the annealed coil must be packaged without inducing additional linear birefringence. By embedding an annealed fibre coil in a high viscosity lubricant containing Teflon, a temperature coefficient of its current sensitivity of about  $1.7 \times 10^{-2} \%$  over a temperature range from -10 to 120°C was reported<sup>13</sup>.

## **Novel Topology Wound Optical Fibre OCT**

In this approach, the bend-induced linear birefringence is employed as a phase retarder<sup>14</sup>. By carefully designing the layout architecture of the sensing element, the bend-induced linear birefringence can be "tied together" at the four corners of the square shaped sensing element with no bend-induced linear birefringence present in the four sensing arms, as shown in Figure 5-7.

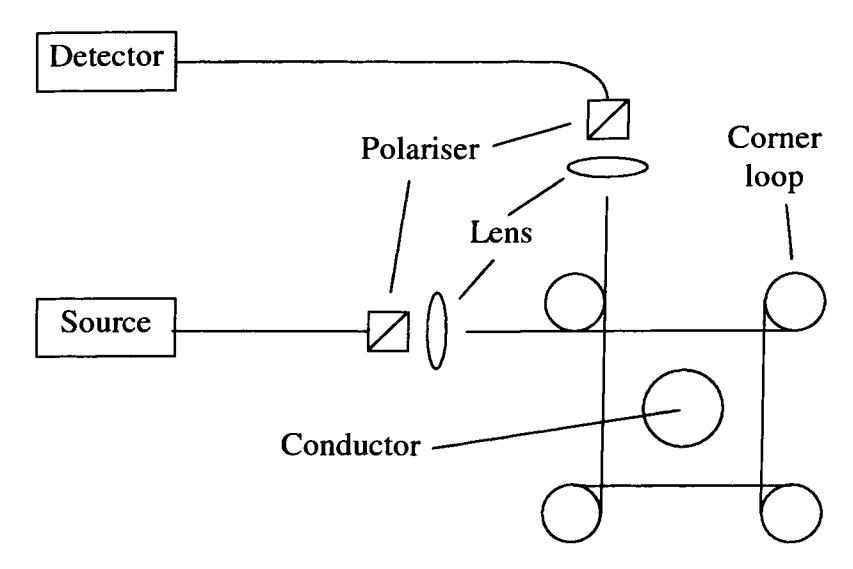


Figure 5-7 The layout architecture of the OCT sensing head

At each corner of this sensor, there are three fibre loops with a 10mm bending radius yielding  $2\pi$  retardation between the two orthogonal components of the linearly polarised light. Since the four sensing arms of the sensing element consist of straight fibre, forming closed loops around the current conductor, the output signal gives only the Faraday rotation defined by Equation 5-4. The main disadvantage of the sensor is that its sensitivity is subject to temperature variations due to the presence of a large degree of bend-induced linear birefringence introduced by the fibre loops.

## Wound Optical Fibre OCT Using a Polarimeter

If the temperature variation occurs over a small range, typically 5-10°C, it is possible to distinguish the current induced variation in the state of polarisation (SOP) of the output light from the influence of temperature by analysing the complete SOP<sup>15</sup>, i.e., by measuring its azimuth and ellipticity simultaneously, and then evaluating the instant

current and temperature by using look-up table. In this detection scheme a polarimeter must be used to determine the azimuth angle and the ellipticity of the output signal. Since the magnetically induced azimuth variation is superposed on the temperature induced variation caused by the twist-induced circular birefringence, it is not possible to separate these two variations by using a polarimeter. In order to eliminate the temperature perturbation on the twist-induced circular birefringence, a back-reflection configuration was used<sup>15</sup>, as shown in Figure 5-8. By using this system to analyse the complete polarisation state, a resolution in azimuth and ellipticity of 0.1° was obtained.

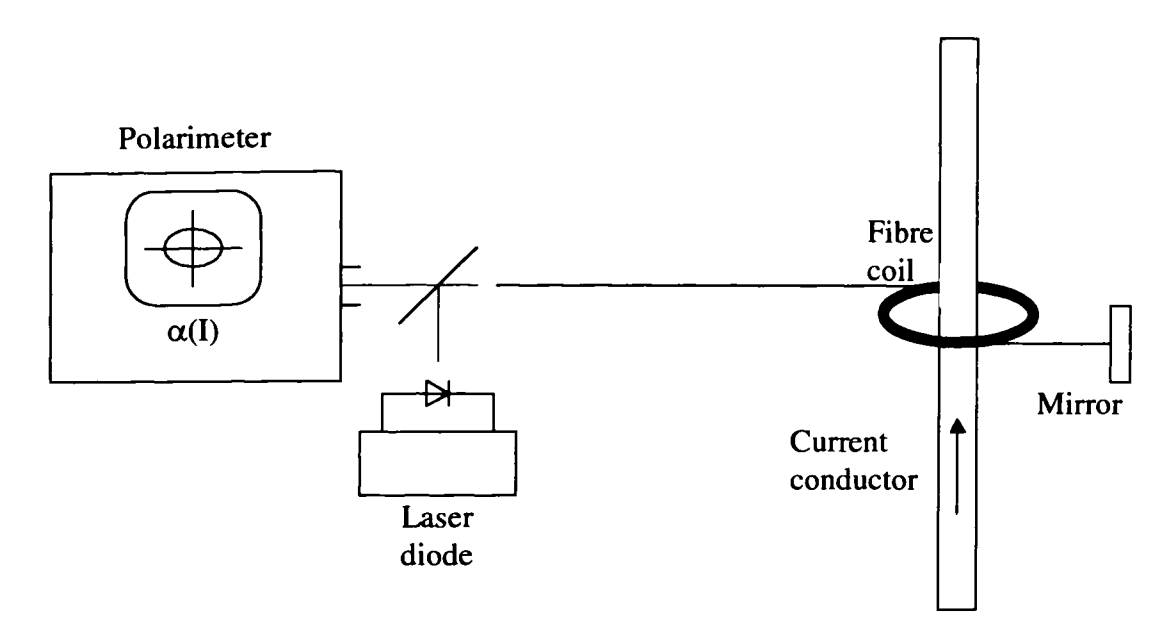


Figure 5-8 Wound optical fibre OCT using a polarimeter

### **OCT Using Highly Birefringent Fibre and a Periodic Conductor Structure**

If a Hi-Bi fibre is subject to a spatially periodic perturbation which has a period of the fibre beat length, linearly polarised light inside one of the two orthogonally polarised eigenmodes of the Hi-Bi fibre can be coupled into another mode by the effect of the Faraday rotation. By configuring an elliptically cored Hi-Bi fibre into a periodic conductor array, a new type of optical fibre current sensor has been demonstrated<sup>16</sup>. In the experimental system, shown in Figure 5-9, linearly polarised light was launched into one of the two orthogonally polarised eigenmodes with an extinction ratio of 30dB. The change in coupling to another mode due to the Faraday effect was

detected using a Glan-Thomson analyser. The detected change was proportional to the applied current. Since the coupling is strongly dependent on the periodic nature of the fibre through the applied field which is defined by the conductor array, external effects such as vibration which are not matched to the period have little effect.

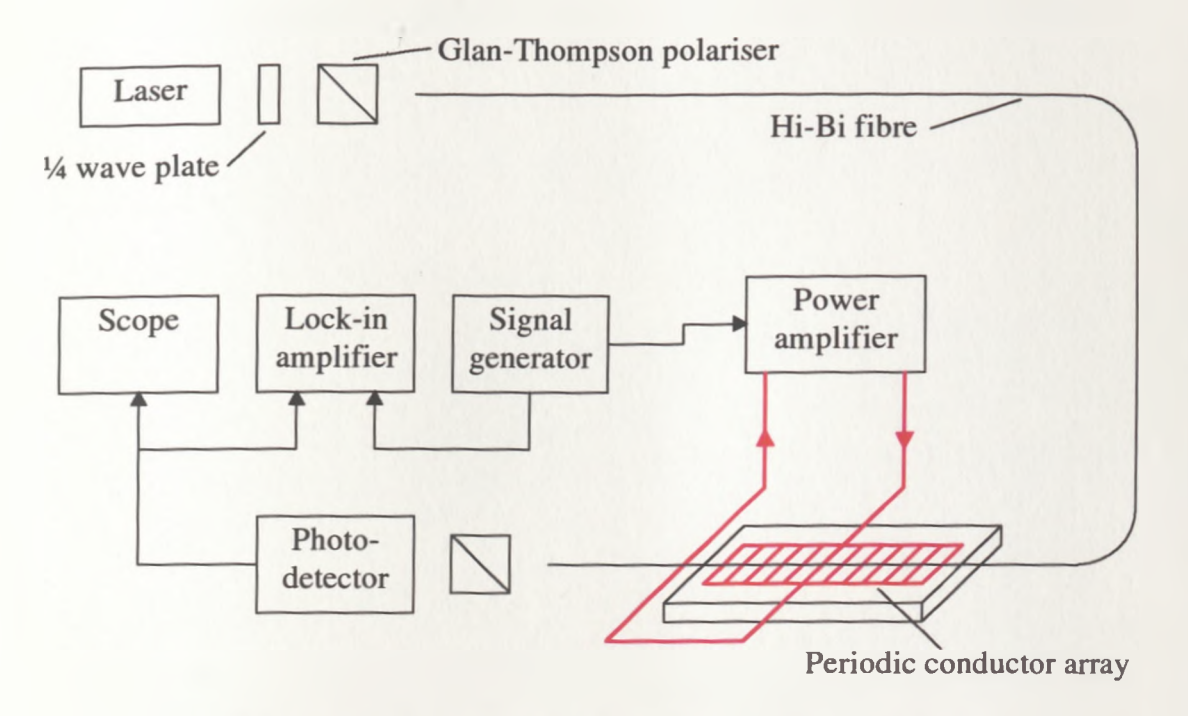


Figure 5-9 Periodic conductor structure for fibre type OCT

Although the reduction in sensitivity to external noise sources, primarily vibration, is an advantage of the proposed scheme, the form of the device is less than practical for use in the electric power industry.

## **Wound Optical Fibre OCT Using Interferometric Detection Schemes**

The Faraday effect can also be represented in terms of the two circularly polarised (left-rotatory and right-rotatory) light beams propagating along the optical fibre (as it was shown in Chapter 3). The phase difference between the two modes caused by the Faraday rotation can be detected using interferometric detection schemes. Numerous optical fibre interferometric current sensors have been investigated and reported over the past years <sup>17,18</sup>. In principle any interferometric configuration may be utilised, but in practice environmental effects restrict the use of most of these, since the fibre interferometer shows considerable phase sensitivity to most physical stimuli, e.g.

temperature and vibration. Only the Sagnac interferometer seems to have any fundamental advantages. The Sagnac interferometer permits the measurement of nonreciprocal effects independently of the influence of any reciprocal perturbations; the two arms of the interferometer counter-propagate light beams in the same fibre loop, so that most stimuli affect each beam equally resulting in a zero net phase difference at the output. The Faraday effect is non-reciprocal, in that the two beams see the impressed field from opposite directions. Hence, the Sagnac interferometer exhibits an inherent environmental insensitivity whilst the Faraday effect is doubled.

One problem of using an all fibre Sagnac interferometer is that it is difficult to propagate a completely circular polarisation state in the ring due to the birefringence properties of the coupler and the fibre; in practice the guided state is generally elliptical. Maximum sensitivity can be achieved for a circular input state, and zero sensitivity for a linear input state.

Figure 5-10 shows the experimental arrangement used to demonstrate the operation of the above OCT<sup>18,19</sup>. The low birefringence monomode fibre was wound in a coil of 45 turns and 30cm diameter. The magneto-optically induced phase shift was recovered using a heterodyne detection system by employing a sinusoidally driven cylindrical piezoelectric phase modulator.

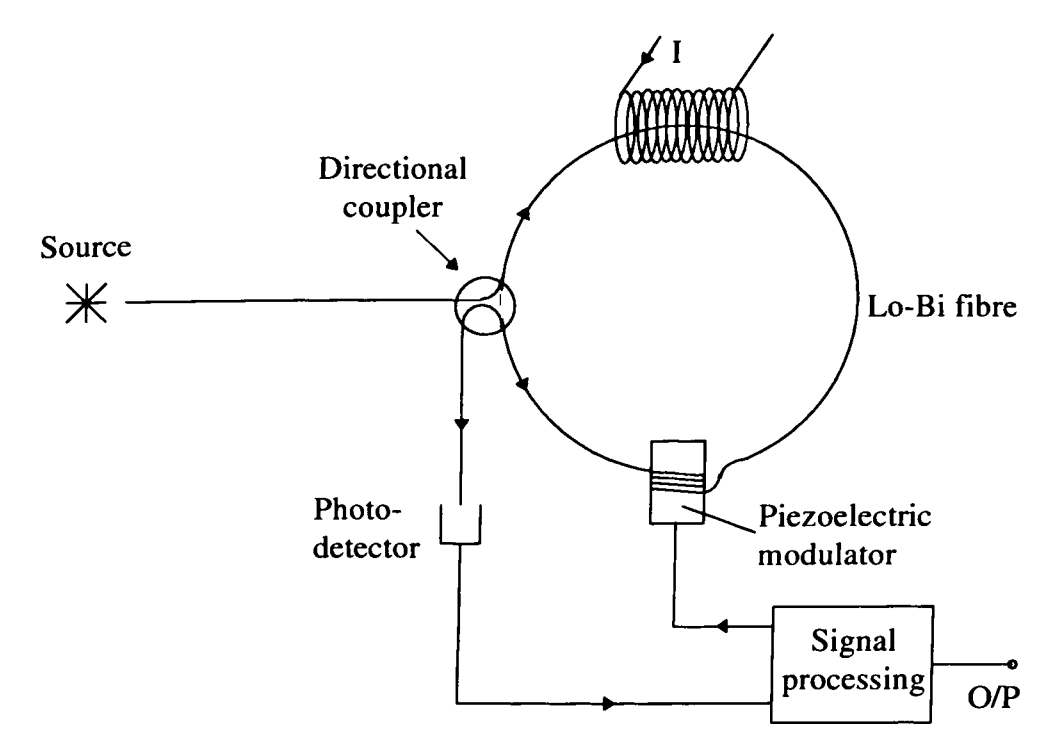


Figure 5-10 Experimental arrangement of a Sagnac interferometer based OCT

#### Wound Optical Fibre OCT Using an Orthoconjugate Reflector (OCR)

For almost all types of optical sensors, optical fibre leads are required to connect the sensing element to the light source and the detection unit within the measurement apparatus. In any practical optical fibre current measurement system, the environmental perturbations such as temperature fluctuations and mechanical vibration on the fibre leads will reduce the signal-to-noise ratio (S/N) of the output and affect the performance of the sensing system. In order to overcome such problems, a novel passive birefringence compensation scheme was introduced, that uses an orthoconjugate reflector (OCR)<sup>20</sup> or a mirrored Faraday rotator (MFR)<sup>21</sup>. This system (see Figure 5-11) consists of a laser diode as a light source, a fibre current sensing coil made of a highly twisted low-birefringence optical fibre (40 turns/m, 0.17 rad/m of linear retardance) and an OCR containing a Faraday rotator, which rotates the azimuth of the light by 45°, and a reflection mirror.

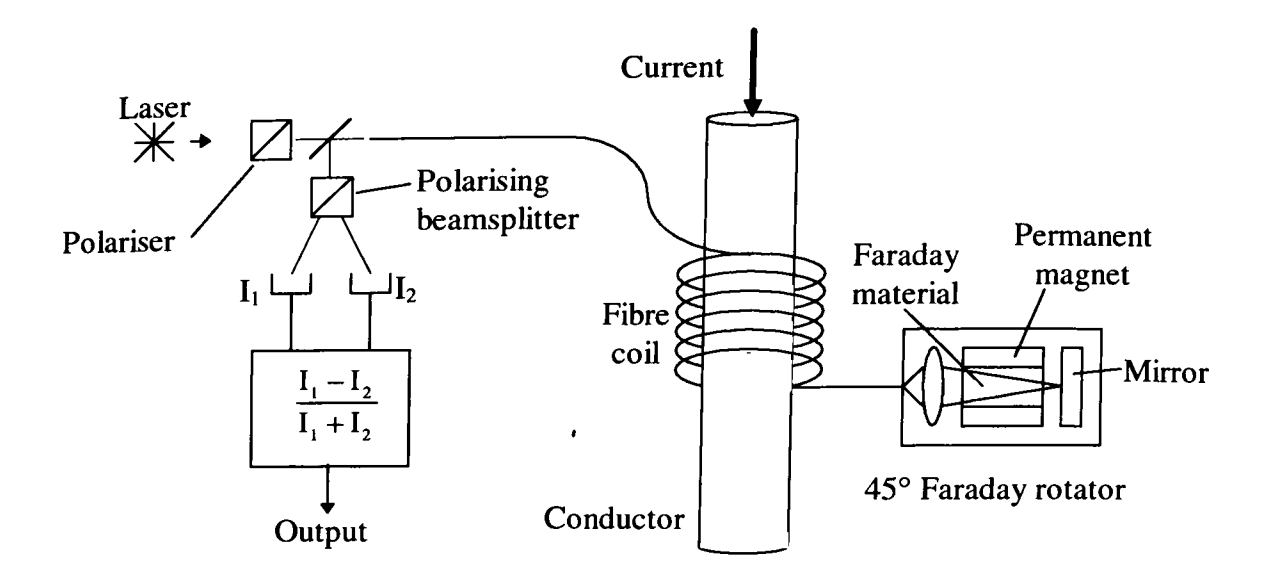


Figure 5-11 OCT employing an orthoconjugate reflector

Since the OCR is able to turn the orthogonal polarisation state back along the fibre such that all reciprocal linear and circular birefringence in the fibre can be undone with the returned SOP being linear and orientated at 90° to the launch state, the effect of any reciprocal birefringence in the fibre leads may be suppressed provided that the ratio of the circular to linear birefringence is maintained at a high level everywhere along the fibre. By using this arrangement, the rejection of the vibration noise was of an order of 30dB.

### 5.2.3.2. Bulk Optic OCT

Many disadvantages of the inherent linear birefringence and fragility of the wound optical fibre types OCTs can be eliminated altogether by using a doped flint glass material which is left in solid form (as opposed to being drawn as fibre) and either a single piece or several separate pieces are assembled to form a glass ring structure surrounding the busbar as shown in Figure 5-12.

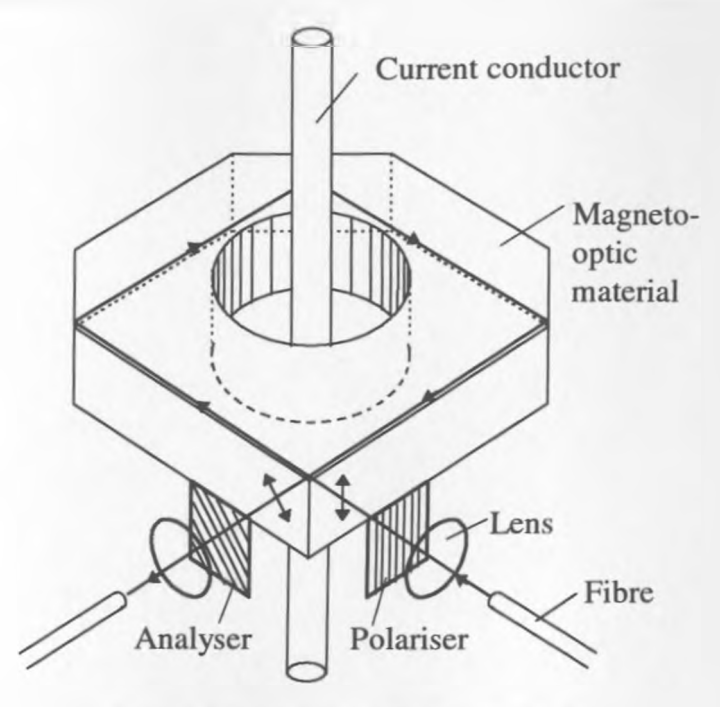


Figure 5-12 Bulk optic current sensor

The major problem of this type of sensor is related to the fact that reflections are necessary to guide the light beam around the conductor. In general, linearly polarised light will become elliptically polarised after reflection. This change affects the sensitivity of the device in a similar way to the birefringence in an optical fibre sensing element.

One solution to overcome this problem is to produce two reflections at each corner of the bulk structure which have a complementary effect on the SOP of the transmitted light<sup>22</sup>. Another method is to design a sensor body in which the light is reflected at angles very close to the critical angle<sup>23,24</sup>, in such conditions the SOP of the reflected light is maintained. The two solutions are shown in Figure 5-13.

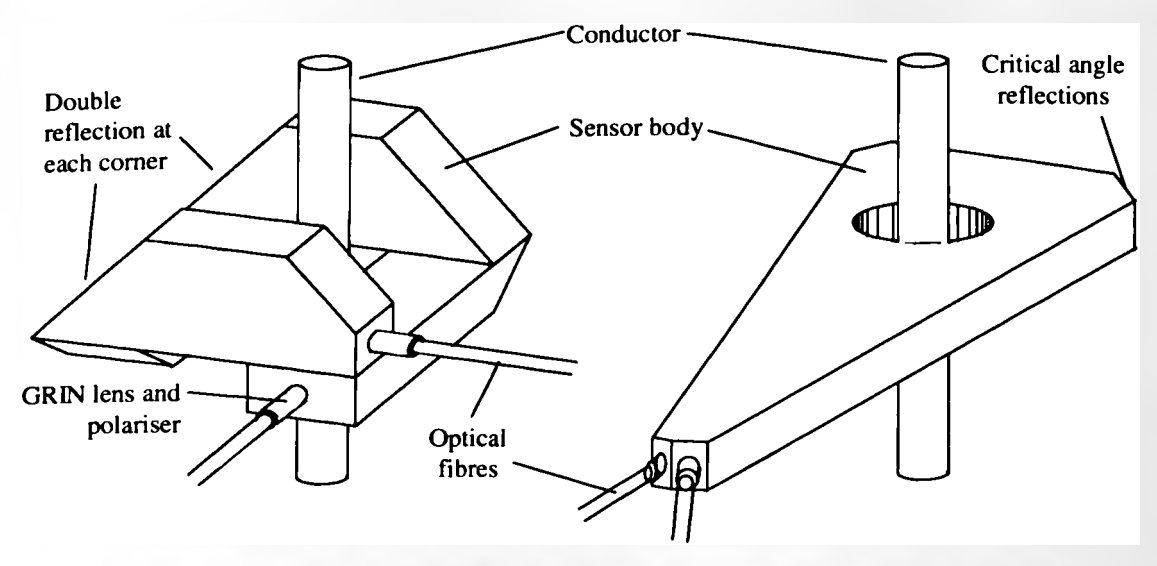


Figure 5-13 Bulk optic OCTs without the detrimental reflections problem

In general bulk optic devices are difficult to manufacture and require many complicated cutting, polishing and assembly tasks. The manufactured device is both relatively heavy and requires a robust housing to support, protect and mount the assembly on the conductor. Nonetheless, the market for these devices currently stands for several hundred per year.

## 5.2.3.3. Faraday Cell OCT

This type of OCT, often called 'point sensor', is based upon magnetic field sensing in near proximity to the current carrying conductor rather then measuring the contour integral of the magnetic field. Provided that the field distribution is constant the reading can be calibrated in terms of the current. Figure 5-14 (similar to Figure 5-5) shows a basic arrangement for a simple linear-design sensor consisting of a rectangular (or cylindrical) sensor body with a polariser and analyser at opposite sides 25,26,27. The advantages of such sensors are derived from the simple, low cost structure, the use of only a small piece of magneto-optic material and hence the possibility of using more expensive exotic materials with higher Verdet constants; due to the nature of the design one sensor can be used for different sizes of conducting busbars. Precautions are necessary to avoid any disturbance (cross-talk) from magnetic fields other than that to be determined, mainly from the two other phase currents. The issue of cross-talk will be investigated in more detail in Chapter 6.

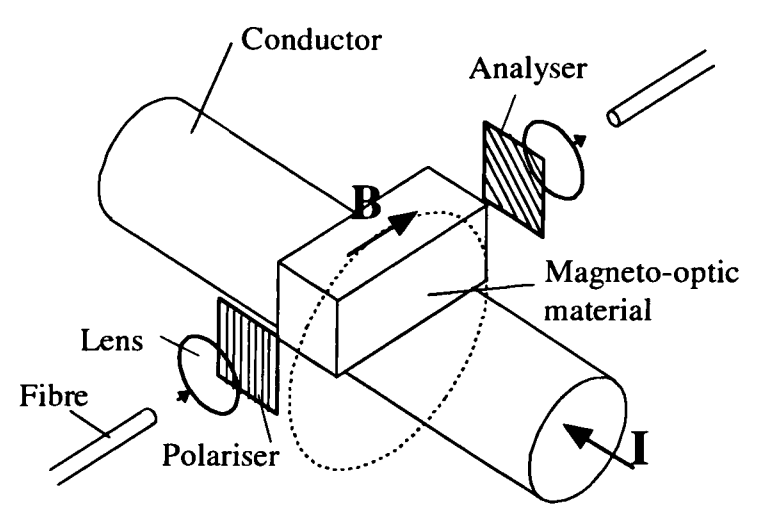


Figure 5-14 Faraday cell OCT

The Faraday cell OCT can be manufactured as a multi-pass device in order to increase the effective sensing path length<sup>9,28</sup> and hence increase the sensor sensitivity. This can be done by a means of multiple light reflections from the two reflective films evaporated on both sides of the Faraday cell as shown in Figure 5-15.

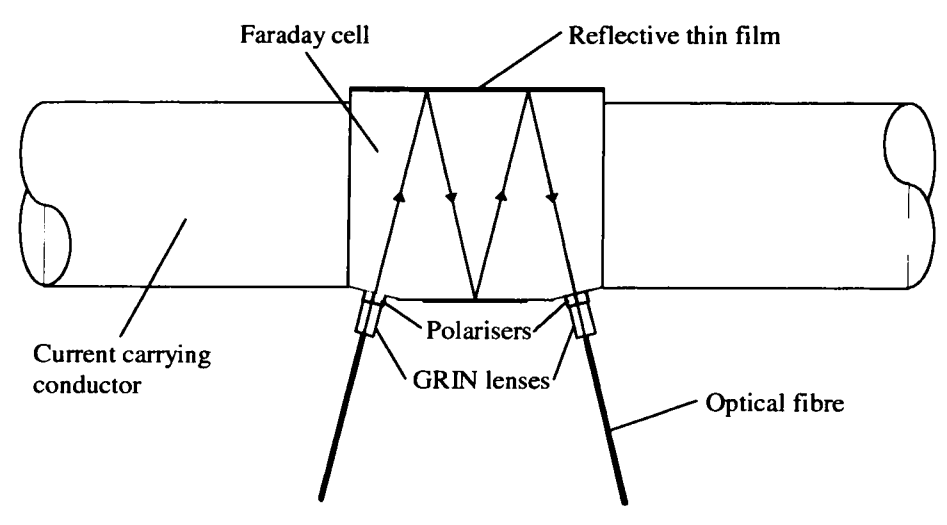


Figure 5-15 Multi-pass Faraday cell OCT

A variety of magneto-optic materials can be used as sensing elements of Faraday cell OCTs. The available optical materials which can produce a Faraday rotation angle large enough to provide sufficient sensitivity to current-induced magnetic filed may be classified into two groups: doped glasses and magneto-optic crystals.

The first group includes<sup>30</sup>: optical glasses; diamagnetic doped glasses containing high concentrations of ions which give rise to large Verdet constants; and rare-earth glasses, i.e., paramagnetic ion-doped glasses which have the largest Verdet constants. The most commonly used materials are Schott Glass SF6 with the Verdet constant of 1489.7deg/Tm at a wavelength of 633nm, dysprosium alumna silicate glass (-3666.9deg/Tm at 633nm), and Hoya FR-5 glass (-4182.6deg/Tm at 633nm).

The second group comprises the rare-earth iron garnets<sup>31</sup> such as yttrium iron garnet, Y<sub>3</sub>Fe<sub>5</sub>O<sub>12</sub> (YIG), which is a widely available commercial crystal, showing transparency in the near-infrared region. The Verdet constant of a YIG material is two to three orders of magnitude larger than that for typical diamagnetic glasses. By substituting some elements (Bismuth or Gadolinum) into a YIG crystal, the Verdet constant and the temperature coefficient of this material can be greatly improved.

In general, iron garnets produce hysteresis which can affect the sensor response and introduce errors. To overcome this problem iron garnets for various applications can be deposited in a form of epitaxial thin films (a few micrometers in thickness) or thick films (up to a few hundred micrometers in thickness)<sup>32,33,34</sup>, made as 1-3mm long optical waveguides. A magnetic field applied in a plane of such films rotates the magnetisation of domains without the effect of domains wall motion which is the cause of hysteresis in bulk structures. The magnetisation rotation also allows for a faster response of iron garnet films as opposed to bulk structures. The research in this area is however still in the experimental stage.

Other important rare-earth garnets include terbium aluminium garnet (TAG), most efficient<sup>35</sup> of all rare-earth aluminium garnets and terbium gallium garnet (TGG) in which Ga is substituted for Al (Tb<sub>3</sub>Ga<sub>5</sub>O<sub>12</sub>). The TGG has a slightly lower Verdet constant than TAG, however, the crystal growth technology allows for the production of larger, more perfect pieces of TGG with reduced manufacture costs. The TGG has twice the Verdet constant (-7448deg/Tm at 633nm) and lower optical losses than that

of a terbium-doped glass which make it well suited for magnetic field sensing applications.

In the author's opinion the Faraday cell OCTs are most promising future commercial devices in power industry applications in terms of potential performance, ease of manufacture and installation. The problem of environmental effects of vibration, temperature and magnetic cross-talk which could introduce measurement errors in these devices and the proposed compensation schemes form the basis of this thesis and will be dealt with in more detail in Chapters 6 and 7.

#### 5.2.3.4. Flux Concentrator OCT

To further increase the sensor sensitivity and achieve the magnetic field contour measurement and the real current sensing capability, the Faraday cell sensor may be placed in the air gap of a flux concentrator<sup>29</sup> as shown in Figure 5-16.

For power frequency measurement this device could be effective and it could be manufactured fairly readily. However, its construction and use of a conventional ferromagnetic core negates many of the benefits of an OCT such as dc and HF measurement, small size and ease of installation, to be widely accepted commercially.

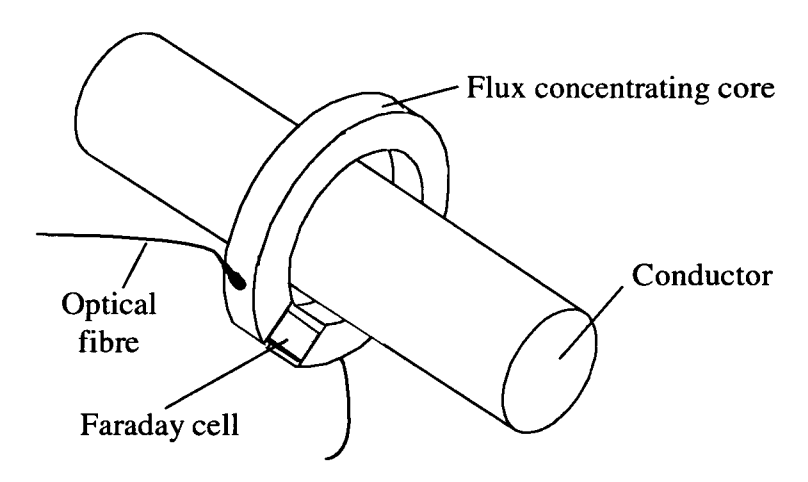


Figure 5-16 Flux concentrator OCT

# 5.3. The Design of the Author's Preferred OCT Type

The previous section reviewed diverse approaches to the construction of an optical current transducer. The conclusion may be drawn that despite the research efforts undertaken during the last several years, commercialisation of the optical current transducer is still not accomplished. Major issues of the influence of environmental effects on the OCT operation are still generally unresolved and there is no compliance of most of the reported current transducers with the function and accuracy requirements relevant to the electricity industry. The lack of confidence in the reliability, repeatability and robustness of the optical counterpart of the current transformer restrict a wide commercial acceptance of this kind of device.

In order to gain widespread acceptance of optical current sensing technology, the OCT should not only be competitive to the CT in terms of its performance and functionality but also in terms of its simplicity and low cost. For this reasons the OCT design should be based on relatively simple and widely used optical and signal processing techniques. The present research work indicates that the Faraday Cell OCT with a polarimetric detection scheme is the arguably best candidate that complies with these design criteria. The use of commercially available and relatively inexpensive optical components and processing electronics based on the Digital Signal Processing (DSP) techniques provides an optimal solution for the OCT construction.

This section will discuss the OCT operation requirements, i.e., its basic function and performance specifications, and will provide a detailed description of the sensor head construction. The optoelectronic components associated with the current measurement system and the issue of digital signal processing will be treated separately in Chapters 7 and 8.

### 5.3.1. OCT Basic Function and Accuracy Requirements

The OCT basic functions are precisely defined in the draft IEC Standard<sup>36</sup> concerning Electronic Current Transducers. In this document, an Electronic Instrument

Transducer is defined as an arrangement consisting of one or more current or voltage sensor(s) which may be connected to a transmitting system and a secondary converter, all intended to transmit a measuring quantity in a proportional quantity to supply measuring instruments, meters and protective or control devices.

An Electronic Current Transducer (the OCT belongs to this category) is defined as an electronic instrument transducer in which the output of the secondary converter in normal conditions of use is substantially proportional to the primary current and differs in phase from it by an angle which is approximately zero for an appropriate direction of the connections.

The electricity supply industry requires from a current transducer high performance specifications for both metering and protection applications. Tables 5-1 and 5-2 illustrate the standard accuracy specifications for metering and protection applications for different levels of the measured current in relation to the rated current<sup>37</sup>. The OCT as a competitive device to the conventional current transformer must comply with appropriate accuracy classes.

Measurement errors within the OCT can be attributed mainly to thermal influences, vibration induced noise, detection of low level optical signals and nonlinearity of the sensor response characteristic at higher current levels. If all the above issues are carefully considered and addressed (more details in Chapters 6, 7 and 8) the OCT can potentially be used as a combined current measuring device for metering and protection applications. The efforts undertaken during the project work programme have attempted to design a current sensor suitable for both these tasks.

Accuracy class	±Percentage c	urrent error at pe	rcentage of rated low	current shown
	5	20	100	120
0.1	0.4	0.2	0.1	0.1
0.2	0.75	0.35	0.2	0.2
0.5	1.5	0.75	0.5	0.5
1.0	3.0	1.5	1.0	1.0

Table 5-1 OCT accuracy specifications for metering applications in relation to the rated current

Accuracy class	Current error at rated primary current (%)	Current error at rated accuracy limit (5,10,15,20,30)x primary current (%)
5P	±1	±5
10P	±3	±10

Table 5-2 OCT accuracy specification for protection applications in relation to the rated current

It is important from the viewpoint of electrical power metering and the operational speed of protection devices that a phase displacement between the primary current and the secondary measurement signal are as small as possible. Maximum phase displacement specifications for current transformers<sup>37</sup> are presented in Tables 5-3 and 5-4.

			±Phase o	lisplacen	nent at p	ercentag	e of rate	d curren	t
			1	ıs			Min	utes	
% of rate	ed	5%	20%	100%	120%	5%	20%	100%	120%
current							1	4	
	0.1	13.9	7.4	4.6	4.6	15	8	5	5
Accuracy	0.2	27.8	13.9	9.3	9.3	30	15	10	10
Class	0.5	83.3	41.7	27.8	27.8	90	45	30	30
	1.0	166.7	83.3	55.6	55.6	180	90	60	60

Table 5-3 Maximum phase displacement specifications for metering current transducers in relation to the rated current

Accuracy class	±Phase displacement at rated primary current		
	μs	Minutes	
5P	55.6	1.8	
10P	-	Miles -	

Table 5-4 Maximum phase displacement specifications for protection current transducers in relation to the rated current

From the above data, it is clear, that the phase displacement specifications for current transformers are very stringent, and although it might be easy to manufacture a conventional CT which complies with these specifications, it is very difficult to design an OCT of such performance. A substantial amount of real time signal processing involved in the OCT operation and deglitch output filters introduce a constant phase delay between the measured current and the output signal. Additionally, a length of optical fibre addressing the sensor introduces some delay which has to be accounted for in the total phase displacement, however this contribution can be neglected if the length of optical fibre is less than 100 metres. A length of 100 metres would introduce approximately a delay of 1µs.

A total measured phase displacement introduced by the DSP system considered in this work (more details in Chapter 7) accounts for 50µs. This figure includes 20µs of digital signal processing time and 30µs delay introduced by the remaining electronics and deglitch output filters. This amount of displacement is within the specification of a protection current transformer and class 1 metering current transformer.

The issue of accurate power measurement while using a transducer introducing a constant phase displacement can be resolved by equalising the phase displacements corresponding to both voltage and current transducers. This problem is raised in the specification concerning electronic instrument transducers<sup>36</sup>. It is proposed to define standard values for the delay time; the proposed rated delay times are 50, 100 and 200µs. Phase displacements indicated in Table 5-3 and Table 5-4 are under such definition the values remaining after the compensation of the rated phase displacement.

In terms of the operational speed of the commonly used protective instrumentation the above delay times are negligible. In general, protective devices require at least a full period of a 50Hz current to take a decision to trip and the above rated delays are only small fractions of this time.

## 5.3.2. OCT Temperature and Vibration Specifications

The optical current transducer should be suitable for indoor and outdoor temperature conditions. According to the specification for current transformers<sup>37</sup> the ambient air temperature is specified by three temperature categories: -5/40, -25/40 and -40/40. In each of these categories the first number represents minimum ambient air temperature and the second number maximum ambient air temperature in °C. The specification indicates that the solar radiation up to a level of 1000W/m<sup>2</sup> should be considered for outdoor applications which implies that the temperature of OCT in service might rise to a higher level than the ambient air temperature. It is believed that the OCT should operate up to 80°C or more while maintaining the current measurement accuracy stated in Tables 5-1 and 5-2.

The vibration specifications should satisfy preliminary vibration limits for Optical Instrument Transducers as proposed by IEC Technical Committee 38, Working Group 27 and supported by the National Grid Company - acceleration of up to 40g at frequencies from 3Hz to 3kHz<sup>36</sup>. The OCT should maintain its current measurement accuracy while subjected to this level of vibration.

The issues of temperature and vibration effects will be discussed in more detail in Chapters 6, 7 and 8.

## 5.3.3. Construction of the Sensor Head

The sensor head is a "heart" of the current measurement system in the Faraday Cell type OCT. It consists of a sensing magneto-optic element in a form of crystal (or slab of glass), polarisers, collimating lenses and supporting components, all housed in a protective package. The sensor head is terminated with two connectors or two pigtailed fibres used for connecting the head to the optoelectronic interrogation system.

The design of the sensor head depends on many factors and should begin from setting the required current measurement range. This prime factor will influence the choice made when selecting a magneto-optic material, which in turn will influence a decision about a wavelength used within the interrogating system. It should be decided in the beginning whether the sensor response characteristic will be linearised or not. Both options are possible. Linearisation allows for a better use of the response characteristic to be made, which improves a signal-to-noise ratio and current measurement resolution but requires additional processing. If the sensor response characteristic is to remain unchanged, the device dynamic range should be increased in order to comply with the accuracy requirements at higher current levels. This involves the use of less sensitive magneto-optic materials and shorter interaction paths between the magnetic field and the polarised light in the sensor. This problem will be discussed in more detail in Paragraph 5.3.3.2.

## 5.3.3.1. OCT Polarisation and Collimating Components

In order to provide a mechanism for transmitting light through the length of the magneto-optic sensing element, Graded Index (GRIN) lenses<sup>38</sup> are employed. These then provide a well collimated, larger diameter ( $\phi \approx 2$ mm) beam of light which passes through the magneto-optic sensing element. A beam of light of approximately the same diameter as the sample of the magneto-optic material ensures that possible crystal structure problems and inclusions are less critical.

The lenses used for the OCT are 2mm in diameter, 0.25 pitch at the chosen wavelength of 850nm. One end of the lens, at its centre, is glued to the optical fibre, and secured within a metal assembly. To the second end a polarisation component (POLARCOR polariser<sup>38</sup>) is glued, which provides linear polarisation of the collimated light beam. The polarisers used are characterised with a high extinction ratio (1:10000) and small size (2x2mm). Figure 5-17 shows a photograph of the GRIN lens assembly pigtailed with a fibre-optic cable and POLARCOR polarisers.



Figure 5-17 GRIN lens assembly and POLARCOR polarisers

# 5.3.3.2. OCT Response Characteristic

The Faraday Cell type OCT is a polarimetric device in which the plane of polarisation of the linearly polarised light passing through the magneto-optic element is rotated in direct proportion to the applied magnetic field (electrical current). In Paragraph 5.2.3 it was shown that the sensor optical output power vs. the input current is not linear and can be expressed by:

$$P(t) = P_0(\cos(\alpha + \theta))^2.$$
 (5-9)

Here  $P_0$  and P(t) are, respectively, the sensor input and output optical powers. The angular rotation  $\theta(t) = BLV$ , where B is the magnetic field component parallel to the direction of the light propagation, L is the interaction length between the magnetic field and the polarised light, V is the Verdet constant of the magneto-optic material, and  $\alpha$  is the angle between the zero field polarisation state and the analysing polariser. The magnetic flux density B is directly proportional to the current passing through the conductor.

Typically, the polarisers are arranged at an angle  $\alpha$  of 45° to maximise the sensitivity of the OCT response and ensure the operation within the linear region of the sensor response characteristic. Under this condition, with no applied field, the output optical power is half the input power. Equation (5-9) can now be expressed as:

$$P(t) = \frac{1}{2}P_0(1 - \sin(2\theta))$$
 (5-10)

or

$$P_{N}(t) = 1 - \sin(2\theta)$$
 (5-11)

where,  $P_N(t)$  is the normalised output power. If the rotation angle,  $\theta$ , is small, the modulated output is a linear function of the magnetic field (Figure 5-18).

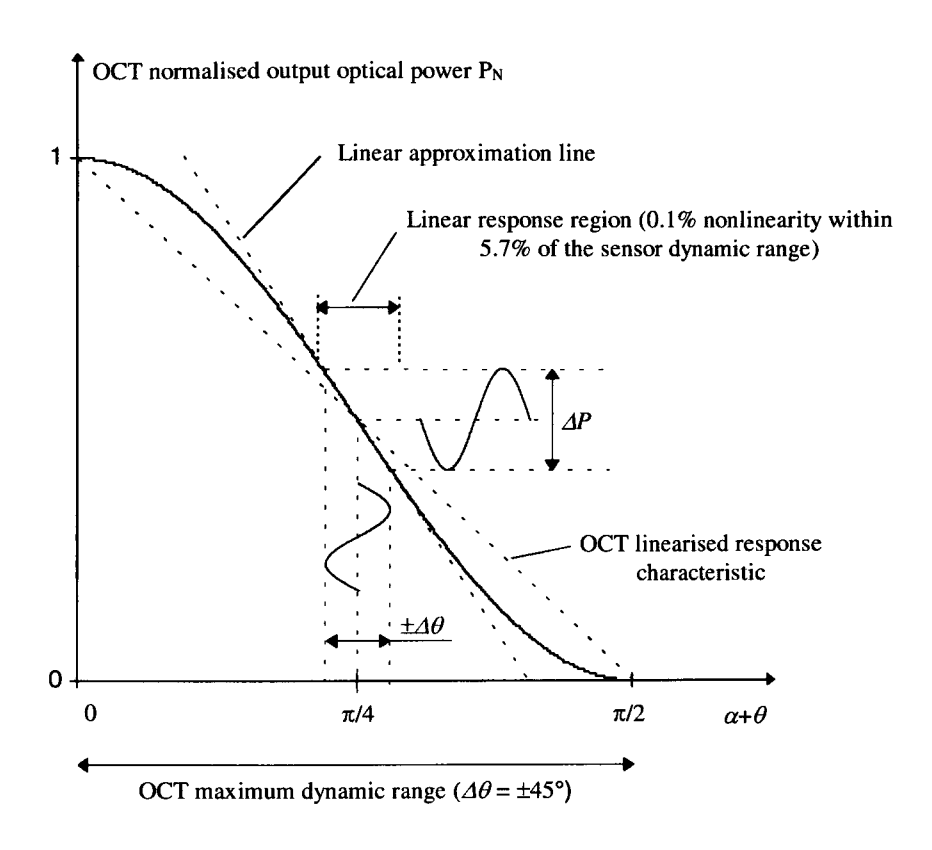


Figure 5-18 Explanation of the OCT linear response region

From Figure 5-18 it is clear that the OCT maximum dynamic range is defined by the two extremes of the angle  $\theta$ . Maximum optical power will be received at the photodetector input when  $\theta = -45^{\circ}$ , and the minimum optical power will be received when  $\theta = +45^{\circ}$ . The minimum received optical power is determined by the extinction ratio of the polarisers used in the particular design of the sensor, and in this discussion is assumed as zero.

Clearly the process of converting the polarisation rotation to intensity is linear only for a small part of the device characteristic. However, with appropriate selection of the sensor dynamic range, a linear approximation can be used to map the output of the OCT to the applied current with a performance accuracy which meets the OCT metering and protection specifications stated in Tables 5-1 and 5-2.

In order to optimise the device performance, the sensor sensitivity should be chosen such, that the error introduced by the linear approximation is of the same value as the error specified for the maximum measured current. This solution provides optimal use of the sensor dynamic range when the OCT characteristic is not linearised with the use of additional signal processing.

Assuming that the rotation  $\theta$  can change at maximum between  $-\frac{\pi}{4}$  and  $\frac{\pi}{4}$  (see Figure 5-18), and that the measured current is in a sinusoidal form,  $\theta$  can be expressed as a sinusoidal function directly proportional to the modulation factor k:

$$\theta(t) = \frac{\pi}{4} k \sin(\omega t) \tag{5-12}$$

where,  $\omega$  is the angular frequency and  $k \in (0, 1)$ .

In Equation (5-11) the second term represents the ac component of the normalised output optical power:

$$P_{ac} = \sin 2\theta(t) \tag{5-13}$$

Its linear approximation function can be expressed as

$$P_{ac\_approx} = 2\theta(t) \tag{5-14}$$

For small values of  $\theta(t)$ , the two expressions are equal.

P<sub>ac</sub> and P<sub>ac\_approx</sub> substituted with Equation (5-12) and expressed as rms quantities can be presented in the following forms respectively:

$$P_{ac}(rms) = \sqrt{\frac{1}{T} \int_{0}^{T} \sin^{2}\left(2 \cdot \frac{\pi}{4} k \sin \omega t\right) dt}$$
 (5-15)

$$P_{ac\_approx}(rms) = \sqrt{\frac{1}{T}} \int_{0}^{T} \left(2 \cdot \frac{\pi}{4} k \sin \omega t\right)^{2} dt$$
 (5-16)

where, T is a period, and the angular frequency  $\omega = \frac{2\pi}{T}$ .

The linear approximation error can be determined as a relative error between the  $P_{ac}(rms)$  and  $P_{ac\_approx}(rms)$ :

$$\sigma(\%) = \frac{P_{ac}(rms) - P_{ac\_approx}(rms)}{P_{cc}(rms)} \cdot 100$$
 (5-17)

Expression (5-17) is calculated using numerical methods for the modulation factor k changing from 0 to 1. Figure 5-19 compares the numerically evaluated OCT linear approximation error  $\sigma(\%)$  with the accuracy specification from Tables 5-1 and 5-2

and displays the optimal use of the OCT dynamic range for metering and protection applications.

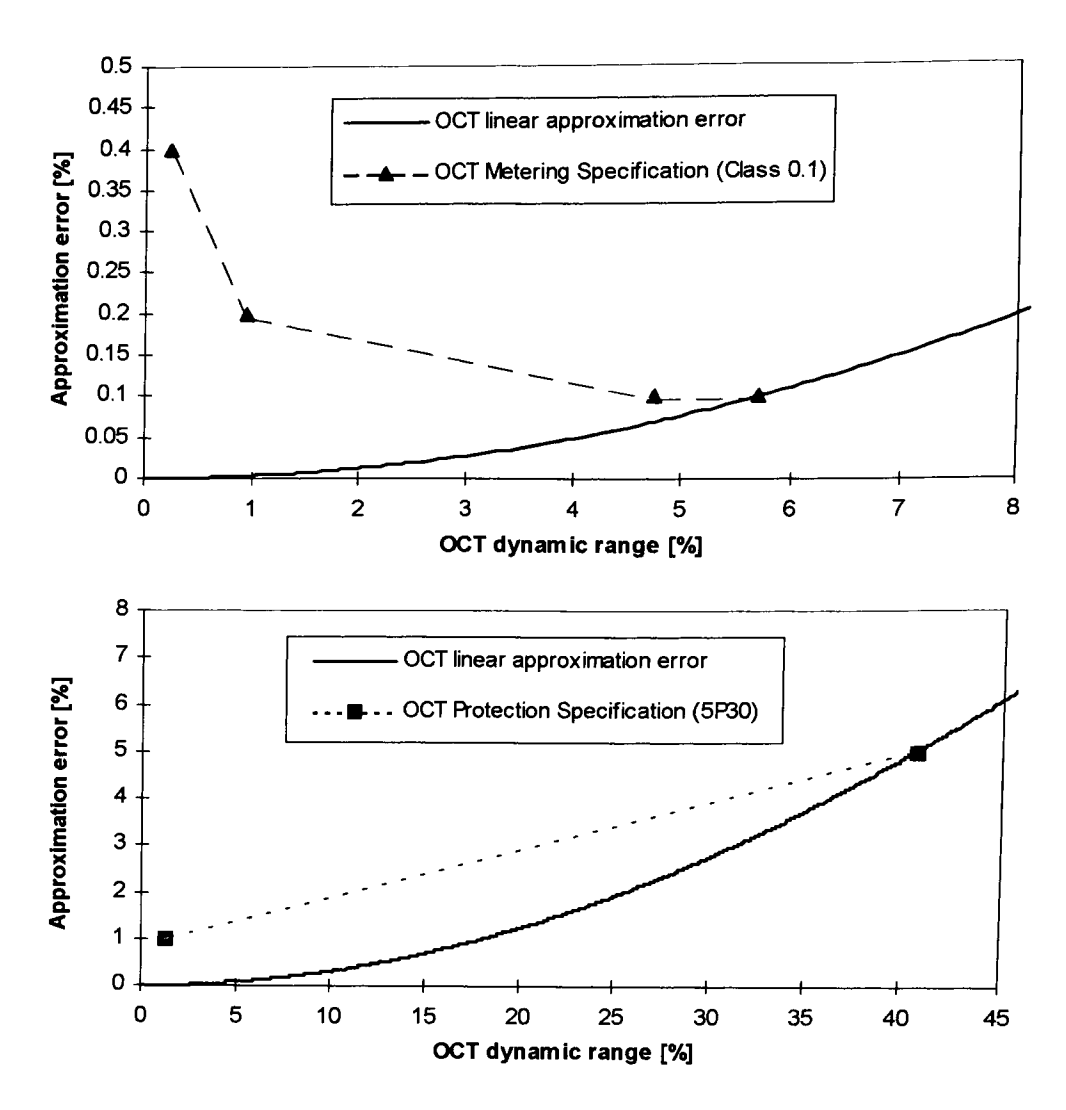


Figure 5-19 Necessary dynamic limitations in order to comply with the accuracy requirements for metering and protection class devices

From Figure 5-19 it is clear, that in order to comply with the accuracy requirements, only 5.7% and 40.8% of the OCT dynamic range can be used for metering and protection applications respectively.

The metering device in particular suffers from poor use of the sensor dynamic range. In this case, the accurate measurement of low current signals is very difficult as the OCT sensitivity is relatively low. Consequently, critical design requirements are

imposed upon the detection part of the optoelectronic system as the electronic noise must be maintained at very low levels. For this reason, it is highly desirable to increase the current sensor sensitivity and use the remaining non-linear part of its response characteristic.

In order to use the whole of the OCT dynamic range, it is necessary to linearise the sensor response characteristic by applying real-time processing of the input signal. This issue will be investigated in more detail in Chapters 7 and 8.

#### 5.3.3.3. Selection of the Magneto-optic Medium

In Section 5.2.3.3 a classification of magneto-optic materials suitable for optical current sensing applications was presented. From this classification four materials have been selected as potential candidates for the prototype design of the optical current sensor. Among the selected materials are three crystals: Bismuth Silicate (BSO), Terbium Gallium Garnet (TGG) and Yttrium Iron Garnet (YIG), and one optical glass material, namely, Hoya FR-5 (Faraday Rotator 5) glass. The last material (as a relatively newly developed magneto-optic medium) was taken into consideration later during the project work programme. The selection of the above magneto-optic materials was made according to the following criteria:

- magnitude of the Verdet constant
- quality of the magneto-optic material
- availability in commercial quantities
- cost.

Some properties of the selected magneto-optic materials are given in Table 5-5.

Material	Properties				
-	Verdet constant, V, x10 <sup>3</sup> (deg/Tm)	Change of V with temperature	Operating wavelength (nm)	Other material properties	
BSO	1.67	<2% (+20°C to +120°C)	850	electro-optic	
TGG	3.37	35% decrease (- 30°C to +70°C)	850	-	
YIG	136.67	6% decrease (- 20°C to +85°C)	1300	electro-optic	
FR-5	2.15	35% decrease (- 50°C to +150°C)	850	-	

Table 5-5 Some properties of magneto-optic materials

Of the three crystal materials YIG was initially the most promising, having the largest Verdet constant and hence highest measurement sensitivity. However, several factors eventually led to YIG being discounted: its electro-optic nature introduces the possibility of measurement interference from the high electric fields surrounding a high voltage conductor; the iron garnets have high insertion losses throughout the visible and into near infrared wavelengths precluding their use at a wavelength of 850nm; the possible operation at a wavelength of 1300nm means that the light source and detector are more expensive and less powerful (in terms of the LED source) than their 850nm counterparts; YIG as an iron garnet produces hysteresis which can potentially affect the sensor response at low current levels.

Similarly BSO was discounted, ultimately due to its electro-optic nature, however there was also concern over the low sensitivity of BSO and thus the requirement to use a longer crystal length. This could introduce difficulties with optical aligning and packaging into a small, yet robust housing.

Finally, two materials have been selected upon which prototype current sensors are based: initially a TGG crystal and later the FR-5 glass. These materials are characterised by a relatively high Verdet constant, and yet a good dynamic range (as shown in the next paragraph); they are not electro-optic and therefore there is no possibility of any interference from the high electric fields found close to the conductor; and lastly they are suitable for use at 850nm, a preferred wavelength due

to the high power output and relative low cost of the light source, detector and associated fibre optic components, i.e., polarisers and lenses.

In addition, the FR-5 material can be easily manufactured in larger pieces, which brings a possibility of producing a reflective, multi-pass type current sensor, as described in Paragraph 5.2.3.3.

# 5.3.3.4. Modelling of the Magnetic Field Surrounding the Busbar

The next step after selecting a suitable sensing material is to evaluate a theoretical sensor response. Faraday Cell type OCT is a device which 'samples' the magnetic field path surrounding the conductor thus the sensor response depends strongly on both the geometry of the conductor and the distance between the conductor and the sensing element. Due to the variety of busbar geometries within the electricity industry, the three most representative conductors have been selected, of which cross-sections are shown in Figure 5-20. The sensor head is usually placed on top of the conductor, in the centre of its cross-section.

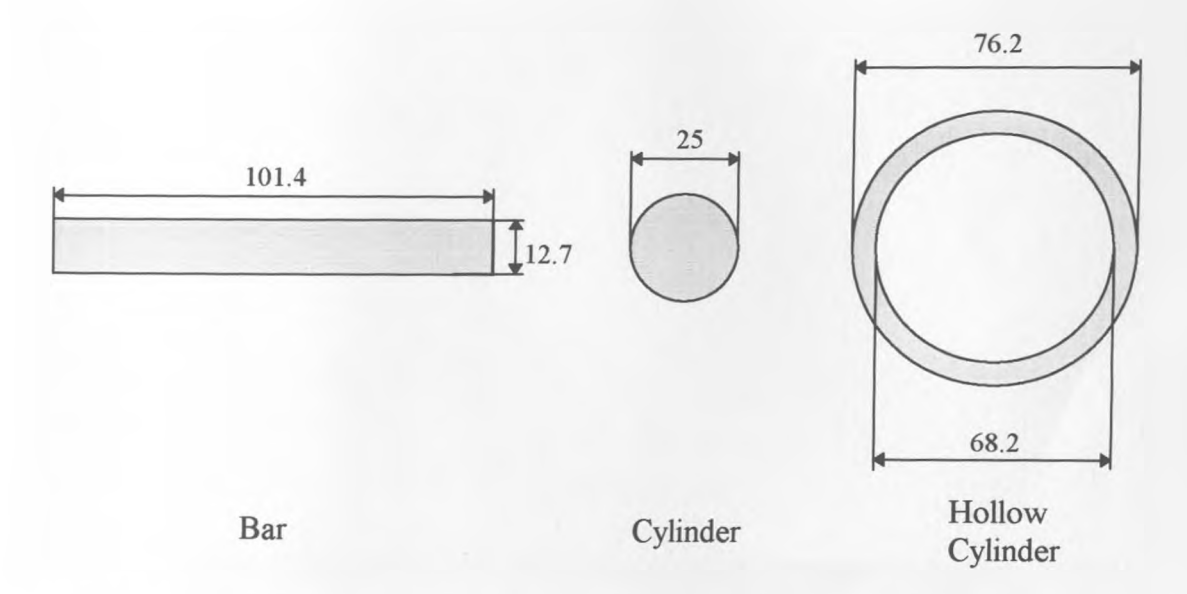


Figure 5-20 Cross-sections of the selected conductors used in the electricity industry

The above rectangular cross-section busbar connected to the high current variac was used as a laboratory OCT trial system. The cylindrical conductor and the hollow

conductor were respectively used in the two field trials of the prototype OCT systems, 132kV Colchester Grid OCT Field Trial and Three Phase, 132kV Eastern Electricity Field Trial at Piccotts End<sup>39</sup>.

In order to evaluate the sensor response it is necessary to define the length of the sensing element and its distance from the conductor. The length of the sensing element was set to 25mm, which is the diameter of the cylindrical conductor shown in Figure 5-20 and a reasonable maximum in terms of the packaging issues. In addition, further increase in length of the sensing element would not provide a proportional increase in sensitivity for this conductor due to the characteristic magnetic field distribution.

The separation distance from the surface of the conductor to the centre of the sensing element cross-section was fixed at 7.5mm (Figure 5-21). This distance was chosen as the best compromise between the available constraints:

- (i) the requirement to position the sensing element as close to the source of magnetic field as possible to maximise the OCT sensitivity and minimise the magnetic cross-talk
- (ii) the requirement to ensure sufficient physical protection to the sensing element and the optical assembly.

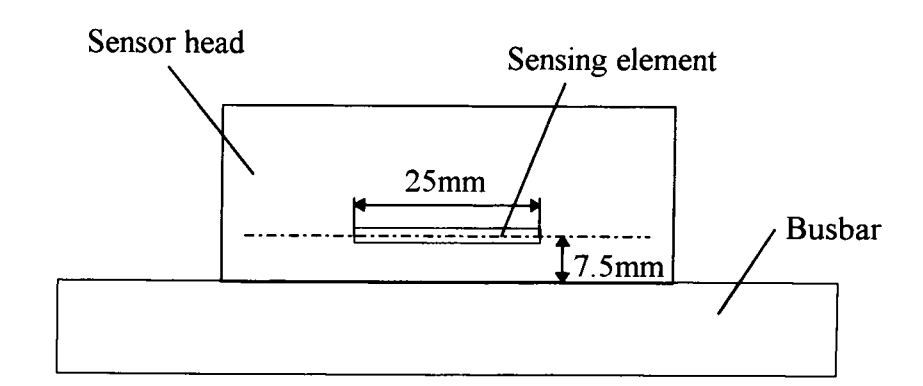


Figure 5-21 Separation distance between the conductor and the sensing element

In order to evaluate the magnetic field behaviour around the conductors shown in Figure 5-20 and calculate the magnetic field density along a longitudinal cross-section of the sensing element, a 2D Time-Harmonic Electromagnetic Design Software package 'OERSTED' was used.

The package uses the boundary element method (BEM)<sup>40</sup> of calculating field distribution and impedances. The program consists of two different solvers -- two-dimensional and rotationally symmetric field solvers. The major advantage of the above software is its ability to consider the skin effect within the conductor, which provides an accurate image of magnetic field distribution around the real conductor.

#### First Case - rectangular cross-section busbar

The skin effect has a significant influence on the magnetic field distribution around the conductor even at a frequency of 50 Hz. Figure 5-22 shows the first modelled case - the copper busbar. The graph displays a magnetic field density versus the conductor cross-section at the level of the earlier defined 'separation distance'. The model is calculated for the 50Hz rms volume current of 1000Amps flowing into the plane of the page. The conductor length is assumed infinite as the software package allows only two dimensional modelling. This assumption has no significant bearing on the accuracy of modelling for conductor lengths down to 20cm, which was confirmed using the 3D package 'FARADAY'<sup>41</sup>. The 3D package could not however be used satisfactorily for non-stationary currents due to its inability to handle the skin effect phenomenon, therefore all the considered cases are evaluated using the 2D 'Oersted'.

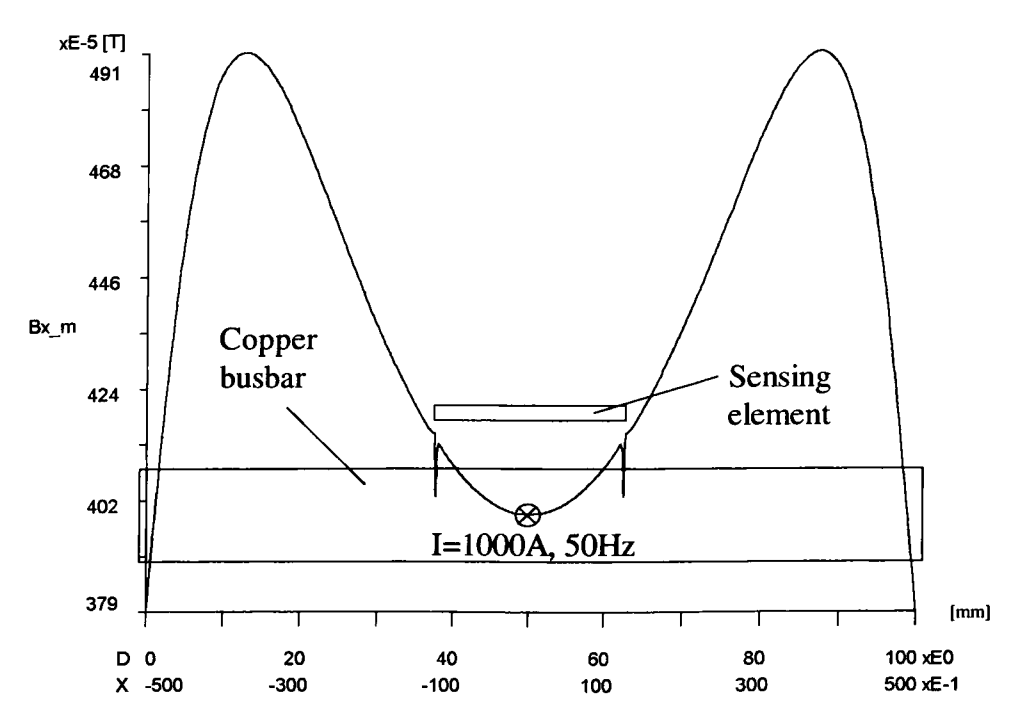


Figure 5-22 Magnetic field distribution at the level of 'separation distance' for the copper busbar

From Figure 5-22 it is apparent that the magnetic field density is much higher at both sides of the copper busbar, which is caused precisely by the skin effect phenomenon. This indicates that care should be taken during mounting the OCT on the conductor. The OCT clamping mechanism should restrict the sensor movements and should maintain precise definition of the sensor position on the busbar.

The calculated rms value of the magnetic field along the cross-section of the sensing element for the 50Hz rms volume current of 1000Amps equals 4.04mT for the above conductor.

#### Second Case - cylindrical conductor

Figure 5-23 displays distribution of the magnetic field density along the longitudinal cross-section of the sensing element placed on top of the cylindrical conductor at the earlier defined 'separation distance'.

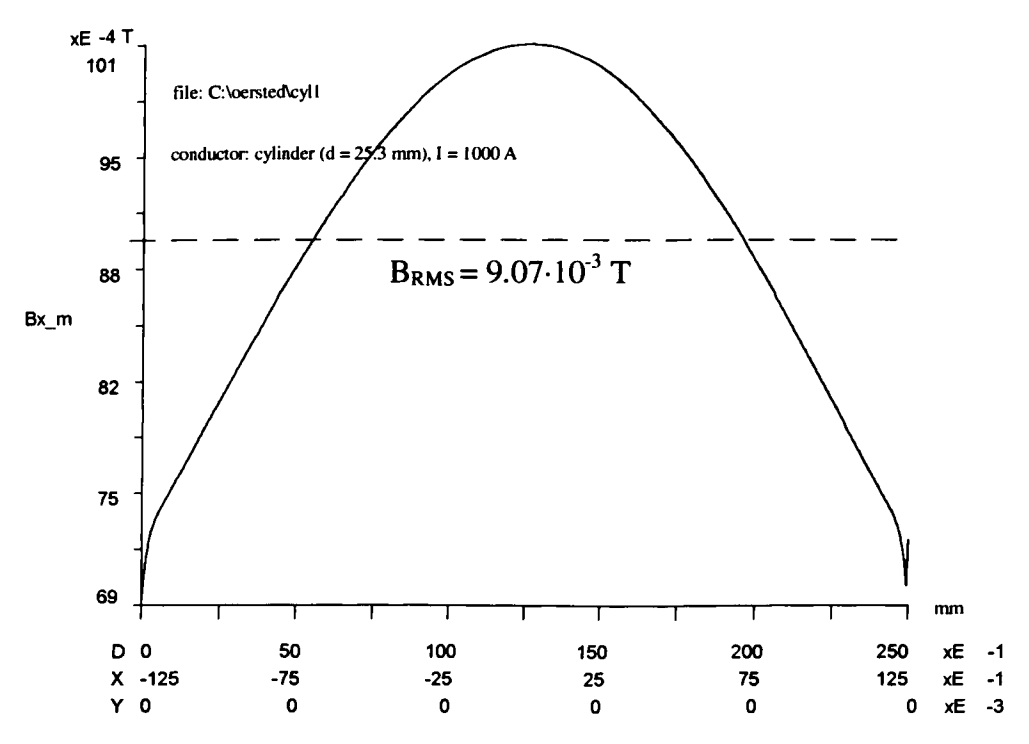


Figure 5-23 Magnetic field density along the longitudinal section of the sensing element for the cylindrical conductor

The field density distribution is different from the first simulation and reaches maximum at the centre of the sensing element. In this case, the calculated rms value of the magnetic field along the cross-section of the sensing element for the 50Hz rms volume current of 1000Amps equals 9.07mT. This is more than twice the value from the first simulation as the magnetic field is much more concentrated for this conductor geometry.

# Third Case - hollow conductor

Figure 5-24 shows distribution of the magnetic field density along the longitudinal cross-section of the sensing element for the hollow conductor. The separation distance and current parameters are the same as in the two previous cases. The calculated rms value of the magnetic field along the cross-section of the sensing element equals 4.28mT, which is a similar value as in the first case.

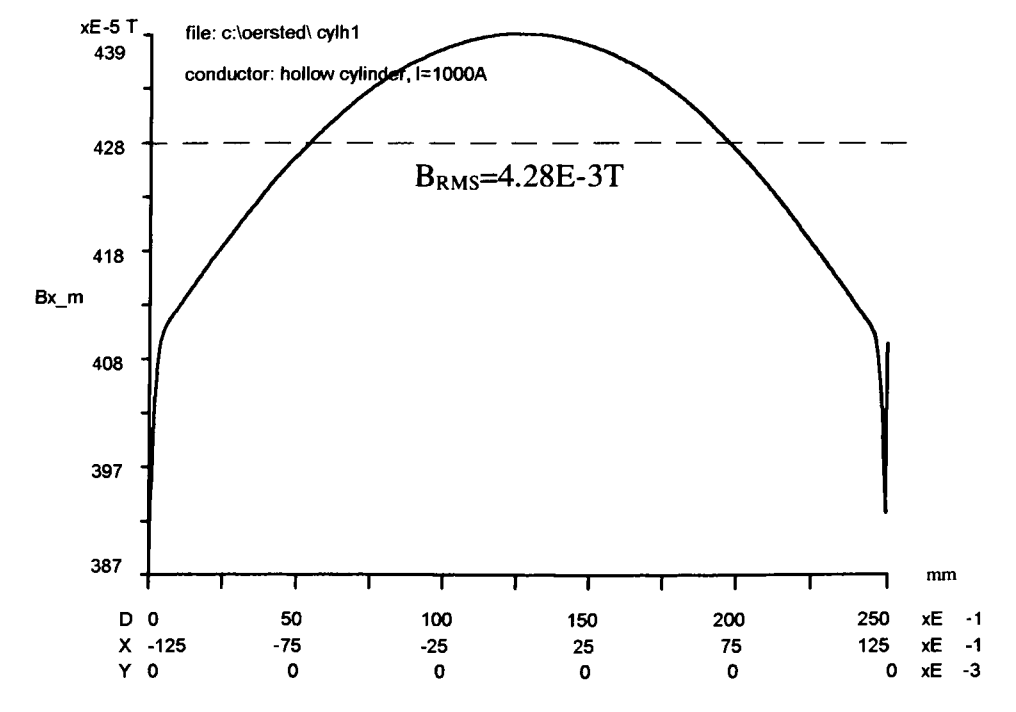


Figure 5-24 Magnetic field density along a longitudinal section of the sensing element for the hollow conductor

#### **Evaluation of OCT Maximum Dynamic Range**

Knowing the average magnetic field density along the length of the sensing element for 1000 Amps, the theoretical sensor response and in particular the OCT maximum dynamic range can now be calculated for the specific conductor geometry. From Figure 5-18, the OCT maximum dynamic is defined for the current level at which the rotation angle  $\theta$  reaches  $\pm \pi/4$ . Equation (5-2) can now be rewritten as:

$$\theta_{\text{max}} = \pm \frac{\pi}{4} = \pm \sqrt{2} \cdot k B_{1000A} LV$$
 (5-12)

where, V is the material Verdet constant ( $\lambda$ =850nm, T=293K), B<sub>1000A</sub> is the average magnetic field density along the length L of the sensing element for a current of 1000Amps and k is a proportionality factor. As the magnetic field density is directly proportional to the current flowing through the conductor, the maximum value of rotation,  $\theta_{max}$ , will be obtained for k times higher current than the value of 1000Amps for which the simulations were made. The  $\sqrt{2}$  factor converts the simulated rms value of the magnetic field density into its amplitude.

Table 5-6 displays OCT maximum dynamic range expressed in kA (rms) for the three above conductor geometries. The OCT working with the cylindrical conductor would have approximately twice as low dynamic range as compared to the rectangular cross-section busbar and the hollow conductor, both of which would produce a similar sensor response.

Maximum dynamic range [kA <sub>rms</sub> ]					
Conductor	Busbar	Cylinder	Hollow		
TGG	93	42	88		
FR-5	147	65	138		

Table 5-6 OCT maximum dynamic range for different conductor geometries

On the basis of the above simulations, two design approaches have been used, each for the different sensing medium: TGG linear-design and FR-5 reflective design.

#### 5.3.3.5. TGG Linear-design

In the early stages of this research work, the possibility of real time linearisation of the OCT response characteristic was not considered. For this reason, in order to maintain the current measurement accuracy, the sensor dynamic range had to be relatively large. The 25mm TGG crystal, having a high dynamic range, was ideally suited for this type of application. Using this crystal length, a range of current transducers with various current ratings could be produced.

In Paragraph 5.3.3.2 it was shown that only 41.8% of the OCT dynamic range can be used for protection application and 5.7% for metering applications. Combining this information with the values of maximum dynamic range for the TGG crystal based OCT from Table 5-6 it can be shown (Table 5-7) that a number of combined current sensors can be produced for measurement and protection applications within the electricity industry. Due to the vast number of possible current ratings<sup>37</sup>, only two examples of possible applications are presented in this analysis: sensors at the rated currents of 1kA and 2kA. These rated currents are optimal in terms of the optimal use

of the sensor dynamic range. Symbol 'P' in Table 5-1 means 'protection'. The number after this symbol indicates the 'Standard Accuracy Limit Factor', i.e., how many times the rated current can be exceeded.

Conductor	Busbar	Cylinder	Hollow
41.8% of I <sub>max</sub> (kA)	39.1	17.4	36.9
5.7% of I <sub>max</sub> (kA)	5.3	2.4	5.0
OCT (rated current: 1kA)	up to P30	up to P15	up to P30
OCT (rated current: 2kA)	up to P15	P5	up to P15

Table 5-7 Possible applications of TGG based OCT in the electricity industry

The above analysis indicates that the proposed TGG crystal rod (25mm in length and diameter  $\phi$ 2mm) is suitable for constructing sensors for the electricity industry applications.

# **Optical Assembly**

The manufacture process of the sensor head begins by producing two pairs of collimating/polarising components by gluing the polarisers to the GRIN lens assemblies. This can be done using the ultra violet (UV) glue compound and adequate irradiation of the assembled components with the UV light. Next, one of the lens/polariser assembly is glued (using the same technique) to one end of the crystal rod. The crystal rod and the second lens/polariser assembly are then mounted on the precision positioning and rotation stages in order to optimise the linear alignment and achieve a polariser bias of 45°. This can be done by launching a constant intensity light from one side and monitoring the output light intensity while the second lens/polariser assembly is rotated. The rotating stage position in which the light intensity is half the maximum light intensity is equivalent to a polariser bias of 45°. This method (called in this work dc method) takes into account a contribution of the natural optical activity effect, potentially present in the crystal rod.

#### **Sensor Housing**

After positioning and gluing of all the optical components, the optical assembly is inserted into a ceramic sleeve, placed inside a machined PTFE housing and potted<sup>39</sup> (see Figure 5-25). The housing is machined such, that the TGG crystal is fixed exactly at the earlier defined 'separation distance' from the bottom of the sensor head. The notches apparent on the outside of the sensor are to accommodate a locating clamp which insures that the sensor is fixed at one position on the conductor.

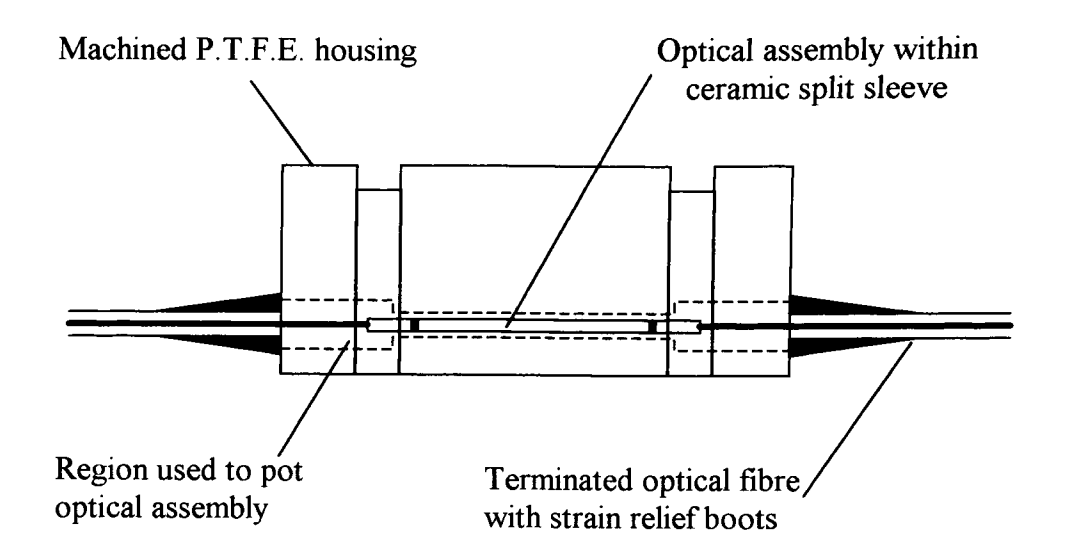


Figure 5-25 TGG sensor head

PTFE was chosen as the housing material due to its low value of thermal conductivity and a high resistance to chemical attack. However, it is relatively expensive compared to other polymer materials, accurate machining is difficult due to its propensity to cold flow and the material has a relatively high coefficient of thermal expansion. For these reasons ongoing work is concentrating on identification of other suitable housing materials, i.e., epoxy resins which are also suitable for direct potting of the optical components assembly.

A range of prototype TGG based sensors has been produced as shown below on the photograph (Figure 5-26). The first prototypes were terminated with SMA type

optical connectors fixed directly in the sensor head. Found very susceptive to external vibration, this design was later replaced with a 'pigtailed' sensor approach.

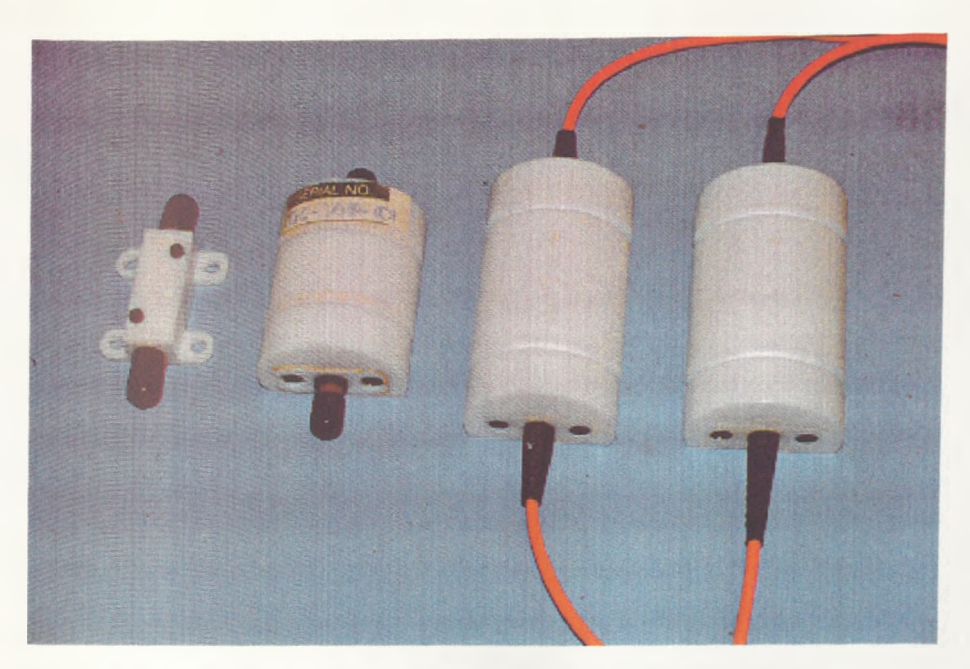


Figure 5-26 A range of prototype TGG based sensors

# 5.3.3.6. FR-5 Reflective-design

An attractive alternative to the linear-design OCT is its multi-pass reflective counterpart. It allows for the use of magneto-optic materials with the smaller Verdet constant and yet due to the mechanism of multiple light traversing along the sensing element, the sensitivity of the OCT can be increased.

The increase in sensitivity involves the necessity of real time linearisation of the sensor response characteristic as the linear approximation is sufficient only for the device limited dynamic range producing high transduction errors at its higher regions. The utilisation of the DSP technology allows for real time processing of the sensor output signal and hence the required linearisation of the device response characteristic is possible (more details will be provided in Chapters 7 and 8).

From Table 5-6, the maximum dynamic range of the single-pass FR-5 based sensor is higher than the dynamic of the TGG sensor. However, the FR-5 glass is commercially

available in larger pieces than the TGG material the price of which would be prohibitive at these crystal sizes. The piece of FR-5 glass can be polished to form a block which can be used to manufacture a reflective type multi-pass current sensor. Choosing the number of times that the light traverses the 25mm long sensing element to four, the following current sensors can be produced for combined metering and protection applications within the electricity industry (Table 5-8).

Conductor	Busbar	Cylinder	Hollow
100% of I <sub>max</sub> (kA)	37	16	35
OCT (rated current: 1kA)	up to P30	up to P15	up to P30
OCT (rated current: 2kA)	up to P15	P5	up to P15

Table 5-8 Possible applications of FR-5 based OCT in the electricity industry

## **Optical Assembly**

The optical components used for the construction of the FR-5 sensor are the same as in the TGG based device except the sensing element which is in the form of block (25x25x2mm) with two angle polished corners at 12° each (Figure 5-27). In order to provide multi-pass light transmission through the sensing element, the two opposite surfaces of the FR-5 block are coated with thin metal films.

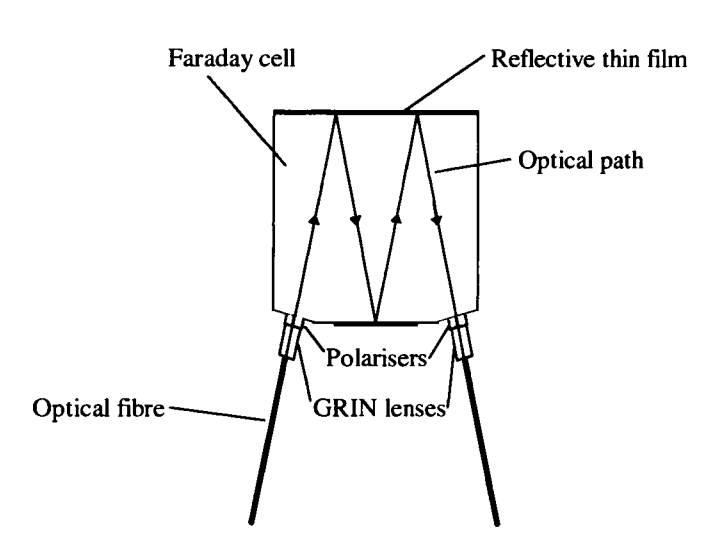


Figure 5-27 Multi-pass Faraday cell OCT

Due to the very long optical path (≈120mm) in this type of device, the optical alignment process is very difficult. Despite the use of standard positioning and

rotation stages, it is extremely difficult to achieve the exact 45° polariser bias point. The dc method (successfully used in the alignment of the TGG sensor) is not sufficient in this case as the slight vertical moves during rotating the output lens/polariser assembly cause high variations in the output light intensity. For this reason, the position of the rotation stage at half of the maximum output light intensity is not necessarily the 45° polariser bias point.

To overcome this problem, a new method of active alignment has been developed based on the idea of using the sensor response to the external ac magnetic field to accurately determine the desired polariser bias point. During the process of alignment, the sensing element is placed inside the coil of wire (≈300 turns) supplied from the sinusoidal current source. Due to the Faraday effect, the plain of linearly polarised light propagating through the sensing element undergoes a rotation according to the changing magnetic field. The rotation is converted into light intensity modulation by the analysing polariser. Now, by analysing the output light intensity, not only the best light transmission through the sensing element can be achieved (maximum dc level), but also by examining the symmetry of the modulated output signal, the 45° polariser bias point can be obtained at the position of the rotation stage when the output ac signal represents a symmetrical sinusoid.

To analyse the sensor output signal during the alignment process, the DSP unit is used build for the prime purpose of real time processing of the OCT output signal (more details in Chapter 7). A specially developed DSP software routine analyses the output signal in real time by comparing the amplitudes of positive and negative halves of the sinusoid in every period. Figure 5-28 illustrates simulated traces of the sensor normalised output signal at different points of the polariser bias  $\alpha$ . Signal normalisation is realised by dividing the output signal by its dc component, which makes it independent of any accidental change of light transmission along the addressing fibres and optical connectors. The magnitude of the rotation angle in Figure 5-28 is set to 12.8°, the value readily achieved from the discussed coil.

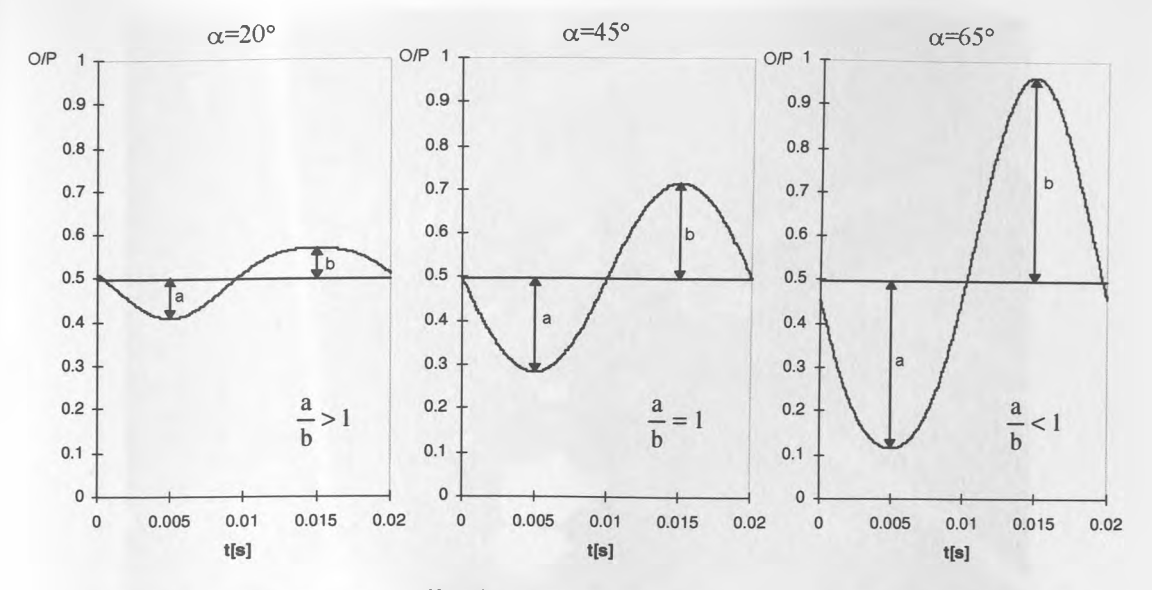


Figure 5-28 Sensor normalised output signal at different polariser bias points

From Figure 5-28 it is clear that the signal represents the 'clear' sinusoid (45° polariser bias point) only when the positive and negative amplitudes are equal, i.e.,  $\frac{a}{b} = 1$ .

The DSP algorithm generates the unique dc error signal directly related to the polariser position and indicates the 45° bias point when the error signal approaches zero. The error signal (after D/A converting) can be monitored by a precision voltmeter which gives the required information to the operator.

Figure 5-29 illustrates set-up of the active alignment method during the process of UV curing after the completed alignment. The FR-5 sensing element fits between the two machined pieces of cured epoxy resin secured inside the coil of enamelled conductor. One of the lens/polariser assembly is held by the rotation stage attached to the XYZ positioning stage. The UV lamp (not seen on the photograph) is fixed above the set-up.

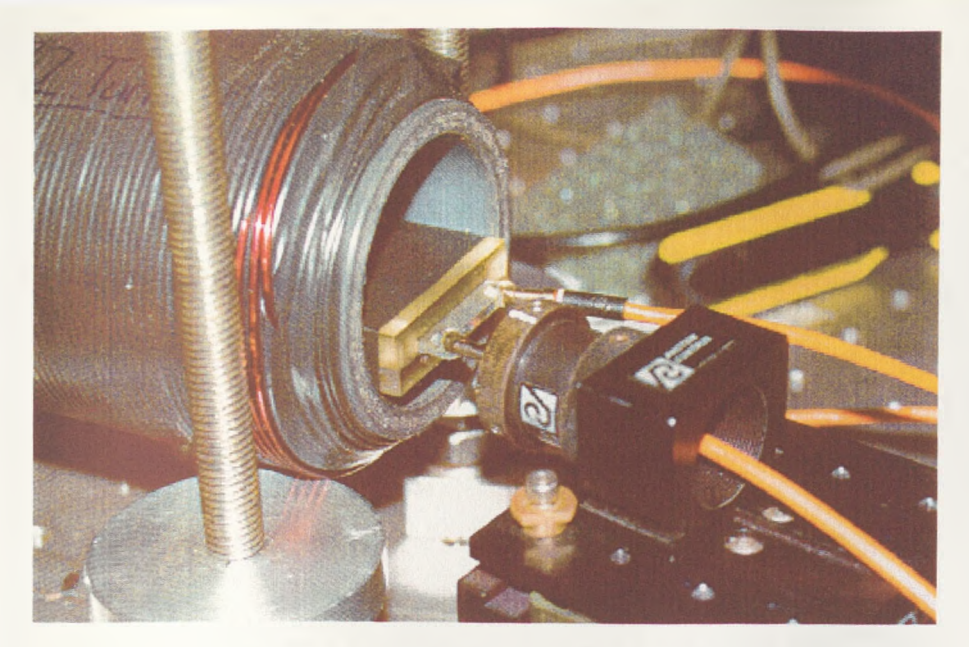


Figure 5-29 Active alignment set-up

#### **Sensor Housing**

In order to simplify the housing manufacture process, it was decided to "pot" the sensor in an epoxy resin mixture which could be used to encapsulate and protect the fragile sensor components. The finished optical assembly was accurately positioned in the nylon former and potted using epoxy resin 'Epofix' from Struers Ltd., characterised by good mechanical and electrical parameters. The FR-5 optical assembly and the completed sensor are pictured below in Figure 5-30.

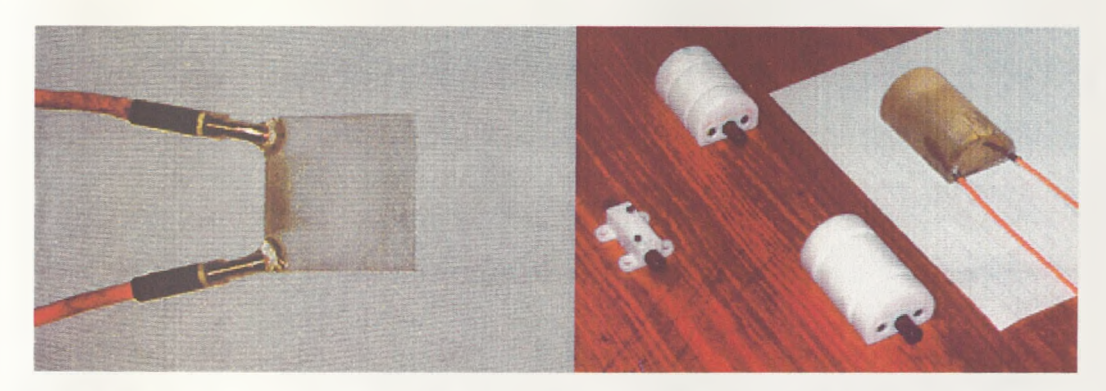


Figure 5-30 FR-5 optical assembly (left) and completed FR-5 sensor (right)

Encapsulating the sensor in this way was thought to provide a quick, cheap and robust housing for the OCT. However, after initial investigations several disadvantages of this technique were discovered. Shrinkage of the epoxy resin during

curing, although small, caused significant stresses on the optical assembly, and in particular on the block of FR-5 glass. This gave rise to stress induced linear birefringence within the sensing element and severely decreased the sensor sensitivity. In addition the sensitivity was found strongly dependent on temperature variations as the internal stress was subject to the temperature variations.

After a series of unsuccessful potting experiments, e.g., the sensor optical assembly was secured within the pre-machined housing elements and potted<sup>42</sup>, or using different types of epoxy resin, the technique has been temporarily abandoned. Instead, a different approach of producing the pair of machined housing elements from cured epoxy resin have been applied. The two housing parts are machined to accommodate the sensor optical assembly and joined using nylon screws. The optical assembly is secured inside the enclosure with the elastic filler compound, resistant to high temperatures. Figure 5-31 pictures the FR-5 optical assembly placed in the machined top part of the sensor housing (on the left) and the dismounted sensor housing (on the right).



Figure 5-31 FR-5 sensor housing

The OCT produced using pre-machined housing elements maintains the intended sensitivity and the temperature effect is dependent only on the temperature characteristic of the Verdet constant.

In the final stage of the sensor development, in particular for the mass production purposes, a resin injection technique could be used in manufacture of a precise housing for the OCT. This would still provide a means for a quick, cheap and robust housing that does not require machining.

# 5.4. Summary

In this chapter a diverse range of optical current measurement methods have been reviewed, in particular those with relevance to the electricity industry. Most of the current transducers reported in the open literature are not compliant with the function and accuracy requirements specified for this sector of commerce. Major issues of environmental effects on the OCT operation are still generally unresolved, and the lack of confidence in reliability, repeatability and robustness of the optical counterpart of the current transformer restrict a wide commercial acceptance of this kind of device. Many of the reviewed optical current sensors are complex in design and with added complexity of the required signal processing they are hardly competitors to the conventional well established current transformers. In contrast, the Faraday Effect based OCT and in particular the Faraday Cell point sensor can effectively compete not only with the remaining optical current sensors but also with the conventional devices.

From Section 5.3 it is clear, that the author's preferred type of OCT has a number of advantages which predestine it to the main place amongst the optical devices. The Faraday cell point sensor is simple to manufacture and is characterised with a small size and light weight, yet without compromising robustness. All the safety benefits offered by optical devices are applicable to this type of sensor. In terms of installation and maintenance, the point sensor is simply the 'clamp-on' device offering reductions

in power system downtime with the reduced requirement for lifting gear and installation personnel.

The performance of this type of OCT suffers in particular from the external environmental factors such as vibration, temperature and magnetic cross-talk effects, and from internal physical limitations such as nonlinear response characteristic. However, the use of latest signal processing technology can significantly assist in improving the overall device performance, inhibited by the above deficiencies. The next chapter will thoroughly investigate the environmental effects of vibration, temperature and magnetic cross-talk on the OCT operation characteristics.

# 5.5. Chapter References

- 1) "Optical Current Transducers for Power Systems: A Review", IEEE Transaction on Power Delivery, vol. 9, No. 4, October 1994, pp1778-1787,
- 2) C. M. Davis, "Phase-modulated fibre-optic current transformer", EPRI Final Report EL-7421, Research Project 2734-3, 1991, Herndon, VA: Optical Technologies, Inc.,
- Y. Hesegawa, Y. Ichikawa, H. Katsukawa, N. Tanaka, and Y. Sakurai, "Development of a new type optical transducer for measuring fault current", Paper 93 SM 370-7 PWRD,
- 4) A. Yariv, H. V. Winsor, "Proposal for the detection of magnetic fields through magnetostrictive perturbation of optical fibres", Optical Letters 5, 19, pp78,
- 5) A. Dandridge, A. B. Tveten, G. H. Sigel, E. G. West and T.G. Giallorenzi, "Optical Fibre Magnetic Field Sensors", Electronic Letters 16, 1980, pp408-409,
- 6) F. Bucholtz, K. P. Koo, A. D. Kersey and A. Dandridge, "Fibre Optic Magnetic Field Sensor Development", SPIE Vol 718 Fibre Optic and Laser Sensors IV, 1986, pp56-65,
- D. M. Dagenais, F. Bucholtz and K. P. Koo, "Elimination of Residual Signals and Reduction of Noise in a Low-frequency Magnetic Fibre Sensor", Applied Physics Letters, Vol 53, 1988, pp1417-1476,

- 8) M. D. Mermelstein, "Fibre Optic Polarimetric dc Magnetometer Utilising a Composite Metallic Glass Resonator", IEEE Journal of Lightwave Technology, Vol LT-4, 1986, pp1376-1380,
- 9) A. J. Rogers, "Optical Measurement of Current and Voltage on Power Systems", Electric Power Applications, Vol. 2, No. 4, Aug 1979, pp. 120-124,
- 10) R. Ulrich and A. Simon, Appl. Opt. 18, 2241 (1979),
- 11) R. I. Laming and D. N. Payne, IEEE J. Lightwave Technology 7, 2084 (1989),
- 12) G. W. Day and S. M. Etzel, Technical Digest International Conference on Integrated Optics and Optical Fibre Communication—European Conference on Optical Communication, Venice, 1985, p. 871,
- 13) D. Tang, A. H. Rose and G. W. Day, SPIE 1267, 29 (1990),
- 14) A. Ben-Kish, M. Tur and E. Shafir, Opt. Letters 16, 687 (1991),
- 15) H. Ahlers and Th. Bosselmann, Proceedings on the 7<sup>th</sup> Optical Fibre Sensors Conference, 1990, p. 81,
- 16) W. Chu, D. McStay and A. J. Rogers, Electron. Letters 27, 207 (1991),
- 17) A.D. Kersey and M. A. Davis, Springer Proceedings in Physics, Vol. 44, Optical Fibre Sensors (Springer, Berlin, 1989), p. 285,
- 18) P. A. Leilabady, A. P. Wayte, M. Berwick, J. D. C. Jones and D. A. Jackson, Opt. Commun. 59, 173 (1986),
- 19) R.P. Tatum, M. Berwick, P. A. Leilabady, J. D. C. Jones and D. A. Jackson, Applications of Faraday Rotation Using Monomode Optical Fibre, SPIE Vol 734, Fibre Optics 87, pp178-192,
- 20) R. I. Laming and D. N. Payne, IEEE J. Lightwave Technol. 7, 2084 (1987),
- 21) N. C. Pistoni and M. Martinelli, Opt. Lett. 18, 314 (1993),
- 22) S. Donati, V. Annovozzi-Lodi and T. Tambosso, IEE Proc. 135, 372 (1988),
- 23) T. Sato, G. Takahashi and Y. Inui, Europe Patent, Publication No. 0088419 A1 (1983),
- 24) Y. N. Ning, B. C. B. Chu and D. A. Jackson, Opt. Lett. 16, 1996 (1991),
- 25) A. Cruden, Z. J. Richardson, J. R. McDonald, I. Andonovic, "Optical crystal based devices for current and voltage measurement", IEEE Transactions on Power Delivery, Vol. 10, No. 3, 1995, pp1217-1223,

- 26) G. A. Massey, D. C. Erikson, R. A. Kadlec, "Electromagnetic field components: their measurement using linear electro-optic and magneto-optic effects", Applied Optics, Vol. 14, No. 11, 1975, pp. 2712-2719,
- 27) V.B Arkhangelshiy, S. F. Glagolev, T. P. Kazakowa, M. N. Chervinskiy, "A magnetooptical method for measuring current strength", Soviet Union Patent No.1453330 A1, 1989,
- 28) E. Nakamura, K. Uchida, M. Koshiishi, T. Mitsui, S. Miyamoto, K. Nakamura, K. Itaka, T. Hara, T. Yoda, "Development of Fault Section Detecting System for Gas Insulated Transmission Lines", IEEE Transactions on Power Delivery, Vol. 1, No. 1, 1986, pp. 19-26,
- 29) G. Katsuta, K. Muraoka, N. Inoue, S. Sakai, T. Tsunekage, K. Ando, "Fault Section Detection System for 66kV Underground Branch Transmission Lines Using Optical Magnetic Field Sensors", IEEE Transactions on Power Delivery, Vol. 7, No. 1, 1992, pp. 1-9,
- 30) N. F. Borrelli, J. Chem. Phys. 41, 3289 (1964),
- 31) S. H. Wemple, J. F. Dillon, L. G. VanUitert, W. H. Grodkiewicz, Appl. Pysics Letters 22, 331 (1973),
- 32) R. Wolfe, R. A. Liebermann, Appl. Phys. Letters 58, 1733 (1991),
- 33) R. Wolfe, E. M. Gyorgy, R. A. Liebermann, V. J. Fratello, S. J. Licht, M. N. Deeter, G. W. Day, Proceedings on the 8<sup>th</sup> Optical Fibre Sensors Conference, 1992, p. 390,
- 34) M. N. Deeter, G. W. Day, R. Wolfe, V. J. Fratello, "Magneto-Optic Magnetic Field Sensors Based on Uniaxial Iron Garnet Films in Optical Waveguide Geometry", IEEE Transactions on Magnetics, Vol. 29, No. 6, 1993, pp. 3402-3404,
- 35) Litton Lambda/Airton Data Shits "Terbium Gallium Garnet (TGG)",
- 36) Draft of IEC 60044-8 International Electrotechnical Commission, "Instrument transformers: Part 8: Electronic current transducers", TC38WG27, 1998,
- 37) IEC 44-1 International Standard, "Instrument transformers: Part 1: Current transformers", December 1996,
- 38) Optics Guide 5, Melles Griot Product Catalogue, 1990,

- 39) A.Cruden, "Electric Current Measurement using crystal based, magneto-optic point field sensors", PhD Thesis, Centre for Electrical Power Engineering, University of Strathclyde, Department of Electronic and Electrical Engineering, June 1998,
- 40) Integrated Engineering Software, "2D Time-Harmonic Electromagnetic Design Software package 'OERSTED'", User Manual, (Internet Address http://www.mbnet.mb.ca/ies/),
- 41) Integrated Engineering Software, "3D Time-harmonic Eddy Current Design Software package 'Faraday'", User Manual,
- 42) Madden, "Report on Fabrication and Testing of an FR5 Optical Current Sensor", CEPE Reference Number RR/OPT/TR/1998-003, December 1998.

# 6. Environmental Factors in the OCT Operation

# 6.1. Introduction

Following the definition of the OCT function and accuracy requirements and the detailed description of the sensor head, this chapter will concentrate on the external factors responsible for the current sensor performance limitations, i.e., vibration, temperature and magnetic cross-talk effects. These effects can potentially deteriorate the measurement accuracy or even introduce false readings from the OCT system. It is likely that most of the mentioned environmental factors will be present at the sensor installation site and therefore some sort of compensation schemes are required to overcome the decrease in the device performance. This chapter will investigate the physical grounds behind the above phenomena, and on this basis, will propose appropriate compensation methods.

# 6.2. Vibration Induced Noise

Vibration and mechanical stress are factors which directly or through other physical phenomena affect light transmission within the optical path of virtually any fibre-optic system. In the light intensity encoded sensor systems, variable transmission losses cause output light intensity changes which can be interpreted as changes in the measurand and hence are the source of error. The OCT optical transmission system, as intensity encoded, is also vulnerable to the above mechanism.

The OCT optical transmission system, as shown in Figure 6-1, includes the transmit/receive processing unit, usually located indoor, and the optical system consisting of connectors, multimode fibre-optic link and the sensor head, usually located outdoor and potentially exposed to various environmental factors, e.g., vibration. Each component of the optical path is affected to a greater or lesser extent by vibration. The next sections will discuss the physical mechanisms in each individual component contributing to the overall vibration effect as shown in Figure 6-1.

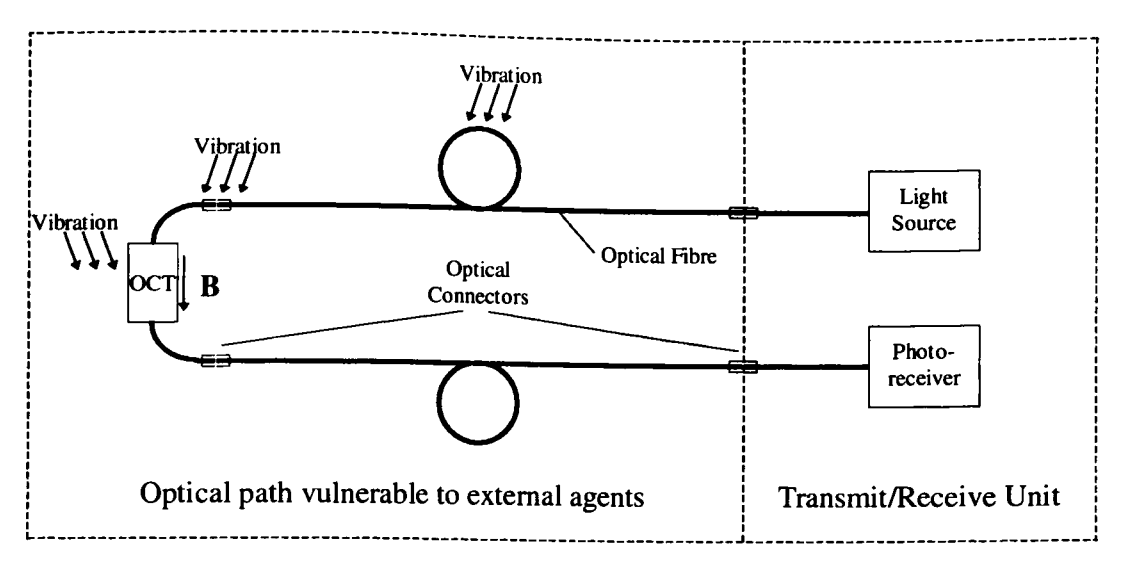


Figure 6-1 OCT optical transmission system

# 6.2.1. Transmission Losses within Optical Fibre

In general, transmission losses within optical fibre have two sources of origin: material losses and wave-guide losses. The first are caused by light scattering and absorption on material inhomogeneities and impurities by metals and ions OH<sup>-</sup>. These losses are constant over a long term period and cannot be modulated by vibration. For this reason they are not further discussed.

The wave-guide losses result from the technology of fibre manufacture and are caused by light scattering at macro-bends, micro-bends and inhomogenities (micro-cracking) on the core/cladding boundary. Moreover, the latest is also vibration independent.

The cylindrical structure of the wave-guide imposes modal propagation of the light wave within the core and cladding of the optical fibre. Apart from modes guided within the optical fibre, there are radiation modes (leaky waves) associated with the energy radiated by the fibre. The radiation losses are in general minor as compared to the internal losses caused by inhomogeneous distribution of the refractive index and non-linear geometry of the optical fibre. Nevertheless, due to mechanical deformation (stress, vibration), they can cause increase in fibre attenuation as a result of unneeded mode mixing of the wave-guide modes and radiation modes.

As mentioned above there are two kinds of classified mechanical deformation: macrobends arising from curvature of the fibre axis, and micro-bends resulting from small inhomogeneities in the fibre such as diameter variations and random microscopic bends which can arise during fibre manufacture, coating and cabling processes.

The curvature loss effects may be explained in terms of the evanescent field mechanism. Every bound core mode has an associated evanescent field tail which extends into the cladding and decays exponentially as a function of distance from the core. Since this field tail moves along with the modal field distribution in the core, part of the energy of the propagating mode travels in the cladding of the fibre. When the fibre is bent, the part of the field tail on the outside of the bend is required to travel faster than that of the inside in order to maintain a waveform perpendicular to the direction of propagation (see Figure 6-2). Hence part of the mode in the cladding needs to travel faster than the velocity of light in the medium (c/n<sub>2</sub>). Since this is not possible, the guidance mechanism of the fibre is inhibited and the energy associated with this part of the mode is lost by radiation. As the radius of curvature is decreased, the phase velocity of the evanescent field at the bend that is equal to the velocity of light in the cladding decreases, and more energy is lost. In multimode optical fibres bending losses depend on the number and kind of propagating modes, the losses increase with an increase of the mode order. The amount of power loss is also strongly dependent on the numerical aperture NA, the losses quickly decrease with an increase of NA ( $\approx 1/NA^3$ ).

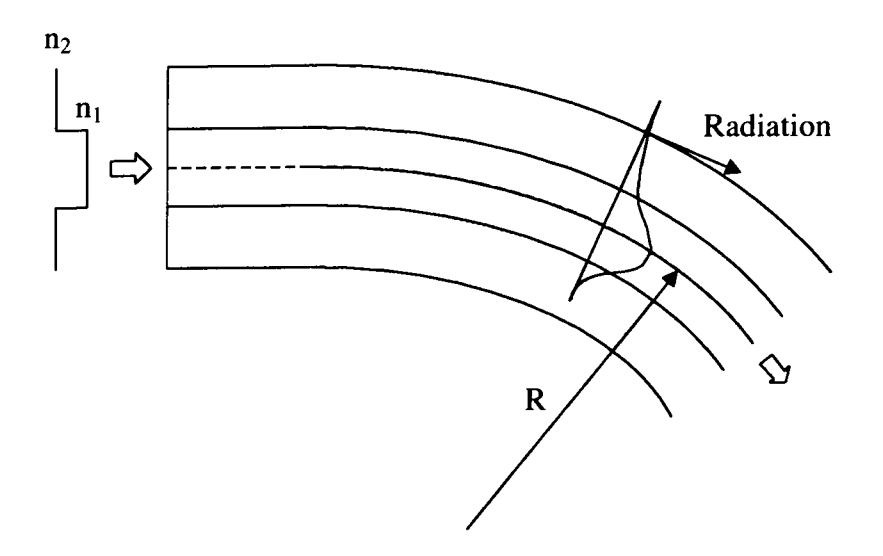


Figure 6-2 Bending loss mechanism

#### **6.2.2. Optical Connection Losses**

Losses of optical power may occur at the point of optical connection between the fibre-optic components, e.g., fibre/fibre, fibre/lens, lens/lens, fibre/LED, etc. These losses can be classified into the following groups: intrinsic (associated with fibre tolerances), extrinsic (associated with inaccuracy of component alignment and Fresnel reflection) and the separate loss mechanism within the multimode optical system, namely modal noise. Most of these loss mechanisms may be modulated to a greater or lesser extent by vibration.

# 6.2.2.1. Intrinsic Losses

Intrinsic losses associated with fibre tolerances directly relate to the quality of fabrication of the optical fibre itself. There are several fibre tolerance problems as shown schematically in Figure 6-3.

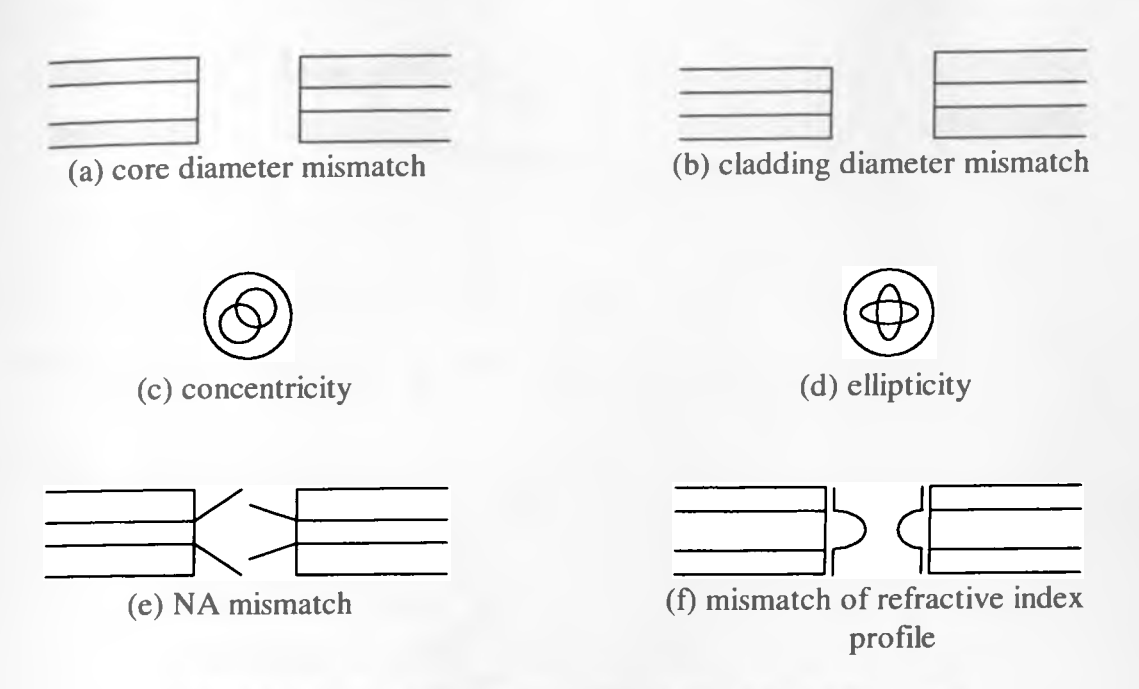


Figure 6-3 Intrinsic Losses Associated with Fibre Tolerances

Figure 6-3 (a) illustrates mismatch in core diameters of transmit and receive fibres, which leads to power losses if light is transmitted from the larger diameter core to the lower diameter core. If light is transmitted in the opposite direction no loss occurs.

Figure 6-3 (a), (b) and (c) show effects which lead to bidirectional light losses as the effective connection areas of the two fibre cores are reduced. If the fibres rotate with respect to each other along the transmission axis (due to some external forces), the power loss at such connections will be modulated.

Figure 6-3 (d) illustrates losses resulted from the difference in numerical apertures (NA) of the two connected step-index fibres. Light entering outside the acceptance cone is transmitted into the cladding and lost. A similar situation occurs, as shown in Figure 6-3 (e), at the connection point of two graded-index fibres with not matched profiles of refractive index.

#### 6.2.2.2. Extrinsic Losses

Extrinsic losses relate to connectors and adaptors, and also apply to GRIN lens assemblies within the sensor head. There are several connection problems associated

with inaccurate positioning of the two optical components or with reflection, as shown schematically in Figure 6-4.

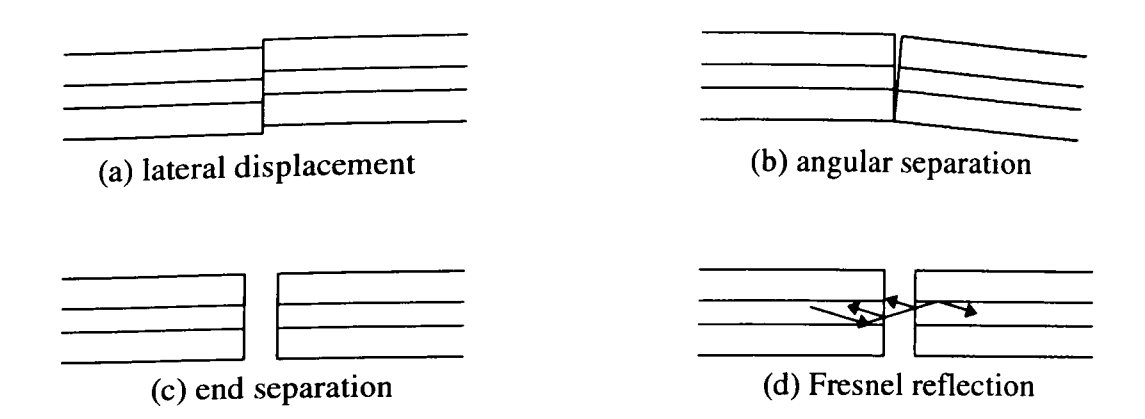


Figure 6-4 Extrinsic Losses

Lateral displacement, angular separation and end separation all result from inaccuracies within the two matching parts of an optical connector or adaptor. This gives rise to optical power losses as light entering outside the core of the receiving fibre is transmitted into cladding and eventually lost. In addition, for cases (a) and (b), connection of graded-index fibres is characterised by higher losses as opposed to step-index fibres. This is due to the local numerical aperture, which applies to graded-index fibres. While for step-index fibres the transmitted optical power is proportional to the coupling area, for graded-index fibres there exist an additional loss in the part of the joining surface for which NA<sub>2</sub><NA<sub>1</sub>.

A separate loss mechanism, shown in Figure 6-4 (d), is caused by the Fresnel reflection which takes place on boundaries between different refractive indices along the optical path, e.g., glass/air and air/glass at the connection of two fibres. If the separation distance is smaller than the coherence length of the light source, then conditions arise for interference, and the intensity of light passing through the connector could be modified. In addition, the Fresnel reflection is particularly problematic within the bi-directional light propagation as in this case the back-reflected light may give rise to an error.

All the above losses would remain constant for stationary environmental conditions, however this situation is very unlikely at the industrial site. Any movement of the connecting parts caused by vibration and/or mechanical stress (as a result of for instance temperature changes of a connector) will introduce modulation of losses and give rise to an error.

# 6.2.2.3. Losses Associated with Modal Noise Effect

Modal noise is a phenomenon giving rise to a parasitic intensity modulation of the optical signal detected at the end of a fibre. This effect is also classified to the connection losses as it occurs at the physical 'break' of the optical path.

Figure 6-5 explains the mechanism of modal noise. At the end of multimode fibre 1 the different propagating modes interfere to give rise to a characteristic speckle pattern<sup>2</sup>. In Chapter 4, it was shown that a discrete set of modes propagating within the fibre core (V-number) is determined by the optical wave parameters, e.g., wavelength and the fibre parameters (Equation 4-3). Within a multimode fibre several thousands modes may propagate at the same instant. When fibre 1 is moved and/or when the source wavelength is varied, the speckle pattern changes and the coupled power from fibre 1 to fibre 2 is intensity modulated. This parasitic intensity modulation of the power is called modal noise.

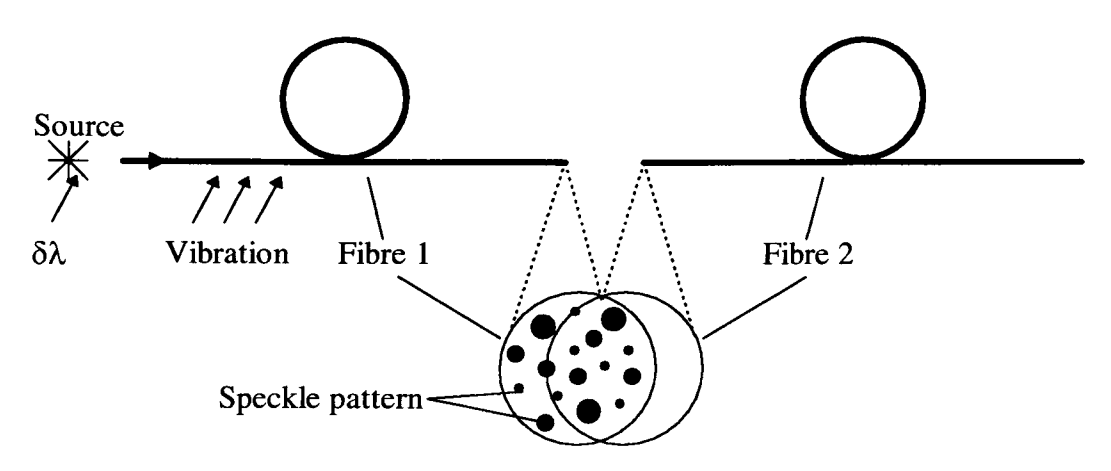


Figure 6-5 Modal noise effect

It has been shown<sup>2</sup> that modal noise is a function of the fibre characteristics (dispersion, number of propagating modes, etc.), of the source properties (wavelength, coherence, etc.) and of the connector and splice losses.

Modal noise decreases with an increasing number of propagating modes, which implies that a low coherent light source such as LED is preferred over the highly coherent lasers or even super-luminescent diodes while used with multimode optical fibres. It has been confirmed experimentally, that if other than LEDs light sources are used with a multimode optical fibre, the detected bidirectional optical signals exhibit uncorrelated with each other responses to the external fibre vibration. This can be explained by the modal noise phenomenon; the use of other than LEDs light sources is not recommended in multimode optical systems.

# 6.2.3. Stress Induced Birefringence within Sensing Medium

In Chapter 3, following the theoretical description of light propagation in an anisotropic media and the definition of birefringence, the photoelastic effect was introduced, also called the effect of stress induced birefringence. The application of a mechanical stress perpendicular to the direction of the propagating light wave induces an increase in the refractive index for light polarised along the stress direction. The effect occurs in virtually all solids (regardless of crystal symmetry), thus isotropic substances become optically anisotropic (i.e., exhibit birefringence), whilst in anisotropic materials the effect becomes directional. Under compression or tension the isotropic material will take on the properties of a negative or positive uniaxial crystal, respectively.

When the OCT sensing element is subjected to large levels of vibration, the associated mechanical stress can be sufficient to introduce significant levels of birefringence which will modify the polarisation state of the light traversing the sensor. In general, the propagating light will take on the form of elliptically polarised light, which will inhibit the sensor measurement sensitivity and hence introduce error.

In general the elasto-optic coefficients are relatively small so that small stresses may only be detected by integrating the effect over a long path length. This condition however can be applied to the FR-5 device which can particularly suffer from the above mechanism.

It can be shown<sup>3,4</sup> that the change in polarisation caused by the photoelastic effect does not depend upon the direction of light propagation; the polarisation states of incoming and returning light waves will be modified to the same extent.

### 6.3. Vibration Compensation

Vibration effects described in the previous section are difficult to quantify as they differ for different optical components used in the OCT optical arrangement, e.g., optical connectors, fibre-optic cable, sensing element, etc., and various mounting methods applied. The experimental investigation reveals (more details in Chapter 8) that the magnitude of vibration induced noise may be sufficient to seriously deteriorate the measurement performance. Consequently, there is a need for an effective vibration compensation method in the practical OCT system.

Several authors have reported details of methods which apply different vibration compensation schemes to either single or multimode optical arrangements of different types of OCTs. Some of these methods have already been described in Chapter 5, as to mention single mode arrangements utilising a Sagnac interferometer, orthoconjugate reflector or periodic conductor structure. Each of these methods have some drawbacks, and due to the use of single mode arrangements they are not applicable to the system which forms the basis of this thesis.

Other authors<sup>3,5,6,7,8</sup> have applied methods making use of the fact that the magneto-optic Faraday effect is a nonreciprocal phenomenon (as described in Chapter 3); the direction of the induced polarisation rotation depends upon the direction of the

propagating light through the optical path. Other changes of optical intensity are assumed reciprocal (independent of direction). Hence, configuring the OCT for bidirectional light propagation, two reference signals can be obtained which are then used to effectively cancel any vibration components in the output signal.

A similar method, developed independently within this research work, has been used in the practical OCT system. The arrangement applies a unique technique which deals with the problem of back-reflection, present in the methods quoted above. In the next paragraphs the proposed vibration compensation scheme will be explained in details.

#### 6.3.1. Background

In order to analyse the output optical signals produced by a Faraday sensor configured for bidirectional light propagation, one may consider a magneto-optic material placed between two polarisers in a constant magnetic field **B** which is aligned parallel to the crystal transmission axis **Z**, while two light beams are launched from the +**Z** and -**Z** directions (Figure 6-6). The polarisers are orientated at angle  $\alpha$  with respect to each other and their axes are parallel to OY and O'Y' respectively.

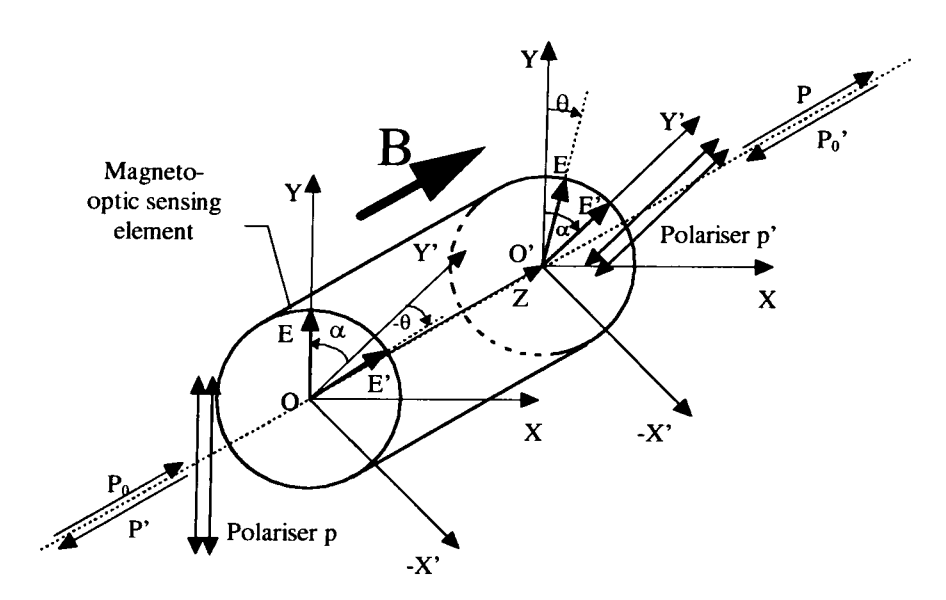


Figure 6-6 Graphical illustration of the nonreciprocal nature of the magneto-optic

Faraday effect

The plane of linearly polarised light undergoes a rotation  $\theta$  which is directly proportional to the magnetic field B, crystal length and Verdet constant characterising the magneto-optic material. For light transmitted in +Z direction,  $\theta$  is in phase with  $\alpha$  at the exit polariser p', and for light transmitted in -Z direction,  $\theta$  is in anti-phase with  $\alpha$  at the exit polariser p, which is due to the nonreciprocal nature of the Faraday effect. By convention this represents the situation where the Verdet constant is negative, alike for the FR-5 glass.

The exit polariser converts the induced angular rotation to light intensity changes and from this point on only power levels of the light P and P' are important. Now signals P and P' may be derived: only parallel components to the polariser axes of the electrical vectors E and E' are transmitted, and one can see that their magnitudes are given by,  $E\cos(\alpha+\theta)$  and  $E\cos(\alpha-\theta)$  respectively. As the optical power is directly proportional to the square of the electric field magnitude of the light wave, P and P' can be expressed by the following equations

$$P = P_0 \left(\cos(\alpha + \theta)\right)^2 = \frac{1}{2} P_0 \left(1 + \cos 2(\alpha + \theta)\right)$$
 (6-1)

$$P' = P'_{0} \left( \cos(\alpha - \theta) \right)^{2} = \frac{1}{2} P'_{0} \left( 1 + \cos 2(\alpha - \theta) \right), \tag{6-2}$$

assuming that there is no insertion loss. As the polarisers are arranged at an angle  $\alpha$  of  $\pi/4$ , Equations (6-1) and (6-2) can now be expressed as:

$$P = \frac{1}{2} P_0 (1 - \sin(2\theta))$$
 (6-3)

$$P' = \frac{1}{2} P'_{0} (1 + \sin(2\theta))$$
 (6-4)

# 6.3.2. The Principle of Compensation

Figure 6-7 depicts the OCT bidirectional arrangement. The conventional optical system (transmitter - fibre - sensor - fibre - detector) is equipped with a second transmitter and detector such that the second light beam propagates in the opposite direction to the first beam.

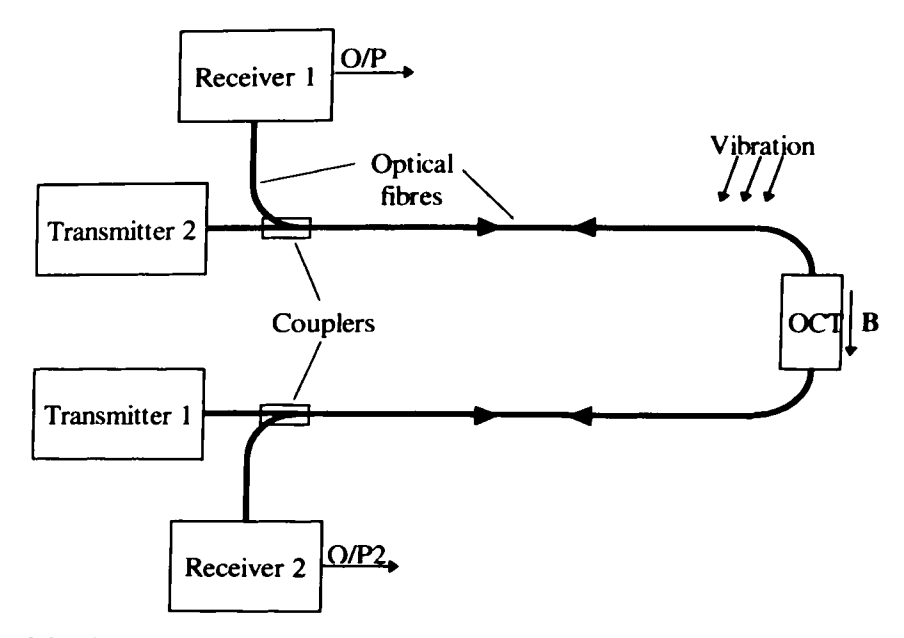


Figure 6-7 The configuration of the bidirectional light propagation in the optical system

The electrical signals from the photodetectors outputs can be expressed in the following forms, analogous to (6-3) and (6-4):

$$e_1 = k_1(1 - L(t))(1 - \sin 2\theta(t)),$$
 (6-5)

$$e_2 = k_2(1 - L(t))(1 + \sin 2\theta(t)),$$
 (6-6)

where

$$k_1 = \frac{1}{8}I_1R_1A_1(1-L_{01})$$
 and  $k_2 = \frac{1}{8}I_2R_2A_2(1-L_{02})$ , and

 $I_1$ ,  $I_2$  are output light intensities of the two light sources,  $R_1$  and  $R_2$  are the detectors responsivities,  $A_1$  and  $A_2$  are the amplifications of the electronic stages,  $L_{01}$  and  $L_{02}$  are the static long-term losses along the optical path in clockwise and anti-clockwise directions, L(t) represents the intensity loss induced by vibration which on the basis of the discussion in Section 6.2 is assumed equal in both directions, and  $\theta$  is a rotation of the linearly polarised light along the sensing medium, proportional to the measured current. Factor 1/8 in  $k_1$  and  $k_2$  comes from using two 2x1 couplers in the optical path.

It can be seen from Equations (6-5) and (6-6), that the terms responsible for the measurement are, due to the nonreciprocal nature of the magneto-optic Faraday effect, inverted in phase while the terms representing vibration are in phase. This phenomenon is used to cancel the vibration signal and preserve the measurement signal, both simultaneously present in the two separate channels. It is essential that  $k_1$  is equal to  $k_2$  for the above compensation scheme. This can be achieved by calibration of the electronics accomplished by adjusting the amplification of the respective photodetectors.

Terms  $k_1$  and  $k_2$  are also responsible for the long term stability of the system. If stable, good quality light sources, detectors and precision electronics are used (more details in Chapters 7 and 8), it is expected that the whole arrangement will perform correctly over the course of time within a certain error margin. Furthermore, the common mode changes in both channels will be compensated due to the symmetrical nature of the system. The components in both channels should have the same origin and similar long-term ageing characteristics. If these conditions are fulfilled, simple signal processing can be employed to derive the final measurement signal e, which is given by

$$e = \frac{e_2 - e_1}{e_1 + e_2} = \frac{2k(1 - L(t))(\sin 2\theta(t))}{2k(1 - L(t))} = \sin 2\theta(t)$$
 (6-7)

where  $k=k_1=k_2$ .

It is apparent from Equation (6-7) that the resultant measurement signal e is free from the vibration components present in e<sub>1</sub> and e<sub>2</sub>. A graphical illustration of the described compensation method is shown in Figure 6-8. It is also clear that the true dc component of the measurement field is preserved and present in the final signal.

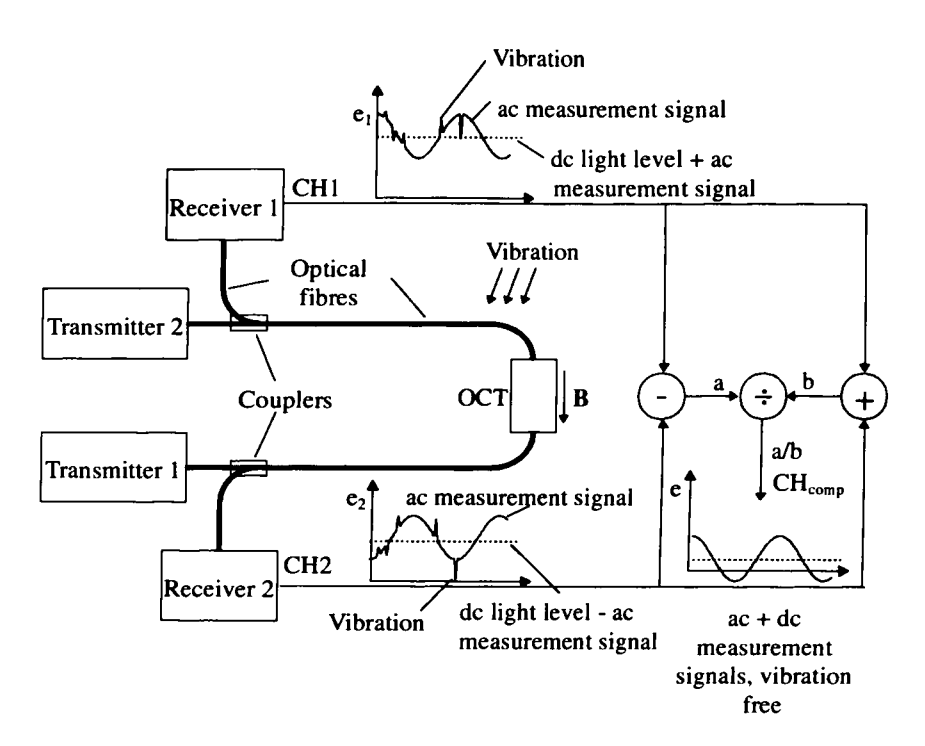


Figure 6-8 A graphical illustration of the proposed compensation method

To achieve improved longer term stability of the measurement and the same vibration compensation capability as in the system presented above, a slight modification of the signal processing block is required. The signals in the separate channels are normalised by dividing the initial signal by its dc component in each channel, in which case all the intensity fluctuations of the transmitter-receiver pair are compensated. This system can be used for high accuracy ac current measurement when a dc current measurement capability is not required. A graphical illustration of the vibration

compensation system with only ac current measurement capability, is presented in Figure 6-9.

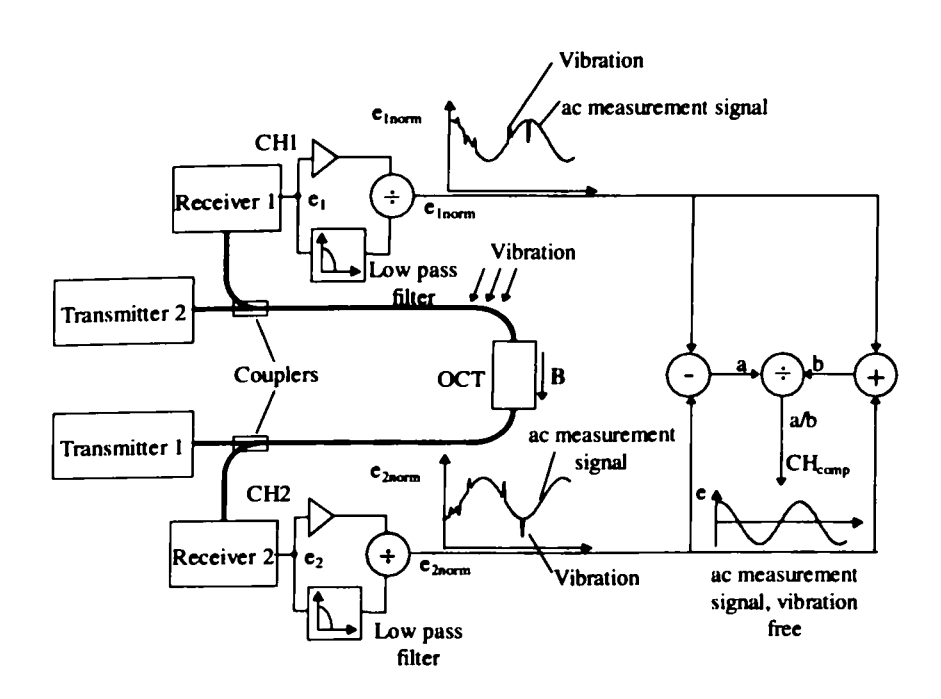


Figure 6-9 A graphical illustration of the ac current measurement vibration compensation system

In this configuration signals  $e_1$  and  $e_2$  remain the same, and  $e_{1\text{norm}}$  and  $e_{2\text{norm}}$  can be expressed as:

$$e_{1norm} = \frac{e_1}{e_{10}} = (1 - L(t))(1 - \sin 2\theta(t)),$$
 (6-8)

$$e_{2 \text{norm}} = \frac{e_2}{e_{20}} = (1 - L(t))(1 + \sin 2\theta(t)),$$
 (6-9)

where  $e_{10}$  and  $e_{20}$  are the dc components of respectively  $e_1$  and  $e_2$  while there are no dc components present in the measured current. It is clear from Equations (6-5) and (6-6), that in this case  $e_{10}$  and  $e_{20}$  are respectively equal to  $k_1$  and  $k_2$  and are derived via a low pass filter from the original signals. The final, vibration free ac measurement signal is given by

$$e = \frac{e_{2 \text{norm}} - e_{1 \text{norm}}}{e_{1 \text{norm}} + e_{2 \text{norm}}} = \sin 2\theta(t).$$
 (6-10)

# 6.3.3. Pulsed Operation of the System

Experimental investigation of the above system showed that the optical arrangement suffers from the problem of backward light propagation caused by Fresnel reflection due to connectors or other optical components in the transmission path. It has been confirmed that the magnitude of the reflected light can exceed the magnitude of the light transmitted through the optical path. This unwanted effect causes a partial, or in the worst cases total, saturation of the detectors and disables the correct operation of the system. As there are at least two connectors used in the current optical system between the coupler and the sensor, then an alternative philosophy had to be considered to achieve the conditions necessary for effective vibration compensation. To circumvent the problems associated with back reflection the transmitter and detector circuit operation was synchronised using high frequency alternate pulsing of the two light sources and triggering of the respective photodetectors. A block diagram of the basic vibration compensation arrangement is shown in Figure 6-10.

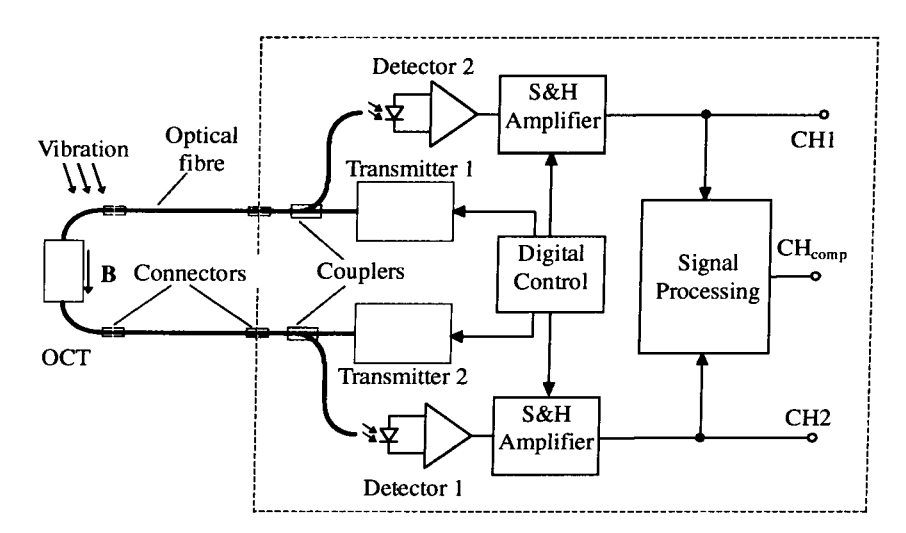


Figure 6-10 A block diagram of the basic vibration compensation arrangement

The above vibration compensation scheme can be realised using analogue signal processing techniques, however the preferred approach is to use real time digital signal processing techniques and implementing the above compensation scheme into the DSP software. This issue will be discussed further in Chapter 7, and the efficiency of the proposed vibration compensation scheme will be reported and discussed in Chapter 8.

# 6.4. Temperature Effect

The Verdet constant in paramagnetic and ferromagnetic magneto-optic materials is proven to be temperature dependent<sup>9-13</sup>. This effect is negligible in diamagnetics, however, in these cases the Verdet constants are too small to build sensitive enough point type optical current sensors. As the sensors developed within this research work employ paramagnetic active materials, i.e., TGG and FR5, it is particularly interesting to derive a general temperature characteristic of the Verdet constant for the paramagnetic materials.

In Chapter 3 the magneto-optic Faraday effect was explained on the basis of the classical physics. Although, the classical model was sufficient to provide the basic description of the above phenomenon, it was incapable of explaining the temperature dependency of the Verdet constant. In 1960s and 1970s several researchers<sup>14-16</sup> attempted to provide more accurate models of the Faraday effect phenomenon on the basis of the quantum physics. These models are in a good agreement with the experimental data obtained for various paramagnetic magneto-optic materials<sup>11, 12, 17</sup>.

According to the above references, the plane of polarisation of the linearly polarised light rotates by an angle  $\theta$  when light of wavelength  $\lambda$  passes through a unit length of a sample at temperature T in a magnetic field H given by  $^{14-16}$ 

$$\theta = AH + BH + C(H, T) \tag{6-11}$$

The angle of rotation can be either positive or negative depending on the relative sizes of A, B and C. By convention, the material in which the angle of rotation is clockwise for light propagation along the direction of the magnetic field (positive angle) is called diamagnetic, while the opposite case (negative angle) represents a paramagnetic material.

In addition, as shown in Chapter 3, the angle of rotation increases as the wavelength of light approaches the electronic absorption peak, which applies to all materials.

In Equation (6-11), A involves electronic transitions in which the ground state is nondegenerate and results in a diamagnetic contribution. B arises from the mixing of energy levels by the magnetic field and gives a temperature-independent paramagnetic term. C arises from transitions from a degenerate ground state to an excited state which may or may not be degenerate. Since the resulting transition probabilities depend on the relative thermal populations of the ground states, this paramagnetic term is temperature dependent.

If the ground state can be characterised by an atomic nSLJ state, the angle of rotation can be written as 16,18

$$\theta = a_0 B_1(x) + b_0 H$$
, (6-12)

where  $B_J(x)$  is the Brillouin function,  $x = Jg\mu_B H/kT$ , J is the angular momentum quantum number, g is the Lande splitting factor,  $\mu_B$  is the Bohr magnetron, k is the Boltzmann constant, and T is the temperature. Note that  $b_0$  combines both A and B from Equation (6-11) and can have either the same or opposite sign as the first term in Equation (6-12).

At high temperatures or low magnetic fields, the Brillouin function can be expanded<sup>19</sup> to give the following simplified expression for the angle of rotation:

$$\theta = \frac{a_0(J+1)g\mu_B H}{3kT} + b_0 H. \tag{6-13}$$

This result is the more familiar relationship for the Faraday rotation angle:

$$\theta = V_0 H, \qquad (6-14)$$

where  $V_0$  is the Verdet constant. Under this approximation, the Verdet constant  $V_0$  can be defined as

$$V_0 = \frac{a_0(J+1)g\mu_B}{3kT} + b_0.$$
 (6-15)

Note that all equations have been normalised to a unit sample length. The above equation may be fitted to the experimental data obtained for different paramagnetic materials and different wavelengths. For known J and g which depend on particular doping of the material with ions, e.g., terbium ions, the constants  $a_0$  and  $b_0$  can be found experimentally<sup>12,17</sup>. This is done by measurement of the optical rotation for the fixed and known sample temperature and changing magnetic field.

# 6.5. Temperature Compensation

In the previous section it was stated that the Verdet constant of paramagnetic materials depends on both the wavelength and temperature. The former dependency can be ignored as the wavelength variation of the light source (LED in this case) is assumed insignificant for the device expected to operate at approximately constant temperature and drive current. However, the temperature dependency of the Verdet constant requires compensation since the OCT can be exposed to changing temperature conditions in a range between -40 and 100°C as specified in Chapter 5.

The Verdet constant in paramagnetics, similarly with Equation (6-15), has the following general temperature characteristic:

$$V = \frac{a}{T} + b$$
, (6-16)

where a and b are coefficients which replace all the constants in Equation (6-15) and additionally include material permeability.

The Verdet constants of the two materials chosen for the construction of prototype OCTs (i.e., TGG and FR5) were estimated for two wavelengths (633 and 850nm) from data supplied by the manufacturer and verified by experiment as 11,12

 $V_{TGG}(633nm) = 2.810 \times 10^6 / T - 2.694 \times 10^3 \text{ deg/(Tm)}$ 

 $V_{TGG}(850nm) = 1.347 \times 10^6 / T - 1.225 \times 10^3 \text{ deg/(Tm)}$ 

 $V_{FR5}(633 \text{nm}) = 1.853 \times 10^6 / \text{T} - 1.708 \times 10^3 \text{ deg/(Tm)}$ 

 $V_{FR5}(850 \text{nm}) = 0.767 \times 10^6 / \text{T} - 0.458 \times 10^3 \text{ deg/(Tm)}$ 

The above Verdet constants are plotted against temperature as shown below in Figure 6-11.

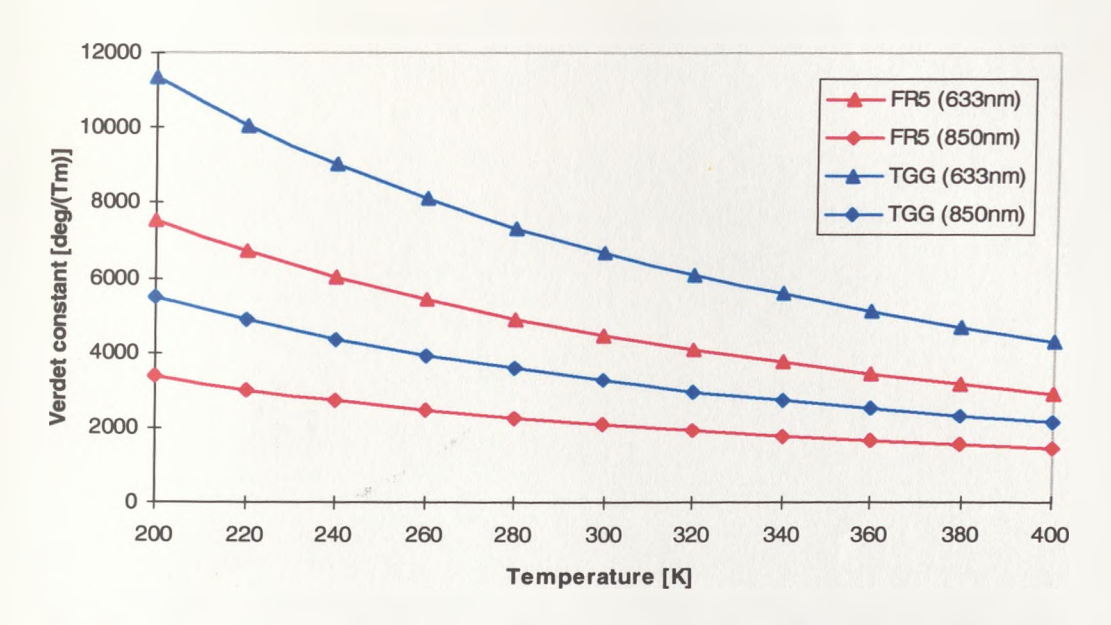


Figure 6-11 Variation in Verdet constants with temperature for TGG and FR5 materials

From Figure 6-11 it is clear that the Verdet constant reaches the highest value for the TGG material and 633nm wavelength, and the lowest value for the FR5 material and 850nm wavelength. The closer inspection of the above data also reveals, that the percentage change of the Verdet constant significantly differs for different materials and/or different wavelengths even within one material. This feature could potentially be used in indirect recovery of the material temperature using two different wavelengths to interrogate the sensor. However, there is a concern that the temperature recovery precision may not be sufficient in this case due to the limited resolution of the demodulation process, which is especially critical at low current levels. This argument is in agreement with an option of a direct temperature measurement using a reliable optical temperature sensor. In order to decide which solution is better, first it is necessary to estimate an impact of the temperature measurement precision on the OCT performance. This is examined in detail in the following section.

#### 6.5.1. Impact of the Temperature Measurement Precision on OCT Performance

The precision with which the temperature of the sensing element must be known to satisfy the OCT accuracy specifications for the particular material/wavelength combination can be estimated by calculating a relative difference in Verdet constant as the temperature T changes by a factor δT representing a small error in temperature. This is shown in Figure 6-12 for the two extreme temperatures (200 and 400K) between which the OCT is designed to operate. The errors reach higher values at 200K due to the higher slope of the Verdet constant curves at this temperature. The Verdet constant errors calculated for the four above material/wavelength combinations are compared with the OCT accuracy specifications.

Figure 6-12 reveals, that the demand for the accurate information about the temperature varies slightly between the particular material/wavelength combinations. The line representing the FR5 material interrogated with 850nm wavelength indicates more relaxed requirements on temperature measurement precision as compared to the

rest of the material/wavelength alternatives. Again, this is due to the lowest temperature dependence of this particular material/wavelength combination.

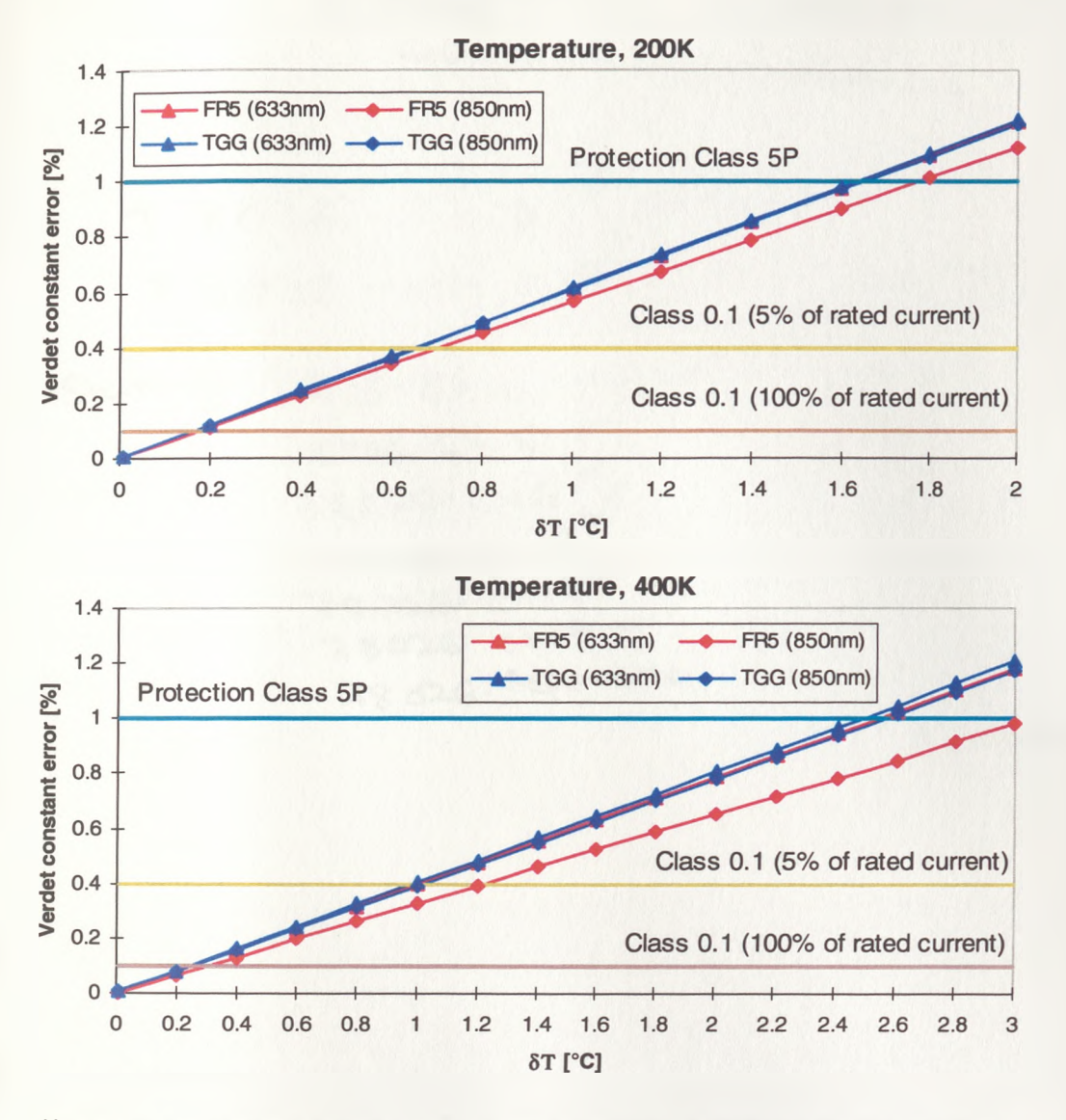


Figure 6-12 Verdet constant error vs. temperature measurement precision, δT

From Figure 6-12 it can be seen, that in order to satisfy the protection class 5P specification, the temperature of the sensing element should be known to approximately 1.6°C and 2.4°C for operating temperatures of 200K and 400K respectively. For the metering class 0.1 specification, the temperature should be known to approximately 0.15°C for a nominal current, and 0.6°C for 5% of the nominal current for the operating temperature of 200K. For the operating temperature of 400K, these figures are 0.24°C and 0.9°C respectively. The above calculations may

be extended for a range of the other OCT accuracy specifications quoted in Chapter 5, however these two extreme cases are sufficient to carry out the remaining part of the analysis.

#### 6.5.2. Indirect Recovery of Sensor Temperature

If the sensor is interrogated by two different optical wavelengths, the respective Faraday rotations can be expressed as follows

$$\theta_1 = BL \left( \frac{a_1}{T} + b_1 \right) \tag{6-17}$$

$$\theta_2 = BL\left(\frac{a_2}{T} + b_2\right). \tag{6-18}$$

In order to extract temperature T from the above equations, the rms values of rotations  $\theta_1$  and  $\theta_2$  must be first calculated. This can be done under the assumption that the magnetic field B representing the busbar current is a periodic signal with a period  $\tau$ :

$$\theta_{1\text{rms}} = \sqrt{\int_{0}^{\tau} \left[ BL \left( \frac{a_1}{T} + b_1 \right) \right]^2 dt} = L \left( \frac{a_1}{T} + b_1 \right) \cdot \sqrt{\int_{0}^{\tau} B^2 dt}$$
 (6-19)

$$\theta_{2\text{rms}} = \sqrt{\int_{0}^{\tau} \left[ BL \left( \frac{a_2}{T} + b_2 \right) \right]^2 dt} = L \left( \frac{a_2}{T} + b_2 \right) \cdot \sqrt{\int_{0}^{\tau} B^2 dt} . \tag{6-20}$$

For  $\theta_{1\text{rms}}$ ,  $\theta_{2\text{rms}} > 0$ , these two equations can be solved for T, yielding:

$$T = \frac{\theta_{1\text{rms}} a_2 - \theta_{2\text{rms}} a_1}{\theta_{2\text{rms}} b_1 - \theta_{1\text{rms}} b_2}$$

$$(6-21)$$

This value of temperature can be inserted in one of Equations (6-17) or (6-18), which gives the temperature compensated value of the rotation and can be scaled to obtain the instantaneous busbar current.

The two-wavelength temperature compensation mechanism could be relatively easily implemented using for example the 650nm and 850nm spectral windows as shown in Figure 6-13. As the detectors respond to the non-respective wavelengths, the two channels must be time gated, similarly as in the vibration compensation scheme. There is also a possibility of using only one photodetector by selecting a photodiode optimised for both wavelengths.

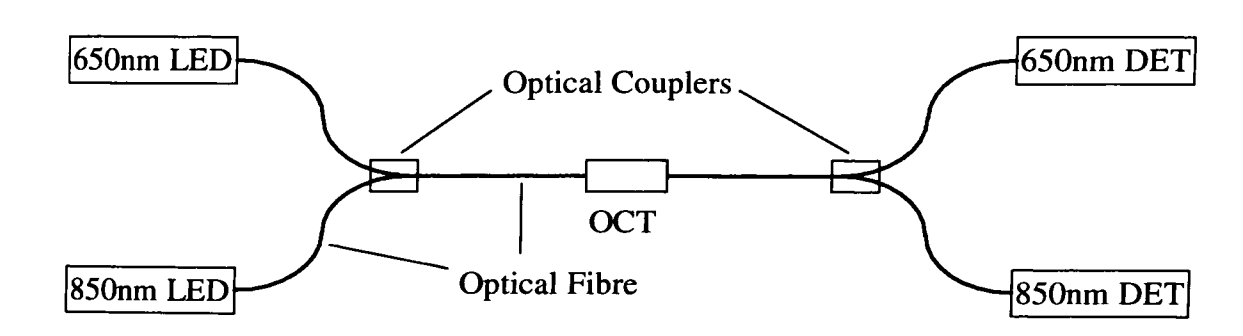


Figure 6-13 Two-wavelength temperature compensation scheme

The above temperature compensation scheme makes a very attractive solution since the exact temperature of the sensing element can be potentially recovered. There is no need for an additional optical device to perform the temperature measurement of the sensor. The scheme could be potentially implemented using already developed OCT monitoring system with minor modifications. However, in the above scheme, the temperature is recovered using two signals which are already subject to a measurement error. Additionally, the  $a_1$ ,  $a_2$  and  $b_1$ ,  $b_2$  coefficients of the material Verdet constants, at the two considered wavelengths, are also subject to experimental errors. All these errors will affect the precision with which the temperature information can be recovered, and should be accounted for in the final OCT performance assessment.

The net effect on the precision with which the temperature can be recovered using the two wavelength interrogation scheme have the rotation recovery errors which are closely related to the photodetector noise performance. The lower the photodetector noise floor the lower values of rotation (current) can be detected, and the higher precision of the temperature recovery can be obtained. To illustrate the sensitivity of the indirect temperature recovery process to the polarisation rotation recovery errors, the precision with which the temperature can be measured was calculated for the changing current. The calculations were carried out for the two extreme temperatures, the same as in the previous analysis. This is illustrated in Figure 6-14 for the two sensors developed during the research work programme, namely: 25mm TGG crystal based OCT, and the FR5 glass based reflective multi-pass device with an active optical path length of 100mm (as described in detail in Chapter 5).

In the calculations it was assumed that the sensors are interrogated by the two wavelengths as in the analysis from the previous section, and that the polarisation rotation can be recovered with a precision of up to 100µdeg. This level of precision is very difficult to achieve for the instantaneous value of rotation even when using the refined design of the photo-receiver circuit (more details in Chapter 8). Note, however, that it is not the instantaneous value but the rms value of rotation from which the temperature information is recovered. The process of calculating the rms value of a signal involves integration over a signal period, which improves the signal-to-noise ratio. In order to improve even more the precision with which the rotation is recovered, the rms value of rotation can be averaged over a longer period of time (i.e., seconds). The temperature change of the sensing element follows a relatively long process of a heat transfer through the sensor housing, hence the long averaging time would not necessarily deteriorate the OCT accuracy. It is believed that using this technique it is possible to recover the polarisation rotation with a precision of up to 100µdeg.

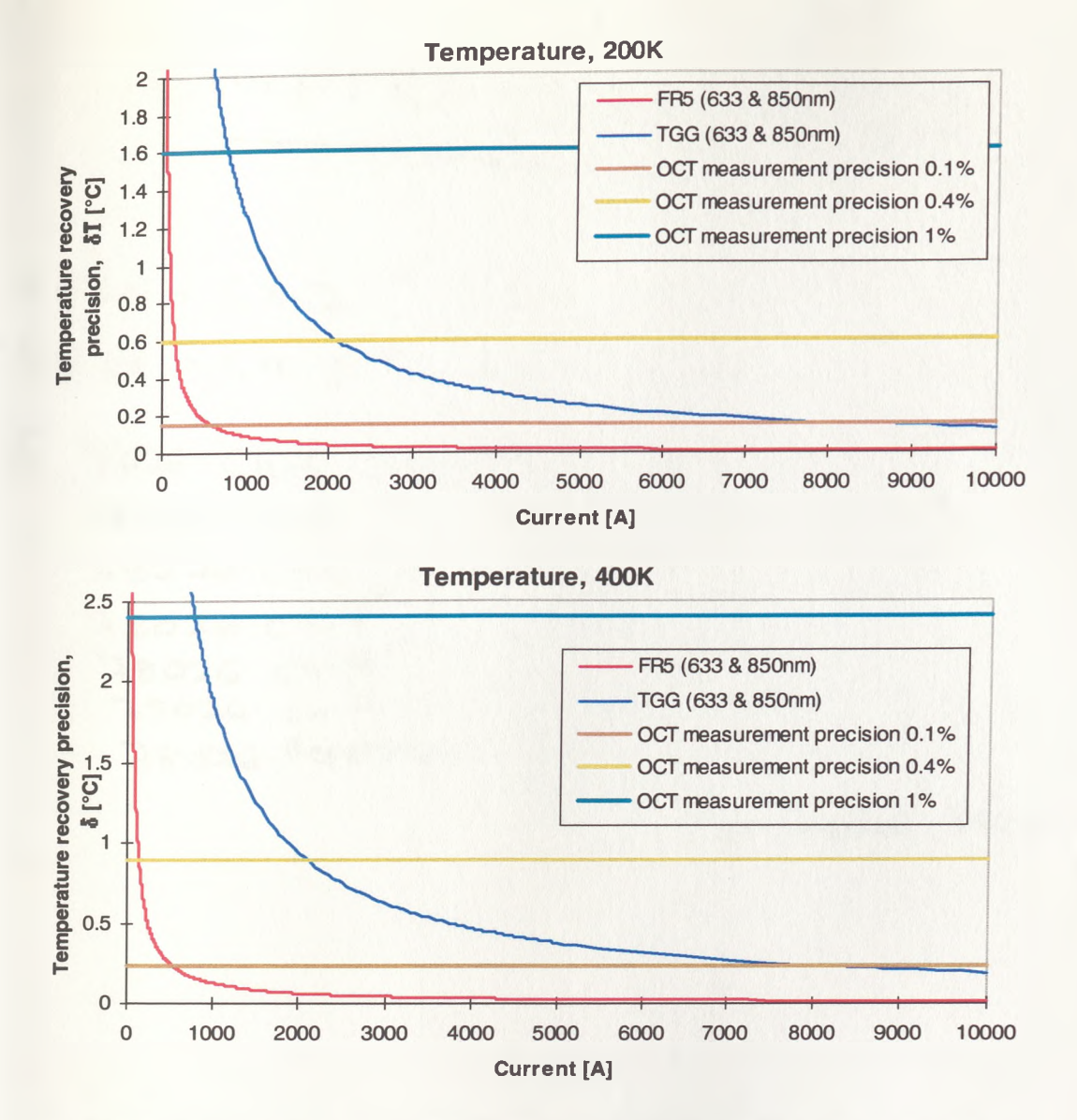


Figure 6-14 Precision of indirect temperature recovery process using two wavelengths,  $\delta\theta = 100\mu deg$ 

From Figure 6-14 it can be seen that less than 60Amps (FR5 sensor) and 800Amps (TGG sensor) is required to recover the temperature with a precision adequate to perform a current measurement with an accuracy better than 1% (protection specification). Note, that only temperature induced errors are considered in this discussion; other errors, i.e., vibration induced noise and magnetic cross-talk would have to be compensated to the same level at the considered current value. In practical applications however, the rated currents of the above sensors could be much higher as they exhibit dynamic ranges of approximately 40kA (FR5 sensor) and 100kA (TGG

sensor). For the FR5 sensor an optimum rated current would be around 1kA and for the TGG sensor 3kA if they were used as the 5P30 protection transducers.

Considering the metering Class 0.1 accuracy requirements, the temperature can be recovered to meet the 0.4% accuracy specification (the level of 5% of the rated current) at the currents of approximately 150A and 2100A for the FR5 and TGG sensors respectively. This implies, that the rated currents for these sensors should be 3kA and 42kA respectively. In this case it would even be possible to use the FR5 sensor as a combined metering and protection device classified as Class 0.1 and 5P10 current transducer. This however could not be achieved for the 25mm TGG sensor.

The above analysis can be extended to the remaining accuracy specifications (as quoted in Chapter 5), however, due to the multitude of the possible cases, each particular application should be considered separately. The aim of this section is to demonstrate the methodology of performing the required analysis, and prove that the indirect temperature recovery process can be successfully used in some specific cases.

#### 6.5.3. Direct Recovery of Sensor Temperature

The indirect temperature recovery process has a major drawback which is very difficult to overcome in some specific practical cases. This occurs when the current level drops for a long period of time below the value which allows a sufficient temperature recovery precision, or when the measured current fades completely. Under such circumstances, after the normal current level is restored, the device ability to meet the accuracy demand is lost for a period that is necessary to regain the ability of the sufficient temperature recovery precision. This can last for a number of seconds, depending on the averaging process applied. If there is a need for detecting the instantaneous value of current straight after a long period of zero current (e.g., awaiting for short-circuit current tests), and the "wake up" time of the measurement system is too long, the measured current signal will be impaired with an error.

In such cases a direct temperature measurement only should be applied which provides a constant temperature information, independent of the current. To sustain all the advantages of the optical fibre technology, the temperature sensors must be realised using all optical solutions. The next sections will describe two such devices based on two different optical techniques to directly measure the temperature.

#### 6.5.3.1. Bragg Grating Temperature Sensor

Bragg gratings are periodic variations in refractive index written into the fibre core using an ultra violet laser<sup>20,21,22</sup>. The process is illustrated in Figure 6-15 which indicates how the angle of intersection of the two beams is used to determine the centre wavelength of the grating (see Figure 6-15).

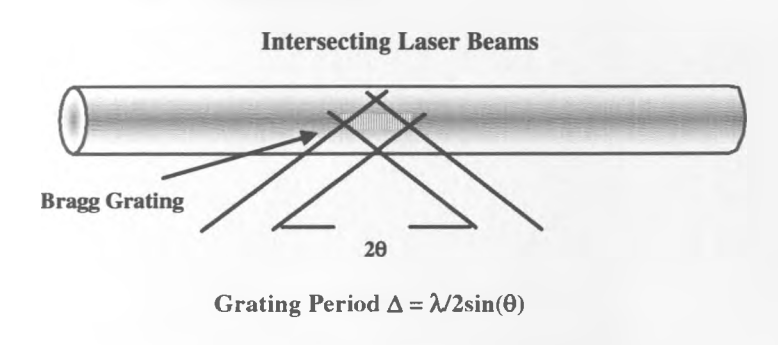


Figure 6-15 Fibre Bragg grating manufacture process

Fibre Bragg Gratings (FBGs) are interrogated using a wide band optical source as shown in Figure 6-16. The grating reflects the portion of light guided within a fibre at the wavelength that is twice the optical spacing between high-index and low-index regions (grating spacing).

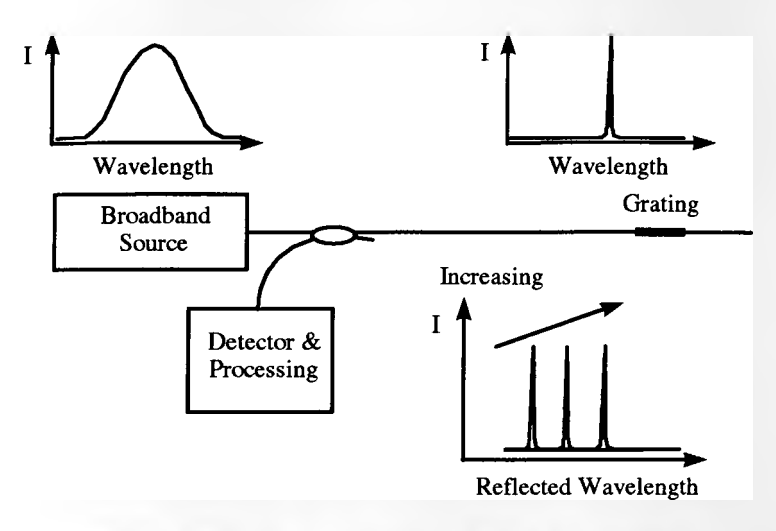


Figure 6-16 Bragg Grating Sensor Operation

Changes in local temperature modulate the grating period and therefore change the wavelength which is reflected and transmitted back up the fibre. Measuring the return wavelength accurately allows temperature, pressure or strain fields at the location of the FBG to be readily determined. The measurement is performed by determining the wavelength change using various interrogation techniques, e.g., scanning Fabry-Perot or acousto-optic filter<sup>22</sup>.

The precision with which the temperature can be determined using the fibre Bragg grating technology<sup>24</sup> can be better than 0.1°C. This is sufficient for the FBG to be used with the OCT device developed within this research work for both protection and metering applications. However, it should be stressed, that the present commercial FBG systems may be expensive. In addition, the single-mode fibre technology used in those systems is not compatible with the multimode fibre technology of the OCT design. Nevertheless, the fibre Bragg grating temperature measurement system has been put on trial with the present OCT. More details about the practical implementation of the above system will be provided in Chapters 7 and 8.

### 6.5.3.2. Absorption Glass Temperature Sensor

Wavelength modulation techniques, as presented in Chapter 4, can be potentially exploited in temperature sensing. This approach can be realised using specially

designed sensing heads incorporating spectral filters which change their characteristics with temperature. In the present section a concept of the optical temperature sensor based on the above techniques is provided, and the potential of applying this solution as a means for the OCT temperature compensation is investigated.

Some colloidally or ionically coloured glasses<sup>24</sup>, used as spectral filters, exhibit sufficient thermal change of a spectral response to be exploited as active mediums in temperature sensors. Thanks to their excellent transmission characteristics in the transmission band they can be used with multimode optical fibres and standard LEDs. There is a vast resource of commercially available glass filters which are relatively cheap. Consequently, the combination of the later with the multimode technology provides an inexpensive final sensor product as compared with the competitive optical solutions.

The basic concept of an absorption glass temperature sensor is presented in Figure 6-17. The sensor head consists of a piece of colloidally coloured glass placed between two GRIN lenses. The selected long-pass absorption filter has a temperature dependent spectral response which is matched to the used LED. The position of the absorption edge of the filter at the minimum specified temperature, T<sub>min</sub>, allows for the approximately whole LED spectrum to be transmitted through the sensor. As the temperature increases the filter absorption edge moves towards longer wavelengths and less light is transmitted through the sensor. This is detected by the photodetector (DET 1) (see Figure 6-17). The second photodetector (DET 2) is blocked by an additional, temperature independent, long-pass absorption filter, and detects only the upper fraction of the LED spectrum. This fraction of the spectrum is unaffected by the operation of the sensor up to the maximum specified temperature, T<sub>max</sub>. The two photodetectors track any change in optical power loss, hence by normalising DET 1 signal to DET 2 signal, the temperature dependent output may be produced, which is unaffected by the optical loss change.

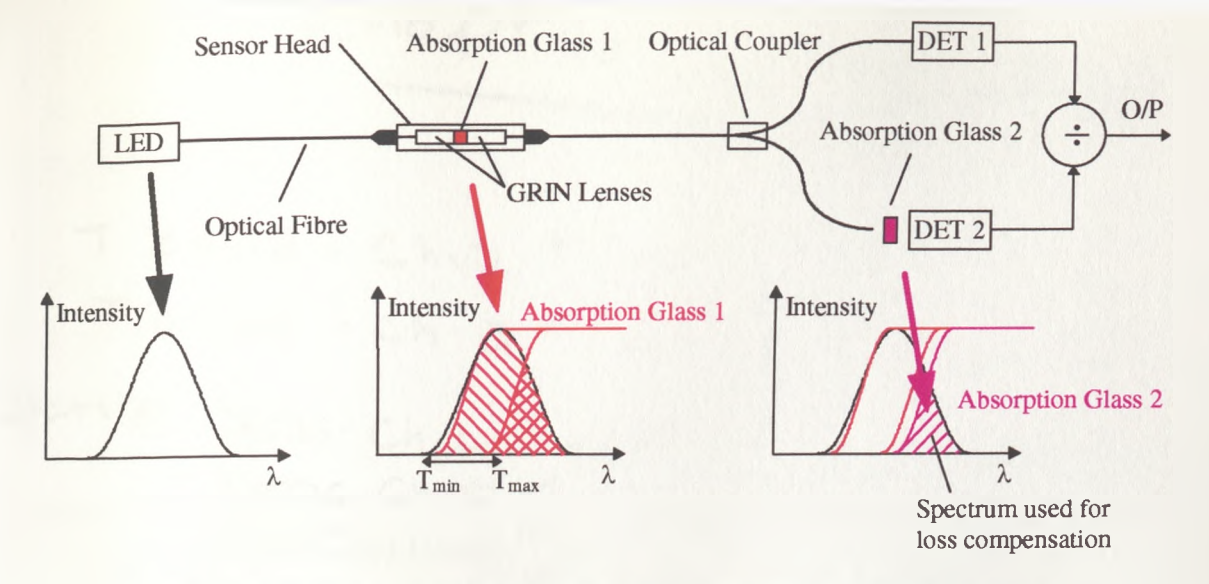


Figure 6-17 Basic concept of absorption glass temperature sensor

In the above system, the dc performance of the photodetectors will have the most effect on the long term accuracy performance of the temperature measurement process. However, due to the low bandwidth which is required in this application, ultra high precision op-amps can be employed in the photo-receiver circuits, and sufficient long term stability can be readily achieved. At present the experimental evaluation of the above concept is carried out in the laboratory conditions, and the initial results are encouraging<sup>25</sup>.

In addition, due to the compatible optical technology applied, the discussed optical temperature sensor can be readily incorporated into the present optical current sensor system. The temperature output signal from the above opto-electronic interrogation scheme must be linearised and scaled, and the temperature sensor must be calibrated before using it to determine the OCT temperature. This can be achieved using digital signal processing facility by storing the sensor calibration function in a look-up table and performing the correction of the sensor output in real time.

# 6.6. Magnetic Cross-Talk Effect

In Chapter 5, it was stressed that the Faraday cell type OCT has a drawback consisting in measuring only a small sector rather than the whole contour integral of

the magnetic field around the current carrying conductor. Consequently, precautions are necessary to avoid any disturbance (cross-talk) from magnetic fields other than that to be determined, mainly from the two other phase currents.

The Faraday rotation can only be induced if the magnetic field is parallel to the direction of light propagation within the sensing element. Hence, the magnetic crosstalk can be minimised if the conductors of the 3-phase current transmission system are positioned in one plane as shown in Figure 6-18. In this case the lines of magnetic field from the neighbouring conductors are approximately orthogonal to the direction of light propagation within the sensing element, which results in the lowest cross-talk.

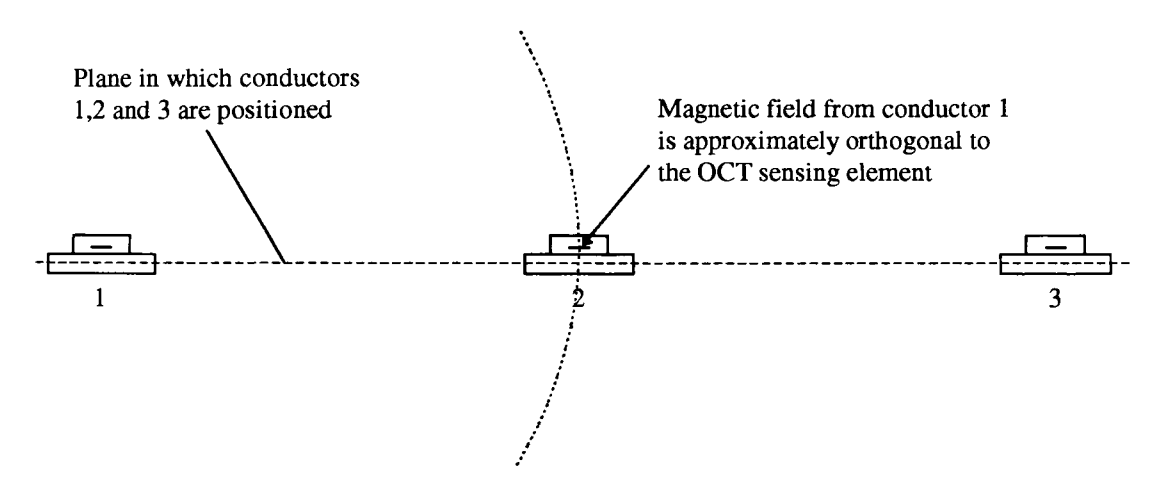


Figure 6-18 Minimal cross-talk for conductors positioned in one plane

While this arrangement may be adequate in cases where the separation distance between the conductors is large, there will always be a small field component from the neighbouring conductors which is parallel to the sensing element. This component introduces errors which become increasingly significant for other geometries or cases where the separation distances are too small.

A simple model of the magnetic field distribution around an infinitely long, and infinitely thin, conductor placed in vicinity of the sensing element (as shown in Figure 6-19) is sufficiently accurate to derive broad conclusions with respect to the significance of cross talk on the measurement process. In the present section this is carried out for a range of representative conditions.

The magnetic flux density B at the distance r from such a conductor can be expressed according to the following formula  $^{26}$ 

$$B = \frac{\mu_0 I}{2\pi r} \tag{6-22}$$

where,  $\mu_0$  is the permeability of the vacuum and I is the current flowing through the conductor.

Vector **B** of the magnetic field crossing the sensing element at any point of its length L may be decomposed into the orthogonal  $\mathbf{B}_h$  and parallel  $\mathbf{B}_x$  components as shown in Figure 6-19.

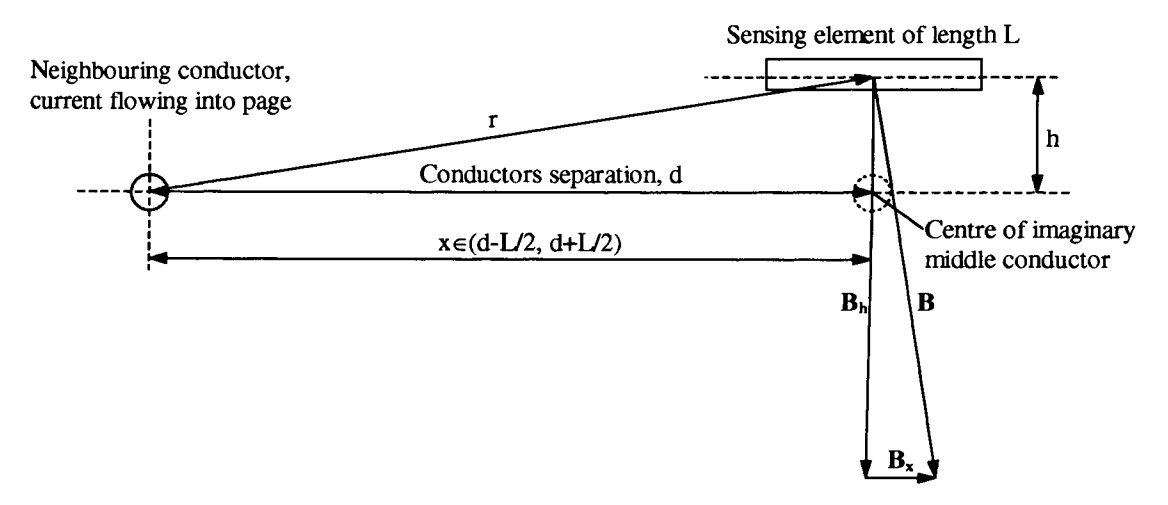


Figure 6-19 Geometrical evaluation of the parallel field component  $\mathbf{B}_{\mathbf{x}}$ 

The average value of the parallel field component,  $B_{average}$ , may be calculated by integrating  $B_x$  along the length L of the sensing element for x changing from d-L/2 to d+L/2 and dividing the result by L:

$$B_{\text{average}} = \frac{\int\limits_{d-L/2}^{d+L/2} B_x dx}{L}$$
(6-23)

Considering Equation (6-22) and substituting r with  $\sqrt{h^2+x^2}$  ,  $B_x$  may be expressed as

$$B_{x} = \frac{\mu_{0}I}{2\pi\sqrt{h^{2} + x^{2}}} \sin \tan^{-1} \left(\frac{h}{x}\right)$$
 (6-24)

The solution to Equation (6-23) may be presented in the following form

$$B_{\text{average}} = \frac{\mu_0 I}{2\pi} \cdot \frac{\tan^{-1} \left[\frac{d + L/2}{h}\right] - \tan^{-1} \left[\frac{d - L/2}{h}\right]}{L}$$
(6-25)

The above equation reveals that the magnetic field which causes the undesirable sensor response (cross-talk) depends on the three main factors:

- the current I flowing through the neighbouring conductor;
- the conductor separation d;
- the distance between the sensing element and the centre of the imaginary middle conductor h.

The factor h is a sum of half the conductor thickness and the distance between the sensing element and the bottom of the sensor head, assuming that the sensor head is mounted on top of the conductor. To obtain quantitative information for the purposes of comparison, three common bus bar configurations have been considered and the influence of cross talk evaluated for an arbitrary nominal current rating of 1000A.

Figure 6-20 depicts the simulated magnetic cross-talk defined by Equation (6-25) versus conductors separation distance for different factors h. These three different factors h, namely: h\_rect, h\_cyl and h\_hol are characteristic of the three conductor

types commonly used in high voltage transmission systems, as considered earlier in Chapter 5 (Figure 5-21). In each of the cases it is assumed that the current I flowing through one of the neighbouring conductors is equal to 1000A which is an assumed rated current. The length L of the sensing element is equal to 25mm which is typical of the sensors that have been fabricated during the research work programme.

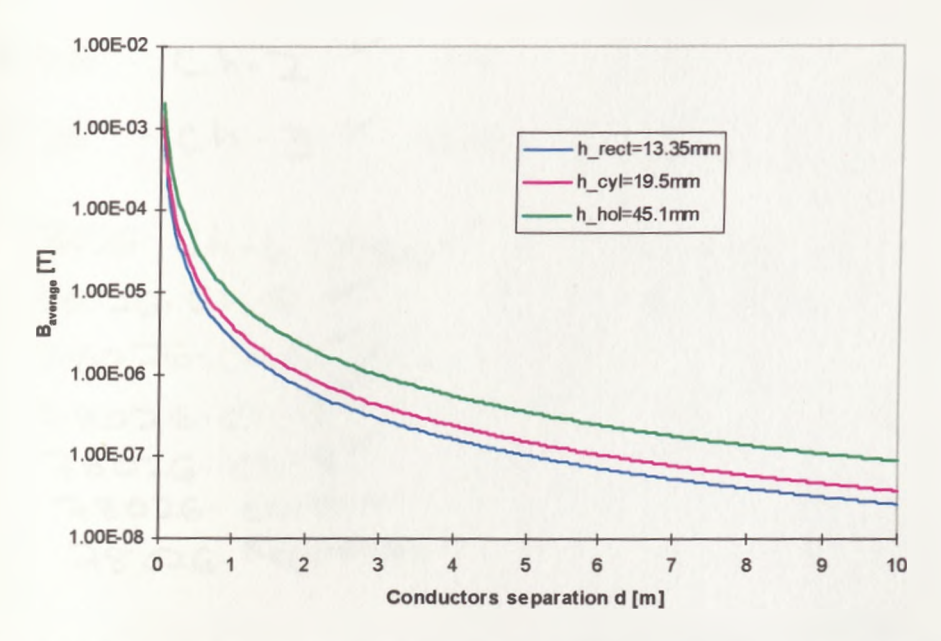


Figure 6-20 Magnetic cross-talk vs. conductors separation distance for different h factors

From Figure 6-20 it is apparent that the magnetic cross-talk drops dramatically with the increasing conductors separation distance and the decreasing factor h (note the logarithmic scale of the vertical axis).

It is interesting to compare the above magnitudes of cross-talk with the respective magnetic flux densities along the sensing element resulting from the three considered conductor geometries, as modelled in Chapter 5. This allows errors similar to those that may occur in the real transmission system to be estimated. From Chapter 5, using the magnetic field modelling software 'Oersted', the three practical cases of the magnetic field distribution were modelled for 50Hz rms current of 1000A and the following values of the magnetic field density along a longitudinal cross-section of the sensing element obtained:

- rectangular busbar 4.04mT;
- cylindrical conductor 9.07mT;
- hollow conductor 4.28mT.

According to the OCT accuracy specifications presented in Chapter 5 the measurement error at 5% of the rated current should not exceed the value of 0.4% for Class 0.1 current transducer. To assess the impact of cross-talk, the cross-talk resulting from current of 1000A passing through an adjacent conductor (Figure 6-20) is compared to the simulated magnetic flux density corresponding to 5% of the rated current, i.e., 50A flowing in the conductor equipped with the OCT. The rms value of these signals is compared in Figure 6-21. Here the phase relationship between the adjacent bus bar currents has been ignored and the analysis therefore represents a worst case scenario where the cross talk signal adds directly to the signal being measured. Figure 6-21 indicates the variation of this worst case error as a function of the conductor separation distance as simulated for the three earlier considered conductor geometries.

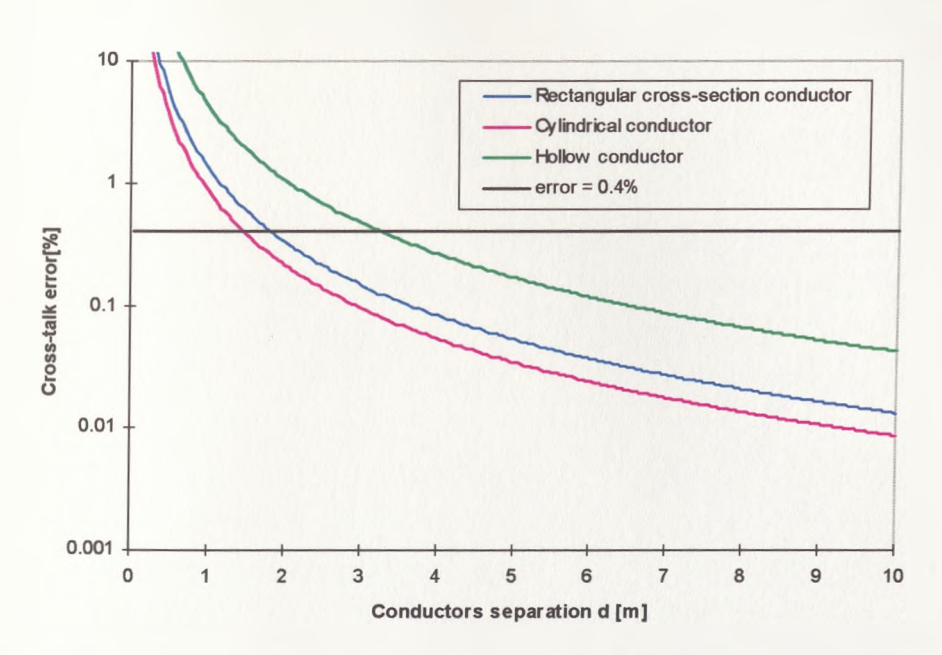


Figure 6-21 Simulated Cross-talk error vs. conductors separation for metering OCT

Clearly these calculations indicate that the cross talk influence is significant in all cases. In terms of the optimum bar geometry (a rectangular conductor) the busbar

separation must be greater than 1.5 m before the metering class performance specification is met. Even greater distances (up to 3 m) are required for other busbar types. For high voltage installations this might be a practical solution. However there are clearly many instances where the conductor separation will be insufficient and the operational requirements will not be met.

To complete the analysis, a similar exercise was carried out for the protection class current transducer 5P30. The accuracy specification requires from this device at least 1% accuracy at the rated current, e.g., 1000A, whereas the current in the neighbouring conductor may reach at least 30kA at an instance of fault. Such a theoretical situation may be exaggerated as faults occur very rarely, however the accuracy specification for current instrument transformers does not permit exemptions even during the fault condition. Figure 6-22 depicts the simulated cross-talk error vs. conductors separation for protection OCT. Again it is clear that the separation distance between the conductors must be very large in order to meet the specified accuracy requirements.

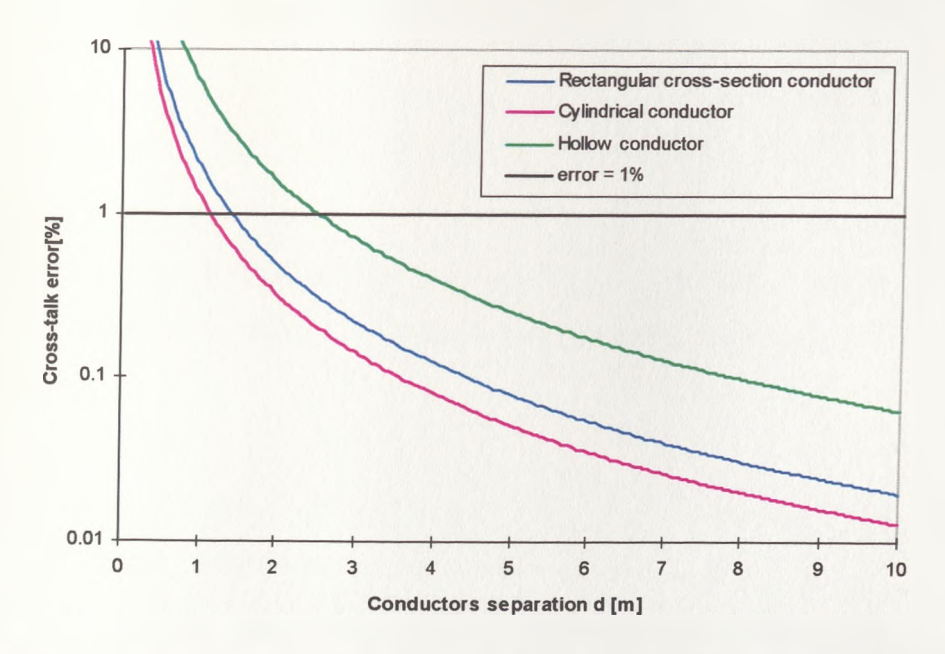


Figure 6-22 Simulated Cross-talk error vs. conductors separation for protection OCT

The cross-talk problem is even worse for 3-phase transmission systems in delta configuration as it takes place in high voltage Gas Insulated Switchgears (GIS)

(Figure 6-23) where the conductor spacing is reduced with the use of the gas insulating layer. In this case the parallel straight field component between neighbouring conductors (the cross-talk) is much higher than in the transmission systems fixed in one plane. Consequently, without compensation, the use of point type OCTs in this application is impractical.

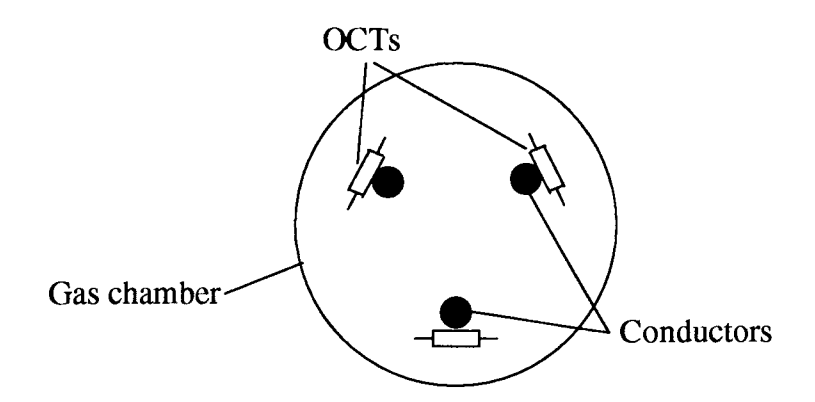


Figure 6-23 Three-phase, high voltage GIS, current measurement chamber

#### 6.7. Cross-Talk Compensation

As shown in the previous paragraph, magnetic cross-talk can be minimised using flat conductors fixed in one plane and separated from each other at the highest possible distance. In many cases however, the conductors separation distance of at least 3 meters is not acceptable. Moreover, the use of conductors arrangements other than in one plane, e.g., delta arrangements in gas insulated switchgears, produces much higher cross-talks which further compromise the measurement accuracy in each phase of the OCT system.

Some attempts have been made to investigate the potential for shielding each individual sensor from the influence of the other conductors using various magnetic materials<sup>27,28</sup>. However this work was not successful since the required magnetic screen thickness was too great in order to significantly decrease penetration of the relatively low frequency fields (50 or 60Hz in most cases). The use of thick shielding

inhibits the main advantages of the optical technology, i.e., small size and light weight of the device, and further compromises the electrical insulation requirements.

For these reasons, an alternative philosophy must be considered for current measurement systems consisting of more than one phase and utilising point type OCTs. In this work a novel active compensation method is proposed which can effectively cancel any magnetic cross-talk from the neighbouring phase conductors.

The compensation method consists in solving in real time the set of linear equations, each representing the instantaneous output signal from one phase current sensor. The equations are created using calibration factors which can be evaluated for the particular conductors arrangement using experimental or analytical methods. The solution of the above set of equations gives the number of sought instantaneous values of currents flowing through the number of conductors in the considered conductors arrangement.

#### 6.7.1. The Principle of Compensation

The compensation procedure is best illustrated through a specific example. Considering the case of a three phase transmission system with conductors arranged in one plane, it may be assumed that the current sensor is placed on top of the first conductor as shown in Figure 6-24. For the case when current flows in conductor 1, and the remaining conductors are imaginary (or they are opened circuits), the output signal  $e_1$  from OCT1 is equivalent to the instantaneous current  $i_1$  multiplied by the calibration factor a, as shown in Figure 6-24 (a). Factor a may be calculated as the proportion  $E_1/I_1$ , where  $E_1$  and  $I_1$  are measured rms values of  $e_1$  and  $i_1$  respectively.

Alternatively, calibration factor a may be evaluated using numerical solutions of the magnetic field distribution  $B_{\rm II}$  across the length of the sensing element L (alike in Chapter 5, using magnetic field modelling software). In this case factor a may be expressed in the following form

$$a = \frac{E_1}{I_1} = \frac{E \cdot \theta(B_{11})}{I_1} = \frac{E \cdot B_{11}LV(T_0)}{I_1}$$
 (6-26)

where, E accounts for all signal processing procedures, i.e., vibration compensation, temperature compensation, linearisation of the sensor response characteristic, etc., and is known for the particular signal processing applied;  $I_1$  is the rms current in conductor 1 for which  $B_{II}$  is determined;  $\theta(B_{II})$  is the Faraday rotation; and  $V(T_0)$  represents the Verdet constant at the reference temperature  $T_0$  (temperature compensated and uncompensated signals are equal at  $T_0$ ).

By analogy, the remaining calibration factors b and c (see Figure 6-24 b and c) may be determined using either experimental or numerical methods. As a result, for currents  $i_1$ ,  $i_2$  and  $i_3$  flowing in the respective conductors the instantaneous output signal from OCT1 can be expressed as shown in Figure 6-24 (d).

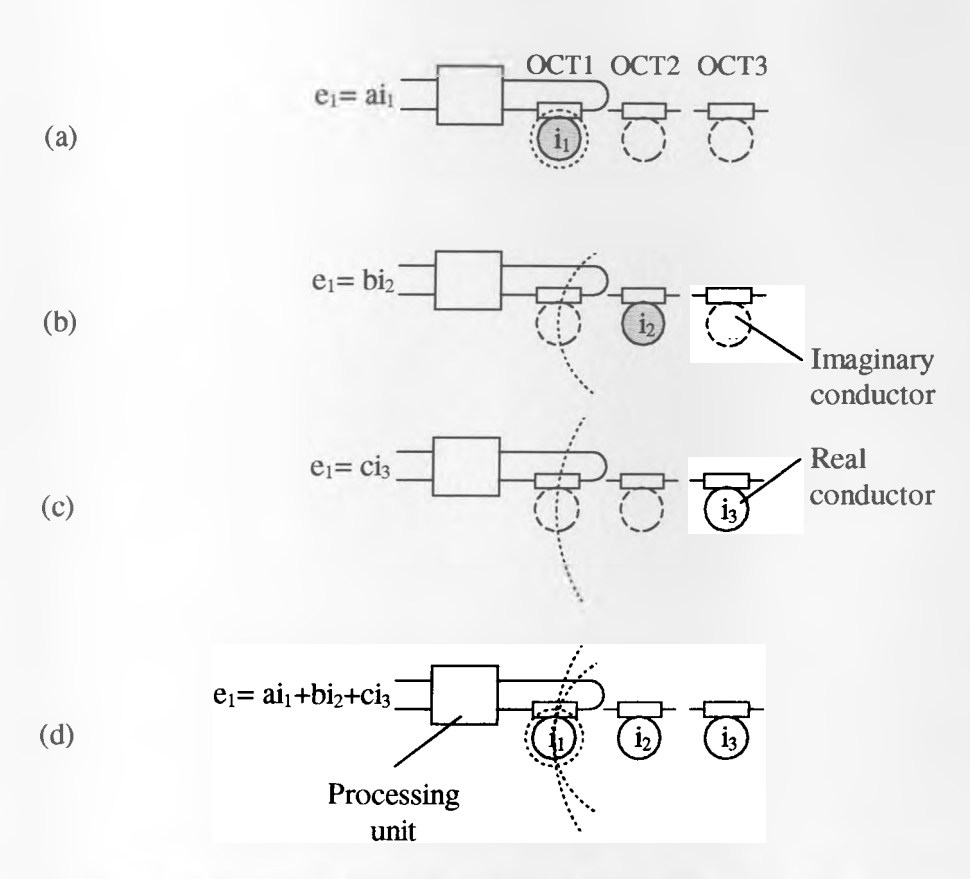


Figure 6-24 Explanation of the calibration process in phase 1

The same calibration procedure may be carried out for the remaining sensors, namely, OCT2 and OCT3. Consequently, the set of three equations can be created representing instantaneous output signals  $e_1$ ,  $e_2$  and  $e_3$  from the three current sensors:

$$e_1 = ai_1 + bi_2 + ci_3,$$
  
 $e_2 = di_1 + ei_2 + fi_3,$   
 $e_3 = gi_1 + hi_2 + ii_3.$  (6-27)

As the current transmission system from Figure 6-24 is symmetrical, the following calibration factors are equal to each other: a = e = i, b = d = f and c = g. Now, the above equations can be presented in the following form

$$e_1 = ai_1 + bi_2 + ci_3,$$
  
 $e_2 = bi_1 + ai_2 + bi_3,$   
 $e_3 = ci_1 + bi_2 + ai_3.$  (6-28)

The above set of equations is characterised by the following determinant

$$D = \begin{vmatrix} a & b & c \\ b & a & b \\ c & b & a \end{vmatrix} = a^3 + 2bc - ac^2 - 2ab^2 \neq 0$$
 (6-29)

The target instantaneous currents i<sub>1</sub>, i<sub>2</sub> and i<sub>3</sub> can now be derived as follows

$$i_{1} = \frac{\begin{vmatrix} e_{1} & b & c \\ e_{2} & a & b \\ e_{3} & b & a \end{vmatrix}}{D} = \frac{(a^{2} - b^{2})e_{1} + (bc - ab)e_{2} + (b^{2} - ac)e_{3}}{a^{3} + 2bc - ac^{2} - 2ab^{2}},$$
(6-30)

$$i_{2} = \frac{\begin{vmatrix} a & e_{1} & c \\ b & e_{2} & b \\ c & e_{3} & a \end{vmatrix}}{D} = \frac{(a^{2} - c^{2})e_{2} + (bc - ab)(e_{1} + e_{3})}{a^{3} + 2bc - ac^{2} - 2ab^{2}},$$
(6-31)

$$i_{3} = \frac{\begin{vmatrix} a & b & e_{1} \\ b & a & e_{2} \\ c & b & e_{3} \end{vmatrix}}{D} = \frac{(b^{2} - ac)e_{1} + (bc - ab)e_{2} + (a^{2} - b^{2})e_{3}}{a^{3} + 2bc - ac^{2} - 2ab^{2}},$$
(6-32)

where, a, b and c are the respective calibration factors, and  $e_1$ ,  $e_2$  and  $e_3$  represent instantaneous output signals from the three current sensors.

For the practical OCT measurement system the above set of equations (6-28) must be solved in real time in order to preserve the amplitude and phase of the measured currents. This can be realised using real time digital signal processing techniques as shown later in Chapter 7.

It should be stressed that the magnetic cross-talk can also result from the various metal parts present in close proximity from the sensor at the installation site. Magnetic field distribution may be affected by both, eddy currents induced in the metal parts and magnetisation of steel enclosures etc. If the sensors are to be installed in close proximity from such metal parts, the calibration factors should be corrected, which again can be done by experimental measurements or simulations.

# 6.8. Summary

In this chapter the influence of environmental effects such as vibration, temperature and magnetic cross-talk on the OCT operation characteristics have been investigated. The physical grounds behind the above effects have been studied which enabled to quantify the potential influence of these factors on the OCT performance.

The vibration induced errors are difficult to quantify, however, it has been confirmed experimentally that they can be sufficient to significantly deteriorate the sensor performance; more details will be provided later in Chapter 8 in which detailed tests results are presented. The vibration induced noise can be eliminated by configuring the OCT for bidirectional light propagation. In this way two reference signals can be obtained which are than used to effectively cancel any vibration components in the output signal. A solution for a practical implementation of this scheme has been provided.

The thermal influence on the operation of the present sensor requires compensation. The relevant analysis to determine the required temperature measurement precision have been performed for the TGG and FR5 based sensors. It has been estimated that it is sufficient to recover the OCT temperature with a precision of up to 1.5°C and 0.15°C for protection and metering applications respectively. These constraints are slightly relaxed for the FR5 sensor interrogated with 850nm light source. Temperature compensation can be realised using direct or indirect temperature recovery methods. The direct method is preferred as in this case the precision of the temperature recovery process is not affected by the level of measured current.

The analysis of the magnetic cross-talk on the sensor operation has demonstrated that for the bulk of the installations within the electricity network, the cross-talk levels from adjacent phases will introduce measurement errors that are outside the required operational specifications. Experimental investigations have indicated that screening of the OCT is not a feasible alternative because of the low frequency of the energising field. Improved measurement sensitivity and a greater degree of cross-talk rejection can be achieved through the use of flux concentrators which encircle the current being measured. However this would ultimately restrict the operational bandwidth of these devices and may compromise many of their attractive features such as reduced size and minimal insulation requirements. A preferred solution is to directly process the information from all three phases to reject the cross-talk components and a methodology to implement this has been developed and presented.

The next chapter will concentrate on the issue of implementing the above three compensation schemes into a robust current measurement sensor system. This is realised using real time digital signal processing techniques.

### 6.9. Chapter References

- 1) H. G. Unger, "Planar optical waveguides and fibres", Oxford University Press 1977,
- 2) P. Megret, E. Januart, J. C. Froidure, M. Blondel and M. Lamquin, "Modal noise in optical fibre transmission systems", CIRED '93, IEE Conf. Publishing No. 373,
- 3) M. Willsch, T. Bosselmann, "Vibration Compensation for a Glass Ring Type Magnetooptic Current Sensor", 11<sup>th</sup> Int. Conf. on Optical Fiber Sensors, 1996, Japan, pp.148-151,
- 4) Tabor and Chen, "Electromagnetic propagation through materials possessing both Faraday rotation and birefringence: Experiments with ytterbium orthoferrite", *J. Appl. Phys.*, vol. 40, no. 7, 1969, p. 2760.
- 5) N. C. Pistoni and Mario Martinelli, "Vibration-insen-sitive fiber-optic current sensor", Optics Letters, vol. 18, no. 4/ February 15, 1993, pp. 314-316,
- 6) X. Fang, A. Wang, R. G. May, R. O. Claus, "A recip-rocal-Compensated Fiber-Optic Electric Current Sensor", Journal of Lightwave Technology, vol. 12, no. 10, October 1994, pp.1882-1889,
- A. J. Rogers, Jincheng Xu, Jialing Yao, "Vibration Immunity for Optical-Fiber Current Measurement", J. of Lightwave Techn., vol. 13, no.7, July 1995, pp. 1371-1377,
- Xiaojun Fang, Richard O. Claus, "Optimal Design of IRIS-Based Polarimetric Intrinsic Fiber Optic Current Sensors", J. of Lightwave Techn., vol. 14, no.7, July 1996, pp.1664-1672,
- 9) P Menke, T Bosselmann, "Temperature Compensation in magneto-optic ac current sensors using an intelligent ac-dc signal evaluation", Journal of Lightwave Technology, Vol.13, No.7, 1995, pp1362-1370,

- 10) S H Zaidi, R P Tatam, "Faraday-effect magnetometry: compensation for the temperature dependent Verdet constant", J. of Measurement Science and Technology, pp1471-1479, Vol.5, 1994,
- 11) HOYA Corporation, USA, FR5 Data Sheet, 1995
- 12) N P Barnes, L B Petway "Variation of the Verdet Constant with Temperature of Terbium Gallium Garnet", Journal of Optical Society of America B, Vol 9, No. 10, pp1912-1915, Oct. 1992,
- 13) W.I. Madden, W.C. Michie, A. Cruden, P. Niewczas, J.R. McDonald and I. Andonovic, "Temperature compensation for optical current sensors", Optical Engineering, Vol.38, No.10, pp.1699-1707, Oct. 1999,
- 14) P. J. Stephens, Adv. Chem. Phys. 35, 197, 1976,
- 15) P. N. Schatz and A. J. McCaffery, Quarterly Review of the Chemical Society, 23, 552, 1969,
- 16) A. D. Buckingham and P. J. Stephens, Ann. Rev. Phys. Chem., 17, 399, 1966,
- 17) J. A. Davis and R. M. Bunch, "Temperature dependence of the Faraday rotation of Hoya FR-5 glass", Applied Optics, Vol. 23, No. 4, February 1984,
- 18) J. Becquerel and J. van den Handel, Physica 7, 711, 1940,
- 19) C. Kittel, "Introduction to Solid State Physics, Wiley, New York, 1971,
- 20) A.D. Kersey, T. Berkoff "Fibre Optic Bragg Grating Differential Temperature Sensor", IEEE Photonics Technology Letters, 4(10) 1992, pp.1183-1185,
- 21) A.D. Kersey, T. Berkoff, W. Morey "High Resolution Fibre Grating Strain Sensor with Interferometric Wavelength Shift Detection", Electronic Lett. 28(3), pp.226-228, 1992,
- J. Dankin, B. Culshaw, "Optical fiber sensors: systems and applications", Volume
   Artech House, Inc., 1989,
- 23) Fibre Bragg Grating Interrogation Unit, MicronOptics Data Sheet,
- 24) Spectral Filters Catalogue, SCHOTT Glass Technologies Inc., Internet address: http://www.shottglasstech.com,
- 25) S. A. Simpson, "Design and Construction of Absorption Glass Temperature Sensor", University of Strathclyde, CEPE Reference No. RR/OPT/TR/1999-007, October 1999,

- 26) D. Halliday and R. Resnick, "Physics", Parts I and II combined, John Wiley & Sons, Inc., 1978,
- 27) M. Imamura, M. Tokubuchi, "Magnetic field analysis for the optical current transformer used for three-phase busbars arranged longitudinally", IEEE Transactions on Magnetics, Vol. 32, No. 5, pp. 4962-4964, 1996,
- 28) A.Cruden, "Electric Current Measurement using crystal based, magneto-optic point field sensors", PhD Thesis, Centre for Electrical Power Engineering, University of Strathclyde, Department of Electronic and Electrical Engineering, June 1998.

# 7. Digital Signal Processing Unit as an Integrated System for Conditioning of the OCT Output

#### 7.1. Introduction

Digital Signal Processing (DSP) is concerned with the digital representation of signals and the use of digital processors to analyse, modify, or extract information from signals. Most signals in nature are analogue in form, often meaning that they vary continuously with time, and represent the variations of physical quantities such as electrical current in the transmission line represented by light intensity modulation within the OCT system. The signals used in most applications of DSP are derived from analogue signals which have been sampled at regular intervals and converted into a digital form.

The specific reason for processing a digital signal may be, for example, to remove interference or noise from the signal, to obtain the spectrum of the data, or to transform the signal into a more suitable form. DSP is now used in many areas where analogue methods were previously used and in entirely new applications which were difficult or impossible with analogue methods. The attraction of DSP comes from key advantages such as the following.

- Guaranteed accuracy. Accuracy is only determined by the number of bits used.
- Perfect reproducibility. Identical performance from unit to unit is obtained since there are no variations due to component tolerances.
- No drift in performance with temperature or age.
- Greater flexibility. DSP systems can be programmed and reprogrammed to perform a variety of functions, without modifying the hardware. This is perhaps one of the most important features of DSP.
- Superior performance. DSP can be used to perform functions not possible with analogue signal processing. For example, linear phase response can be achieved

- (very important from the point of view of electrical power measurement), and complex adaptive filtering algorithms can be implemented using DSP techniques.
- In some cases information may already be in a digital form and DSP offers the only viable option.
- Advantage is always taken of the tremendous advances in semiconductor technology to achieve greater reliability, smaller size, lower cost, low power consumption, and higher speed. For example, in recent years it has become possible to produce high speed, low power integrated circuits using CMOS technology<sup>1-5</sup>. As a result newer DSP chips are predominantly CMOS devices instead of bipolar.

DSP is not without disadvantages. However, the significance of these disadvantages is being continually diminished by new technology.

- Speed and cost. DSP designs can be expensive especially when large bandwidth signals are involved. At the present, fast A/D and D/A converters (analogue-to-digital and digital-to-analogue converters) either are too expensive or do not have sufficient resolution for wide bandwidth DSP applications. Currently, only specialised integrated circuits can be used to process signals in the megahertz range and these are relatively expensive. Furthermore, most DSP devices are still not fast enough and can only process signals of moderate bandwidths. Bandwidths in the 100MHz range are still processed only using analogue methods. Nevertheless, DSP devices are becoming increasingly faster.
- Design time. Unless one is knowledgeable in DSP techniques and have the necessary resources (software packages and so on), DSP designs can be time consuming and difficult. The acute shortage of suitable engineers in this area is widely recognised. However, the situation is changing as commercial companies begin to recognise and exploit the advantages of DSP in their products.

Due to the complexity and speed of the required signal processing, the real time DSP technology seems to be the only solution for processing the output signal of the

optical current transducer. It allows for effective implementation of the required compensation schemes and signal conditioning using integrated software solutions.

This chapter describes in detail the design, construction and operation of the prototype DSP unit and the respective optoelectronics built for the purpose of controlling the OCT and for real time digital processing of the measured output current signal. The digital signal processing unit is used to calibrate the OCT optoelectronic system, to compensate the sensor against vibration and temperature effects and linearise its response characteristic. Additionally it can be used as a means to implement fully software programmable digital filters in order to discriminate unneeded frequencies from a spectrum of the processed signal.

The aims of the work described in this chapter can be outlined as follows:

- to develop a flexible digital signal processing unit for use with the OCT, fully controlled by software,
- to implement in a DSP software vibration and temperature compensation schemes, autocalibration routines, and linearisation of the sensor response characteristic,
- to develop a system that meets the accuracy requirements for measurement and protection class instrument within power industry,
- to demonstrate the ac and dc current measurement capabilities of the system,
- to identify and facilitate additional uses of the OCT, monitored and controlled by the DSP system,
- to investigate a potential for DSP implementation of the magnetic cross-talk compensation scheme.

# **7.2.** DSP Unit Hardware (Single Phase System)

The DSP monitoring unit for use with optical current sensors has been developed in a way that provides a high degree of flexibility of interrogating different OCTs working in either ac or dc configurations without changing any hardware. Only loading of

different software components from a PC to the processor internal memory is required in order to provide appropriate signal processing.

In order to meet stringent accuracy and speed requirements, which in general counter act each other, a 16-bit analogue-to-digital conversion resolution was predetermined. It is believed that this scale of precision is sufficient to comply with the required accuracy specification, and is an issue which will be investigated further in Section 7.7. Simultaneously the system must operate at a speed which will enable real time processing of higher frequency signals, e.g., higher harmonics or fast transient signals often present in electricity network systems. It is believed that a bandwidth of several kHz is sufficient to comply with these requirements.

The DSP monitoring system consists of an Analog Devices DSP development board of type EZ-KIT 21XX with an ADSP-2181 fixed point digital signal processor, analogue interface boards, logic boards, light source drivers, photodetectors and power supply. A diagram of the system is presented in Figure 7-1.

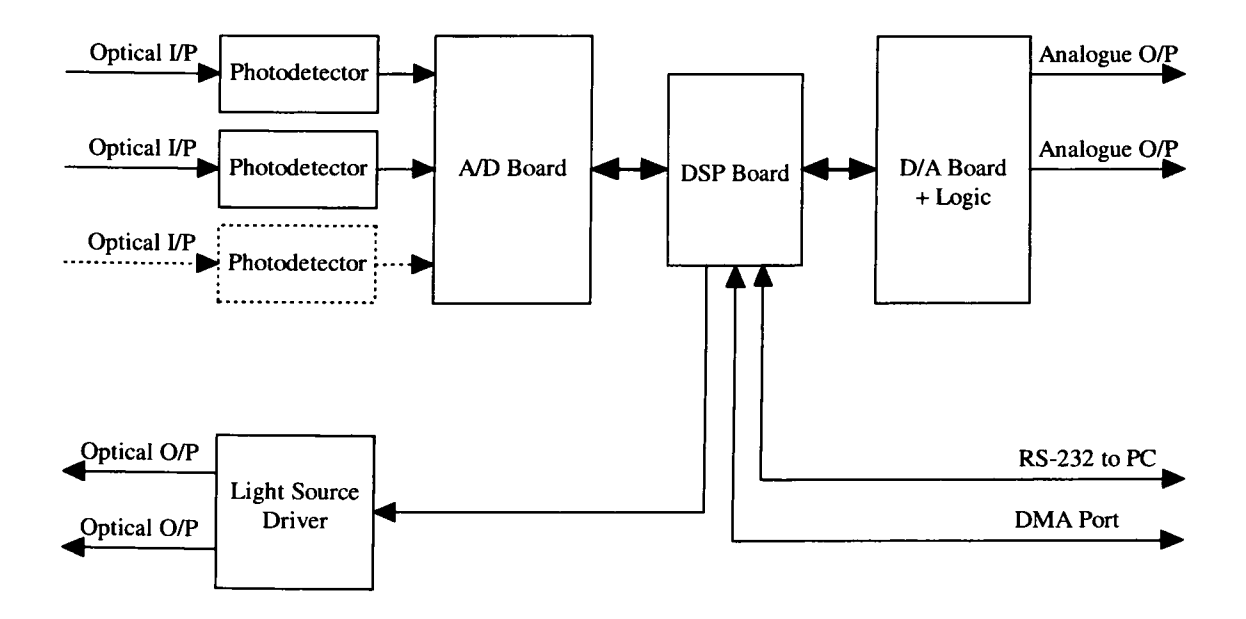


Figure 7-1 Block schematic of the DSP monitoring system

The system is designed as a self-contained unit interfaced to the OCT through optical connectors and to a PC via an RS-232 serial communication port. The PC can be

disconnected after the appropriate software is downloaded to the internal memory of the DSP chip. The next sections will provide a detailed description of each part of the above system.

#### **7.2.1. DSP** board

The DSP EZ-KIT 21XX board consists of an ADSP-2181 fixed point digital signal processor with internal memory and expansion connectors through which all the microprocessor pins can be accessed by external devices. The DSP board also contains an integral EPROM memory in which the Monitor Program resides, automatically loaded into the on-chip program and data memories at reset. This program is responsible for self testing of the DSP registers and on-chip memories and communication between the board and a PC. The DSP board with the clear view of the ADSP-2181 microprocessor and the EPROM memory is pictured in Figure 7-2.

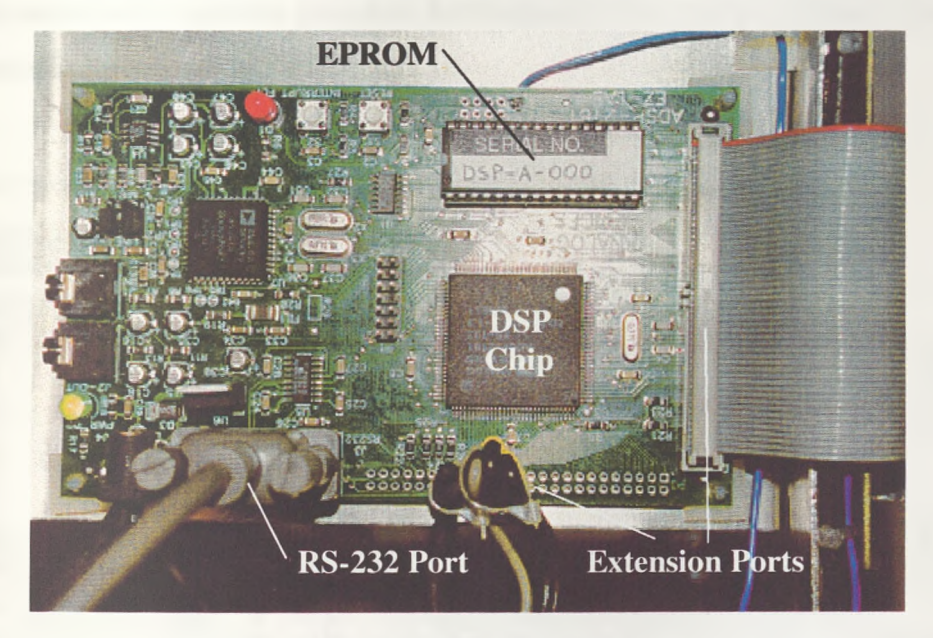


Figure 7-2 DSP board

# 7.2.1.1. ADSP-2181 processor

The heart of the above DSP board is the ADSP-2181 microprocessor optimised for digital signal processing and other high speed numeric processing applications. It combines the ADSP-2100 family base architecture (three computational units, data

address generators and a program sequencer) with two serial ports, a 16-bit internal Direct Memory Access (DMA) port, a one byte DMA port, a programmable timer, Flag I/O, extensive interrupt capabilities, and on-chip program and data memory. The microprocessor integrates 80k bytes of on-chip memory configured as 16k words (24-bit) of program RAM, and 16k words (16-bit) of data RAM. In addition, the ADSP-2181 supports new instructions, which include bit manipulations (bit set, bit clear, bit toggle, bit test), new ALU constants, new multiplication instruction (x squared), biased rounding, result free ALU operations, I/O memory transfers and global interrupt masking for increased flexibility.

The ADSP-2181 instruction set provides flexible data moves and multifunction (one or two data moves with a computation) instructions. Every instruction can be executed in a single processor cycle. The ADSP-2181 assembly language uses an algebraic syntax for ease of coding and readability. A comprehensive set of development tools supports program development. The functional block diagram of the device is shown in Figure 7-3.

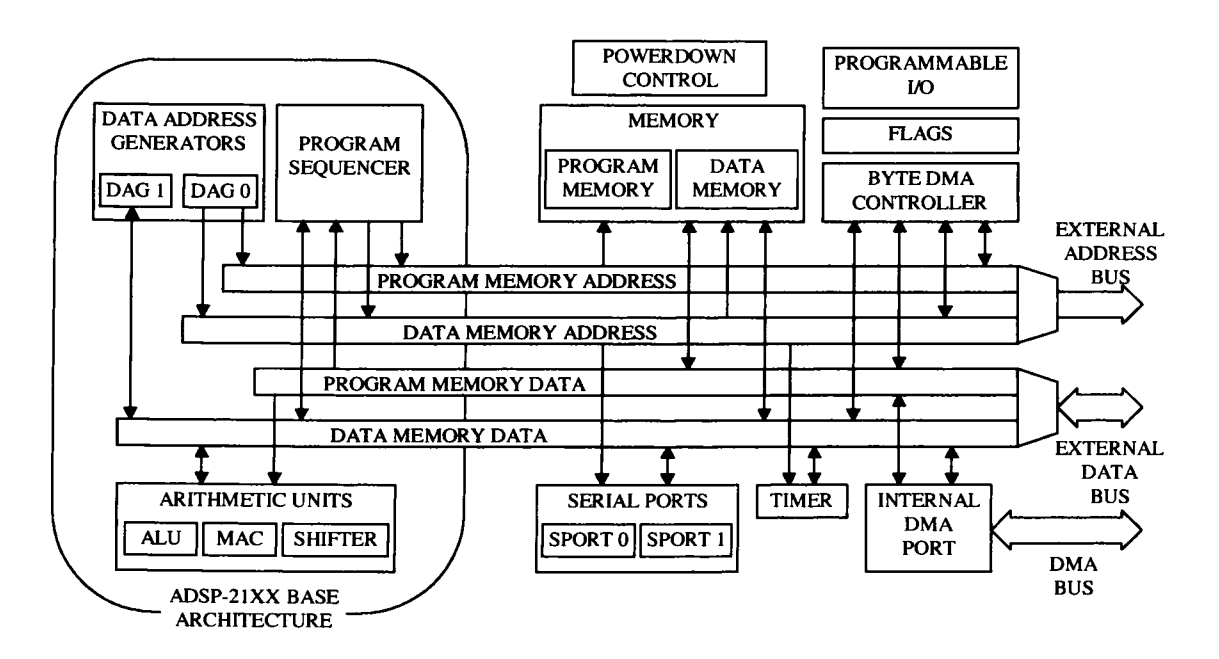


Figure 7-3 Functional block diagram of the ADSP-2181

The processor contains three independent computational units: the ALU, the multiplier/accumulator (MAC) and the shifter. The computational units process 16-bit

data directly and have provisions to support multi-precision computations. The ALU performs a standard set of arithmetic and logic operations; division primitives are also The MAC performs supported. single-cycle multiply, multiply/add and multiply/subtract operations with 40 bits of accumulation. The shifter performs logical and arithmetic shifts, normalisation, denormalisation and derive exponent operations. The shifter can be used to efficiently implement numeric format control including multi-word and block floating-point representations. The internal result (R) bus (not shown in Figure 7-3) connects the computational units so that the output of any unit may be the input of any unit on the next cycle.

A powerful program sequencer and two dedicated data address generators ensure efficient delivery of operands to these computational units. The sequencer supports conditional jumps, subroutine calls and returns in a single cycle. With internal loop counters and loop stacks, the ADSP-2181 executes looped code with zero overhead; no explicit jump instructions are required to maintain loops.

Two data address generators (DAGs) provide addresses for simultaneous dual operand fetches (from data memory and program memory). Each DAG maintains and updates four address pointers. Whenever the pointer is used to access data (indirect addressing), it is post-modified by the value of one of four possible modify registers. A length value may be associated with each pointer to implement automatic modulo addressing for circular buffers.

Efficient data transfer is achieved with the use of five internal buses:

- Program Memory Address (PMA) Bus
- Program Memory Data (PMD) Bus
- Data Memory Address (DMA) Bus
- Data Memory Data (DMD) Bus
- Result (R) Bus

The two address buses (PMA and DMA) share a single external address bus, allowing memory to be expanded off-chip, and the two data buses (PMD and DMD) share a single external data bus. Byte memory space and I/O memory space also share the external buses.

Program memory can store both instructions and data, permitting the ADSP-2181 to fetch two operands in a single cycle, one from program memory and one from data memory.

In addition to the address and data bus for external memory connection, the ADSP-2181 has a 16-bit Internal DMA port (IDMA port) for connection to external systems. The IDMA port provides transparent, direct access to the DSPs on-chip program and data RAM.

The ADSP-2181's flexible architecture and comprehensive instruction set allow the processor to perform multiple operations in parallel. In one processor cycle the ADSP-2181 can for instance: generate the next program address, fetch the next instruction, perform one or two data moves, update one or two data address pointers and perform a computational operation. This takes place while the processor continues to: receive and transmit data through the two serial ports, receive and/or transmit data through the internal DMA port, receive and/or transmit data through the byte DMA port and decrement timer.

All these features make the ADSP-2181 processor a powerful tool for fast digital signal processing applications; additionally several memory interfacing features provide easy communication with peripherals, e.g., other microprocessors, A/D and D/A converters, PC Bus Interface, etc. Figure 7-4 shows a typical basic system configuration with the ADSP-2181: two serial devices, I/O peripherals, DMA system interface, a byte-wide EPROM, and optional external program and data overlay memories. Programmable wait state generation allows the processor connects easily

to slow peripheral devices. The ADSP-2181 also provides four external interrupts (or six external interrupts if only one serial port is used), and programmable I/O flags.

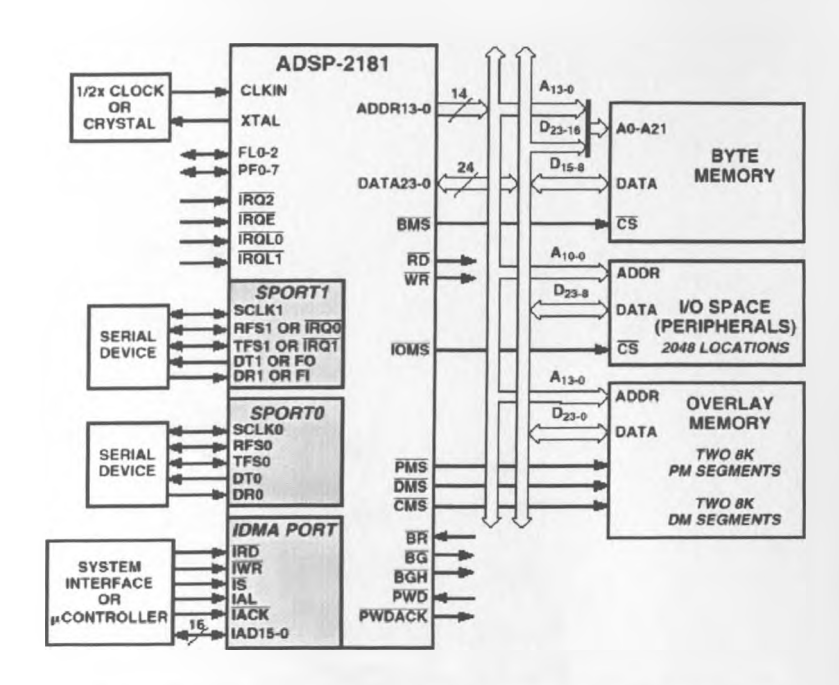


Figure 7-4 ADSP-2181 basic system configuration

The ADSP-2181 is the clear leader when compared to the other similar class DSP microprocessors, e.g., Motorola DSP56002 or Texas Instruments TMS320C53. With its large internal RAM, integrated DMA control and I/O interfaces, the ADSP-2181 provides more system support than any other 16-bit, fixed point DSP. Table 7-1 provides comparison of the basic hardware characteristics of the above three microprocessors.

Comparison	ADSP-2181	DSP56002	TMS320C53
Features			
On-Chip Memory	32k words	1.5k words	3.5k words
Off-Chip Memory Access	2 accesses per DSP instruction cycle, no decode hardware needed	1 access per DSP instruction cycle possible, external decode hardware needed for memory and I/O	I access takes two DSP instruction cycles, external decode hardware needed for memory and I/O
I/O Peripheral Interface	Integrated I/O space support, no decode hardware needed	No I/O space support	Integrated I/O space support, external decode hardware needed for memory and I/O
Direct Memory Accessing	Integrated DMA support, 'one cycle stealing' DMA	No DMA support	Support for an external DMA controller, but DSP operation is suspended during DMA transfers

Table 7-1 Comparison of the DSP microprocessors

In addition, Analog Devices recently disclosed plans for production of a new ADSP-219x series with speeds beyond 300MIPS, this new series is ADSP-2181 code-compatible, which will provide an easy means for future system upgrades.

#### 7.2.2. Analogue Interface Board

The DSP board is interfaced via expansion connectors to 16 bit A/D and D/A converter boards. The A/D converter board consists of three identical A/D channels connected to the outputs of the respective photodetectors. Two channels (CH2 and CH3) can be sampled alternately with respect to each other and are used for ac and dc current measurement and vibration compensation, as they receive information directly from the OCT. The remaining channel (CH1) is used to digitise temperature information from an optical temperature sensor for the purpose of providing temperature compensation of the OCT. Each A/D converter is buffered by an additional amplifier with step adjustable gain which acts as a basic anti-aliasing filter.

The anti-aliasing could not be fully implemented in CH2 and CH3 as their respective A/D converters need to sample already "chopped" signals at the Nyquist frequency to implement the back-reflection insensitive vibration compensation scheme. It is believed that the signals present on the power line at frequencies in the aliasing region are below any detectable level in the normal power system operation. This, however could potentially be an issue during the fault condition when the high frequency travelling wave is generated in the transmission line. The solution to this problem is proposed in Chapter 9, concerned with the future project work, and could be devised by additional modulation of the light sources (more details are provided in Chapter 9).

The digital signal, processed in the DSP board, is converted using one of the D/A converters into an analogue signal which is available from the output of the D/A. The second D/A converter can be used as a reference channel for the purpose of comparing the compensated and uncompensated measurement signals. Figure 7-5 shows a photograph of the DSP unit with removed top and front panels. The A/D, D/A and logic boards are fixed on the top shelf of the chassis and are interfaced to the situated below DSP board via ribbon cable.

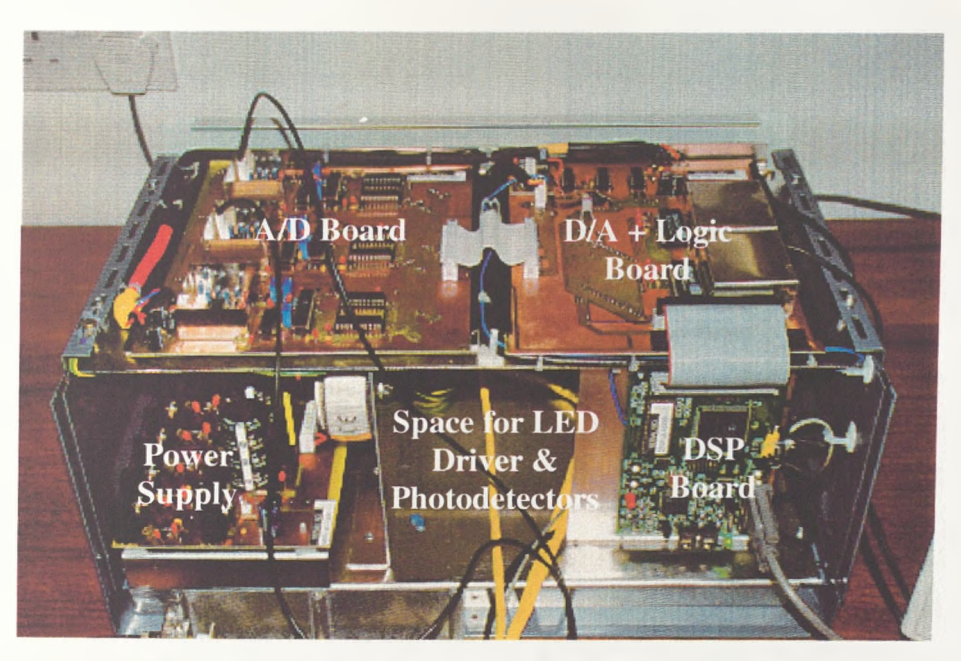


Figure 7-5 DSP unit with removed top and front panels

# 7.2.2.1. A/D Converters

The A/D converters chosen for use with the analogue interface are Analog Devices AD976A components, capable of sampling the input signal at specific time intervals (S&H input circuits). This capability is essential in order to provide appropriate synchronisation with pulsed input signals coming from the photodetectors.

The AD976A is a high speed (200kSPS throughoutput rate), low power 16-bit A/D converter that operates from a single 5V supply. The part contains a successive approximation<sup>6</sup>, switched capacitor A/D converter, an internal 2.5V reference, and a high speed parallel interface, fully compatible with the used DSP processor. The A/D converter is factory calibrated to minimise all linearity errors. The analogue full-scale input is the standard industrial range of ±10V. The AD976A is comprehensively tested for ac parameters such as SNR and THD, as well as the more traditional parameters of offset, gain and linearity. The part is fabricated on Analog Devices' proprietary BiCMOS process, which provides high performance bipolar devices along with CMOS transistors. The AD976A offers a highly integrated solution containing an accurate ADC, reference and on-chip clock.

#### 7.2.2.2. D/A Converters

The D/A converters used in the analogue interface board are Analogue Devices AD669 components. The AD669 is a complete 16-bit monolithic D/A converter with an on board reference and output amplifier. The AD669 chip includes current switches, decoding logic, an output amplifier, a buried zener reference and double-buffered latches.

The on-chip output amplifier provides a voltage output settling time of 10µs to within ½ LSB for a full-scale step<sup>7</sup>. Data is loaded into the converter in a parallel 16-bit format. The double-buffered latch structure eliminates data skew errors and provides for simultaneous updating of D/A converters in a multi-D/A converter system. The

output range of the AD669 is pin programmable and can be set to provide a unipolar output range of 0V to +10V or a bipolar output range of -10V to +10V.

# 7.3. Analogue Optoelectronic System

In order to provide bidirectional light propagation through the OCT, two alternately pulsed 850nm LEDs are used as the light sources in the optical system with two 2x1 multimode couplers, and are synchronised with their respective PIN photodetectors. The light is transmitted to the sensor head via 100/140 micron graded index multimode fibre optic cable connected to the unit through optical ST connectors. This type of optical fibre (not as widely used as 50/100 and 62.5/100) was chosen for the prime purpose of the increased efficiency in light coupling from the light source to the fibre. This provides a marked improvement in the optical power budget within the OCT arrangement. The optical system is presented in Figure 7-6.

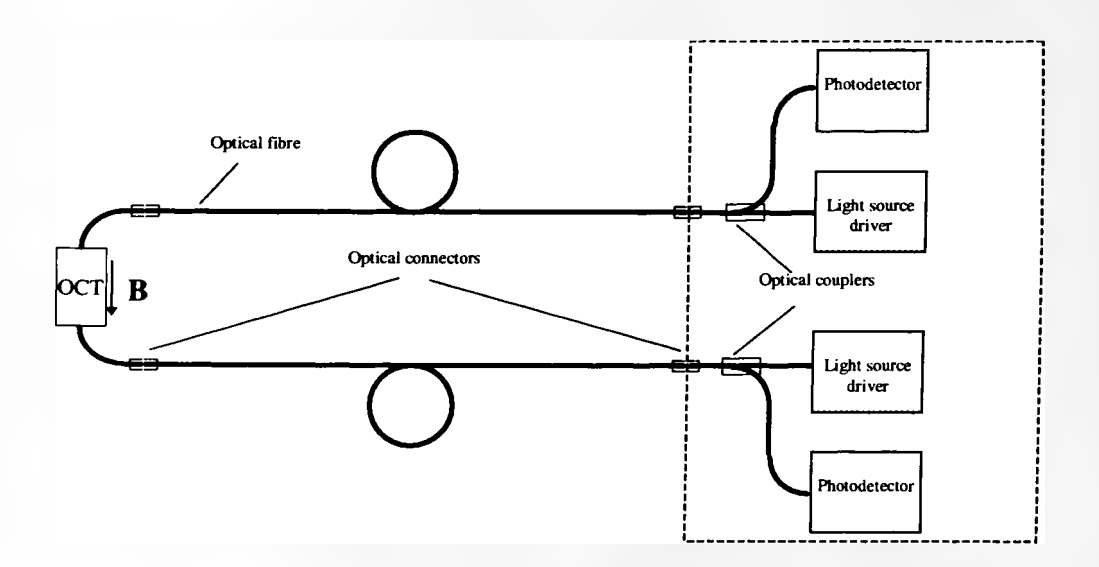


Figure 7-6 Optoelectronic part of the OCT monitoring system

# 7.3.1. Light Source Driver

The light source driver is designed primarily for use with the bidirectional light propagation optical system shown in Figure 7-6. It consists of two voltage controlled

current sources based on power operational amplifiers. The current level in each channel is controlled by a high precision bandgap reference voltage, and it can be adjusted within the current range from zero to the current limit by adjusting the corresponding trim-pots. The trim-pots can be replaced by precision fixed resistors if a long term, high stability current is required.

There are three current ranges that can be programmed by the set of precision resistors for the purpose of driving different light sources. The driver is capable of providing a current of up to 300mA in each channel.

The driver enables alternate pulsing of the two light sources to be synchronised with the respective A/Ds. The DSP board provides appropriate (software programmable) signals to control the light source driver logic. Alternate pulsing of the light sources is used to circumvent the problem of back reflection from the optical connectors as bidirectional light propagation through the OCT is required for the purpose of vibration compensation, as discussed in Chapter 6. Figure 7-7 shows a photograph of the light source driver mounted in the metal enclosure.

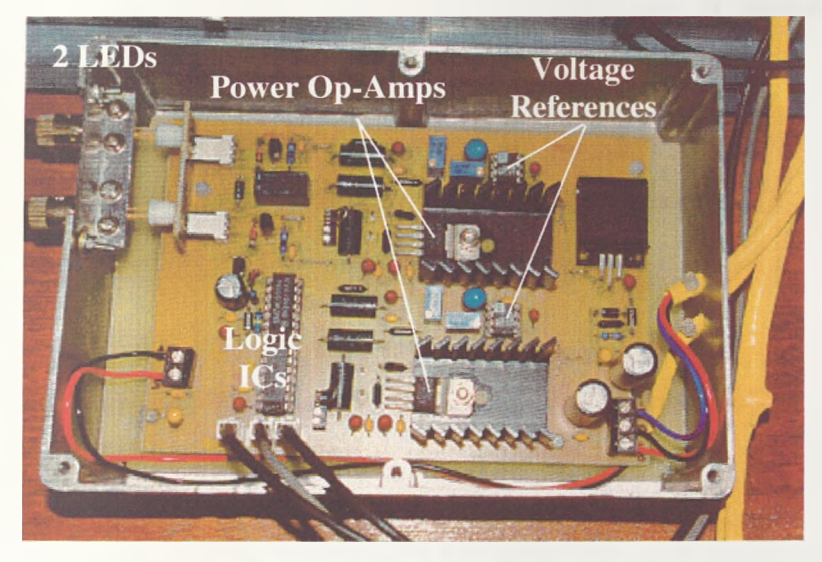


Figure 7-7 Light source driver

At the left side of the enclosure two high power LEDs are mounted used as light sources in the above system. The chosen LED type is ABB HAFO model 1A191

which works in the 850nm transmission window and provides approximately  $700\mu W$  of optical power coupled to the 100/140 micron fibre. The chosen LED and its operational wavelength are the best compromise between the optical power level achieved, sensor sensitivity (Verdet constant,  $V \propto \frac{1}{\lambda}$ ), and lifetime of the device.

#### 7.3.2. Photodetectors

The photodetectors used in the optoelectronic system are low noise high performance circuits which convert input optical power levels into electrical signals. The photodetectors work in a transimpedance configuration and they consist of J-FET input stages in order to minimise output noise level. The semiconductors and other passive components are carefully chosen to provide stable dc operation of the photodetectors as they directly affect the accuracy of the complete measurement system.

As the photodetector performance is crucial from the point of view of the entire current measurement system accuracy, a detailed design description and testing of the above circuit will be presented in Chapter 8.

# 7.4. DSP Software Development

The complete set of software design tools for ADSP-21xx processors allows for a fast and efficient design of the specific DSP application. Figure 7-8 shows how the software and hardware tools are typically used in the development process.

The software development tools include the following programs: System Builder, Assembler, Linker, Simulator and PROM Splitter. Additionally, the development process may be supported by C Language Tools, namely: C Compiler, C Runtime Library, and C Source-Level Debugger.

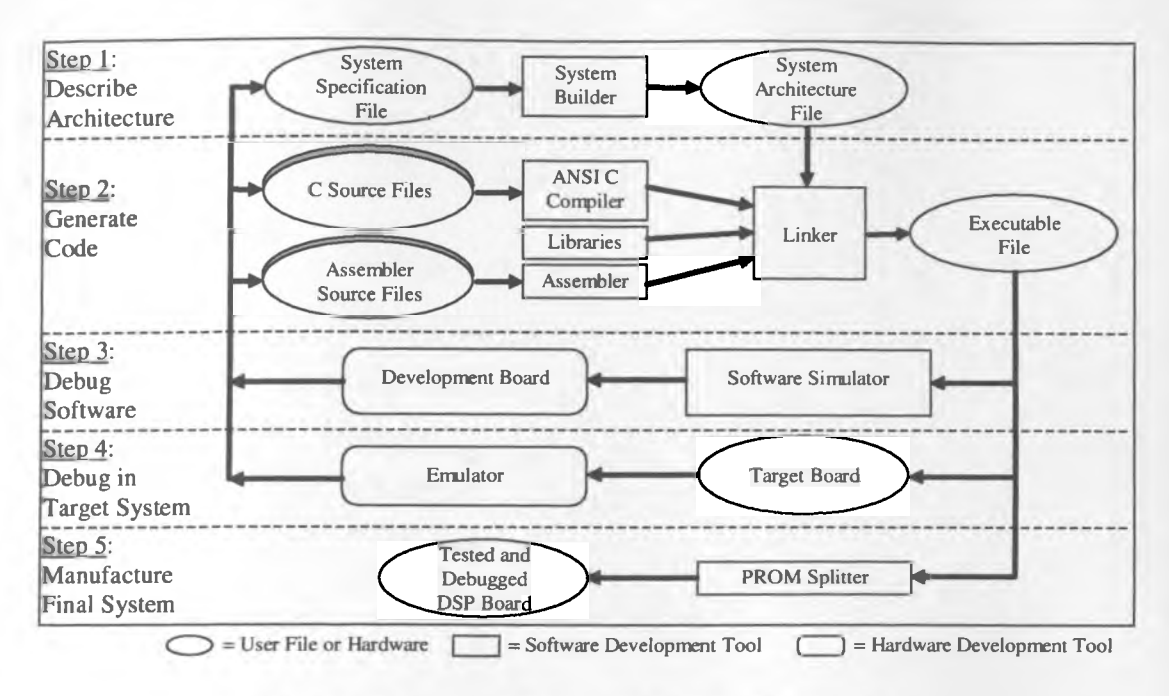


Figure 7-8 System development process overview

The System Builder reads the system specification file and then generates an architecture description file that passes information about the target hardware to the linker, simulator and emulator. Code generation begins with the creation of an assembly language and/or C language source code modules. These modules are compiled/assembled separately and then linked together to form an executable program (memory image file).

The highly readable algebraic syntax of the ADSP-2100 Family instruction set eases programming in assembly language. Many instructions are written in the same manner as the actual equation. For example, the algebraic statement:  $r = r + x \cdot y$ , is coded in assembly language as: mr = mr + mx0 \* my0.

The simulator configures program and data memory according to the architecture description file and simulates the I/O space to enable debugging the system and analysing its performance. After simulating the software it is possible to use the emulator with the prototype hardware to test circuitry, timing, and real-time software execution.

The PROM splitter is used to translate the linker output executable file into an industry-standard file format for a PROM programmer. Once the code is written into a PROM device and plugged into the ADSP-2181 processor board, the prototype is ready to run.

The PROM programming is not necessary with the board used in the earlier discussed DSP unit as it consists of an EPROM memory with a residing communication program ("Monitor Program"). The Monitor Program allows direct loading of user created DSP software to the microprocessor internal memory.

# 7.5. Downloading Software to the DSP Unit

The DSP unit can be run only when a relevant software program is downloaded to the internal memory of the DSP chip. This can be done after the unit is switched on and the DSP board has been reset (reset button on the front panel). The system is ready for downloading when the red LED on the front panel is flashing. During the time of loading the RS-232 port of the DSP unit has to be connected to a serial port of a PC. The EZ-KIT Host Program (provided by the manufacturer) installed under the Windows environment on the PC enables direct loading of the user-created software to the DSP board. When the EZ-KIT program is executed the main dialogue box appears. The user chooses Loading and then Download user program and go. By double-clicking on the selected filename.exe file the user executes the loading procedure and the EZ-KIT Host Program communicates that the program filename.exe has been successfully downloaded. From this point on the DSP unit performs autonomously according to the downloaded software and the RS-232 can be disconnected. Further programs may be loaded after resetting the DSP board. More details about the Monitor Program and EZ-KIT Host Program can be found in the ADSP-2100 EZ-KIT Lite Reference Manual published by Analog Devices<sup>9</sup>.

# 7.6. Software Created for the Use with the DSP Unit

The software created within this research work enables full operation of the DSP monitoring unit connected software to the OCT. The module: Optical\_Current\_Transducer (see Appendix) creates a time frame of alternate pulsing and sampling of the appropriate channels (CH2 and CH3) and within each sampling period additional software procedures perform the relevant real time signal processing. The frequency of sampling and therefore the maximum measurement frequency of current depends on a constant written into the TPERIOD register of the internal timer of the DSP chip. The maximum sampling frequency can be set at 200kHz, which is the limit of the A/D converter, however due to the limited bandwidth of the photodetectors and degraded performance of the light-source driver at this frequency, the sampling limit has been set at 50kHz. This sampling frequency imposes a limit on the measured current frequency of 25kHz. It is possible to sample the A/D converters at a higher frequency but the accuracy of the system will be degraded.

The system can operate in two software configurations of the current measurement: dc-and-ac, and ac-only modes. The difference between these two configurations consists in different processing of the initial input signals from the two channels and different autocalibration routines applied. Theoretical considerations regarding these two measurement modes were described in detail in Chapter 6.

# 7.6.1. Initialisation

After the software program is downloaded into the on-chip memory, a declaration of the used constants, variables and buffers takes place, and then their initialisation (see Appendix). Next, the interrupt vector table is defined, i.e., reset, calibration, and timer interrupts. The timer interrupt creates the earlier discussed sampling time frame. Then, the actual initialisation of the DSP chip occurs, i.e., set up of the processor internal memory, set up of flags (controlling A/D sampling and pulsing of the LEDs), and set

up of the serial ports. Finally, the program starts executing the infinite loop interrupted periodically by timer in order to collect and process the data.

#### 7.6.2. Autocalibration

After the system initialisation, the software forces the autocalibration procedure (see Appendix) to occur during which the two photodetectors offsets and gains are read and a series of correction coefficients are calculated and written to the internal memory. These correction coefficients are then used by the microprocessor to null any offsets and to equalise the gains of the two channels during normal system operation. This condition is necessary from the point of view of the vibration compensation theory which requires absolute symmetry between the two channels.

The autocalibration procedure is simplified in the ac-only measurement mode, as only the photodetectors offsets are read from the A/Ds and written to the microprocessor internal memory. The difference in gains of the two photodetectors is compensated for continually, as the two input signals are divided by their dc components as described in Chapter 6.

Although the autocalibration routine is forced straight after the program starts its execution, it is recommended to calibrate the system (autocalibration button on the front panel) after approximately half an hour of operation in order to allow temperature stabilisation inside the enclosure. When the system is calibrating, no current or vibration should be present if the dc-and-ac-mode of current measurement is loaded. This is not the case however for the ac-only measurement configuration; due to the continual gain correction provided in this mode of operation, the system calibration can be performed even when current is flowing through the busbar.

#### 7.6.3. DC Filtering

As shown in Chapter 6, the low-pass filters are necessary to perform extracting the dc components from the respective channels in the ac-only mode of system operation.

This cannot be performed by a means of analogue filtering as the input optical signals are in a form of high frequency pulses (which is essential in terms of rejecting the back-reflected light). For this reason, digital implementation of a low-pass filter has been considered and realised as one of the DSP program subroutines.

A digital filter is a mathematical algorithm implemented in hardware and/or software that operates on a digital input signal to produce a digital output signal for the purpose of achieving a filtering objective. The term digital filter refers to the specific hardware or software routine that performs the filtering algorithm. In the case of the DSP system considered in this work, the hardware is minimised to the DSP microprocessor, hence the filtering algorithms can be fully implemented in software.

Digital filters are broadly divided into two classes, namely infinite impulse response (IIR) and finite impulse response (FIR) filters. Either type, in its basic form, can be represented by its impulse response sequence<sup>4,5,10</sup>, h(k) (k = 0, 1, ...), as shown in Figure 7-9.

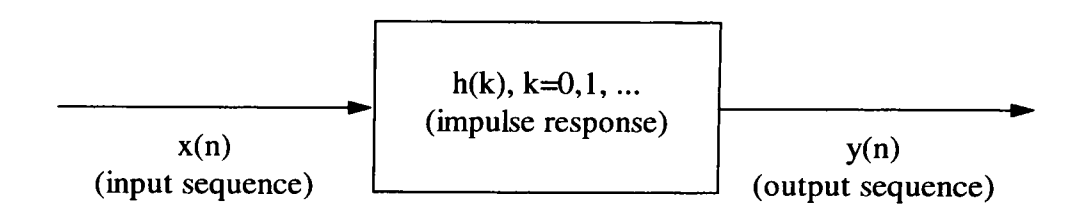


Figure 7-9 A conceptual representation of a digital filter

The input and output signals to the filter are related by the convolution sum, which is given in Equations (7-1) for the IIR and in (7-2) for the FIR filter.

$$y(n) = \sum_{k=0}^{\infty} h(k)x(n-k)$$
 (7-1)

$$y(n) = \sum_{k=0}^{N-1} h(k)x(n-k)$$
 (7-2)

It is evident from these equations that, for IIR filters, the input response is of infinite duration whereas for FIR it is of finite duration, since h(k) for the FIR has only N values. In practice, it is not feasible to compute the output of the IIR filter using Equation (7-1) because the length of its impulse response is too long (infinite in theory). Instead, the IIR filtering equation is expressed in a recursive form:

$$y(n) = \sum_{k=0}^{\infty} h(k)x(n-k) = \sum_{k=0}^{N} a_k x(n-k) - \sum_{k=0}^{M} b_k y(n-k)$$
 (7-3)

where the  $a_k$  and  $b_k$  are the coefficients of the filter. Thus, Equations (7-2) and (7-3) are the difference equations for the FIR and IIR filters respectively. These equations, and in particular the values of h(k), for FIR, or  $a_k$  and  $b_k$ , for IIR are very important objectives of the filter design. Note, that in Equation (7-3), the current output sample, y(n), is a function of past outputs as well as present and past input samples, that is the IIR is a feedback system of some sort. This should be compared with the FIR equation in which the current output sample, y(n) is a function only of past and present values of the input.

The choice between FIR and IIR filters depends largely on the relative advantages of the two filter types:

- FIR filters realised nonrecursively, that is by direct evaluation of Equation (7-2), are always stable with respect to oscillations. The stability of IIR filters cannot always be guaranteed<sup>4,5</sup>.
- FIR filters do not tend to accumulate errors due to their finite memory of past events. Precision of 12 to 16 bits is generally adequate for FIR filters. An IIR filter may require 16 to 24 bits (to handle truncation and roundoff errors) for comparable performance.

- FIR requires more coefficients for sharp cutoff filters than IIR. Thus for a given amplitude response specification, more processing time and storage will be required for FIR implementation. However, one can readily take advantage of the computational speed of the multirate techniques to improve significantly the efficiency of FIR implementations.
- In general, FIR is algebraically more difficult to synthesise, if CAD support is not available. However, at present there are many relevant books and publications<sup>4,5,10</sup> which are provided with ready to use software packages, greatly assisting in the filter design.

From the above discussion, it is clear, that for the purpose of the earlier discussed application the FIR filter is superior over its IIR counterpart. On this basis the low-pass decimating FIR filter have been designed, consisting of three decimation stages interlaced with four filtering stages (see Appendix).

The decimation stages are necessary in order to effectively implement a very low pass filter (3dB cut-off frequency at 0.7Hz) within the relatively high sampling rate of 50kHz. This technique (called multirate digital signal processing<sup>5,10</sup>) significantly reduces the number of necessary filter coefficients and the overall troughoutput of the filtering routine.

Each filtering stage uses the same FIR coefficient table containing 60 coefficients and therefore creating a 60 tap linear phase response digital filter by direct implementation of Equation (7-2). The table of coefficients have been calculated using the Remez Exchange Algorithm<sup>5</sup> which optimises the filter response for stop-band ripples and pass-band deviation. The number of coefficients is chosen as 60 in order to optimise the speed and accuracy of the procedure.

The procedure performs filtering of the two input signals simultaneously and writes the results to the appropriate registers at the same time (approximately every 1.3s), which insures that the dc correction coefficients are refreshed in the two channels at

the same moment. This feature is essential from the point of view of the vibration compensation routine, which requires symmetry of the dc components in the two input signals. The two resultant dc coefficients are used further in normalising the input measurement signals.

#### 7.6.4. Offset Zeroing and Normalisation

This part of the program performs simple arithmetic operations for the purpose of nulling the two photodetectors offsets and normalising gains in the two channels. The relevant coefficients used in this subroutine are produced by the autocalibration routine and/or dc filtering routine.

#### 7.6.5. Vibration Compensation

The two corrected signals in either ac-and-dc or ac-only configurations are passed to the vibration compensation procedure (see Appendix). The real time signal processing involves performing a subtraction and addition of the two respective channels and then the resultant difference is divided by the sum. This simple procedure is a straight implementation of the vibration compensation theory, described in detail in Chapter 6, and it takes only 19 instruction cycles (570ns) to perform. The routine produces a resultant, normalised and vibration free signal.

It is important to mention that the measurement signal at this point, unlike as in the other detection schemes, is independent of the dc light level in the optical path and depends only on the physical parameters of the current sensor, the conductor geometry and the distance between the sensor and the conductor. The magnitude of light intensity in the optical path affects only the noise performance of the system.

#### 7.6.6. Linearisation of the OCT Response Characteristic

As discussed earlier (Chapter 5), the magneto-optic Faraday effect based OCT is a polarimetric device and although the magneto-optic element rotates the linearly

polarised light with a direct proportionality to the applied magnetic field (electrical current), the sensor optical output power versus the input current is not linear. In order to facilitate the whole of the OCT dynamic, it is necessary to linearise the sensor sinusoidal response characteristic by real-time processing of the input signal.

Digital signal processing can provide a relatively easy solution to this problem by implementing fast function generation techniques. In this case the  $\sin^{-1}(x)$  function would have to be generated in order to return a linearised sensor response. There are three basic approaches for function computation which give real-time output with adequate accuracy<sup>5</sup>: lookup table, lookup table with linear interpolation and direct calculation (recursive solution or polynomial expansion).

The lookup table approach requires the most memory as opposed to direct calculation which requires the most computation; interpolation technique is intermediate. Lookup methods work for any function, even a table of numerical data, while direct calculation methods require an analytic form. While a lookup table with interpolation requires a derivative, the function need not be analytic, since the derivative can be precalculated numerically.

#### 7.6.6.1. Direct Lookup Table

A lookup table stores precomputed values of a function in memory. The x-input is truncated to the nearest address-value to generate the lookup address. The data at that address is the approximate value of the function. Because the same y value is output for any x-input value between adjacent addresses, direct lookup table has a significant error. To reduce the error, the memory size would have to be increased. Lookup table is therefore demanding on memory, although it is the fastest approach, since the only computation is an address-generation.

As mentioned in Section 7.2.1.1, the used DSP chip has a finite data memory. For this reason, the lookup table of a compromised number of values may only be implemented unless additional off-chip memory is provided. In order to assess the

error of the direct lookup table approach, the lookup table of the sin<sup>-1</sup>(x) was generated and the maximum output error across input values simulated for the table containing 256 coefficients (Figure 7-10). This number of coefficients was chosen arbitrarily with the main objective of using up the lowest possible memory space. Note, that the number of table coefficients is a multiple of 2, which is a requirement of the applied DSP algorithm.

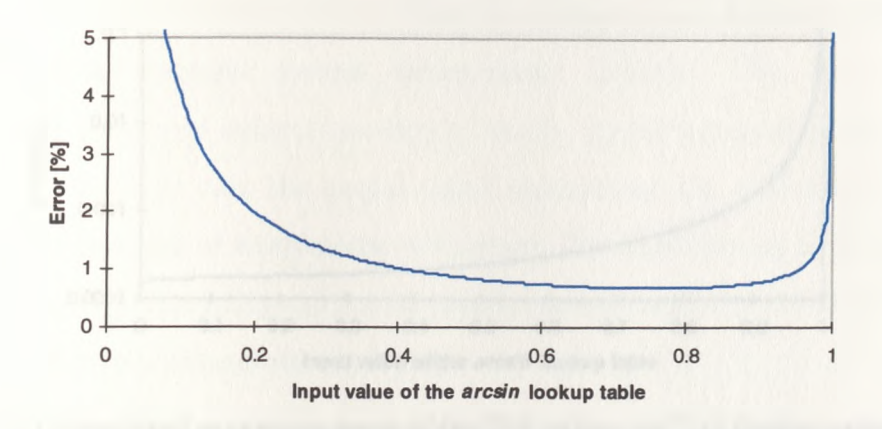


Figure 7-10 Simulated maximum error of the 256 values sin<sup>-1</sup>(x) direct lookup table

The maximum error of the derived output values for this particular table is very high (approximately 1% at its minimum) and neither a measurement nor protection class device would meet the accuracy requirements if the output was generated using this table. For this reason a second, more complex approach was taken into consideration - a lookup table with linear interpolation.

# 7.6.6.2. Lookup Table with Linear Interpolation

Linear interpolation provides a significant reduction in the errors. The method can be described as follows. The x-value is truncated to the nearest lookup address, x(n), which generates the first approximation, y(n). Then the increment, (x-x(n)), generates the interpolation correction,  $\Delta y$ , to be added to y(n). The interpolation computation reduces throughput by about a factor of 2 compared to a direct lookup table, but the error is reduced significantly. Even though the table must store both the function and its derivative values, the number of memory locations is considerably fewer than that

needed for a lookup table of comparable accuracy without interpolation, since fewer function values need to be stored.

The table of interpolation correction coefficients for the  $\sin^{-1}(x)$  lookup table from the previous section was calculated and the maximum error of output across input values simulated for the table with linear interpolation as shown in Figure 7-11.

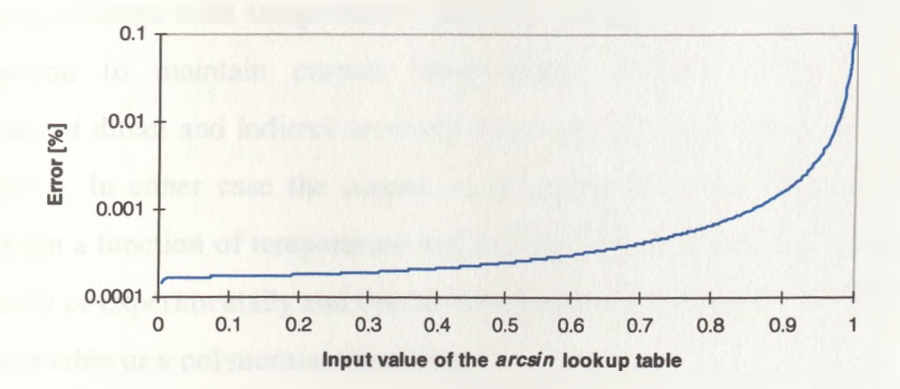


Figure 7-11 Simulated maximum error of the 256 values sin<sup>-1</sup>(x) lookup table using the linear approximation approach

The output error is maintained below 0.01% up to the input value of 0.95 and below 0.1% up to the input value of 0.995. It is very unlikely that the current sensor will be operating up to its maximum dynamic range, therefore the computation performance of the 256 coefficients  $\sin^{-1}(x)$  lookup table with linear interpolation is satisfactory in this application.

A further approach was investigated, namely direct calculation of the output function, and in particular the polynomial expansion of the  $\sin^{-1}(x)$  function; however due to the nature of  $\arcsin$  (the curve is tangential to the straight line passing through x-value = 1), it was impossible to achieve as good results as for the lookup table with linear interpolation.

The lookup table with linear interpolation routine is realised precisely as described above. The program consists of 256 coefficients of first approximation table  $\sin^{-1}(x)$  and 256 interpolation coefficients (see Appendix). The performance of this routine

may be affected by the additional round-off errors, present in the table of coefficients, and caused by the limited resolution of a number representation in the processor memory. This issue will be investigated in more detail in Chapter 8.

#### 7.6.7. Temperature Compensation

As shown in Chapter 6, the Verdet constant of the magneto-optic sensing material undergoes a change with temperature, thus the optical sensor requires temperature compensation to maintain current measurement accuracy. The two different approaches of direct and indirect recovery of sensor crystal temperature are detailed in Chapter 6. In either case the output signal representing the measured current is derived from a function of temperature and current. This function can be found either theoretically or experimentally and can be directly incorporated into the DSP software as a lookup table or a polynomial expansion.

In the present DSP software, relevant temperature compensation is realised using a polynomial approximation of the OCT inverted temperature characteristic to calculate the temperature compensated current output of the OCT. The OCT temperature characteristic is measured across the operating temperature range, e.g., -40C and +100C at a constant current, e.g., 2000A. Then it is inverted and scaled, and polynomial coefficients from 'a' to 'e' are evaluated. The subroutine uses these coefficients to calculate y(T) polynomial function (see Appendix):

$$y(T) = a + bT + cT^{2} + dT^{3} + eT^{4}$$
(7-4)

where T is the sensor temperature, and it is provided using either direct or indirect temperature recovery scheme. The output, temperature compensated signal, e(I), is generated according to the following expression

$$e(I) = e_0(I,T) \cdot y(T) \cdot k \tag{7-5}$$

where,  $e_0(I,T)$  is the input temperature and current dependent signal after normalisation and vibration compensation, and k is the intercept coefficient. The intercept coefficient is used to set the reference temperature for example at  $T_{ref} = 20C$ . At this temperature the compensated output is equal to the non-compensated one, i.e.,  $e(I) = e_0(I, T_{ref})$ , and  $y(T_{ref}) \cdot k = 1$ .

At present, the direct recovery scheme is used to supply the temperature signal to the DSP unit. This is realised using the fibre Bragg grating temperature sensor. More detailed information about this compensation scheme will be provided in the next chapter, concerned with the tests results of the prototype OCT current measurement system.

# 7.7. DSP Implementation of the Cross-Talk Compensation Scheme (Three-Phase System)

In Chapter 6, the influence of magnetically induced cross-talk on point type optical current transducers was analysed. The analysis demonstrated that for the bulk of the installations within the electricity network, the cross-talk level from adjacent phases will introduce measurement errors that are outside the required operational specifications. The solution to this problem, as presented in Chapter 6, is to directly process the information from all three phases to reject the cross-talk components. The preferred processing method is digital signal processing as the discussed compensation scheme requires solving in real time a set of equations in order to recover instantaneous currents in each phase. In addition, as the output signals from the sensors are already in a digital form, it seems most appropriate to carry out further processing without involving any D/A and A/D conversion.

The present DSP technology allows for a multi-processor operation of hardware and software within one integrated system. This is supported by the ADSP-2181 microprocessor which is a heart of the system developed within this research work.

As described in Section 7.2, the IDMA port (internal direct memory access port) in the above microprocessor can be used for efficient communication with the host system. The IDMA may be thought of as a gateway to all internal memory locations on the DSP and it does not require any ADSP-2181 processor intervention to maintain data flow. The host system can access the processor internal memory directly, without going through a set of 'mailbox' registers as it takes place in many other digital communication systems. Direct access to DSP memory increases throughput for block data transfers. Through the IDMA port, internal memory access can be performed with an overhead of only one DSP processor cycle per word.

The above feature of the DSP microprocessor allows for a design of an integrated 3-phase optical current measurement system with all required signal conditioning, and vibration, temperature and magnetic cross-talk compensation schemes directly implemented into DSP software. The concept of such a system is presented in Figure 7-12.

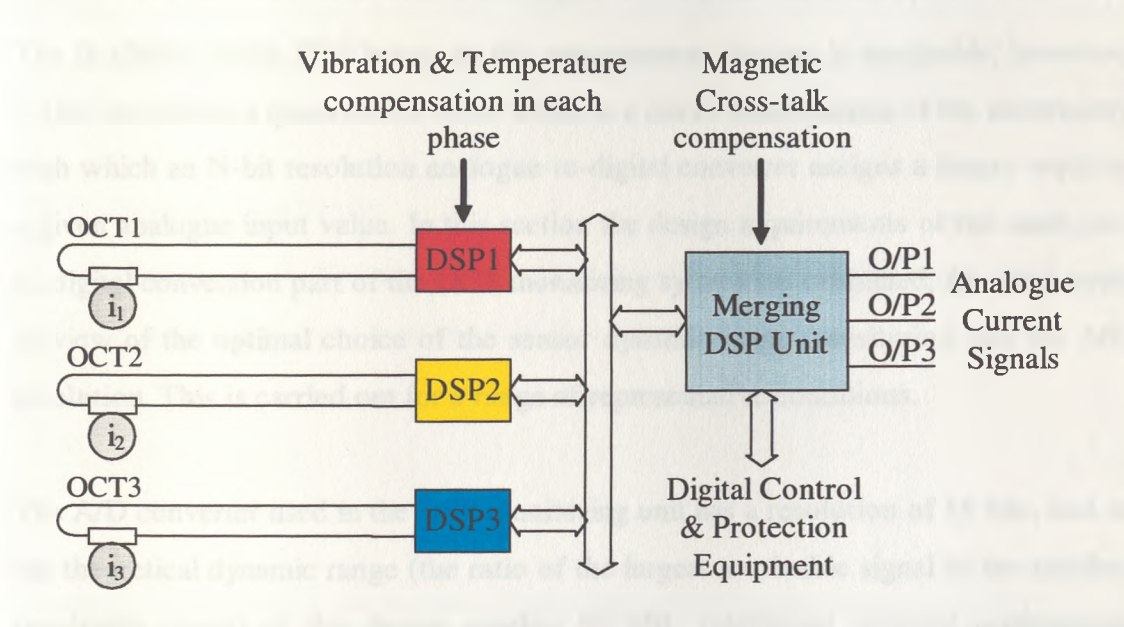


Figure 7-12 DSP implementation of magnetic cross-talk compensation scheme

In the above system, 1-phase single DSP processor units (as developed within this research work) are connected through their IDMA ports to the merging 3-phase DSP system. The merging unit controls the single phase units, performs magnetic cross-talk

compensation and generates three resultant output signals in a digital and/or analogue forms. The output signals may be easily adapted to the communication standards and protocols of a particular substation and the control metering and protection equipment used.

Even greater integration may be achieved using latest DSP technology. The present semiconductor industry, mostly driven by the computer market, is now able to produce fast (120 Mbytes/s) 32-bit floating point DSP microprocessors with large on-chip memories. With the present technology, even four of such processors may be integrated into one package and used separately in a multi-processing system<sup>3</sup>. These devices suit perfectly the application presented above; the complete 3-phase optical current measurement signal processing system may be implemented directly into one compact DSP multiprocessor module.

# 7.8. Error Associated with Analogue-to-digital Conversion Process

The flexibility which DSP brings to the measurement process is invaluable, however, it also introduces a quantisation error which is a direct consequence of the uncertainty with which an N-bit resolution analogue-to-digital converter assigns a binary word to a given analogue input value. In this section the design requirements of the analogue-to-digital conversion part of the OCT monitoring system are examined, from the point of view of the optimal choice of the sensor dynamic range (sensitivity) and the A/D resolution. This is carried out for a range of representative conditions.

The A/D converter used in the DSP monitoring unit has a resolution of 16 bits, and so the theoretical dynamic range (the ratio of the largest resolvable signal to the smallest resolvable signal) of this device reaches 96.3dB. Additional physical performance limitations of this device are not considered in this discussion, since the main concern is focused on assessing an error caused only by the limited resolution of the A/D converter.

The A/D converter samples the photodetector output signal that can change from the offset level (±several millivolts), when no optical power is being received, to the A/D maximum positive input voltage range of +10V. The photodetector offset can be either positive or negative, therefore the A/D converter must work in a bipolar configuration. This means that only approximately half of the A/D dynamic range is effectively used but seems unavoidable without involving null analogue circuits which could introduce additional dc drifts.

The measurement signal monitored by the A/D converter can oscillate around the dc bias voltage which is determined by the light intensity in the optical system and the photodetector gain. The dc bias can be set at any level between the photodetector offset and the A/D full-scale positive input, by adjusting the light source drive current and/or the photodetector gain. If the dc bias voltage is lower than half of the A/D full-scale positive input (0 to 5V in this case) the measurement dynamic is limited only by the OCT maximum dynamic range. However, if the dc offset exceeds half of the A/D full-scale positive input (5V to 10V), the measurement range is limited by the upper part of the measurement signal, which will be clipped for large currents.

#### 7.8.1. Quantisation Error

The maximum quantisation error of the sampled analogue measurement signal, for the case where the values are rounded up or down is equal to

$$e_{\text{max}} = \pm \frac{q}{2} \tag{7-6}$$

where q is the interval between the quantisation levels, and can be expressed by:

$$q = \frac{V_{fs}}{2^{N} - 1} \approx \frac{V_{fs}}{2^{N}}$$
 (7-7)

where  $V_{fs}$  is the full-scale input voltage range of the N-bit resolution A/D converter  $(V_{fs} = 20 \text{V} \text{ and } \text{N} = 16 \text{ bits in the system analysed above}).$ 

The quantisation error for each sample, e, is normally assumed to be random and uniformly distributed in the interval  $\pm q/2$  with zero mean<sup>4</sup>. In this case the quantisation noise power, or variance, is given by

$$\sigma_{e}^{2} = \int_{-q/2}^{q/2} e^{2} P(e) de = \frac{1}{q} \int_{-q/2}^{q/2} e^{2} de = \frac{q^{2}}{12}$$
 (7-8)

where, P(e) is the probability of value e occurring for each sample.

The square root of the above result, i.e.,  $\frac{q}{2\sqrt{3}}$ , represents the standard deviation and is equivalent to the rms value of the quantisation noise or the measurement uncertainty. On the other hand, assuming that the current varies sinusoidally with an angular frequency  $\omega = \frac{2\pi}{T}$ , the rms current measurement signal at the A/D input may be expressed in the following form:

$$E_{\rm rms} = \sqrt{\frac{1}{T} \int_0^T u^2 dt}$$
 (7-9)

where, the instantaneous input signal u is given by

$$u = E_0 \sin(2LVB_{max} \sin \omega t). \tag{7-10}$$

Here,  $E_0$  is the earlier discussed dc bias voltage, L is the length of interaction between the magnetic field and the polarised light passing through the magneto-optic material, V is the Verdet constant, and  $B_{max}$  is the amplitude of the sinusoidal magnetic field induced by the sinusoidal current.  $B_{max}$  is directly proportional to the busbar current

and, for example, for the earlier simulated case of the rectangular cross-section busbar,  $B_{max}$  can be expressed in terms of the current as

$$B_{\text{max}} = I \cdot \frac{0.00404 \cdot \sqrt{2}}{1000} \tag{7-11}$$

where I is the rms current in the busbar. Note, that for rms current of 1000A, the simulated rms magnetic flux density along the longitudinal cross-section of the magnetooptic element is 0.00404T.

Consequently, the OCT current measurement error associated with the analogue-todigital conversion process can be expressed in the following form:

$$\sigma(\%) = \frac{\sigma_e}{E_{rms}} \cdot 100 = \frac{q}{2\sqrt{3}} \cdot \frac{100}{E_0 \sqrt{\frac{1}{T} \int_0^T \sin^2(2LVB_{max} \sin \omega t) dt}}$$
(7-12)

The above expression may be solved using numerical methods (i.e., Mathcad software package) and plotted with respect to the changing parameters: sensor sensitivity (LV), dc bias voltage, A/D resolution, or busbar current.

# 7.8.2. Case Studies

The initial calculations based on Equation (7-12) reveal that the errors associated with quantisation of the OCT analogue signal may significantly inhibit the overall sensor performance. This takes place in cases were resolution of the A/D converter is not matched to the sensor maximum dynamic range (or sensitivity) and can be best illustrated through specific examples. In the present section this is shown for the range of sensors developed over the course of research, namely: 15mm and 25mm linear-design OCTs based on TGG magneto-optic crystals, and 100mm multi-pass reflective design based on FR5 glass. These three sensors exhibit different sensitivities and

assuming that they operate with the earlier considered rectangular busbar their maximum dynamic ranges are as follows:

- TGG 15mm, 157kA,
- TGG 25mm, 93kA,
- FR5 100mm, 36kA.

Depending on the rated current, these sensors may be used in various applications in high voltage transmission systems, i.e., protection, measurement and/or combined protection and measurement applications. In most of the practical arrangements, nominal current ratings vary from several hundred Amps to 5kA. In this discussion, a nominal current rating of 1000A is chosen, in which case the most sensitive sensor from the above OCTs (FR5 100mm) may be used as a protection device (Protection Class 5P30 or 10P30 in which the nominal current may be exceeded 30 times).

The remaining TGG sensors have much higher dynamic ranges and could successfully operate with higher than 1000A rated currents. However, in order to expose compatibility problems that might occur when selecting inappropriate combinations of sensors and resolutions of A/D converters this value of nominal current seems exquisite. It can be shown, that even in these cases, the sensors can meet required accuracy specifications if the A/D resolution is sufficiently high.

#### 7.8.2.1. Protection Applications

As shown in Chapter 5, accuracy specifications for the protection class 5P30 and 10P30 current transducers are respectively 1% and 3% at the rated current (1000A) and 5% and 10% at the maximum operational current (30kA). Figure 7-13 compares these accuracy specifications with the quantisation errors for the three above sensors working at the nominal current of 1000A, as derived from Equation (7-12). The dc bias voltage, E<sub>0</sub>, is set for each sensor to the maximum possible level, such that at the 30kA current, the upper part of the signal reaches the positive full-scale of the A/D converter input range.

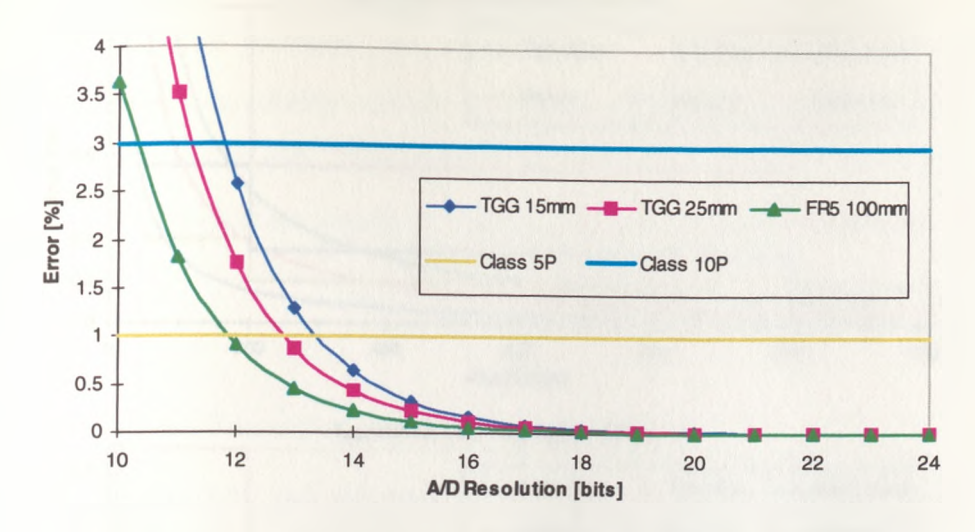


Figure 7-13 Quantisation errors vs. A/D resolution at 1000A

In Figure 7-13 it is clearly shown that 12 bits of resolution is sufficient to meet the protection class 10P for all the sensors and 14 bits of resolution to meet the protection class 5P.

### 7.8.2.2. Metering Applications

The metering accuracy specifications for current transducers as shown in Chapter 5 (Table 5-1) are more complex than the protection specifications. In Figure 7-14 the following metering classes: Class 0.1, Class 0.2 and Class 0.5, are compared with the performance of the previously considered OCTs operating with 16 and 18 bit A/D converters. Again, the dc bias voltage, E<sub>0</sub>, is shifted right up to the maximum level for each sensor, allowing a measurement of 1.5kA at a maximum.

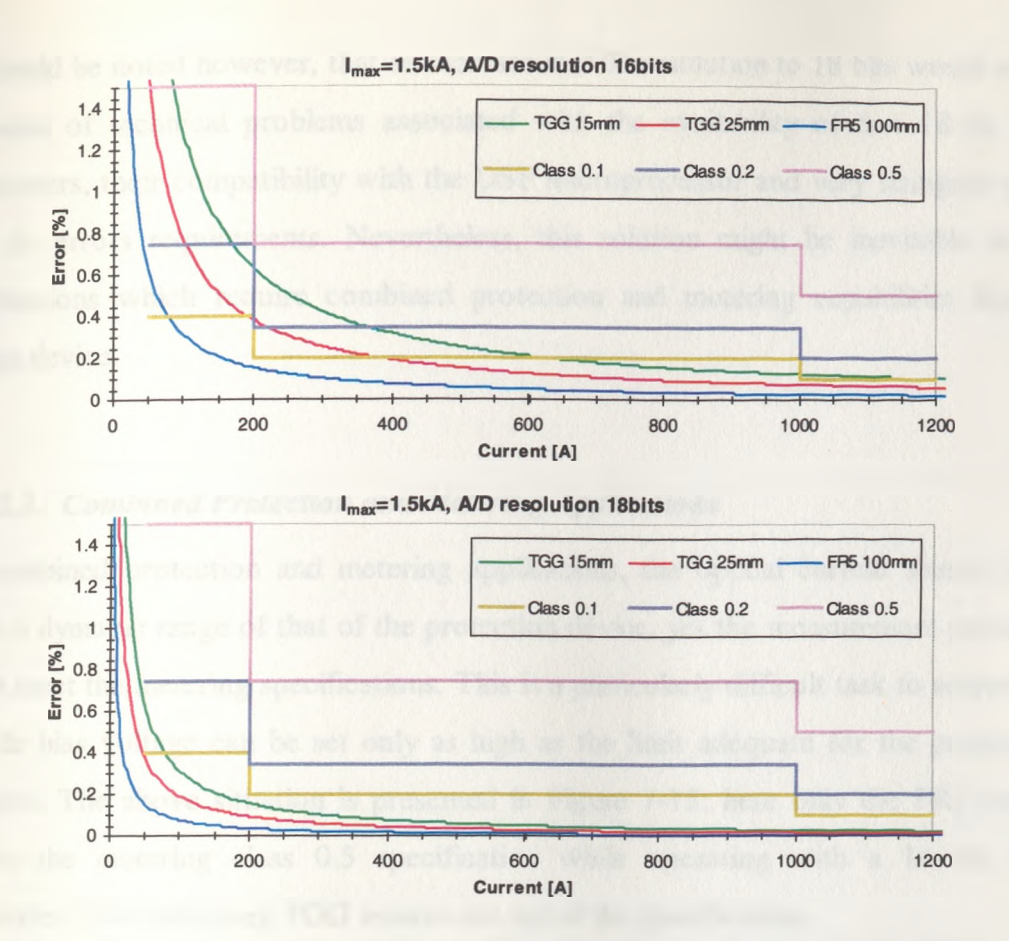


Figure 7-14 Quantisation errors vs. current for 16 and 18 bit A/D converters compared with metering class specifications

Clearly, none of the above sensors meets the metering Class 0.1 specification while working with a 16 bit A/D converter. Class 0.2 and 0.5 specifications are met by the FR5 100mm, however the remaining TGG sensors are clearly not matched to this A/D resolution and/or rated current. It would be desirable to either increase the sensor sensitivity or choose an application in which the nominal current rating is higher than 1000Amps.

Alternative solution would be to increase the A/D resolution to for example 18 bits. In this case all sensors meet the metering Class 0.2 specification and the two sensors, FR5 100mm and TGG 25mm can even comply with the metering Class 0.1 specification (see Figure 7-14).

It should be noted however, that an increase in A/D resolution to 18 bits would cause a series of technical problems associated with the availability of fast 18-bit A/D converters, their compatibility with the DSP microprocessor and very stringent noise and dc errors requirements. Nevertheless, this solution might be inevitable in the applications which require combined protection and metering capabilities from a single device.

#### 7.8.2.3. Combined Protection and Metering Applications

In combined protection and metering applications, the optical current sensor must have a dynamic range of that of the protection device, yet the measurement precision must meet the metering specifications. This is a particularly difficult task to achieve as the dc bias voltage can be set only as high as the limit adequate for the protection devices. The above situation is presented in Figure 7-15; here only the FR5 sensor meets the metering class 0.5 specification while operating with a 16 bit A/D converter. The remaining TGG sensors are out of the specification.

The measurement performance improves dramatically as the A/D resolution is increased to 18 bits. In this case all sensors meet the metering class 0.5 specification and the FR5 sensor even complies with the Class 0.1 specification.

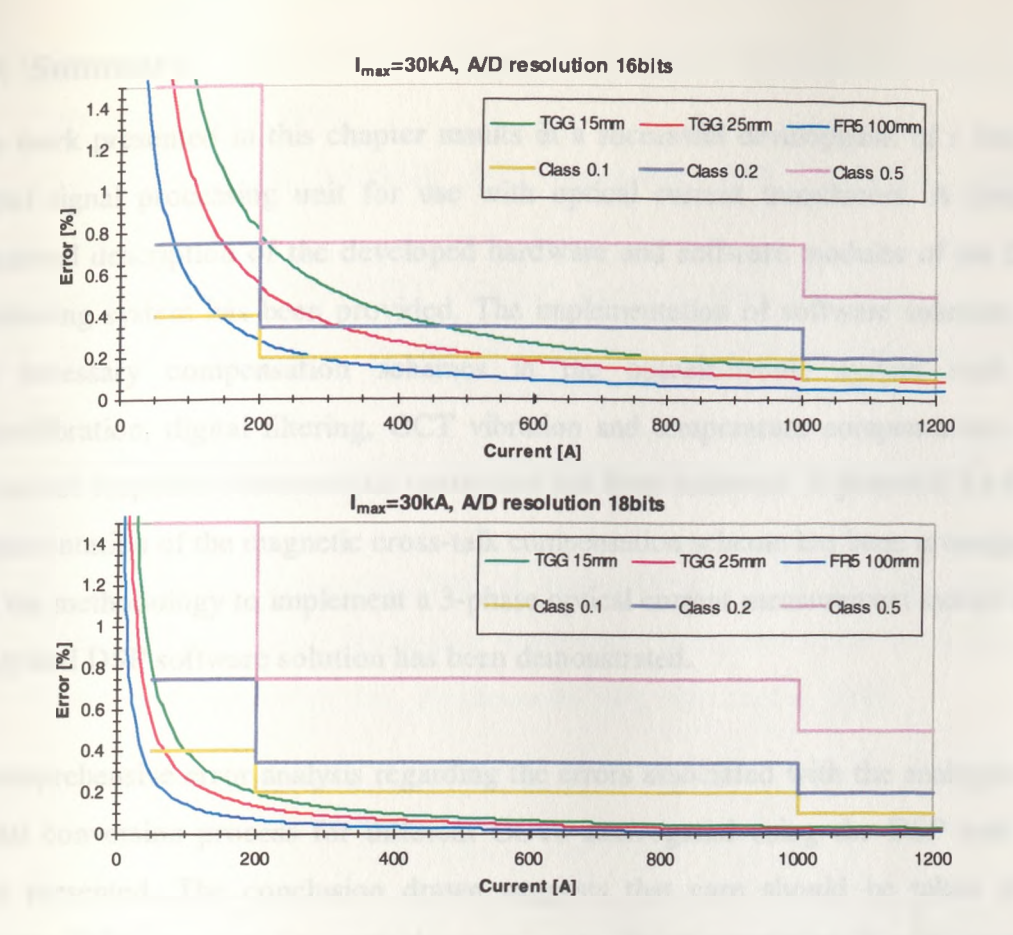


Figure 7-15 Performance of the combined metering and protection OCTs

To summarise the above discussion, some recommendations to provide the required accuracy of the OCT monitored by the DSP system, are given:

- it is desirable to use the whole of the sensor response characteristic in order to relax the harsh design requirements of the photodetector circuit and utilise more sensitive OCTs;
- the sensor maximum current measurement capability should only slightly exceed the specified maximum operating current in both protection and metering applications;
- the dc bias voltage should be maintained at the highest possible level matched to the particular application;
- the A/D resolution should not be lower than 18 bits for the combined metering and protection applications unless the metering class 0.5 is satisfactory in the particular application; in that case the resolution of 16 bits is sufficient.

### 7.9. Summary

The work presented in this chapter results in a successful development of a flexible digital signal processing unit for use with optical current transducers. A detailed functional description of the developed hardware and software modules of the DSP monitoring system has been provided. The implementation of software solutions for the necessary compensation schemes in the optoelectronic system such as: autocalibration, digital filtering, OCT vibration and temperature compensation, and the sensor response characteristic correction has been achieved. A potential for DSP implementation of the magnetic cross-talk compensation scheme has been investigated and the methodology to implement a 3-phase optical current measurement system into integrated DSP software solution has been demonstrated.

A comprehensive error analysis regarding the errors associated with the analogue-to-digital conversion process for different OCTs interrogated using the DSP unit has been presented. The conclusion drawn suggests that care should be taken while selecting OCTs for operation with the analogue-to-digital converters, in order to meet stringent accuracy requirements for metering and protection class instruments within the power industry.

The ac and dc current measurement capabilities of the system will be demonstrated in the next chapter concerned with the comprehensive testing of the discussed DSP unit and the relevant OCTs.

# 7.10. Chapter References

- 1) "DSP Microcomputer: ADSP-2181", Analog Devices, Inc., 1995,
- 2) "ADSP-2106X SHARC DSP Microcomputer Family", Analog Devices, Inc., 1996,
- 3) "Quad-SHARC DSP Microcomputer Family", Analog Devices, Inc., 1997,
- 4) E. C. Ifeachor, B. W. Jervis, "Digital Signal Processing a practical approach", Addison-Wesley Publishers Ltd., 1993,

- 5) R. J. Higgins, "Digital Signal Processing in VLSI", Prentice-Hall, Englewood Cliffs, New Jersey, 1990,
- 6) "16-Bit, 200 kSPS BiCMOS A/D Converters: AD976/AD976A", Analog Devices data sheets,
- 7) "Monolithic 16-Bit DACPORT: AD669", Analog Devices data sheets,
- 8) P. Horowitz, W. Hill, "The Art of Electronics", Cambridge University Press, 1996,
- 9) "ADSP-2100 Family, EZ-KIT Lite Reference Manual", Analog Devices, Inc., 1995,
- 10) The Applications Engineering Staff of Analog Devices, DSP Division, edited by A. Mar, "Digital Signal Processing Applications using the ADSP-2100 Family", Volume 1, Prentice-Hall, Inc., Englewood Cliffs, New Jersey, 1992.

# 8. Tests Results

#### 8.1. Introduction

In order to verify the operational characteristics of the developed optical current measurement system several comprehensive tests have been carried out in the laboratory and field conditions. The testing concentrated on the experimental evaluation of the range of prototype current sensors, interrogation optoelectronics, signal processing hardware and the relevant DSP software routines. This chapter reports on this work and provides a detailed description of the experiments carried out during the various stages of the research.

A key component in the successful operation of the OCT system is a high gain, low noise photo-receiver which must be optimised in terms of sensitivity, bandwidth, gain, dc offset and stability over a wide range of operational temperatures. The design of this unit formed a significant portion of the research effort and consequently is described in some detail in the following text.

In addition, this chapter describes the evaluation of the linearisation procedure used to relate the OCT response characteristic to the applied current along with a detailed explanation of the parameters which limit its overall performance. Following this, comprehensive vibration and temperature testing of the OCT is reported, and an assessment made of the efficiency of the proposed vibration and temperature compensation schemes implemented in hardware and software, and tested over a range of representative conditions. This chapter also discusses the ac and dc current measurement capabilities of the OCT system, and presents the initial results of the OCT field trial at the British Short-Circuit Testing Station (BSTS). The tests results from the field trial are compared with the similar independent testing carried out at the Strathclyde University.

# 8.2. Low Noise Photodetector Design

The photodetectors used in the optoelectronic system convert input optical power levels into electrical signals. The photodetector performance is crucial from the point of view of accuracy of the entire optical current measurement system, therefore more space was allocated to this aspect of the work.

#### 8.2.1. Design Criteria

The photodetector circuit required for the OCT must combine excellent noise characteristics with a relatively wide operational bandwidth to implement the vibration compensation scheme as discussed in Chapter 6. This imposes additional requirements of a high sensitivity and a relatively wide bandwidth on the photodetector while the light source has to be pulsed with a high frequency to permit appropriate recovery of the measurement signal. In addition, the use of the multi-pass FR-5 device gives rise to a high attenuation in the optical path, which must be compensated for by applying high gain to the photo-receiver circuit. Finally the requirement for high accuracy and dc current measurement by the OCT implies highly stable dc operation from the amplifier. All these requirements contradict each other which adds to the complexity of the photodetector design.

The design criteria of the photo-receiver can be outlined as follows:

- to choose an optimal photodiode circuit configuration,
- to achieve relatively high bandwidth, good dc performance and linear response from the photodetector,
- to achieve high sensitivity and reduce the noise of the designed unit.

# 8.2.2. Choice of the Photodiode Circuit Configuration

Amongst a variety of the circuit configurations a transimpedance amplifier was chosen to monitor the PIN photodiode. This circuit configuration, with its simplicity (Figure 8-1), directly transforms a photodiode current into a voltage on the output of the op-

amp and provides a linear relationship between the input optical power and the output signal,  $E_{out}$ , with a very high amplification<sup>1,2</sup>:

$$E_{out} = I_p R_f \tag{8-1}$$

where,  $I_p$  is the photodiode current directly proportional to the incident light power and  $R_f$  is the feedback resistor.

The photodetector chosen for the receiver was a PIN (P-type, Intrinsic, N-type of semiconductor doping) photodiode. This photodiode does not require high biasing voltages, as is the case with an avalanche photodiode (typically 100V), therefore it is relatively straightforward to use.

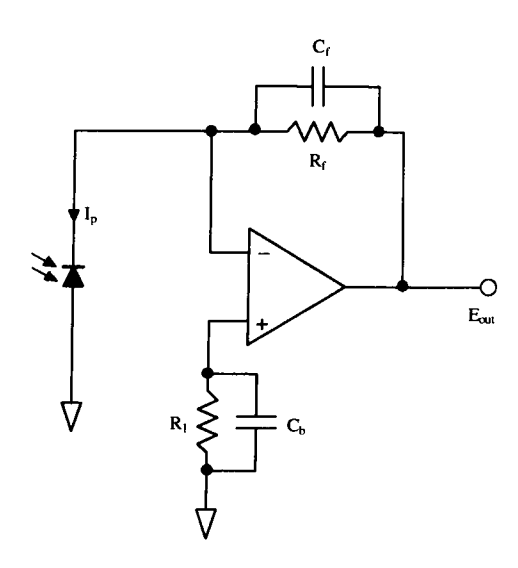


Figure 8-1 Transimpedance configuration of the photodiode monitoring op-amp

#### 8.2.2.1. DC Performance and Bandwidth

To achieve high amplification,  $R_f$  should be made as large as other constraints permit. At higher resistance levels, the amplifier begins to develop significant thermal dc voltage drift due to the temperature coefficient of the amplifier input current. To mitigate against this error, an equal resistance  $R_1$  is commonly connected in series with the op-amp non-inverting input and capacitively bypassed to remove most of its

noise. The remaining dc error is determined by the mismatches between the amplifier input currents and between the two resistors. An op-amp with low initial dc input voltage and current levels and low temperature drifts of these parameters should be selected to minimise the dc errors.

The 3dB bandwidth is determined by R<sub>f</sub> and C<sub>f</sub> according to the equation:

$$f_{3dB} = \frac{1}{2\pi R_f C_f} \tag{8-2}$$

For the circuit incorporating the vibration compensation scheme, the necessary bandwidth is near 500kHz to achieve a correct shape of the amplified  $\approx$ 50kHz square wave signal present at the input of the photodetector. In order to ensure a stable operation of the amplifier,  $C_f$  has to be around 0.7pF (value determined experimentally for the used type of an op-amp), then the highest possible feedback resistor  $R_f$  is approximately 500k $\Omega$ .

Another constraint affecting the bandwidth of the photodetector is the op-amp bandwidth or slew-rate. Assuming that the op-amp will have to operate with a square shape signal with a period of  $10\text{-}20\mu\text{s}$  and amplitudes between 0 and 10V, the slew-rate should exceed  $10\text{V}/\mu\text{s}$ .

In the present design the photodiode maximum operating frequency is 3 orders of magnitude higher than the required bandwidth therefore its performance does not affect the photodetector bandwidth.

## 8.2.2.2. Noise Performance

As mentioned above, the value of the feedback resistor  $R_f$  in a current-to-voltage converter largely determines noise and bandwidth as well as gain. Noise contributed directly by the resistor has a spectral density<sup>1,2,3</sup> of  $\sqrt{4kTR_f}$ , where k is Boltzman's

constant and T is the temperature and appears directly at the output of the current to voltage converter without amplification. If the input optical power is assumed constant, an increase in resistance not only raises the output noise by a square root relationship but also increases the output signal in direct proportionality. Signal-to-noise ratio, then, tends to increase by the square root of the resistance.

Noise from the op-amp also influences the output due to the high feedback resistance and the diode capacitance. The amplifier noise sources are modelled in Figure 8-2 as an input noise current,  $i_n$ , the input noise voltage,  $e_n$ , and the feedback resistor noise voltage,  $e_{Rf}$ .

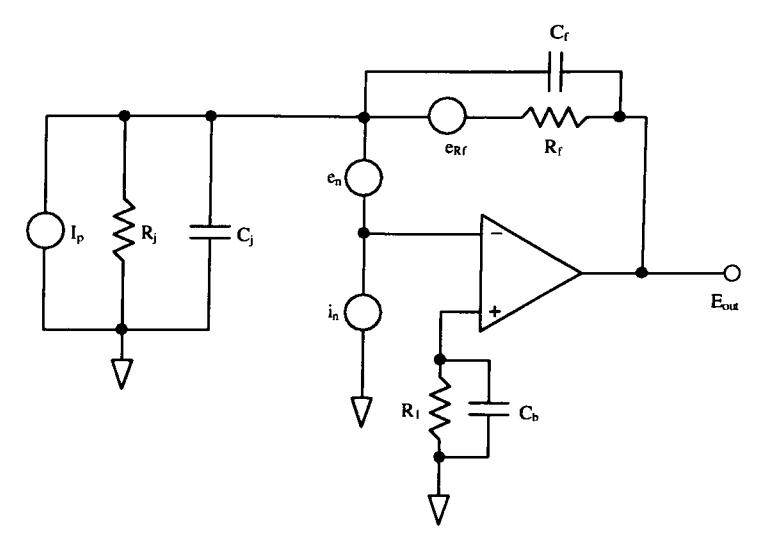


Figure 8-2 Main sources of noise in the photo-receiver circuit

The current noise flows through the feedback resistor experiencing the same gain as the signal current. It consists of the shot noise of the input bias current and signal current and has a noise density<sup>2,3</sup> of  $\sqrt{2qi}$ , where i is either bias current or signal current and q is an electron charge. Selecting an op-amp with input currents in the picoamp range makes the bias noise component negligible for practical levels of feedback resistance.

The input noise voltage of the amplifier would at first seem to be transferred with low gain to the output. That is true at dc where its gain  $1+R_f/R_j$  is kept small by the large

diode resistance,  $R_j$ . The capacitance,  $C_j$ , of the diode alters the feedback at higher frequencies adding very significant gain to  $e_n$ . A diode with  $C_j$  as small as possible should be selected to minimise the voltage noise gain which becomes  $1 + C_j/C_f$  at the frequency  $f_{3dB}$  of the amplifier. This gain remains at this level far beyond the amplifier bandwidth and is eventually suppressed by the op-amp bandwidth limit.

#### 8.2.3. Selection of an Op-Amp

As mentioned above, a relatively fast op-amp should be selected to meet the required value of slew-rate or bandwidth. Fast op-amps however tend to have poorer dc and noise performance compared to their slower alternatives. The essential factors are then:

- input voltage and current offsets and their temperature drifts,
- equivalent input voltage and current noise densities,
- op-amp bias current.

All of these factors should be kept as small as possible, however this conflicts with the required speed of the device. An ideal choice for this application would be a FET opamp having very low values of bias current and therefore enabling the shot noise to be maintained at a low level. However, these amplifiers are relatively slow, or if they are made fast, their noise performance is unacceptable for this application.

Eventually, a bipolar precision operational amplifier OP-37 was chosen as the most appropriate device for this purpose. This op-amp has a relatively high slew-rate of  $17V/\mu s$ , low voltage noise of  $3nV/\sqrt{Hz}$  (1kHz) and low input offset voltage of  $10\mu V$  with its temperature drift of only  $0.2\mu V/^{\circ}C$ .

#### 8.2.4. Preliminary Tests

A photodetector as shown in Figure 8-1 was built and placed inside a shielded metal enclosure along with the photodiode. An additional reverse biasing of the photodiode

was implemented to reduce diode capacitance C<sub>j</sub>. The power supply to the photodetector was carefully filtered.

The prime objective of the test was to measure the output noise of the photodetector as well as the dc offset and its temperature drift.

#### 8.2.4.1. Noise Performance

The level of noise on the output of the photodetector was so low that accurate measurement of the noise floor was very difficult with the available equipment. To measure this level of noise an additional low noise, wide bandwidth ac amplifier was built whose prime task was to amplify the output noise of the photodetector to a detectable level by the digital oscilloscope. The noise amplifier bandwidth was matched to the photodetector bandwidth (500kHz). A block diagram of the test setup is shown below in Figure 8-3.

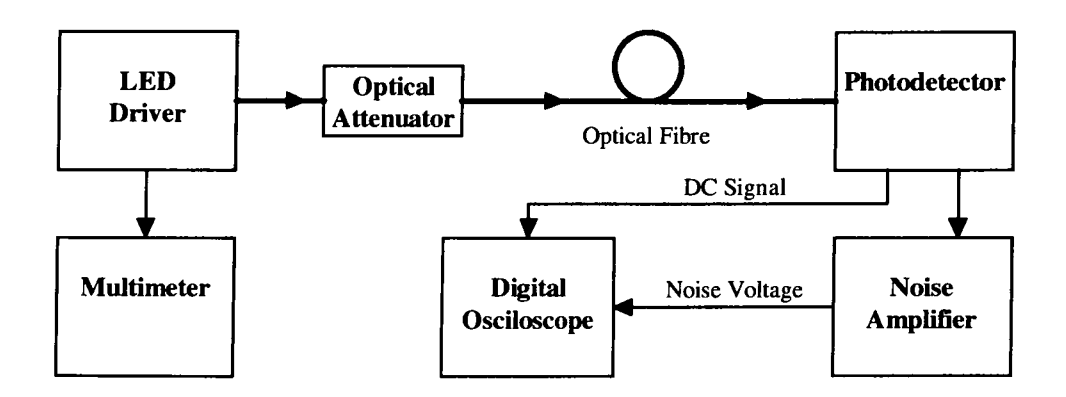


Figure 8-3 Experimental set-up

An OCT or optical couplers or their combination were used as an optical attenuator to adapt the level of optical power at the photodetector input. Additionally, the level of received optical power could be controlled by a means of the drive current of the transmitting LED.

Using the above set-up, the initial output noise voltage of the photodetector (scaled down by the noise amplifier gain) was measured to be 1.4mV (pk-pk) with an

uncertainty of 0.06mV, which was the total noise of the measurement equipment and noise amplifier. This error along with the errors of the measurement equipment did not exceed 5% of the measured value. This level of error was acceptable, as the main objective of the test was to assess the approximate minimum detectable input optical power and compare the photodetector performance over a range of prototypes. Figure 8-4 shows values of measured noise voltage on the photodetector output with a gradually increased output dc signal, proportional to the input optical power.

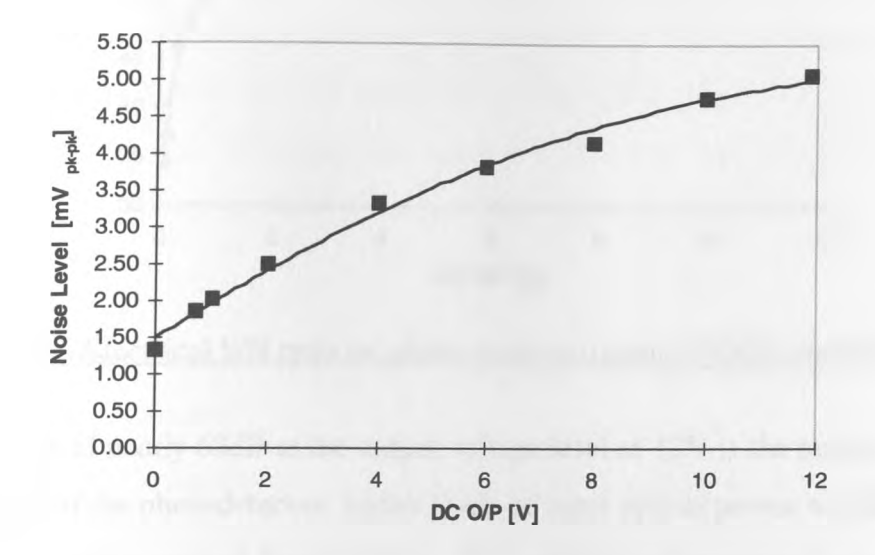


Figure 8-4 Photodetector noise vs. output voltage (500kHz bandwidth)

On the basis of the above results, the minimum detectable optical power of the unit can be calculated using Equation (8-1) as  $5.08 \, \mathrm{nW}$  (-53dBm). Note, that in this case a feedback resistor value was set to  $492 \, \mathrm{k}\Omega$ , and the photodiode responsivity was 0.6A/W. The maximum limit of the received optical power can be calculated when the output of the photodetector reaches 13V (power supply of the circuit was  $\pm 15 \, \mathrm{V}$ ); the maximum detectable power is then  $44 \, \mathrm{\mu W}$  (-13.6dBm). The photodetector dynamic range is the ratio of these two figures and is approximately 40dB in terms of the received optical power levels.

If the signal from the photodetector output increases, following an increase of optical power, the noise also increases, as described in Paragraph 8.2.2 and shown in Figure 8-4. It is convenient to use the S/N (Signal-to-Noise) ratio parameter to illustrate this

relationship. In this case the signal is represented by the photodetector output voltage rather than the optical power level. Figure 8-5 shows an improvement of S/N ratio with the increasing output voltage (proportional to the received optical power).

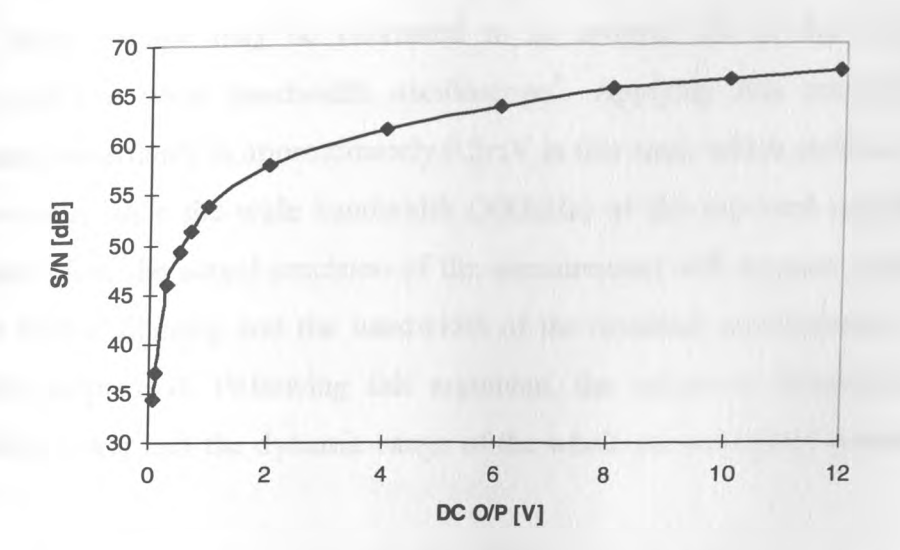


Figure 8-5 Electrical S/N ratio vs. photo-receiver output (500kHz bandwidth)

The S/N ratio of nearly 68dB at the output voltage level of 13V is the maximum noise performance of the photodetector, higher levels of input optical power would saturate the op-amp circuit supplied from  $\pm 15$ V in this particular experimental set-up. Note, that the photo-receivers are supplied from  $\pm 18$ V when configured to work with the DSP unit.

In this discussion, peak-to-peak values of noise and dc output signals are taken into consideration. However, most commonly, the S/N ratio is defined as the ratio of rms values of signal and noise as uncorrelated signals over the limited bandwidth<sup>8</sup>. This would be the most appropriate approach, but is extremely difficult to implement using the available test equipment. Since the levels of noise in this particular case are very low, only peak-to-peak values could be successfully (with low but sufficient accuracy) measured using an oscilloscope. For this reason, the above results of S/N values are calculated only for the purpose of comparison between the range of photo-receiver prototypes and the operational conditions of the circuit.

Considering the case when the dc output limit is set at the operational level of 7.5V, the rms signal modulated by the TGG sensor with a crystal length of 25mm is equal to approximately 100mV for a corresponding busbar current level of 1000A<sup>4</sup>. According to the above noise measurement results, the pk-pk noise level is approximately 4mV. The rms noise voltage may be estimated to be around 1/8 of the pk-pk value measured using a wide bandwidth oscilloscope<sup>3</sup>. Applying this assumption, the measurement uncertainty is approximately 0.5mV in this case, which yields an error of 0.5%. However, since the wide bandwidth (500kHz) of the received signal is taken into consideration, the actual precision of the measurement will increase as the signal undergoes further filtering and the bandwidth of the resultant measurement signal is significantly suppressed. Following this argument, the minimum detectable optical power will be lower and the dynamic range of the whole measurement system will be increased.

#### 8.2.4.2. DC Performance

To assess the dc behaviour of the photodetector a simple test of the dc output voltage was carried out while there was no light at the photodiode and the photodetector was heated to approx. 60°C. The dc offset vs. temperature is shown in Figure 8-6.

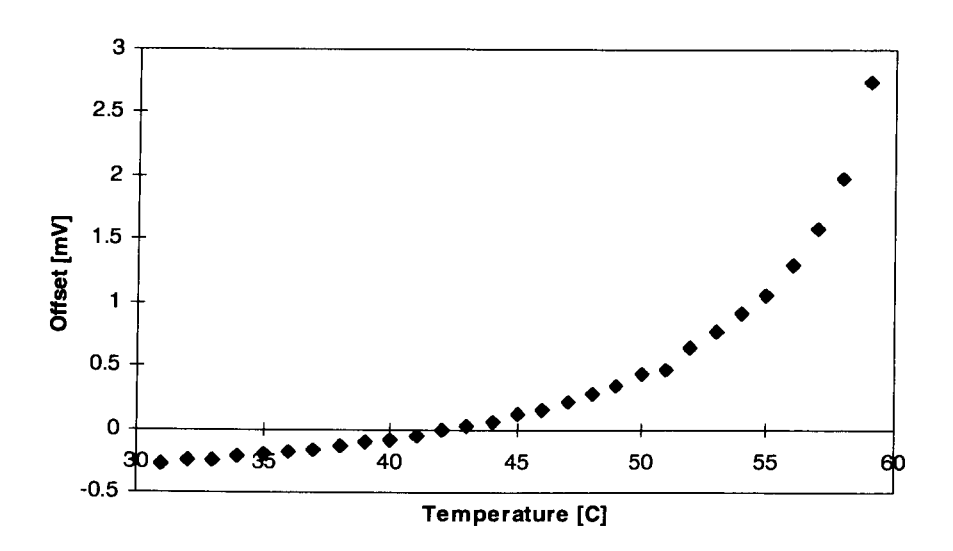


Figure 8-6 Photodetector offset drift vs. temperature

The photodetector offset is around 0.3 mV at  $30^{\circ}\text{C}$  (feedback resistor  $R_f = 492 \text{k}\Omega$ ) and rises up to approximately 3 mV at  $60^{\circ}\text{C}$ . However, the initial slope of the curve presented in Figure 8-6 is equal to only  $0.25 \text{mV}/10^{\circ}\text{C}$ , which gives an error of  $\pm 0.25 \text{mV}$  when the temperature of the unit changes of  $\pm 10^{\circ}\text{C}$ . Assuming that there is no additional error, i.e., noise, gain error etc., and the operational level of the output is set to 7.5V, an error in the measurement of 1000A current by using the same type of sensor (TGG, 25mm) would be 0.18% and at 12V, 0.06%. However, this error could be minimised by keeping the whole unit at a semi-constant temperature and subtracting the initial offset within the autocalibration procedure as discussed in Chapter 7.

#### 8.2.5. Photodetector with J-FET Input Stage

The initial 1.5mV pk-pk noise of the photodetector (Figure 8-4) that is mainly caused by the op-amp input bias current could be decreased by adding a low noise J-FET amplifier at the op-amp input. The circuit from Figure 8-1 was modified as shown below in Figure 8-7. The J-FET in front of the op-amp functions as a source follower, but it is connected to the op-amp and feedback loop in such a way that it does not change the basic impedance structure. The photon current flows to the J-FET gate and generates a voltage change. The source follower transfers the voltage variation to the non-inverting input at a lower impedance. In its negative feedback loop, the op-amp also reacts by varying its output voltage, which causes a current to flow through the feedback network until the source voltage equals the voltage at the non-inverting input.

The source follower provides no voltage gain but enough current gain that the noise caused by biasing the op-amp is removed. The main noise source of the circuit presented here is the input current noise at the J-FET gate, which is about 1pA/Hz<sup>1/2</sup> at 100kHz for the 2N4338 transistor used<sup>5</sup>.

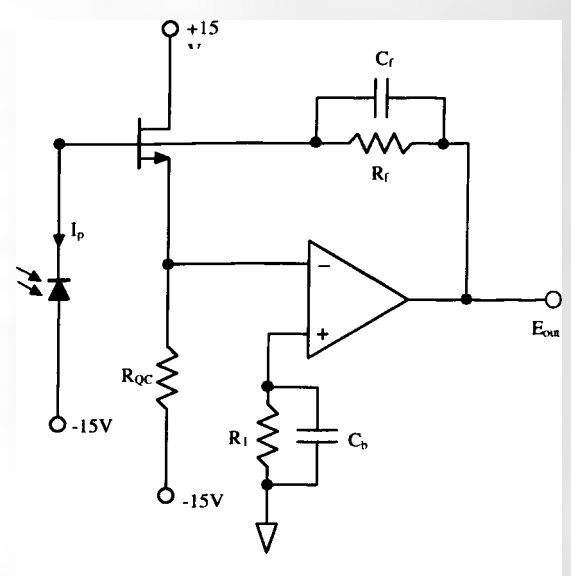


Figure 8-7 J-FET photodetector circuit

To assess the circuit performance analogues tests were carried out as for the previously considered conventional design of the photodetector (see Figure 8-3).

#### 8.2.5.1. Noise Performance

By using a high impedance input stage, the initial noise of the photodetector was suppressed by a factor of 3. In this case the minimum received optical power over the 500kHz bandwidth is near -58dBm. Figure 8-8 shows a comparison of the noise levels on the outputs of the two photodetectors, the conventional one and the J-FET. Figure 8-9 shows signal-to-noise ratios of the two designs; it is clear that the higher the output voltage, the lower the difference between the two units. This can be explained by the fact that with the increased optical power, the shot noise becomes the main contributor to the noise level of the two circuits. The initial noise level could be still suppressed by the use of ultra low noise J-FET transistors.

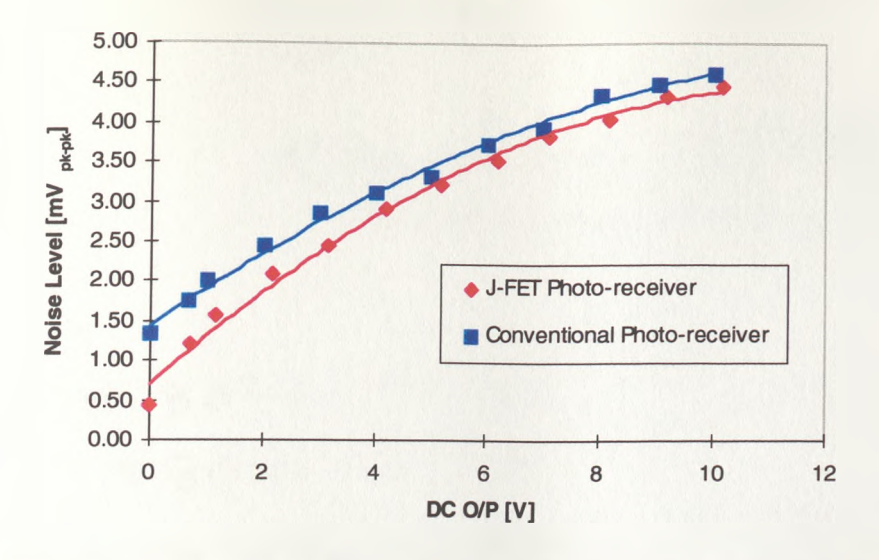


Figure 8-8 Comparison of the two photodetectors output noise levels

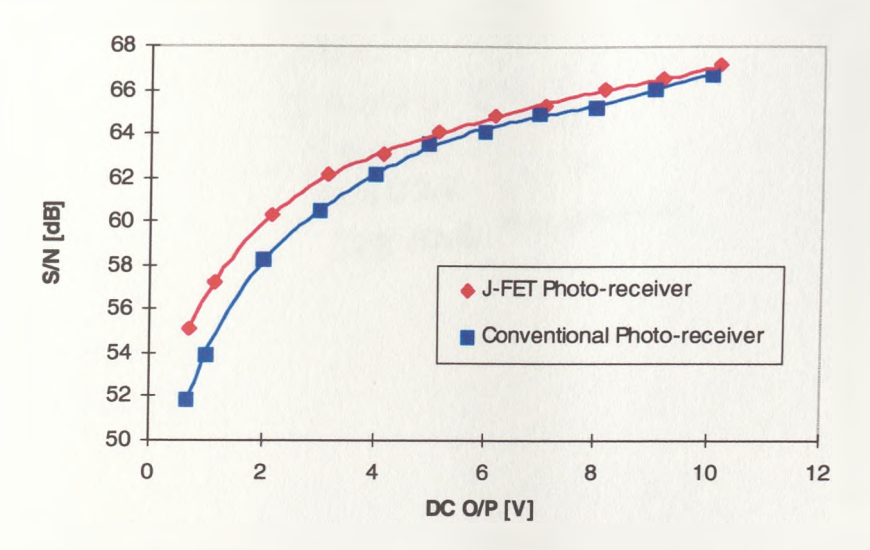


Figure 8-9 Comparison of the two photodetectors S/N ratios

### 8.2.5.2. DC Performance

An analogous test to that in Section 8.2.4 was carried out in order to determine the dc performance of the J-FET photodetector design. To compare the differences in dc offsets of the two photodetectors the two curves are plotted in one graph (Figure 8-10).

It is obvious that the magnitude of the dc offset of 1.1V and its temperature coefficient of -7.4mV/10°C is not acceptable for the high precision measurement

device. Such high dc offset is caused by the unbalanced source current of the J-FET. To improve the performance of the source follower, an additional J-FET transistor was used as a current source for the original transistor. The modified circuit is shown in Figure 8-11.

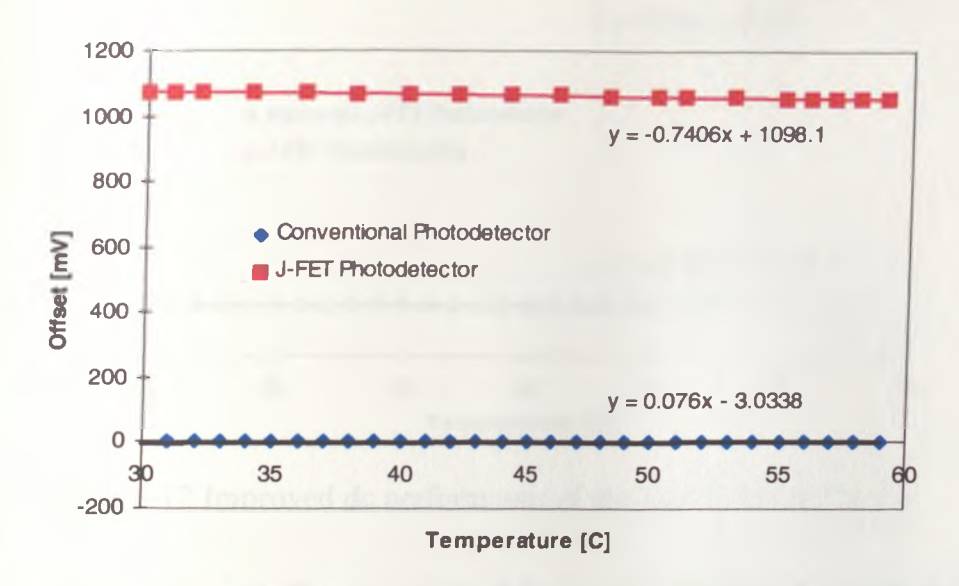


Figure 8-10 The dc performance of the J-FET prototype and the conventional photodetector design

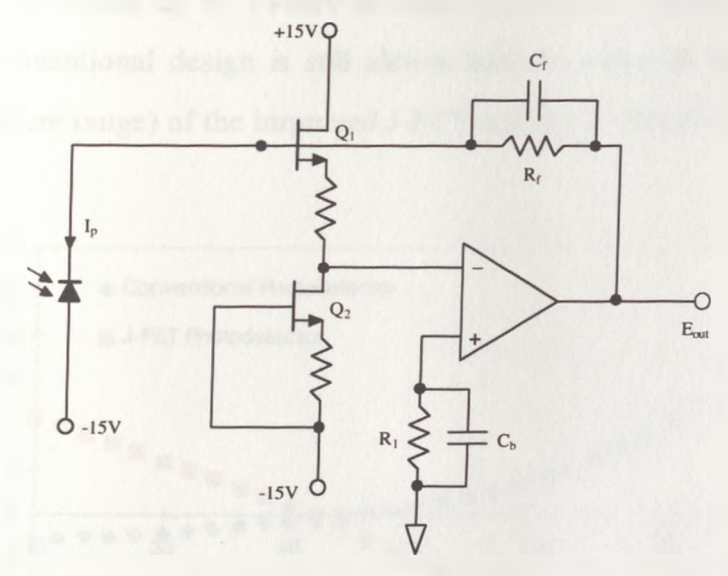


Figure 8-11 The modified source follower in the J-FET photodetector circuit

In the above circuit, transistor  $Q_2$  sinks the bias current of transistor  $Q_1$  and therefore the supply voltage is equally distributed between the two transistors. This

improvement substantially reduces the photodetector output dc offset and its drift which are now both suppressed by a factor of 7 (Figure 8-12).

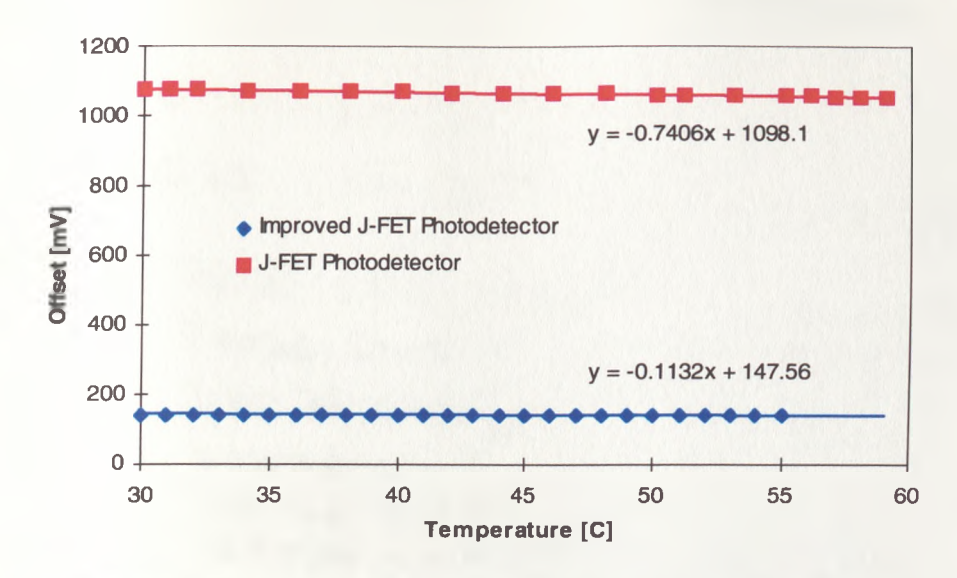


Figure 8-12 Improved dc performance of the J-FET photodetector

Finally in order to compare the conventional design and the improved J-FET circuit, both temperature drifts are shown in Figure 8-13. The curve representing the J-FET photodetector is shifted up by 144mV in order to compare offset drifts. The offset drift of the conventional design is still almost half the value (0.76mV/10°C at the whole temperature range) of the improved J-FET circuit (-1.13mV/10°C).

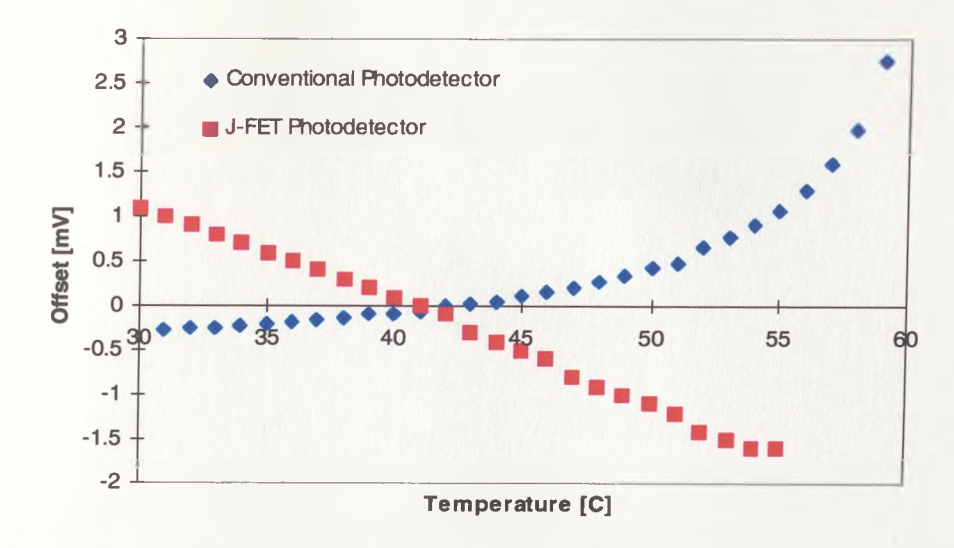


Figure 8-13 DC offset drifts of the conventional photo-receiver and the improved J-FET photodetector (shifted by average offset value of 144mV)

In order to further improve the dc performance a matched pair of J-FET transistors can be recommended, both kept at the same temperature, ideally produced on a single chip of silicon.

#### 8.2.6. Demand for Input Optical Power

In Section 8.2.2.1 it was stated that the feedback resistance R<sub>f</sub> should be made as large as other constraints allow. This is true for a given and constant input optical power. However, if there is a possibility to increase the received power, it is highly recommended to do so, in order to minimise the photodetector amplification. This is done by reduction of the feedback resistance. For the doubled input power, the feedback resistance has to be decreased twice to maintain the same level of the photodetector output voltage. This not only reduces noise originated from the R<sub>f</sub>, but keeping in mind that the shot noise is proportional to the square root of the photodiode current, proportional increase of this current gives improvement in signal-to-noise ratio by square root proportionality.

To prove these theoretical considerations, another test was carried out. The feedback resistance was reduced from  $492k\Omega$  to  $237k\Omega$  and the optical attenuation was also reduced in order to achieve the same output voltage signal from the photodetector. The photodetector bandwidth was maintained by doubling the  $C_j$  capacitance. Figure 8-14 shows the improvement in signal-to-noise ratio for the circuit with a lower  $R_f$ .

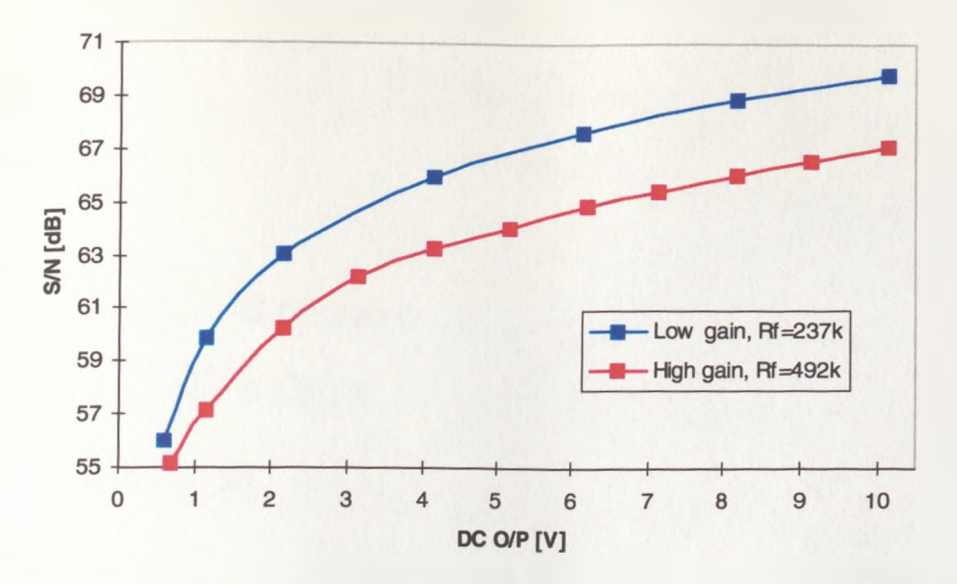


Figure 8-14 Improvement in S/N ratio for the circuit with a lower feedback resistance  $R_f$ 

The feedback resistance cannot be decreased infinitely since the photodetector gain would not be sufficient to amplify the input signal. The compromise has to be found between the maximum achievable optical power at the photodiode input and the minimum value of the R<sub>f</sub>. The maximum achievable optical power at the photodiode input depends upon many factors, i.e., light source and its coupling efficiency to the optical fibre, optical components used in the system, length of the optical path in the sensing magneto-optic material, etc.

It has been determined that the required magnitude of optical power at the input of the photodetector can be achieved in the present system (utilising the ABB HAFO 1A191 LED and the S5971 Hamamatsu pin photodiode). Naturally, the devices with longer interaction paths, such as the FR-5 sensor described in Chapter 5, bring higher attenuation to the optical path. However, they also provide much greater signal modulation due to the increased sensitivity, hence the increase in noise due to higher attenuation can be effectively compensated for. Nevertheless, the work is being carried out at present to identify suitable replacement components which would refine the present optical arrangement. The semiconductor industry provides increasingly more efficient light sources which, when used with larger diameter fibres may significantly improve the performance of the discussed current measurement system.

To summarise the above discussion, the transimpedance photodetector with the preceding J-FET stage shows improved noise performance as compared to the conventional bipolar op-amp design; the initial noise level is suppressed by a factor of 3 and the signal-to-noise ratio is increased by 3-9dB at low output signals and 1-2dB at high output signals (see Figure 8-9). At present, the J-FET photodetector dc stability is slightly worse as compared to the conventional design but can be improved by using a matched pair of J-FET transistors.

In order to eliminate any electro-magnetic interference, the above electronic circuit and the pin photodiode are housed in the shielded metal box as shown in Figure 8-15.

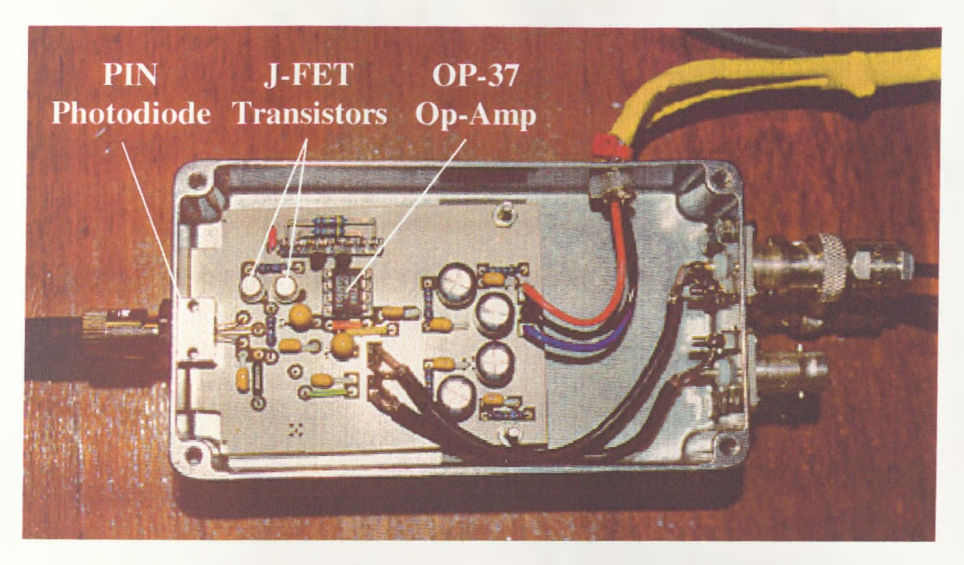


Figure 8-15 J-FET photo-receiver

# 8.3. Laboratory Evaluation of the OCT Measurement System

# **8.3.1.** Accuracy Tests of the DSP Monitoring Unit

Several comprehensive laboratory tests were carried out in order to verify the accuracy of the DSP monitoring unit. At first the correct operation of the individual blocks of the system (Figure 8-16) was verified and the analogue interface board was calibrated. The metering equipment used in the experiment consisted of a precision calibrator (Fluke, Model 515 A) and a precision digital voltmeter (Datatron). Each

A/D and D/A converter was calibrated according to the manufacturer's recommendations<sup>6,7</sup>.

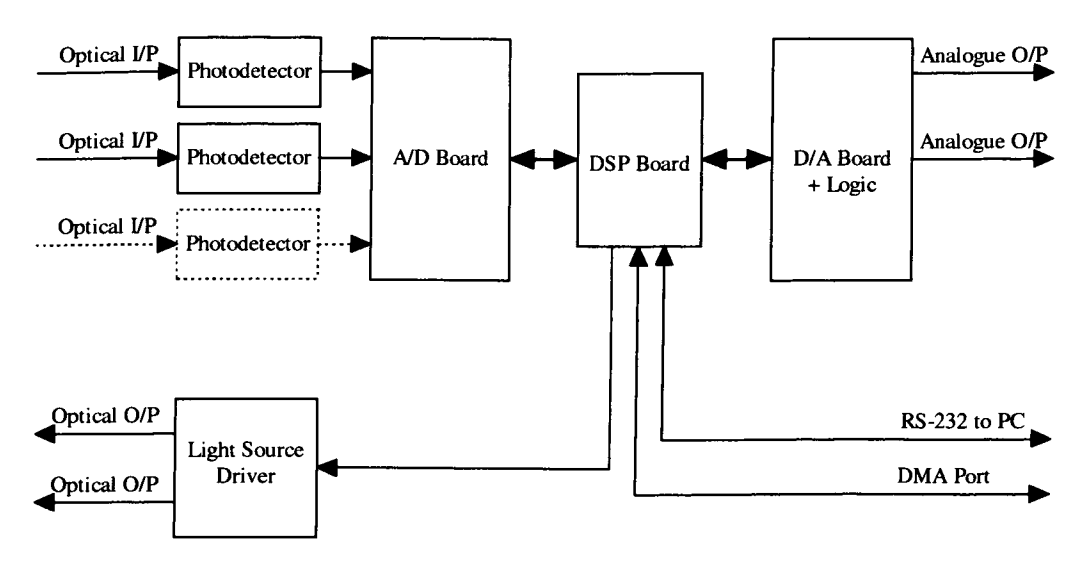


Figure 8-16 Block schematic of the DSP monitoring system

The calibrated unit was tested in terms of the accuracy of the individual A/D-D/A channels, the input step adjustable amplifiers, and the output deglitch filtering stages. In this test, the operation of the DSP processor was limited only to transmitting the signal from the A/D to the D/A converter without involving any signal processing. The calibrator was used as a step adjustable dc input reference voltage.

The typical accuracy of the complete transmission channel is shown along with the accuracy of the measurement equipment in Figure 8-17. The accuracy of the individual A/D-D/A channel is very good and is comparable with the accuracy of the test equipment used in the experiment.

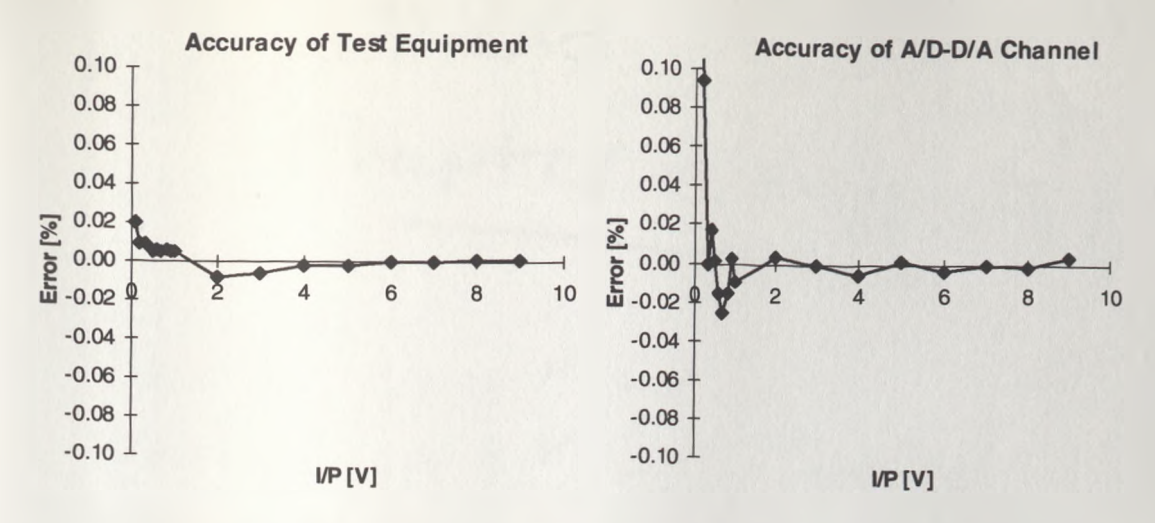


Figure 8-17 Accuracy of the measurement equipment and the A/D-D/A channel

The errors of the transmission channel are mostly the quantisation errors, introduced by the analogue-to-digital conversion process. The absolute values of the experimental data from the above graphs are compared with the calculated maximum quantisation error, as shown below in Figure 8-18. The maximum quantisation error was calculated assuming that the input value is rounded up or down (Equation 7-6) by the A/D converter, which is the case with the used A/D converter in the discussed DSP unit.

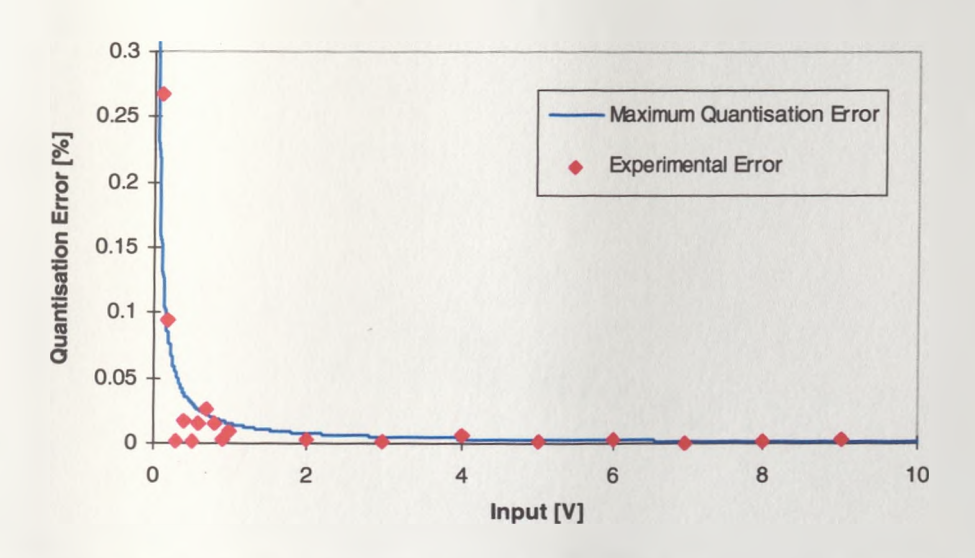


Figure 8-18 Maximum quantisation error compared with experimental data

The additional experimental error was caused by the influence of very low dc offset errors due to different earth potentials in the DSP unit and the test equipment, very difficult to eliminate in this particular laboratory experiment.

From the above discussion it is clear that the typical errors are an order of magnitude lower than the specified OCT accuracy requirements. Consequently, the presented level of performance is satisfactory for the DSP monitoring unit to be suitable for the purpose of using it with metering or protection class optical current transducers. This can be fulfilled when the sensor dynamic range (sensitivity) is matched to the dynamic range of the A/D converter, as discussed earlier in Chapter 7.

### 8.3.2. Linearisation Routine of OCT Response Characteristic

In order to verify the accuracy of the *arcsin* look-up table routine used to linearise the sensor response characteristic, and compare the theoretical and experimental errors associated with signal conversion and processing, a similar test to above was carried out. The measured *arcsin* characteristic and its deviation from the theoretical function expressed as a percentage error are shown in Figure 8-19.

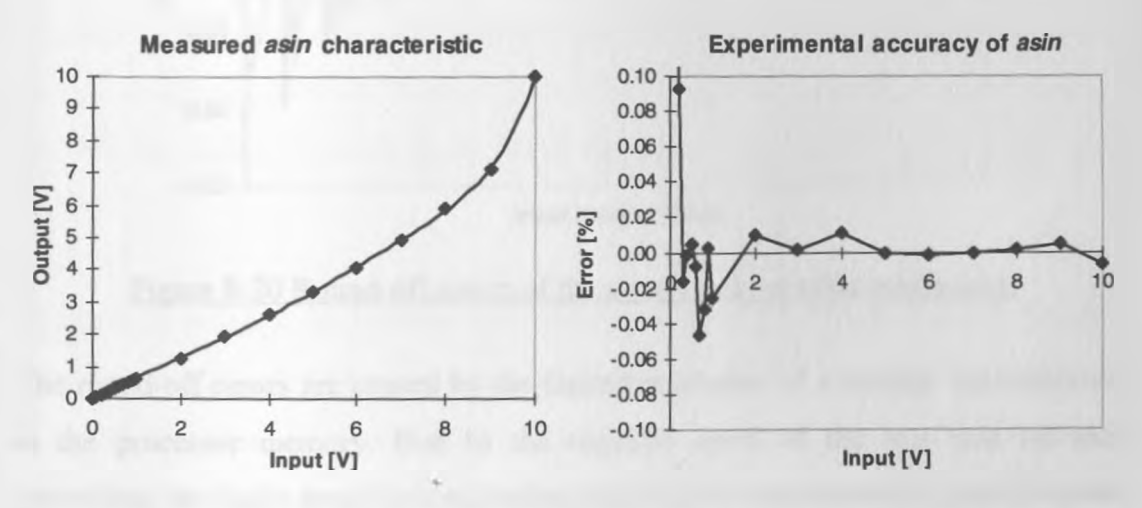


Figure 8-19 Accuracy of the measured arcsin look-up table using linear interpolation

The testing was carried out only for the positive part of the function in a range between 0 and 10V. Note, that the input voltage level of 10V is equivalent to the integer value of 1 after converting to a digital form. The processor returns the result which after converting to the voltage level is in the range between -10 and 10V. Note, that the above *arcsin* function is scaled to  $\pi/2$  integer value, so that the output level of 10V is equivalent to  $\pi/2$ .

From Figure 8-19, the errors are slightly higher in comparison to those of the transmission input/output channel. It is believed that this is due to the additional round-off errors present in the coefficients of the *arcsin* look-up table. This is particularly noticeable for near-zero values for which the relative round-off errors are most significant. To support these arguments, the round-off errors of the coefficients used in the above look-up table were calculated and are plotted against the input integer values as shown in Figure 8-20.

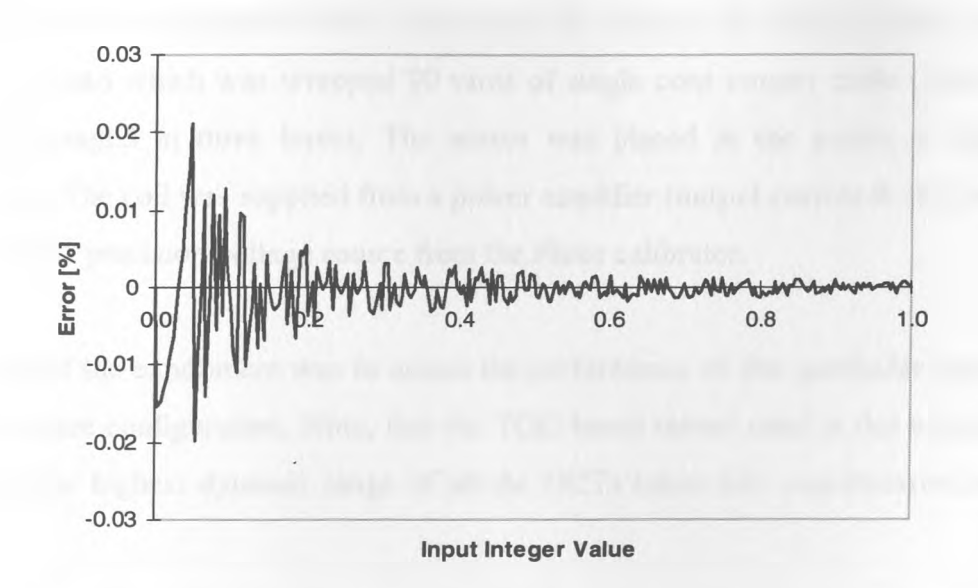


Figure 8-20 Round-off errors of the arcsin look-up table coefficients

The round-off errors are caused by the limited resolution of a number representation in the processor memory. Due to the required speed of the real time software procedure, the single precision calculation could only be implemented, hence the table coefficients could be represented only with a maximum resolution of 16 bits. Nevertheless, these errors are considerably below the level specified even by the most demanding accuracy requirements of the OCT.

# 8.3.3. Accuracy of the Monitored TGG 15mm Sensor

The complete electronic system and appropriate software was then tested with an OCT connected to the DSP unit. The tests were performed while using two different software programs created for use with an OCT: ac-only and ac-and-dc current measurement modes. The programs consisted of all the software components as described earlier in Chapter 7, except the temperature compensation routine. However, the sensor temperature was maintained constant in this particular experiment.

The OCT based on the TGG magneto-optic crystal of 15mm length was interrogated by the DSP monitoring unit. The current sensor was placed inside a coil of wire. The coil assembly was produced from a coil former (ID 38mm, OD 51mm, length 120mm, perspex) onto which was wrapped 90 turns of single core copper cable (7x0.67mm cable) arranged in three layers. The sensor was placed in the centre of the coil assembly. The coil was supplied from a power amplifier (output current 0-10A) driven by a 400Hz precision voltage source from the Fluke calibrator.

The aim of the experiment was to assess the performance of this particular hardware and software configuration. Note, that the TGG based sensor used in this experiment showed the highest dynamic range of all the OCTs taken into consideration in this work.

Figure 8-21 presents the combined test results as the DSP unit ran first under the aconly and then ac-and-dc measurement configurations of software respectively. The dc offset voltage at the photo-receiver output was set at approximately 7V. The current axis in Figure 8-21 represents the current flow in the sensor coil assembly scaled as if the sensor was placed on top of the earlier considered rectangular cross-section busbar (101.4x12.7mm). For example for a coil current of 5A, this represents a simulated busbar current of approximately 1133A. The errors are calculated as a relative deviations of the measured output values from the best fit line intercepting

zero, and are compared with 1% protection class accuracy specification of a current transformer.

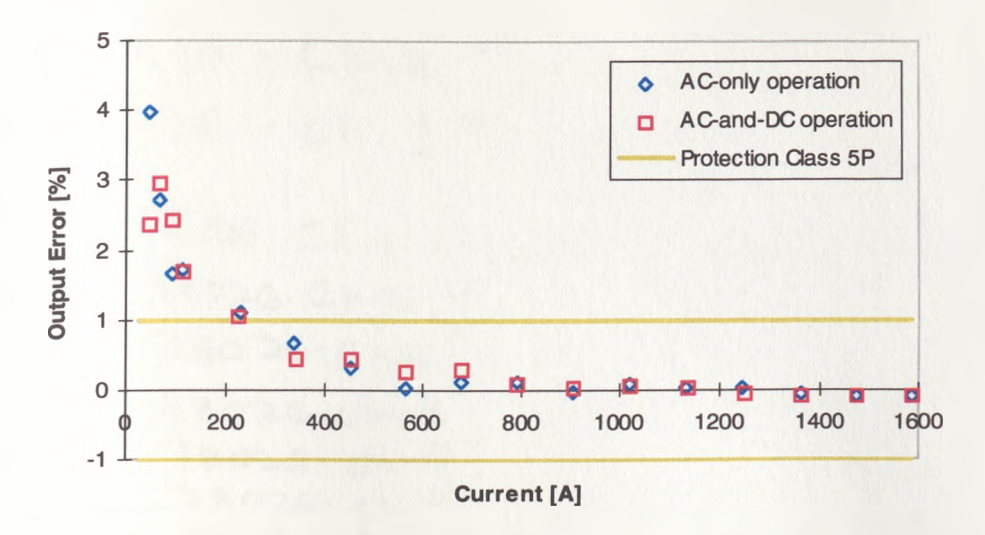


Figure 8-21 Errors of the OCT measurement system compared with the protection class 5P specification

From Figure 8-21 it can be seen, that the errors drop below 1% (protection specification) at the current level of approximately 300A, and below 0.75% (class 0.2 metering specification) at 400A. In principle, the sensor could be used as a combined metering class 0.2 and protection class 5P20 for the nominal current rating of 8000A. Note, that the maximum sensor dynamic is approximately 160kA.

The above results can only be regarded as a rough sensor performance assessment as the sensor was not affected by vibration and/or a temperature change.

As discussed earlier in Chapters 6 and 7, the accuracy of the ac-and-dc mode of operation would deteriorate during the course of time due to the insufficient compensation of the long-term changes in the characteristics of the light sources and down-lead attenuation. This is not so critical when the OCT is configured in the ac-only mode of operation since the signals are normalised with respect to their dc components, and any long term changes of the optical power level are effectively compensated.

#### 8.3.4. Accuracy of the Monitored FR-5 Sensor

This test was performed using the DSP software including both the vibration and temperature compensation schemes and the sensor linearisation routine. The software was set up in the ac-only mode of operation. The sensor temperature information was derived using a fibre Bragg grating (more details about this temperature measurement system will be provided later in this chapter). The current source used was a main variac controlled step down transformer having a 415V, 15kVA input and providing up to 6kA output into a direct short circuit. The photograph of the variac and a connected copper busbar is shown below in Figure 8-22. The FR-5 sensor was placed on top of the busbar and the current was measured using a class 0.1 metering current transformer mounted around the busbar.



Figure 8-22 Current source in the Strathclyde University Laboratory (max. current ≈ 6000A)

In the above configuration the variac provided a maximum current of 4kA. The results analogues to those from the previous paragraph are presented in Figure 8-23.

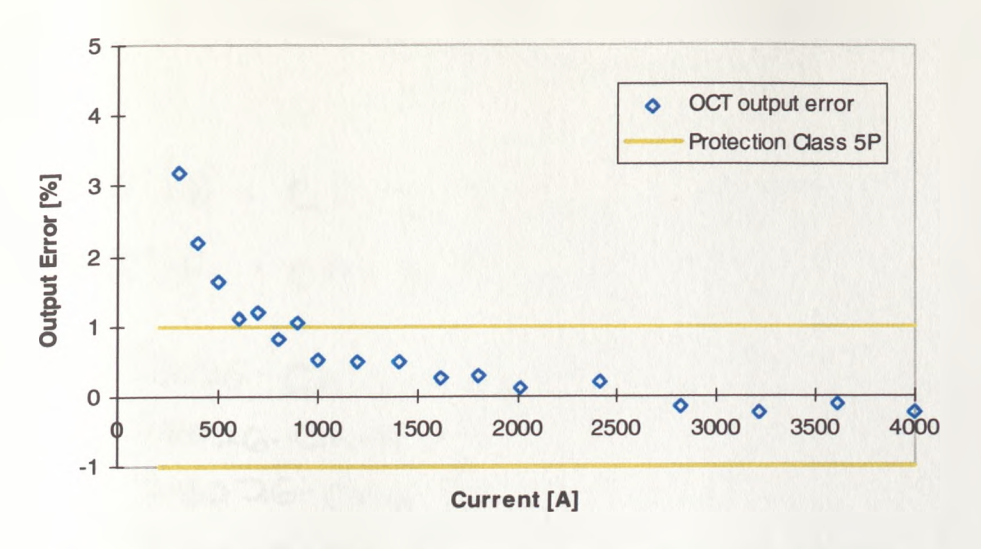


Figure 8-23 Output errors of the fully compensated FR-5 sensor

The FR-5 sensor demonstrates higher output errors as opposed to the TGG sensor. This is caused by the lower signal-to-noise ratio of the photodetector outputs due to the much greater light attenuation within the FR-5 OCT. Nevertheless, with the present technology, the FR-5 sensor can still be used as a protection class device.

#### 8.4. Vibration Tests

To assess the influence of the vibration effect on the OCT current measurement performance and to evaluate the proposed in Chapter 6 vibration compensation scheme, several tests were carried out at the Reyrolle Protection Ltd in Hebburn (latterly VATech Reyrolle Ltd) using specialised laboratory equipment. The tests were carried out twice during the research programme, first in 1997 with the prototype vibration compensation unit utilising the analogue technology to perform basic signal processing, and the second in 1999 with the DSP unit in which the signal processing was realised in software and allowed vibration and temperature compensation schemes to be implemented simultaneously (as described in Chapter 7). In addition, the tests in 1997 were carried out using the TGG based sensors (15mm and 25mm), and in 1999 using a new design FR-5 glass reflective type OCT. The results of these tests are described in detail in the following sections.

#### 8.4.1. Vibration Tests (1997) - Proof of Principle

To confirm that the proposed vibration compensation method functions according to theory and to test the prototype vibration compensation unit with regard to its compensation efficiency and accuracy, several vibration and accuracy tests were carried out.

The prototype vibration compensation unit was built in a configuration that was capable of sensing dc and ac currents (see block diagram in Figure 6-10, Chapter 6). The tests results compare the susceptibility to external mechanical vibration of the two output channels, 'uncompensated' channel and 'compensated' channel. The prototype unit, due to the use of analogue technology was capable of providing only vibration compensation. It was assumed that the sensor temperature was constant during the tests, and since the applied currents were relatively low ( $\approx 5\%$  of the sensor maximum dynamic range), the influence of the device nonlinear characteristic could be neglected.

Two 850nm LEDs were used as the light sources in the optical system, two 2x1 multimode couplers and two PIN photodetectors. The light was transmitted to the sensor head via 100/140 micron graded index multimode fibre optic cable.

Two types of sensor were used in the tests: a 'pigtailed' sensor and an 'unpigtailed' sensor. A pigtailed sensor was defined as a sensor where the addressing optical fibres were an integral part of the sensor housing and gave rise to 'flying' leads (of approximately 1m length in this case) which were then terminated in optical connectors (allowing connection to optical fibres from the OCT electronics). The pigtailed sensor was the latest generation of sensor housing produced in 1997 and was noted for its good, repeatable optical transmission and robustness.

An unpigtailed sensor was defined as a sensor where the addressing optical fibres simply thread, or otherwise connect, directly to the sensor housing without any 'flying' leads. This was an early generation design of sensor housing and suffered

from poor repeatability of optical connection and subsequent difficulties ensuring good optical transmission. This type of sensor was particularly prone to vibration effects as the optical connectors were prone to moving within their mating bores on the sensor housing, causing appreciable changes in the optical transmission. The unpigtailed sensor, due to its poor vibration performance was used to demonstrate the compensation efficiency of the vibration compensation system subjected to extreme operational conditions.

### 8.4.1.1. Description of the Test System

The tests were carried out by securing the sensor head within a coil of wire and then by fastening the coil assembly to the flat table of the vibration unit as pictured in Figure 8-24. The coil assembly was produced from a coil former (ID 38mm, OD 51mm, length 120mm, perspex) onto which was wrapped 90 turns of single core copper cable (7x0.67mm cable) arranged in three layers. The sensor was placed in the centre of the coil assembly. The experimental set-up is shown in Figure 8-25.

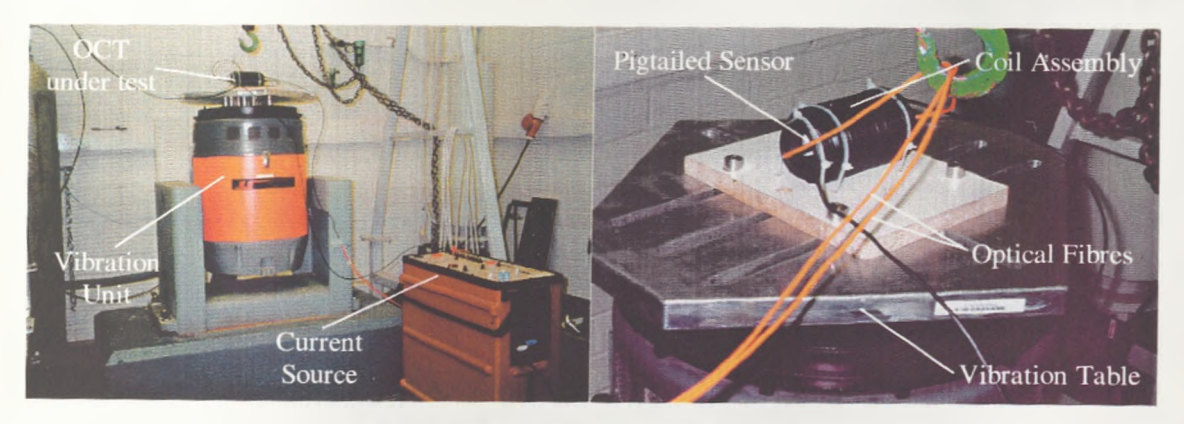


Figure 8-24 OCT vibration testing

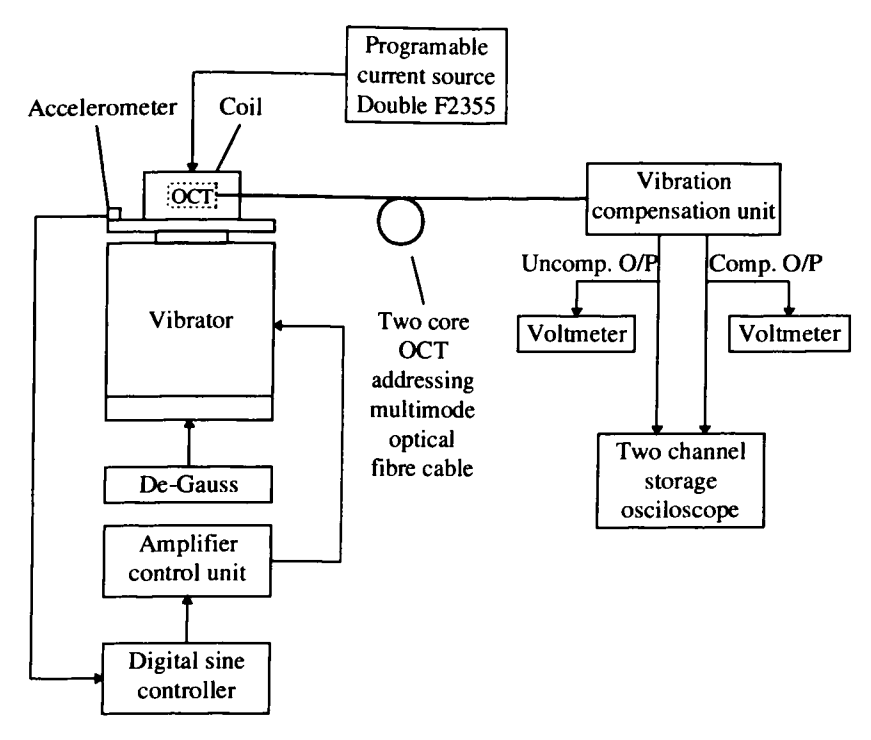


Figure 8-25 Experimental set-up for vibration testing

The current source used (F2350 Double) was capable of currents from 0-100A in varying steps dependent upon the current range used, and capable of varying frequencies from 50-500Hz.

The vibration unit (Environmental Equipment Ltd.) was capable of providing accelerations of up to 10g at frequencies between 20Hz and 3kHz. To provide a constant acceleration, independent of the vibration frequency, an accelerometer was attached to the vibration table and its output served as a reference to the system controlling the vibration unit.

The vibration direction was chosen as vertical, as the sensor head is normally fixed on the bus bar in the way shown in Figure 8-26, where the vertical component of the vibration is the most severe.

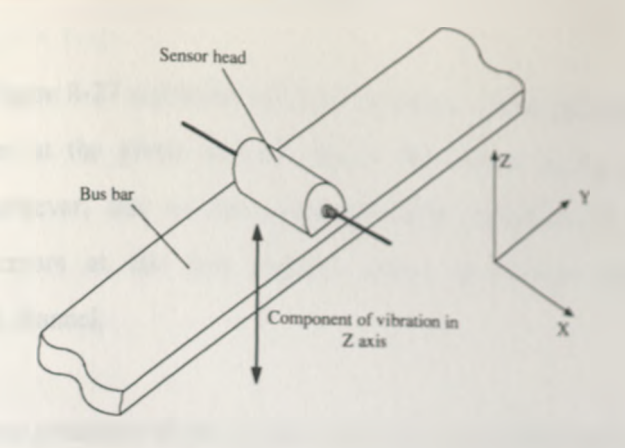


Figure 8-26 Vertical vibration as the most severe case

The tests results reported in the next paragraphs are presented in such a way to allow easy comparison between the uncompensated and compensated channels.

#### 8.4.1.2. Accuracy Tests

Prior to the vibration tests, the prototype vibration compensation unit and the two TGG sensors had undergone the accuracy tests. The coil current was increased gradually and the sensor output was measured using a precision voltmeter. Figure 8-27 displays a series of graphs that represent the current response and output errors of the pigtailed OCT (no vibration applied), while the coil was supplied with an ac 50Hz current. Due to the additional gain in the compensated channel, its output was twice as high as the uncompensated one.

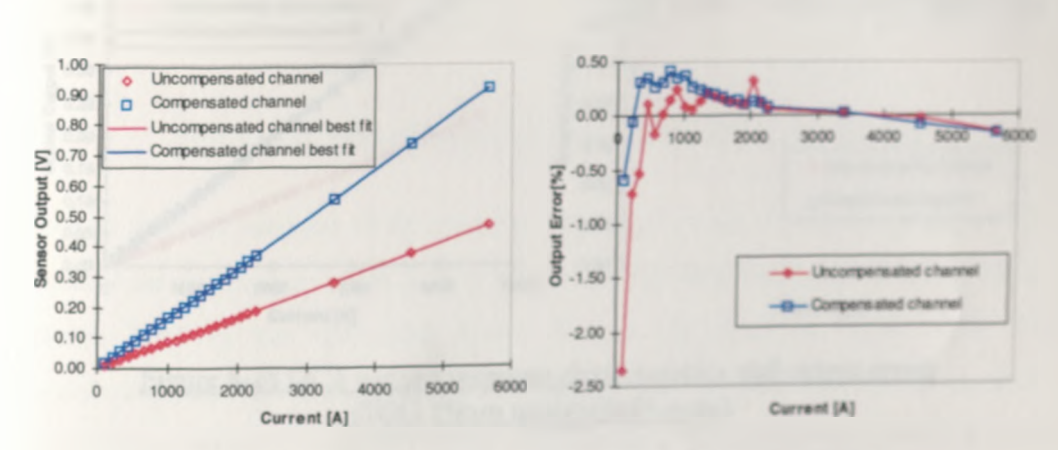


Figure 8-27 OCT current response characteristics and output errors (TGG 25mm pigtailed sensor)

The errors in Figure 8-27 represent relative deviations of the OCT output values from the best fit line at the given current values. The errors in the two channels are comparable, however, due to the common mode rejection in the compensated channel, the errors at the low current values are lower than those in the uncompensated channel.

The measurement precision of the system when the unpigtailed sensor is used is worse than that of the pigtailed sensor. This is due to the fact that the unpigtailed sensor incorporates a shorter sensing crystal (15mm as opposed to 25mm in the pigtailed sensor) which would have the net effect of decreasing the signal to noise ratio. This is reflected in the output errors as shown below in Figure 8-28, along with the sensor current response characteristics.

It can be seen that the errors at the low current values are higher when compared with the data from the previous section, where the same 15mm TGG sensor was interrogated by the DSP unit. This is due to the unrefined electronics used in the prototype analogue system. Note, that the bandwidth of the prototype unit was only 5kHz as opposed to 20kHz of the DSP based system.

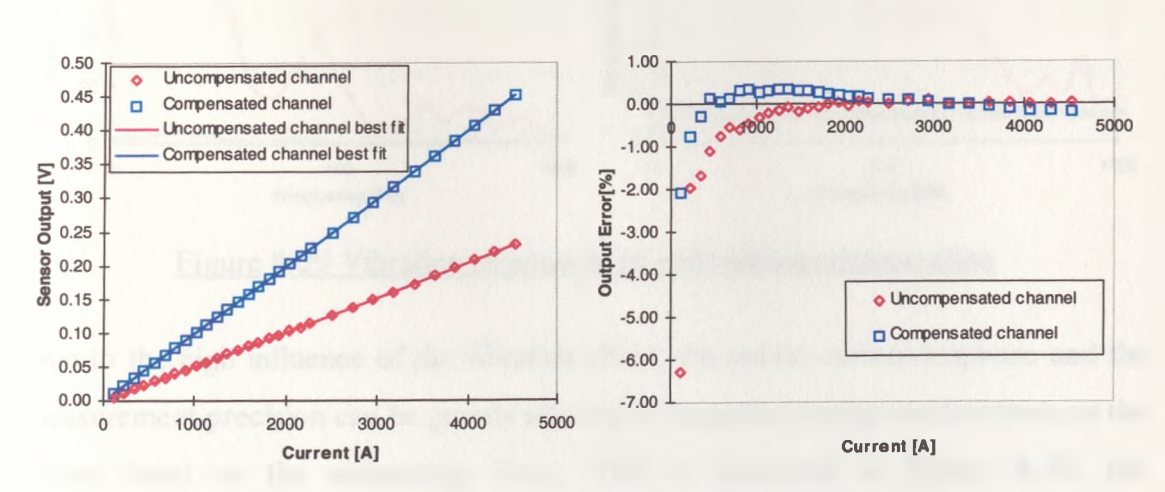


Figure 8-28 OCT current response characteristics and output errors (TGG 15mm unpigtailed sensor)

#### 8.4.1.3. Vibration Tests

To assess the influence of the vibration effect on the sensor performance and the compensation efficiency of the basic compensation arrangement, vibration tests without current were first carried out. The frequency of vibration was changed from 10Hz to 1kHz in 10Hz steps up to 100Hz, then every 50Hz up to 300Hz, and finally every 100Hz up to 1kHz. An acceleration of 2.65g was imposed on the sensor at vibration frequency 10Hz, and then from 20Hz the acceleration was increased to 6.63g. The results for both the unpigtailed and pigtailed sensors are shown in Figure 8-29. The magnitude of the induced disturbance is particularly high for the unpigtailed sensor and the compensation efficiency in this case is in the range of 30dB. The pigtailed sensor is characterised with a much better immunity to vibration due to the improved, more robust design. Also in this case, the applied vibration compensation scheme works very well since the compensated signal only slightly exceeds the noise level in a steady state condition.

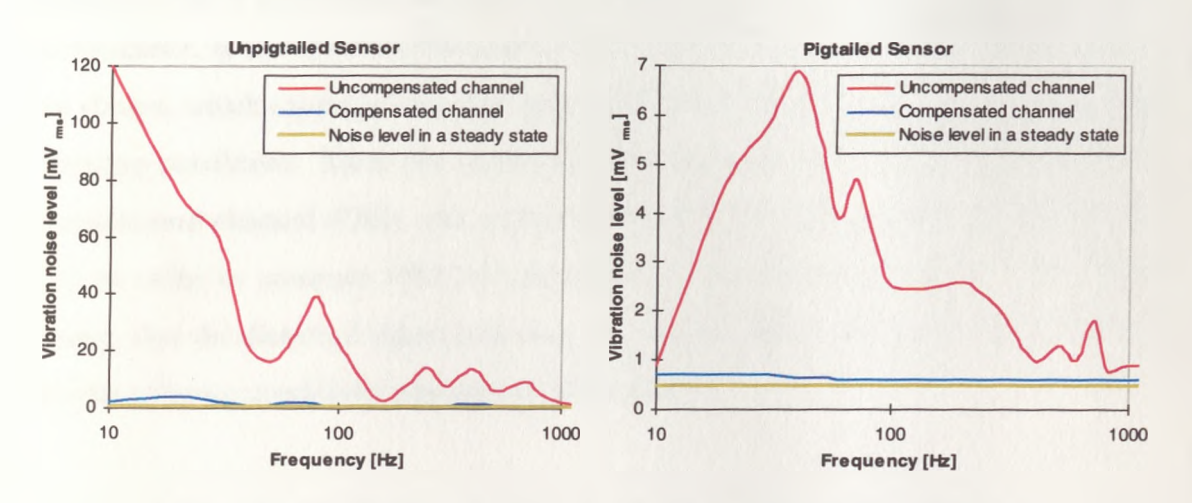


Figure 8-29 Vibration response with and without compensation

Due to the high influence of the vibration effect, the sensor current response and the measurement precision can be greatly affected by imposing strong accelerations on the sensor head or the addressing fibres. This is illustrated in Figure 8-30, the uncompensated current response characteristic is severely affected by the vibration disturbance while the measured output values visibly deviate from the best fit line. In this case the sensor was exposed to a vibration level of acceleration 6.63g at a fre-

quency of 26Hz. The relative output errors in the uncompensated channel reach very high values, however, in the compensated channel the vibration influence is neutralised to the level only slightly exceeding that from the tests in a steady state condition.

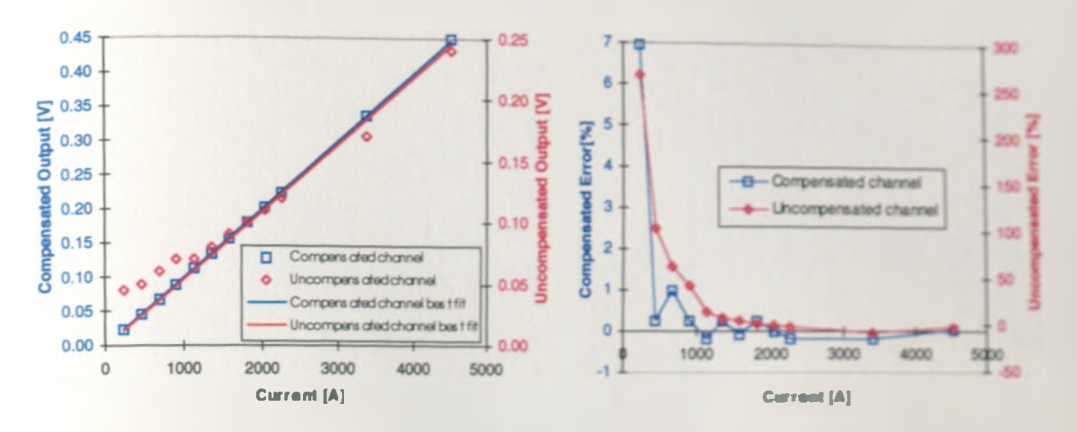


Figure 8-30 Unpigtailed sensor output errors (vibration: 26Hz, 6.63g)

Another way of portraying the influence of the high vibration levels on the system performance, is to record oscilloscope traces during testing. In Figure 8-31 two traces are shown, which represent the uncompensated and compensated channels at the same vibration conditions. Since the additional electronic gain of 2 was introduced in the compensated channel (Ch2), the vertical scale for Ch2 is shown twice as large as for Ch1 in order to compare effective magnitudes of the measured signals. It is clearly shown, that the distorted signal (top trace) is almost entirely recovered (bottom trace) despite extreme conditions imposed on the sensor.

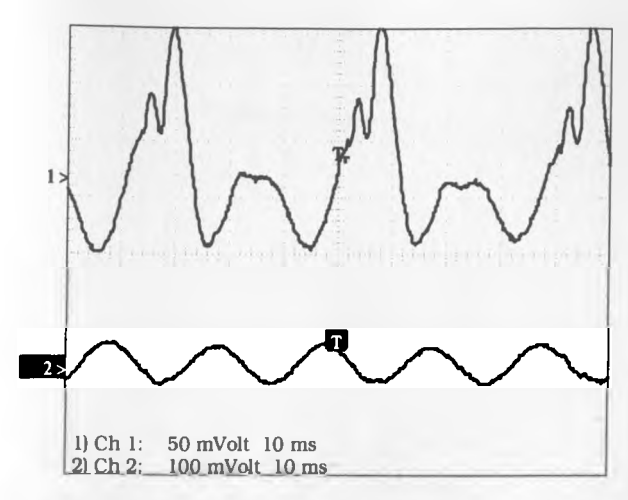


Figure 8-31 Oscilloscope traces of the two OCT outputs during the vibration test (vibration: 26Hz, 6.63g, equivalent current: 230Amps)

To demonstrate the effect of vibration on the pigtailed sensor an oscilloscope record was taken while the sensor and flying leads were subjected to vibration levels of acceleration 6.63g at frequency 26Hz (no current). Compared to the unpigtailed sensor the magnitude of the vibration noise is much lower even in the uncompensated channel. This demonstrates that the new generation of the sensor housing and the pigtailed design provided a much better performance than the previous sensors. The effect of vibration on the uncompensated channel and its compensation are shown in Figure 8-32.

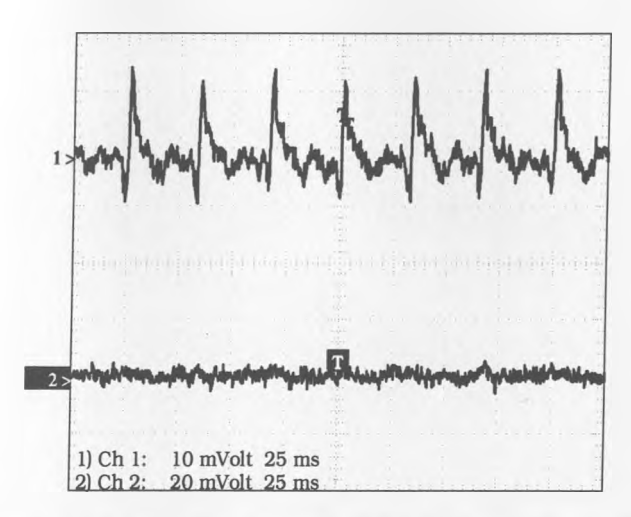


Figure 8-32 Oscilloscope traces of the two OCT outputs during the vibration test (pigtailed sensor, vibration: 26Hz, 6.63g, no current)

The above tests were very encouraging despite the use of a basic design of the interrogating and processing unit. It was then decided, that the work should be continued taking full advantage of digital signal processing and possibility of incorporating additional functions into one integrated system.

### 8.4.2. Vibration Tests (1999) - Utilisation of DSP Unit

This time the new DSP unit and the FR5 based reflective OCT were comprehensively tested in order to assess the sensor performance in steady state conditions and while exposed to extreme environmental disturbances. The tests results again compare the two output channels, 'uncompensated' channel and 'compensated' channel. The uncompensated channel provided measured current information which was affected by the nonlinear characteristic of the OCT and could be influenced by vibration or temperature variation. On the contrary, the compensated channel provided linearisation of the OCT response characteristic, vibration compensation and temperature compensation.

Monitoring the two output channels allowed to preliminarily assess the current measurement accuracy of each of them, and make evident the actual influence of the environmental factors on the OCT performance both with and without compensation.

#### 8.4.2.1. Description of the Test System

The tests were carried out by securing the sensor head within a coil of wire and then by fastening the coil assembly to the flat table of the vibration unit as in the tests from the previous section. The coil assembly was produced from a coil former (ID 77mm, OD 82mm, length 120mm, nylon) onto which was wrapped 340 turns of enamelled copper wire (1.6mm diameter) arranged in four layers. The coil was made bigger to accommodate a larger FR5 sensor.

The same current source and vibration unit were used as in the previously reported tests. Due to the higher coil impedance, the current levels obtained were in the range

of only up to 13A. However, since the coil inductance was also higher in this case, the maximum magnetic field obtained was similar to that from the previously used coil.

The OCT was interrogated by the DSP unit to provide both the compensated and uncompensated channel outputs which were monitored using a digital storage oscilloscope and two precision voltmeters. The OCT temperature was measured using a fibre Bragg grating sensor monitored by the FBG system which was connected to a PC via an interface card. The temperature information was constantly derived using a LabView software running on the PC and sent to the DSP unit via an interface card. More details about this system will be provided later in the sections concerned with the temperature tests. The PC was also used as a platform for downloading software to the DSP unit. The laboratory test set-up is shown in Figure 8-33.

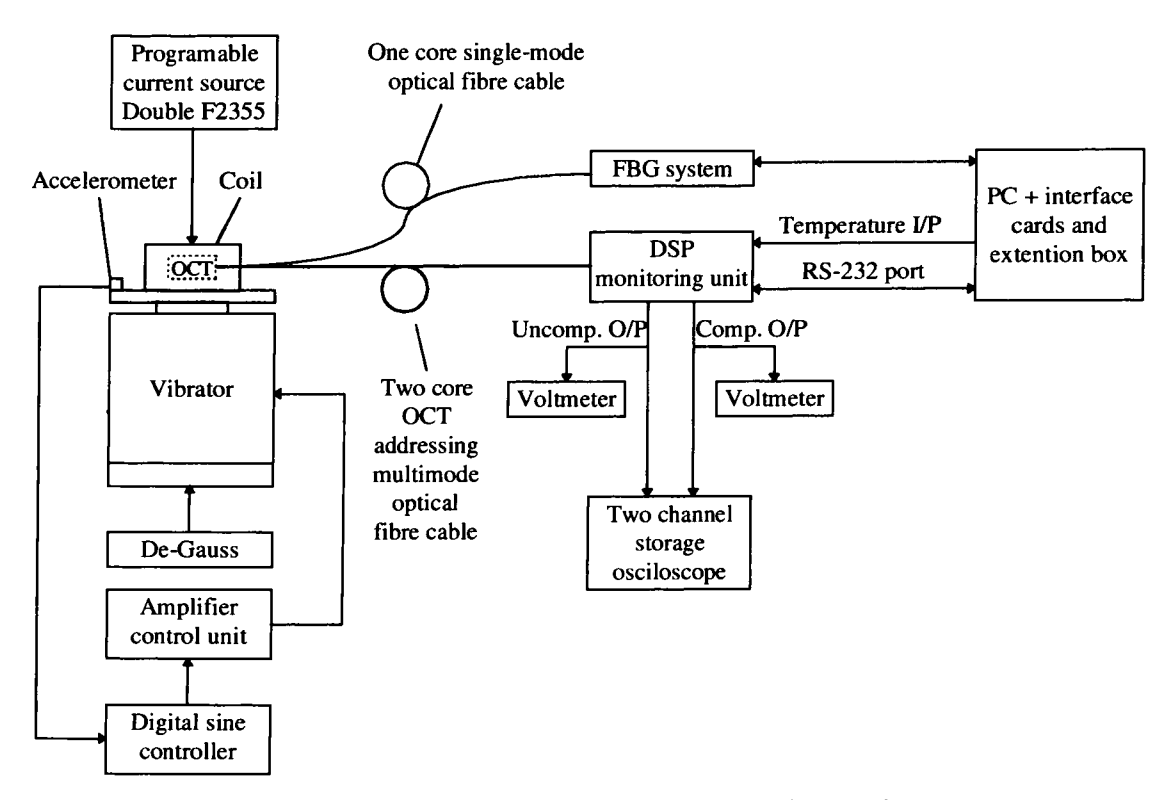


Figure 8-33 Experimental set-up for vibration testing

#### 8.4.2.2. OCT Accuracy Tests with no Vibration Present

The accuracy tests were carried out first in order to measure the OCT current response characteristic and determine percentage errors calculated as deviations of

measured values from the best fit line intercepting zero. During the test the sensor head was not exposed to vibration and the OCT temperature was approximately constant. Figure 8-34 shows OCT current response characteristics of the compensated and uncompensated channels and the respective output errors. Note, that the OCT current response differs for the compensated and uncompensated channels which is due to the linearisation of the sensor response characteristic applied in the compensated channel; the two outputs would have been equal at the OCT maximum current limit.

The limited power from the current source used in the experiment did not allow to characterise the OCT to its maximum current range. The 50Hz input sine wave became distorted at approximately 13A. Nevertheless, the sensor was correctly characterised up to 10Amps which was equivalent to 8.3kA current flowing through a busbar (cross-section 101.4x12.7mm) as if the OCT was placed on top of the busbar. This current level is approximately 23% of the sensor maximum current limit.

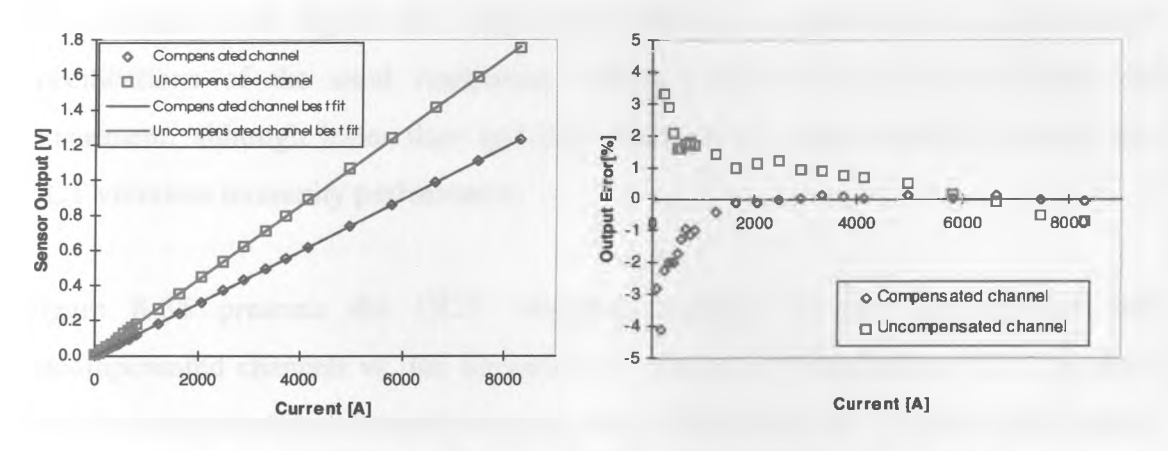


Figure 8-34 OCT current response characteristics and output errors

Output errors of the uncompensated channel are generally higher than these of the compensated one, which is caused mostly by the nonlinear response of the uncompensated channel and its possible signal variation due to a temperature change. High errors at the low current levels are mostly due to the limited precision of the measurement caused by output noise since the photodetector signal had to be additionally amplified due to the higher attenuation of the used FR5 sensor.

The results obtained from this experiment indicate that this particular OCT and the interrogation system are within the current transformer protection class 5P30 for a nominal current rating of 1000A.

#### 8.4.2.3. Vibration Tests

Vibration tests were carried out firstly for the case when the OCT was vibrated and the optical connectors secured to the static frame. The frequency of vibration was changed from 10Hz to 1000Hz. For most of the measurement points a maximum acceleration of 10g was achieved. Lower acceleration levels were applied at 10 and 20Hz, 3 and 6g respectively, and for 900 and 1000Hz, 4 and 5g respectively. This was due to very high displacements at lower frequencies and resonances at the highest frequencies which caused excessive power demand from the system driving the vibrator coil.

Acceleration levels higher then 10g were difficult to achieve due to the limited specifications of the used equipment, however the levels achieved during the experiment, although lesser than specified in Chapter 5, were sufficient to test the OCT vibration immunity performance.

Figure 8-35 presents the OCT vibration response of the compensated and uncompensated channels vs. the frequency of vibration. From Figure 8-35 it is clear that the uncompensated channel was much more affected by the vibration disturbance than the compensated channel in which the vibration effect caused only slight increase of noise above the noise level in a steady state condition.

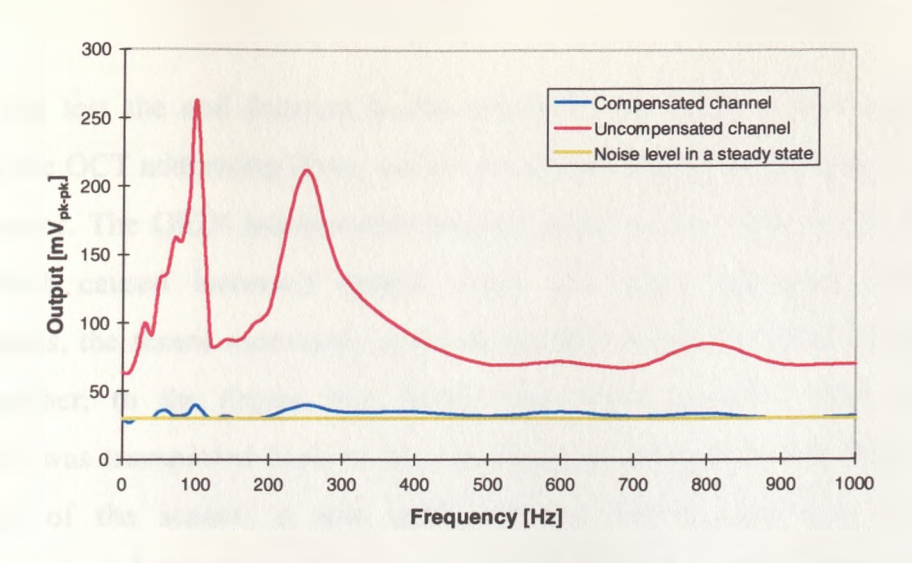


Figure 8-35 OCT vibration response of the compensated and uncompensated channels vs. vibration frequency (connectors not vibrated)

The above test was carried out in order to determine the worst case of the OCT sensitivity to vibration. It appears that vibration at frequencies around 100Hz and 250Hz caused the highest disturbance which was due to resonances of the mechanical system. At certain resonance frequencies the sensor head began to move inside the coil assembly which increased the OCT vibration response. An example of a relatively high vibration disturbance on the OCT operation captured using a digital oscilloscope is presented in Figure 8-36. Vibration frequency was set at 70Hz and the acceleration at 10g. Top trace represents the compensated output which is only slightly affected by the vibration, and bottom trace the severely affected uncompensated output.

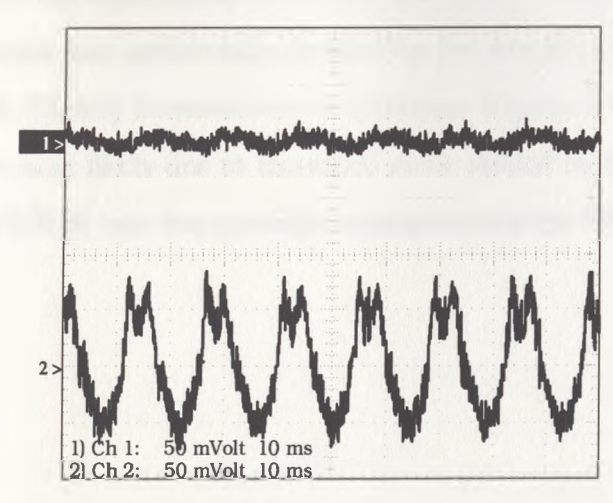


Figure 8-36 Oscilloscope traces of the two OCT outputs during the vibration test (vibration: 70Hz, 10g, no current, connectors not vibrated)

During this test the coil fastened to the vibration table became lose and moved, stressing the OCT addressing fibres, which unfortunately caused a permanent damage to the sensor. The GRIN lens/polariser became detached from one side of the FR-5 glass which caused increased optical losses and hence increased noise level. Nevertheless, the sensor recovered, as the elastic filler pulled the optical components back together, to the degree that further tests were possible. Later, after the equipment was transported back to the University of Strathclyde and after a closer inspection of the sensor, it was confirmed that the damage was permanent. Arrangements are being made at present to improve the OCT mechanical durability.

### 8.4.2.4. OCT Accuracy Tests (sensor head vibrated)

After the test described in the previous section the fastening of the coil assembly was improved and the sensor head was again secured inside the coil which subsequently restricted its moves in order to prevent additional effects at resonance frequencies.

The accuracy test as described earlier was then repeated, however this time the sensor head was subjected to vibration. The acceleration was set to 5g and the vibration frequency to 100Hz.

These conditions did not significantly affect the sensor performance (see Figure 8-37). The vibration response was additionally damped by the restricted moves of the sensor head inside the coil. Slightly increased errors (compare Figures 8-34 and 8-37) at low current levels were most likely due to increased noise caused by the decreased optical transmission as the GRIN lens was partially separated from the FR-5 glass.

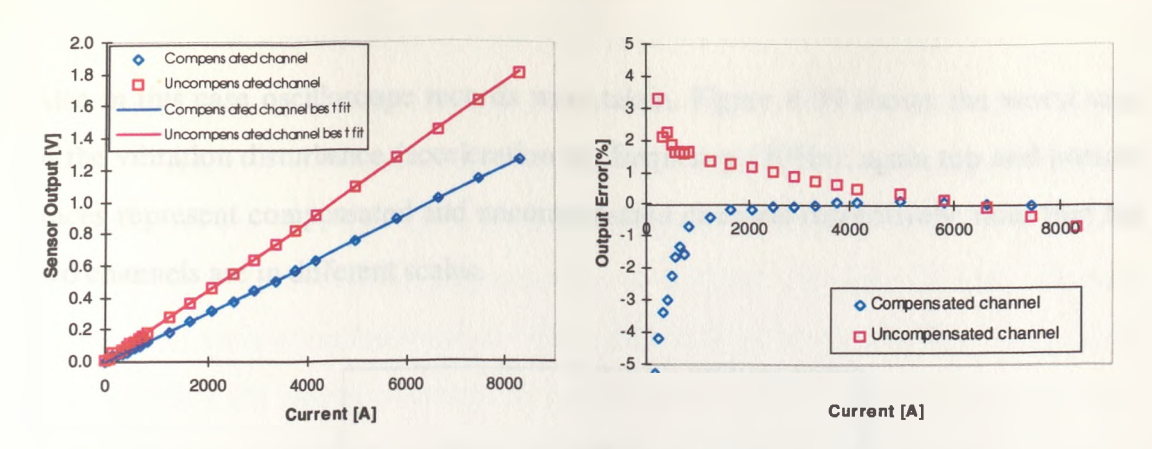


Figure 8-37 OCT current response characteristics and output errors (vibration 5g, 100Hz, connectors not vibrated)

#### 8.4.2.5. Vibration Tests (optical connectors vibrated)

This test was similar to the test described in Section 8.4.2.3 with the only difference that the OCT optical connectors were attached to the vibration table. Figure 8-38 shows the OCT vibration response of the compensated and uncompensated channels vs. the frequency of vibration. The vibration response in this case is much higher than the one shown in Figure 8-35. Again, it is clear that the uncompensated channel was much more affected by the vibration disturbance as opposed to the compensated channel in which the vibration effect caused only slight increase of noise above the noise level in a steady state condition.

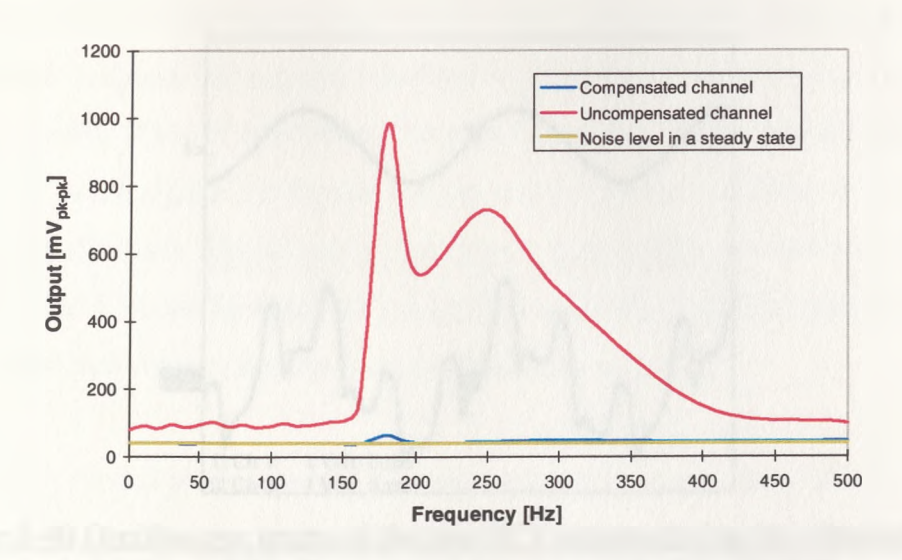


Figure 8-38 OCT vibration response of the compensated and uncompensated channels vs. vibration frequency (connectors vibrated)

Also in this case oscilloscope records were taken. Figure 8-39 shows the worst case of the vibration disturbance (acceleration 8g, frequency 180Hz); again top and bottom traces represent compensated and uncompensated channels respectively; note that the two channels are in different scales.

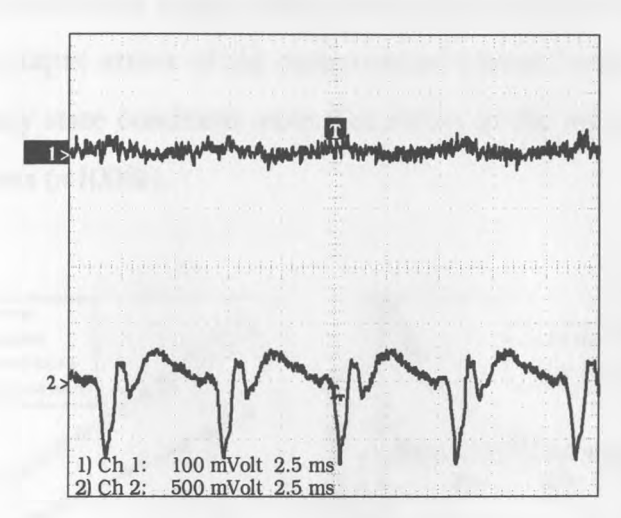


Figure 8-39 Oscilloscope traces of the two OCT outputs during the vibration test (vibration: 180Hz, 8g, no current, connectors vibrated)

Figure 8-40 shows a similar situation, however the coil was energised with a current of 4Amps (equivalent of 3.3kA). The compensated signal (top trace) is completely recovered despite the severe vibration effect on the uncompensated signal (bottom trace).

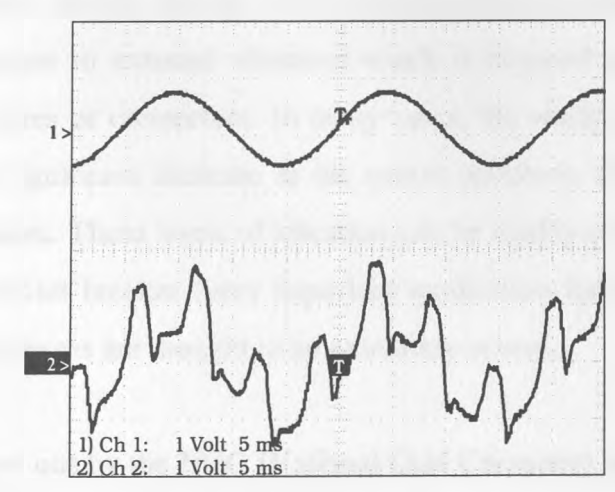


Figure 8-40 Oscilloscope traces of the two OCT outputs during the vibration test (vibration: 180Hz, 8g, current: 4Amps, connectors vibrated)

# 8.4.2.6. OCT Accuracy Tests (sensor head and connectors vibrated)

Once again the accuracy test was repeated, this time however, the sensor head and the optical connectors were both subjected to vibration. Figure 8-41 illustrates the OCT compensated and uncompensated current response characteristics and the respective errors. The uncompensated characteristic is severely affected by the vibration disturbance, the measurement values visibly deviate from the best fit line. Despite the high vibration the output errors of the compensated channel remain similar to those measured in a steady state condition; note that errors of the uncompensated channel reach very high levels ( $\approx 100\%$ ).

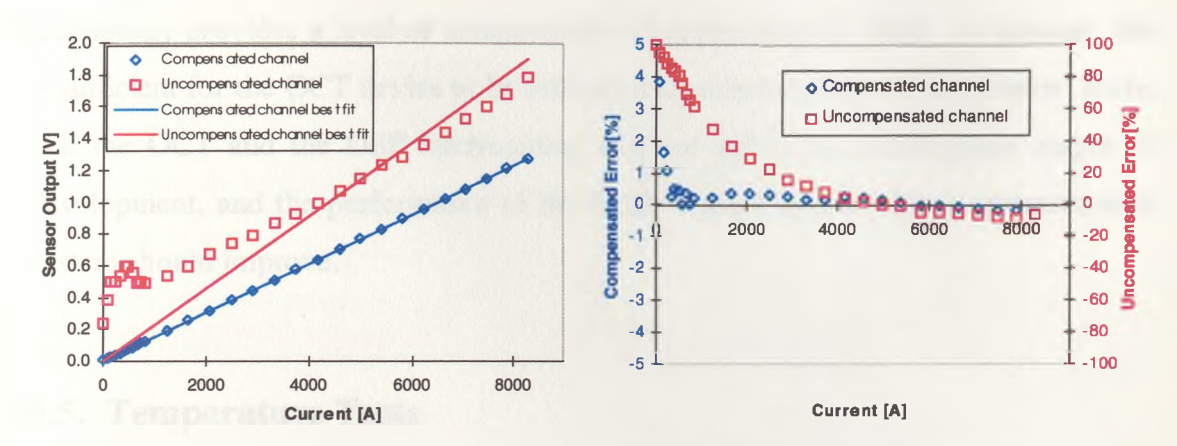


Figure 8-41 OCT current response characteristics and output errors (vibration: 180Hz, 10g, connectors vibrated)

The above tests have shown, that the OCT uncompensated channel demonstrates an unacceptable response to external vibration which is imposed either on the sensor head, addressing fibres or connectors. In many cases, the vibration levels of even up to 10g may cause significant decrease in the sensor accuracy, shifting it outside the required specifications. These levels of vibration can be readily exceeded if an OCT is integrated into a circuit breaker (very important application for this type of device), where vibrational stresses are thought to be extremely severe.

The research carried out by the NGC (National Grid Company) have shown<sup>8</sup> that the OCT in the circuit breaker configuration could be exposed to vibration levels from 10g, for the two-break spring mechanism circuit breaker connected by flexible

conductors, to up to 180g, for a multiple break air blast circuit breaker connected via busbars (2-3m long), and the frequency of significant accelerations may be in a range from a few Hertz to 2kHz. Most certainly, the sensor output signal would have to be compensated in such cases in order to retain the device measurement performance. The tests described in the previous paragraphs did not include such severe cases, however, the obtained level of vibration allowed for the assessment of the sensor response to the external mechanical vibration.

The tests carried out within this research have demonstrated a success of the proposed active vibration compensation method which with the presently used technology provides a level of compensation of approximately 30dB. At present, this is sufficient for the OCT device to be utilised as a protection current transducer. Note, that the OCT and the DSP interrogating unit are still in pre-prototyping stages of development, and the performance of the finally refined optical current measurement system should improve.

# **8.5.** Temperature Tests

Temperature testing of the range of developed OCTs was primarily carried out in the Strathclyde University Laboratory. The tests go back in time to year 1995 when the prototype TGG sensors were temperature cycled, and the work on the temperature compensation was initiated. These tests are reported in the number of internal Strathclyde University documents<sup>9,10</sup> and are not included in this thesis. This section will concentrate on the description of the temperature test system developed within this research work programme, and testing of the new FR-5 sensors and the DSP based temperature compensation scheme utilising a fibre Bragg grating system as a means of deriving the OCT temperature.

## 8.5.1. Description of the Test Set-up

The test set-up in which the majority of the temperature tests have been carried out is shown in Figure 8-42. The sensor head was placed inside a PTFE thermal enclosure

secured on top of the conducting busbar. The busbar was connected to the high current variac and supplied with a constant current of 2000A.

The heat exchange between the sensor and the surrounding air was devised around a heat sink which embraced the sensor head and was connected via a Peltier heat pump to an outer heat sink. The Peltier element (two 72W units connected in parallel) allowed heat to be transferred in either direction, depending on the direction of the Peltier current, thereby heating or cooling the sensor head. The desired sensor temperature was obtained by setting the Peltier current to a constant value between the minimum and maximum operating currents.

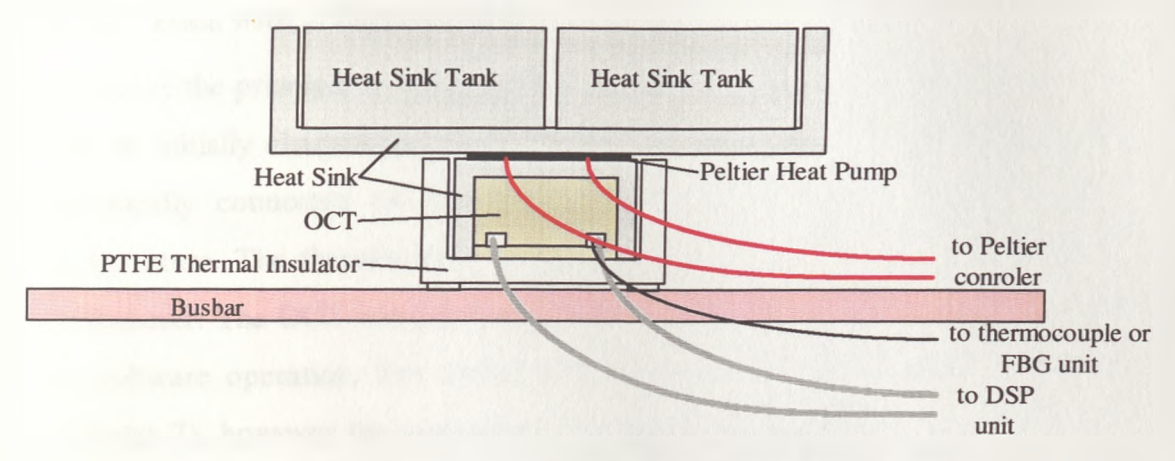


Figure 8-42 Schematic of the temperature test system

To obtain the sensor temperatures lower than approximately 5-10°C, additional cooling of the outer heat sink was required as the heat could not be effectively dissipated by air convection or radiation. This was realised by loading the heat sink tanks with ground dry ice and methylated spirit. The lowest temperature achieved using this method was approximately -25°C.

The heating of the sensor head was easier to achieve, and was controlled only by the Peltier current. The maximum obtained temperatures were in a range of 100°C. The photograph of the laboratory temperature test system is shown in Figure 8-43.

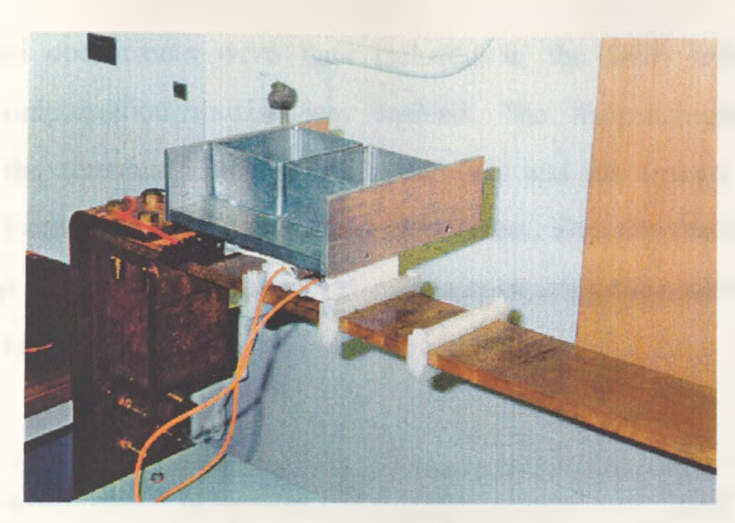


Figure 8-43 OCT temperature testing

## 8.5.2. Tests with a Thermocouple

To prove the principle of temperature compensation as described in Chapters 6 and 7, and to initially characterise the FR-5 sensor temperature response, a thermocouple (physically connected to the sensing element) was used to derive the sensor temperature. The thermocouple output was amplified and monitored by a precision multimeter. The OCT was interrogated by the DSP unit working in the ac-only mode of software operation. The software consisted of all the modules (as described in Chapter 7), however the temperature compensation routine was still disabled as the compensation function was yet unknown. The output signal was also monitored using a precision multimeter.

The OCT was temperature cycled from the room temperature to approximately 110°C. Each measurement was taken after an hour from a single increase of the Peltier current to allow adequate temperature stabilisation of the sensor. This was repeated several times, and the testing could take up to 3 days to complete. A temperature inverse line was then fitted to the obtained measurement points, and was used to generate polynomial coefficients of the compensation function according to the methodology described in Chapter 7.

The polynomial coefficients were then included in the DSP software and the temperature compensation routine was enabled. The thermocouple output was connected to the remaining input of the DSP unit and the system was ready to evaluate the effectiveness of temperature compensation. This was performed again by temperature cycling of the OCT, and the results comparing the uncompensated and compensated channels are shown in Figure 8-44.

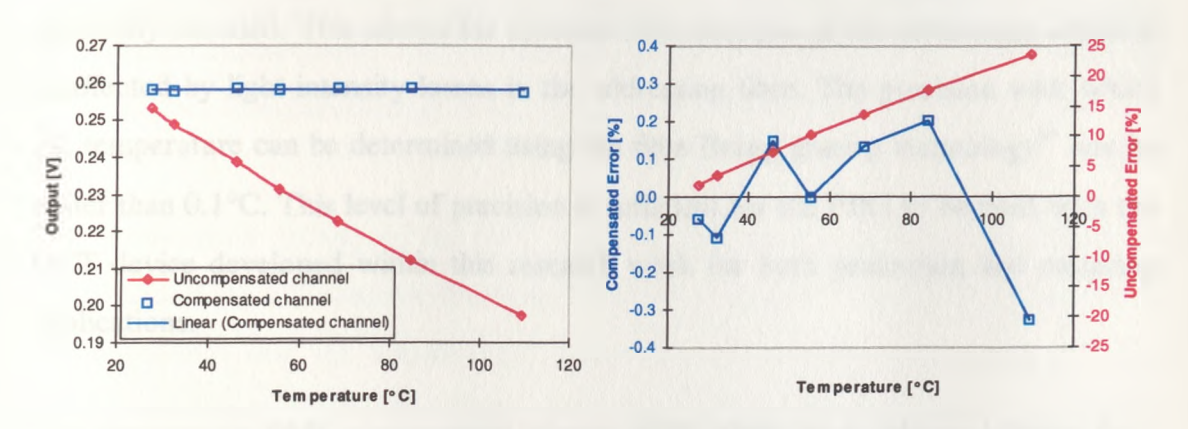


Figure 8-44 OCT temperature compensation using a thermocouple

The temperature effect within the OCT is compensated to approximately  $\pm 0.4\%$  over the temperature range between 25°C and 110°C (errors are calculated as relative differences from the average output value). Over the same range of temperatures, the uncompensated channel decreases approximately by 25%.

## 8.5.3. Temperature Compensation Using FBG Sensor

The compensation methodology and the used algorithms were proven to operate accordingly in the tests from the previous paragraph. However, in order to fully appreciate the fibre-optic technology in the proposed current measurement system, the thermocouple had to be replaced by an optical temperature sensor. As described earlier in Chapter 6, this could be accomplished using various optical methods, including indirect recovery of the OCT temperature. Since both the optical filter based temperature sensor and the indirect temperature recovery method are still in the experimental stages of development, a commercially available fibre Bragg grating system was adapted to derive the temperature information at the OCT point. The

system was developed for the prime purpose of a one year engineering evaluation of the FR-5 sensor, which is currently taking place at the British Short-Circuit Testing Station in Hebburn, UK. These tests will be reported later in this chapter.

## 8.5.3.1. Fibre Bragg Grating System

As described earlier in Chapter 6, the information from a fibre Bragg grating sensor is spectrally encoded. This allows for accurate determination of the measurand which is unaffected by light intensity losses in the addressing fibre. The precision with which the temperature can be determined using the fibre Bragg grating technology<sup>11</sup> can be better than 0.1°C. This level of precision is sufficient for the FBG to be used with the OCT device developed within this research work for both protection and metering applications.

The commercial FBG measurement system (FLS 3100) from Micron Optics Inc., designed to interrogate up to 30 fibre Bragg gratings in line, was used for the purpose of deriving the temperature at the OCT point. The system employed a temperature stabilised scanning Fabry-Perot interferometer to determine the wavelength change from the single Bragg grating.

The interrogating unit could operate only with a PC used to control the hardware and process the wavelength information from the FBG sensors. The software used for this purpose (created using LabView package) was provided by the instrument manufacturer, and was adapted to allow the temperature information to be derived from the FBG wavelength change information.

The system was calibrated by temperature cycling of the used FBG, and the relevant coefficients were incorporated into the LabView software routine. The temperature and wavelength values could be displayed on the PC monitor and also passed to the DSP unit through an additional extension card. Figure 8-45 shows two pictures: fibre Bragg grating probe, and the complete system incorporating all the necessary components for accurate current measurement using an OCT.

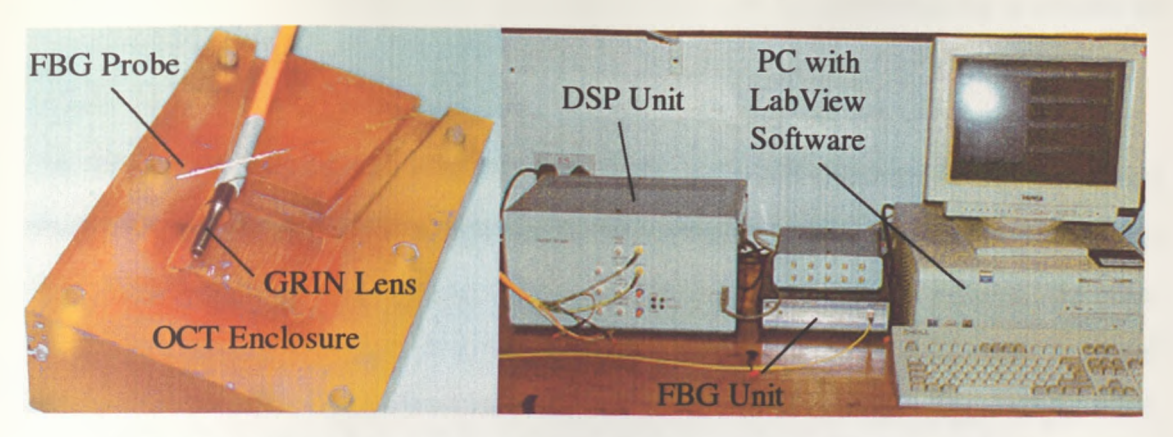


Figure 8-45 FBG probe (to the left), and the complete OCT interrogating system (to the right)

The temperature cycling of the OCT with the fibre Bragg grating was once again repeated and the full temperature characteristic was recorded. The DSP software was reprogrammed and the temperature compensation efficiency was evaluated. The results are shown below in Figure 8-46. In addition, the measured temperature characteristic is compared with the FR-5 manufacturer's data (graphs to the left), and the results are in a good agreement.

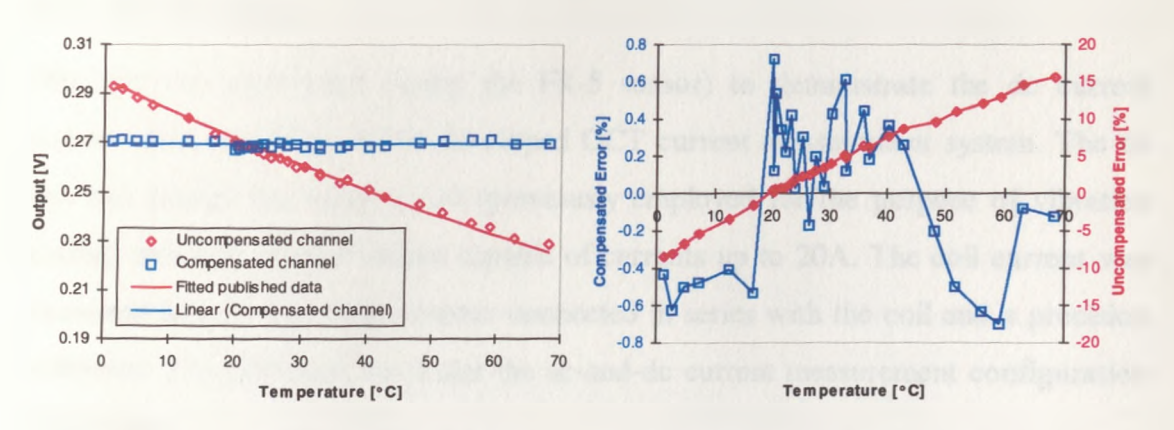


Figure 8-46 OCT temperature compensation using a fibre Bragg grating

The errors of the compensated channel, calculated as relative differences from the mean output value, are within the range of  $\pm 0.8\%$ . The compensation efficiency is worse than that of the previous tests with a thermocouple, and it is believed that this was due to the possible stressing of the FBG probe inside the OCT enclosure. Nevertheless, the obtained results satisfy the protection class instrument accuracy

specification. It is believed, that the above effect can be eliminated by a means of appropriate pre-housing of the FBG probe, which is currently under investigation.

The above tests have proven the principle of the proposed temperature compensation algorithms (using the thermocouple), and demonstrated a potential of employing the fibre Bragg grating technology to derive the OCT temperature. At present, the fibre Bragg grating interrogation system is still price prohibitive to be utilised in the final product OCT. The solution to this problem could be found in employing a single FBG system to derive temperatures of several OCTs within a substation. This would significantly reduce the total cost of the integrated current measurement system within the substation, and could even be competitive with the relatively inexpensive absorption glass optical temperature sensor solution (currently under development). When the development of the absorption glass based temperature sensor for a specific use with the OCT is completed, the two solutions may be assessed from the economic point of view.

# 8.6. DC Testing

This test was performed (using the FR-5 sensor) to demonstrate the dc current measurement capability of the developed OCT current measurement system. The dc test was carried out using a coil (previously employed for the purpose of vibration testing) and a dc current source capable of currents up to 20A. The coil current was measured using a low value resistor connected in series with the coil and a precision voltmeter. The DSP unit ran under the ac-and-dc current measurement configuration of software.

The OCT dc current response characteristic and the respective output errors are shown in Figure 8-47. The current axes represent the equivalent dc current flowing in the earlier considered rectangular cross-section busbar, and the sensor is thought to be placed on top of the conducting busbar.

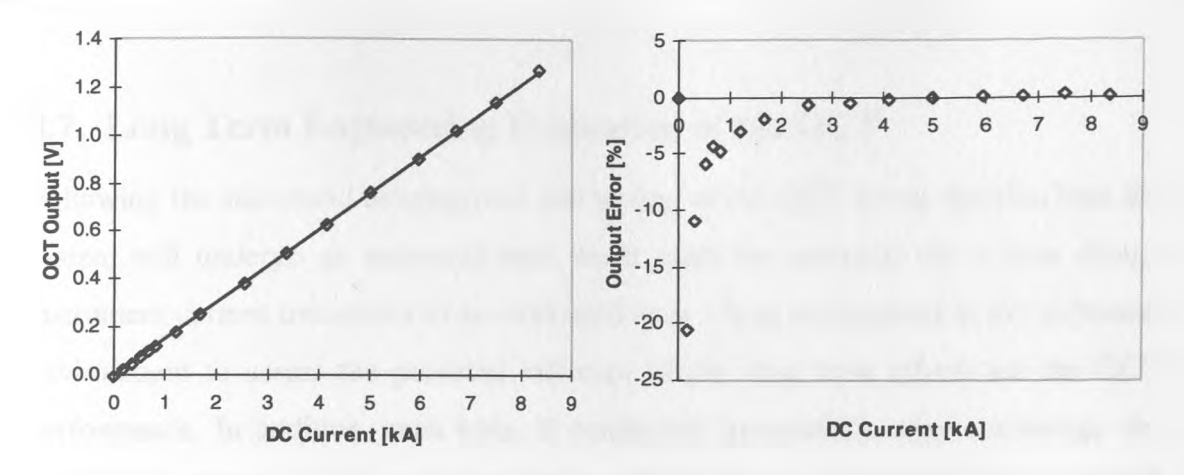


Figure 8-47 DC Output errors

It should be noted that the dc response of the sensor operating with the rectangular cross-section busbar is approximately 20% higher than the response to a 50Hz current of the same rms value. As discussed earlier in Chapter 5, this is caused by the different field distribution around the busbar with response to currents of different frequencies. The magnetic field density across the longitudinal cross-section of the sensing element, modelled for a 1000Amps dc current using the Oarsted package is shown in Figure 8-48. The results of this simulation can be compared with the results of magnetic field modelling for a 50Hz current, presented earlier in Chapter 5 (see Figure 5-22).

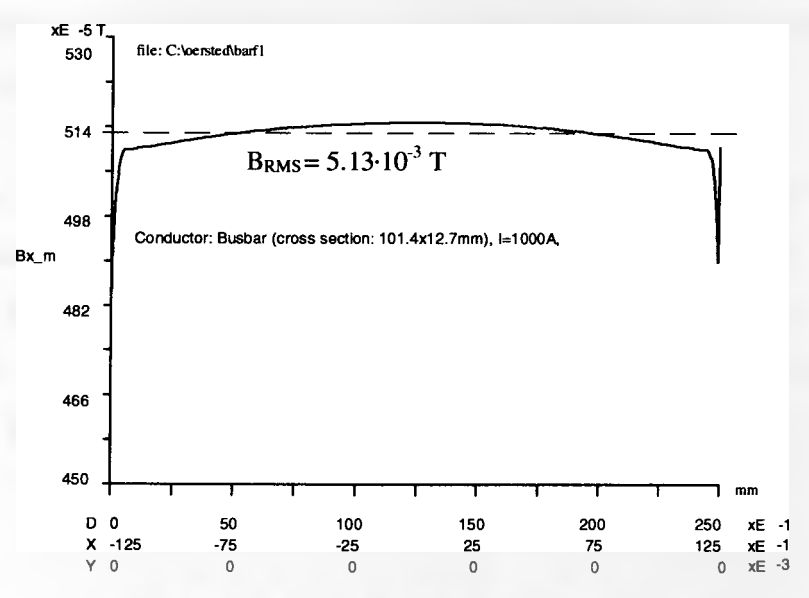


Figure 8-48 DC magnetic field modelling

# 8.7. Long Term Engineering Evaluation of the OCT

Following the successful development and testing of the OCT it was decided that the system will undergo an industrial trial. Such trials are essential for a new design instrument current transducer to be evaluated over a long term period in the industrial environment to assess the potential influence of the long term effects on the OCT performance. In addition, such tests, if conducted successfully, may encourage the industrial partners to put more trust in the new technology, and provide more funding in this area of research.

The trial of the OCT has started in August 1999 and is taking place at the British Short-Circuit Testing Station (BSTS) in Hebburn, UK, fully accredited by internationally accepted ASTA Certification Services.

#### 8.7.1. Description of the Field Trial Set-up

The test programme at the BSTS concerns both symmetrical and asymmetrical short-circuit current tests, most of which are of a maximum duration of 150ms, and are repeated several times over a one day period. The peak available current is in the range of 50kA, which is sufficient to examine the operational characteristics of the used FR-5 sensor to the device maximum dynamic range.

The sensor head is clamped to one of the busbars of the 22kV three phase transmission system, as shown in the photographs below (Figure 8-49). The addressing fibres of the OCT and the FBG sensor are run through a composite insulator to an extension box, and then to the control room which is situated some 100 metres from the test bay.

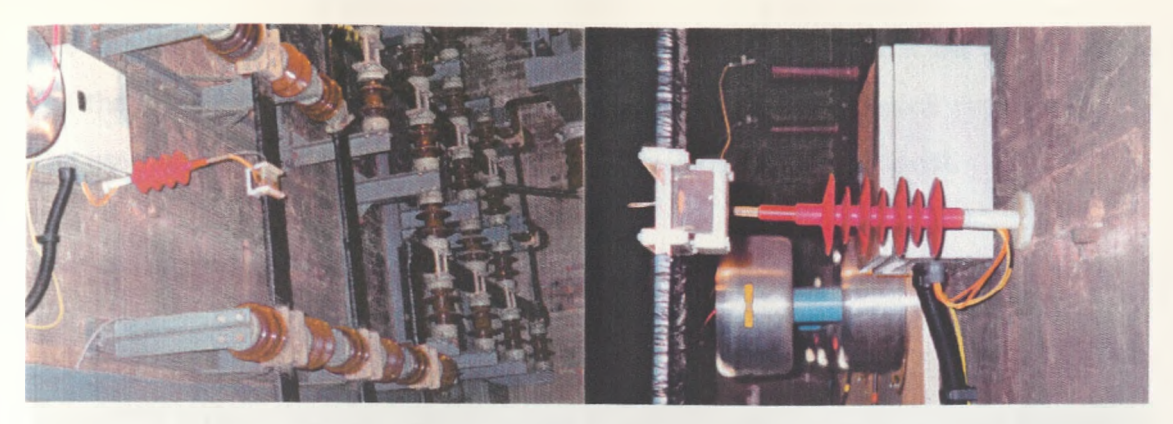


Figure 8-49 OCT single phase installation at the BSTS

The fully developed DSP unit with all the compensation algorithms included in the DSP software is used at BSTS to interrogate the OCT. The system runs in the ac-only mode of operation and provides vibration compensation, linearisation of the sensor characteristic and temperature compensation. The OCT temperature is derived using the fibre Bragg grating system interfaced to a PC.

To collect the data from the DSP unit and the BSTS reference signal, an additional data acquisition card is used mounted in the previously mentioned PC. The card allows for monitoring of up to 8 channels with a total sampling frequency of 200kHz. For the purpose of this trial, only 3 channels are monitored, namely, the OCT compensated and uncompensated channels, and the BSTS reference signal. The card also enables the OCT temperature information to be passed from the PC to the DSP unit.

The data acquisition card is controlled by a LabView software programme, specially created for this trial, and allows for a constant automatic data recording and storing on the hard drive. The single record is triggered by the OCT compensated signal which follows the short-circuit current event in the busbar. To make sure that the whole event is recorded the data acquisition software is set up in the pre-triggering mode of operation.

The application works in parallel with the software used to control the FBG system, and the temperature information is also appended at the and of each current record. The user interfaces of the above programmes are shown in Figure 8-50.

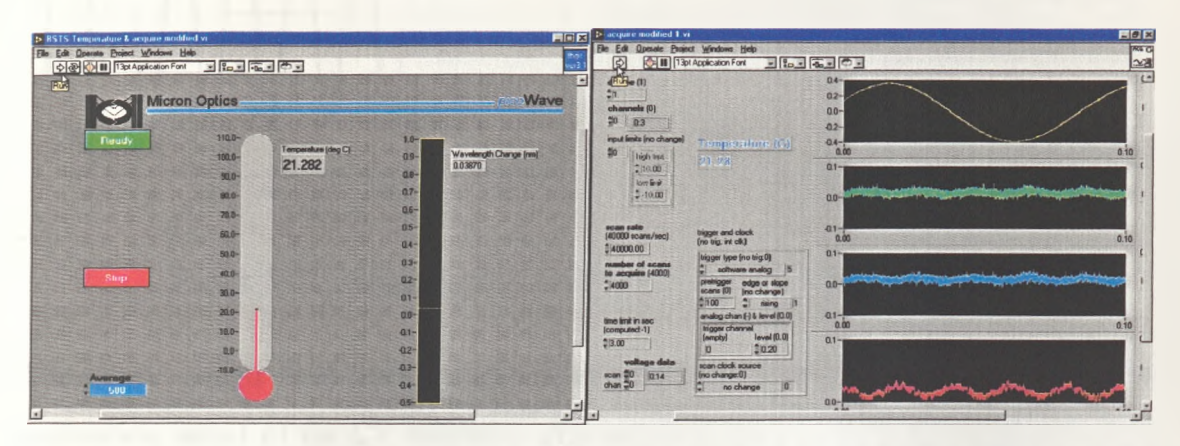


Figure 8-50 User interface of the modified FBG software (to the left), and the data acquisition window (to the right)

#### 8.7.2. Initial Tests Results

Over a hundred records, including symmetrical and asymmetrical currents of various magnitudes, were registered during the first 3 months of the trial. The most representative examples of the symmetrical and asymmetrical current records are shown below in Figures 8-51 and 8-52.

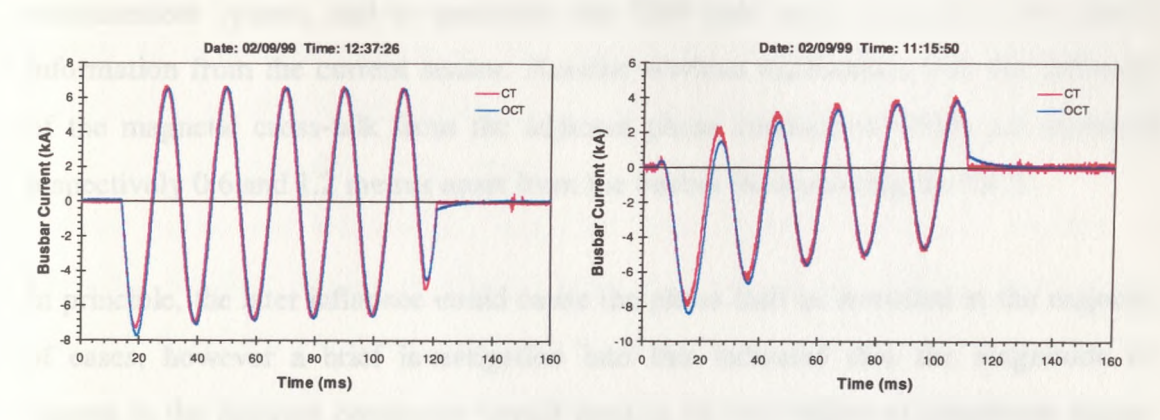


Figure 8-51 Example of recorded current signals (medium currents)

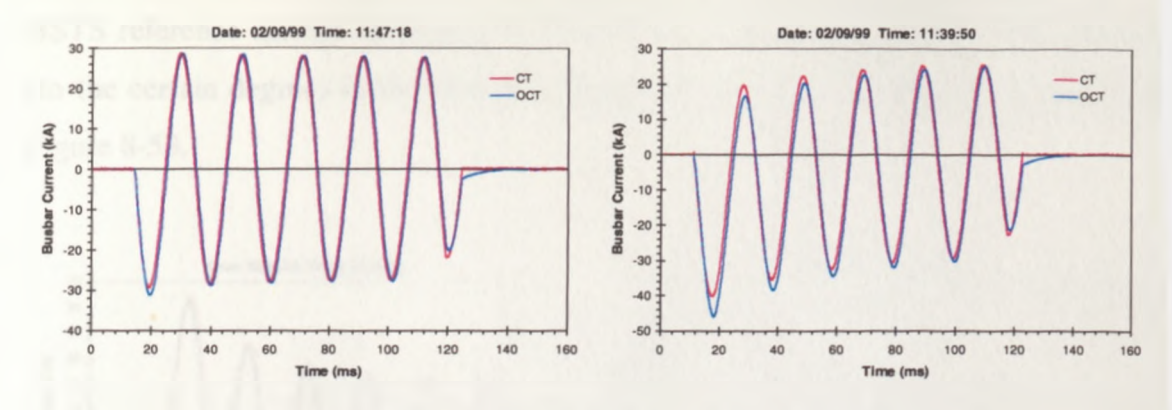


Figure 8-52 Example of recorded current signals (high currents)

The above graphs have been generated from the originally captured data using the calibration factor of the CT reference channel from the particular test and the OCT calibration factor derived as an average value from a large number of tests.

There are three noticeable differences between the captured OCT and CT signals:

- (i) initial amplitude difference,
- (ii) 600µs shift between the two signals,
- (iii) exponential tail of the optical signal.

Initially, it was believed that the above trace anomalies were generated by the OCT measurement system, and in particular the DSP unit used to process the optical information from the current sensor. Another obvious explanation was the influence of the magnetic cross-talk from the adjacent phase conductors which are mounted respectively 0.6 and 1.2 metres apart from the busbar incorporating the OCT.

In principle, the later influence could cause the phase shift as recorded in the majority of cases, however a brief investigation into this indicated that the magnitude of current in the adjacent conductor would have to be two orders of magnitude higher than the current in the conductor incorporating the OCT.

The later tests revealed, that the phase shift between the OCT and reference signals could be opposite. This occurs when the transduction sensitivity of the reference

signal is changed for the particular test purpose, resulting in the OCT trace leading the BSTS reference instead of lagging it. In addition, the exponential tail is also present (to the certain degree) in the reference signal. An example of such tests is shown in Figure 8-53.

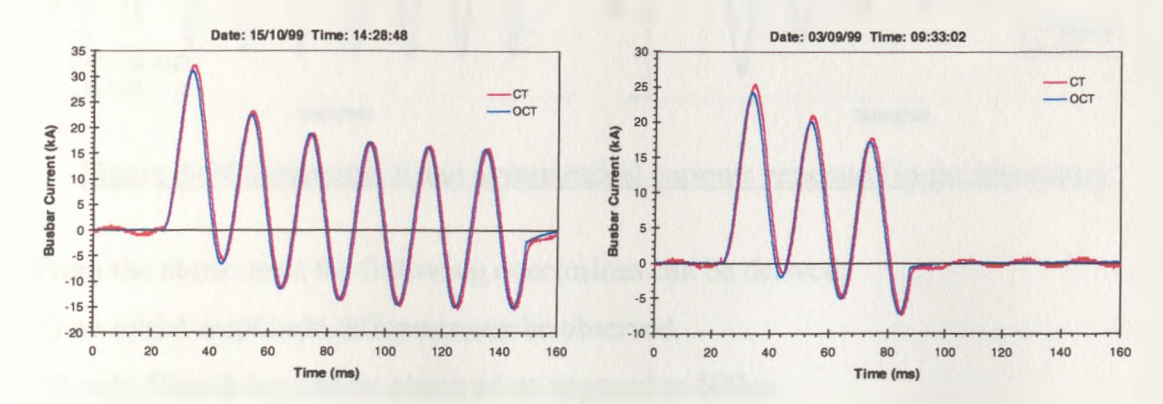


Figure 8-53 Illustration of 'phase lag' of the reference signal

To investigate further the above trace anomalies, independent tests were set up in the fully controlled and known laboratory test conditions. The results of these tests are reported in the following sections.

## 8.7.3. Laboratory Investigations

The duplicates of the OCT, DSP unit and the relevant software were once again subject to a detailed inspection. The BSTS test conditions were replicated as accurately as possible in the Strathclyde University laboratory. The sensor was placed in the coil of enamelled cable which was energised using two different current sources: variac and transformer, and then fault injection equipment capable of providing transient signals (similar to those recorded at the BSTS). The current reference signal was measured across a low value resistor connected in series with the coil. The maximum obtained magnetic field was equivalent to a current of approx. 10kA at the BSTS. The examples of the recorded OCT and reference signals of the symmetrical and asymmetrical currents are shown in Figure 8-54.

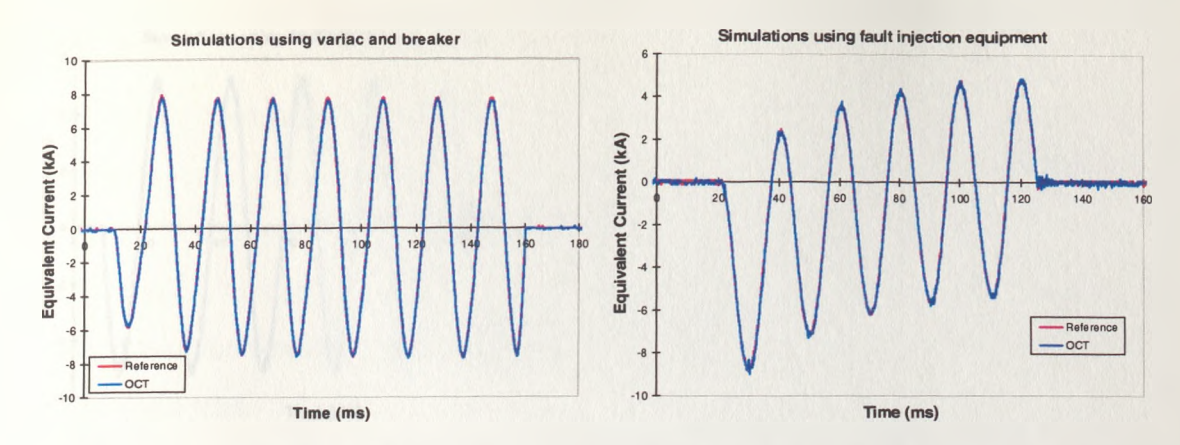


Figure 8-54 Symmetrical and asymmetrical currents generated in the laboratory

From the above tests the following conclusions can be derived:

- (i) no initial amplitude difference can be observed,
- (ii) only 50μs delay can be observed as opposed to 600μs,
- (iii) no exponential tail is present, even when the current is broken before the zero crossing (not shown in Figure 8-54).

The two signals retrace each other almost perfectly, the 50µs delay of the OCT signal is caused by signal processing and the remaining electronics of the DSP unit as described in Chapter 5, and satisfies the draft IEC specification concerned with the electronic current transformers.

Additional investigations were carried out including tests in which the current was broken before the zero-crossing. This could potentially explain the exponential tail present in the data recorded at the BSTS as there was a suggestion that the DSP filtering routine could introduce this anomaly. The results of the discussed tests are presented in Figure 8-55.

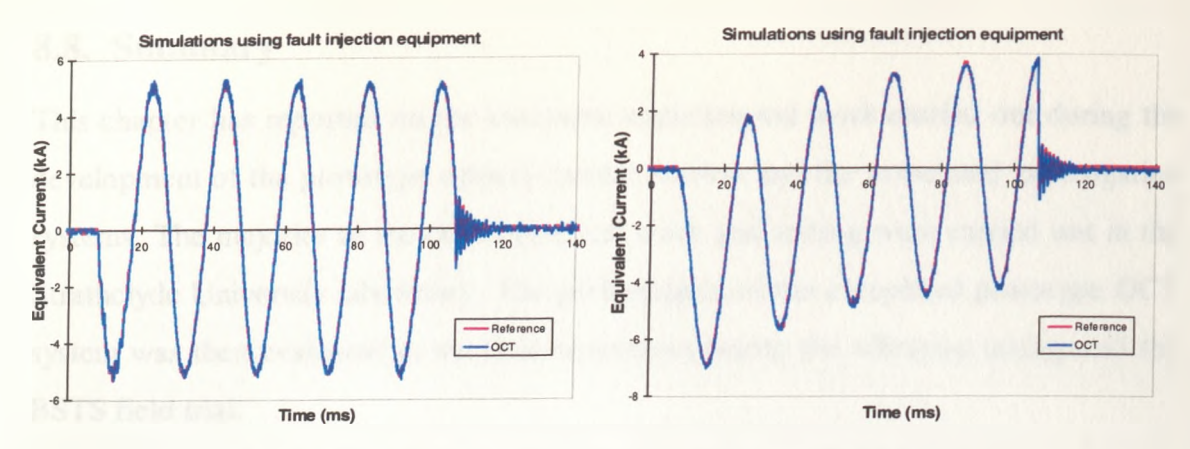


Figure 8-55 Current broken in non zero-crossing point

Even if the current is broken before the zero-crossing point, the exponential tail is not present in either the reference or the OCT signals. Due to the excessive output impedance of the power amplifier used to supply the coil, the tails of the above traces oscillate, however, the OCT signal still precisely follows the reference signal. This is shown in more details in Figure 8-56 in which the time scale of one of the above graphs is expanded.

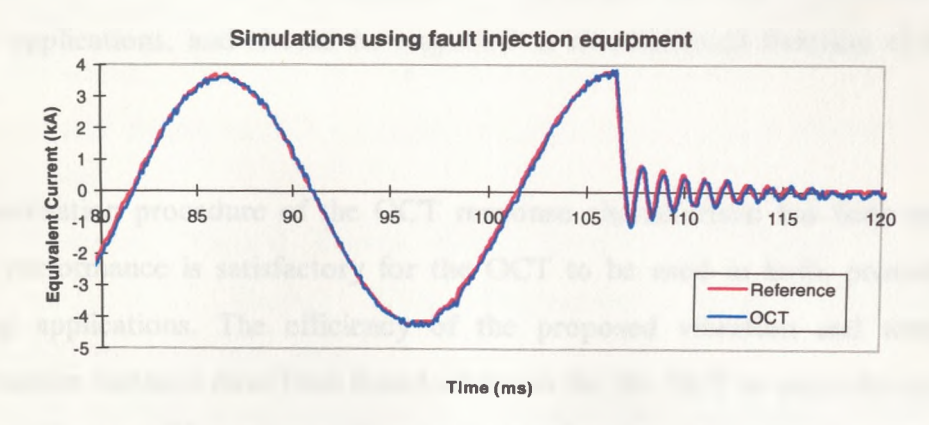


Figure 8-56 Oscillations in the power amplifier

The above tests lead to the conclusion that it is very unlikely that the tested OCT measurement system causes the trace anomalies as experienced during the initial stage of the BSTS field trial. A detailed investigation of the possible causes of the above trace anomalies is being carried out at present. It is proposed that an independent, calibrated current reference signal will be provided to allow an effective evaluation of the OCT system.

## 8.8. Summary

This chapter has reported on the extensive experimental work carried out during the development of the prototype optical current sensors and the associated interrogation systems. The majority of the developmental work and testing were carried out in the Strathclyde University laboratory. The performance of the completed prototype OCT system was then evaluated in the field conditions during the vibration testing and the BSTS field trial.

The ac and dc current measurement capabilities of the OCT system have been demonstrated. This is achieved by loading two different software programs to the DSP processor internal memory. The accuracy achieved at present satisfies the IEC protection class specification of an instrument current transformer for the system configured in the ac-only mode of operation. The dc current measurement performance needs to be improved, in particular in terms of the long term stability of the system. Nevertheless, the dc current sensing facility can still be valuable in some specific applications, and should be regarded as an additional function of the OCT system.

The linearisation procedure of the OCT response characteristic has been evaluated, and its performance is satisfactory for the OCT to be used in both, protection and metering applications. The efficiency of the proposed vibration and temperature compensation methods have been found adequate for the OCT to meet the protection class specification. This was confirmed after performing a range of comprehensive vibration and temperature tests.

The initial results of the industrial field trial at the BSTS are very encouraging. The OCT system has been functioning correctly for over 6 months in the industrial environment. The possibility of installing additional two current sensors on the remaining phases is currently under discussion, and if concluded with a positive response, the experimental assessment of the proposed magnetic cross-talk compensation scheme (as described in Chapters 6 and 7) will be feasible.

## 8.9. Chapter References

- 1) G. Tobey, J. Greame, L. Huelsman, "Operational Amplifiers Design and Applications", McGraw-Hill, 1971.
- 2) Burr-Brown Applications Handbook, 1990,
- 3) P. Horowitz, W. Hill, "The Art of Electronics", Cambridge University Press, 1996,
- 4) P. Niewczas, B. Yi, "Results of Accuracy Tests of Optical Crystal based Current Sensors", CEPE RR/OPT/TR/1996-003, 1996,
- 5) "2N4338 N-Channel JFET", Temic Semiconductors Data Sheet,
- 6) "16-Bit, 200 kSPS BiCMOS A/D Converters: AD976/AD976A", Analog Devices data sheets,
- 7) "Monolithic 16-Bit DACPORT: AD669", Analog Devices data sheets,
- 8) N., A. Pilling, "Interim report on circuit breaker vibration levels for IEC', The National Grid Company plc, Technology & Science Division, 1995,
- P. Niewczas, "Principle of Temperature Compensation in Optical Current Transducer Based on TGG Crystal", CEPE Reference No. RR/OPT/TR/1996-005, 1996,
- P. Niewczas, "Optical Crystal Based Devices for Current and Voltage Measurement - Project Work Programme", CEPE Reference No. RR/OPT/PR/1996-006, 1996,
- 11) "FLS 3100, Fibre Bragg Grating Unit", Micron Optics user manual, 1998.

# 9. General Conclusions and Future Work

# 9.1. Principal Results and Contributions

The research work reported in this thesis has resulted in the successful implementation of the Faraday effect based optical current transducer as a replacement device for conventional high voltage current transformers. Laboratory trials have shown that the present optical current measurement system satisfies the accuracy requirements specified for the protection class current transformer within the electricity industry. The device also provides an inherent high voltage insulation, intrinsically safe failure modes and a significantly wider measurement bandwidth than conventional CTs. Although the benefits of this novel approach in current measurement are unquestionable, the OCT device has been found vulnerable to the influence of the environmental factors, such as vibration, temperature and magnetic cross-talk effects, detrimental to the device performance. This thesis provides a comprehensive analysis of the errors associated with these effects and proposes optimal methods for active compensation of the above factors using digital signal processing techniques.

The vibration induced errors, although analysed in depth within this research work, have been found difficult to quantify even in the specific OCT system. The sensor vibration response depends on various parameters of the optical arrangement and on the way the vibration itself is applied. It has been confirmed experimentally that these errors can be sufficient to significantly deteriorate the performance of the present sensor system. In the proposed compensation technique, the vibration induced noise is eliminated by configuring the OCT for bi-directional light propagation. In this way two signals are obtained, both containing measurement and vibration components. Due to the non-reciprocal property of the Faraday effect, the measurement components are found to be in anti-phase while the vibration components are consistent in phase. These two signals are then used to effectively cancel any vibration components in the output signal. The tests reported in this work have demonstrated a success of the proposed active vibration compensation method which with the

currently used technology provides a level of compensation of approximately 30dB. This is sufficient for the OCT device to be utilised as a protection current transducer.

The thermal influence on the operation of the present sensor also requires compensation. The relevant analysis to determine the required temperature measurement precision have been performed for the TGG and FR5 based sensors. It has been estimated that it is sufficient to recover the OCT temperature with a precision of up to 1.5°C and 0.15°C for protection and metering applications respectively. Temperature compensation may be realised using direct or indirect temperature recovery methods. However, the direct method is preferred as in this case the precision of the temperature recovery process is not affected by the level of measured current. In the present series of experiments a commercial fibre Bragg grating sensor was used to directly derive a temperature information at the OCT point. The efficiency of the temperature compensation scheme has been found adequate for the OCT to meet the protection class specification. This was successfully demonstrated after performing a range of comprehensive temperature tests.

The analysis of the magnetic cross-talk on the sensor operation has demonstrated that for the bulk of the installations within the electricity network, the cross-talk levels from adjacent phases will introduce measurement errors that are outside the required operational specifications. Experimental investigations have indicated that screening of the OCT is not a feasible alternative because of the low frequency of the energising field. Improved measurement sensitivity and a greater degree of cross-talk rejection can be achieved through the use of flux concentrators which encircle the current being measured. However this would ultimately restrict the operational bandwidth of these devices and could compromise many of their attractive features such as reduced size and minimal insulation requirements. A preferred solution, as proposed in this thesis, is to directly process the information from all three phases to reject the cross-talk components and a methodology to implement this has been developed and presented.

It is also proposed, that the DSP system developed within this research can facilitate the linearisation of the sensor response characteristic in real time operation. This gives a benefit of increasing the maximum modulation level of the measured signal and allows for use of an extended sensor dynamic range to relax some critical design requirements of the photo-receiver circuit.

The thesis also reports on the research work concerned with the development of a low noise photo-receiver circuit, suitable for the operation with the proposed DSP unit. The improved design of a transimpedance photodetector with a preceding J-FET stage shows an enhanced performance in terms of the signal-to-noise ratio as compared to the conventional bipolar op-amp design. The initial noise level is suppressed by a factor of 3 and the signal-to-noise ratio is increased by 3-9dB.

Although, the developed DSP system provides a great degree of flexibility in processing the sensor output signal, it also introduces quantisation errors, directly related to the analogue-to-digital conversion process. These errors are analysed and quantified, and recommendations are provided with respect to the selection of an OCT for operation with a given analogue-to-digital converter (and vice-versa) in order to meet stringent accuracy requirements for metering and protection class instruments within the power industry.

The thesis also provides a detailed description of the sensor head manufacture using a multi-pass reflective arrangement of a sensing element with implementation of a novel active alignment method as developed within this research work. The active alignment method allows for a precise definition of the required 45° bias point with respect to the output polariser orientation, and facilitates the optimal light transmission through the sensor. The new approach to the sensor encapsulating technique by directly 'potting' the sensing element in the epoxy resin was also investigated. The difficulties encountered while using this approach, mainly due to the mechanical stress applied on the sensing element during the final stage of epoxy curing, were overcome by producing a two-part enclosure from a pre-cured epoxy block. It is believed, that a

resin injection technique could be applied to manufacture a precise sensor housing, similar to that produced using machining.

Finally, the thesis reports on the industrial field trial at the British Short-Circuit Testing Station in Hebburn, UK, which started in August 1999, and has so far demonstrated a success of the optical current measurement system developed within this research work. A great number of current records have been collected and the initial results are very encouraging. The OCT system has been functioning correctly for over 6 months in harsh environmental conditions and during this time no decrease in performance has been detected. The possibility of installing additional two current sensors on the remaining phases is currently under discussion, and if concluded with a positive response, the experimental assessment of the proposed magnetic cross-talk compensation scheme will be possible.

The novelty of the research reported in this thesis lies primarily in the following areas:

- manufacture of a sensor head using multi-pass reflective arrangement of a sensing element with implementation of a novel active alignment method
- development of a robust sensor interrogation unit based on a digital signal processing system and real time software procedures for conditioning of the OCT output signal
- development and real time software implementation of a vibration compensation technique for the OCT, based on the non-reciprocal property of the Faraday effect and bi-directional arrangement of the current sensor interrogation scheme with alternately pulsed light sources and time gated photo-receivers
- development and real time software implementation of a temperature compensation technique with utilisation of a Fibre Bragg Grating sensor used to derive the OCT temperature
- real time software implementation of the OCT linearisation routine
- demonstration of both ac and dc current measurement capabilities of the current sensor and the accuracy compliance with the electricity industry protection specification for the instrument current transducer

 development of a methodology for magnetic cross-talk compensation based on a parallel processing of the information from all three phases to reject the cross-talk components

## 9.2. Future Work

The research and further work identified in this section are areas which, in the author's opinion, will prove to be particularly beneficial.

At present, the cost of the fibre Bragg grating interrogation system prohibits its use in the final product OCT. The solution to this problem could be found in employing a single FBG unit to derive temperatures of several OCTs within an electrical substation. This would significantly reduce the total cost of the integrated current measurement system within the substation, and could even be competitive with the potentially inexpensive absorption glass optical temperature sensor solution (currently under development). When the development of the absorption glass based temperature sensor for a specific use with the OCT is completed, the two solutions may be assessed from the economic and functional points of view.

The development of a 3-phase optical current measurement system using an integrated DSP interrogation unit, as proposed within this thesis, will enable direct implementation of the proposed magnetic cross-talk compensation scheme. The experimental research work associated with this concept is continuing and a full evaluation of the cross-talk performance will be performed in due course. At this stage an experimental evaluation of the performance of the processing routine proposed here will be provided.

The DSP interrogation unit developed within this research work can be used directly as a platform to process the measurement signal derived from an optical voltage transducer (OVT). In this case, only the software components would have to be modified to provide the signal processing relevant for the OVT operation.

Consequently, the OVT development process should proceed much faster as it will be restricted mostly to the sensor head manufacture.

Although, the present DSP interrogation unit is sufficient for the OCT to meet the protection accuracy specification, the work should continue to achieve the metering class 0.1 specification, and in particular the performance of a combined metering and protection device. This can be achieved when the signal-to-noise ratio of the measurement system is further increased. The noise analysis of the photo-receiver circuit, carried out in this thesis, indicates that more optical power is required at the photo-receiver input to improve the signal-to-noise ratio. The work is being carried out at present to identify suitable replacement components which would refine the present optical arrangement. The semiconductor industry provides increasingly more efficient light sources which, when used with larger diameter fibres may significantly improve the performance of the discussed current measurement system.

In addition to that, a radical way of improving the system performance could be devised using high frequency modulation of the input optical signal along with appropriate demodulation on the receiving end. The optical current sensor would modulate the amplitude of the high frequency carrier which additionally would have to be chopped in order to incorporate the bi-directional arrangement of the vibration compensation scheme. The encoded information about the measured current could be extracted using a narrow band filter followed by a rectifier and low pass filter. This could be implemented using analogue techniques rather than DSP due to the high bandwidth of the processed signal. However, signal processing in this case is not complex and standard analogue filtering methods could be employed to effectively implement this demodulation scheme. The measurement signal processed in this fashion could then be directly fed in to the existing DSP electronics. The application of the above technique would bring the following advantages:

• Limiting the noise bandwidth to a narrow spectral band of the demodulation filter.

The noise power of the photo-receiver circuit at higher frequencies is much lower

- than that at low frequencies. The above solution could significantly improve the signal-to-noise ratio of the processed signal.
- DC offsets and their drifts in the photo-receiver circuits would no longer cause the
  decrease in accuracy of the measurement process since the dc components are
  filtered out by the demodulation scheme.
- The whole dynamic of the A/D converter could be used as opposed to the present arrangement in which only half of the dynamic is used due to the requirement of the dc component monitoring.

The above technique adds to the complexity of the measurement system hardware, however, the advantages could be invaluable. The work is being carried out at present to assess the potential of the engineering feasibility of the presented solution.

The issues of the sensor head manufacture and packaging are very important areas within the OCT development. More research effort should be committed towards automation of the optical assembly alignment process, based on the active alignment technique developed within this research work, and the actual packaging which would protect the sensor from mechanical vibration and chemical attack. This would enable faster prototyping of the sensor head and the related technology transfer to the industry domain.

Finally, in terms of the device functionality, it would be beneficial to define the communication standards for Intelligent Electronic Devices (IEDs) around an electrical substation which would enable the OCT to directly output its measurement information for use in protection and monitoring applications. The proposed DSP platform provides a direct access to the processor internal memory which could be readily exploited as a communication port. The current measurement information can be coded within the DSP system to form any standard communication protocol. The work is being carried out at present by the International Electrotechnical Commission on the specifications for the Electronic Current Transducers, which should also cover the communication's aspects.

## **Appendix**

.module/RAM/ABS=0

The two software modules of Optical\_Current\_Transducer assembler source code are included in the following text: ac-and-dc measurement configuration and ac-only measurement configuration.

## AC-and-DC measurement configuration

```
Optical_Current_Transducer_ac_dc.
ξ
       This program was written by Pawel Niewczas
       Centre For Electrical Power Engineering.
       University of Strathclyde, Glasgow, UK
{
{
       This program is for the use with the DSP
       interrogation system of an Optical Current
{
       Transducer.
 Features:
       - AC + DC current measurement.
       - autocalibration of the system,
  - vibration compensation of the OCT,
       - sensor response characteristic correction,
       - temperature compensation of the sensor.
{memory mapped ADSP-2181 control registers}
.const IDMA=
.const BDMA_BIAD=
                                           0x3fel:
.const BDMA_BEAD=
                                           0x3fe2:
.const BDMA_BDMA_Ctrl=
                                           0x3{e3:
.const BDMA_BWCOUNT=
                                           0x3fe4:
.const PFDATA=
                                           0x3fe5:
.const PFTYPE=
                                           Ox3fe6:
.const SPORT1_Autobuf=
                                           Ox3fef:
.const SPORT1_RFSDIV=
                                           0x3ff0:
.const SPORT1_SCLKDIV=
                                           0x3ff1:
                                           0x3ff2:
.const SPORT1_Control_Reg=
.const SPORTO_Autobuf=
                                           Ox3ff3:
                                           Ox3ff4:
.const SPORTO_RFSDIV=
                                           0x3ff5:
.const SPORTO_SCLKDIV=
                                           0x3ff6:
.const SPORTO_Control_Reg=
                                           0x3ff7;
.const SPORTO_TX_Channels0=
                                           Ox3ff8:
.const SPORTO_TX_Channels1=
                                           0x3ff9;
.const SPORTO_RX_Channels0=
                                           0x3ffa:
.const SPORTO_RX_Channels1=
                                           0x3ffb:
.const TSCALE=
                                           0x3ffc;
.const TCOUNT=
.const TPERIOD=
                                           0x3ffd:
                                           Ox3ffe:
.const DM_WAIT_REG=
                                           0x3fff:
.const System_Control_Reg=
                                           (23C int, f = 1.3095 th 2 14 forme
             f = b#0101100011101101;
(********************** Variable and Buffer Declaration
(sampling control variables:)
.var/dm stat_togg_flag;
.var/dm
              stat_read;
(input/output buffers:)
         CH1;
.var/dm
              CH2:
.var/dm
.var/dm CH3;
.var/dm output_1;
.var/dm output_2;
(autocalibration)
.var/dm stat_autocalibration,
```

```
.var/dm
             offset_1;
.var/dm
               offset_2;
.var/dm
              magnitude_1;
.var/dm
              magnitude_2;
.var/dm
               k1:
.var/dm
               k2;
.var/dm
              correct_coef[8]:
{OCT response characteristic}
.var/dm
              asin_delta_coef[512];
{Temperature compensation}
.var/dm/circ temp_coef[5];
.var/dm
                input_temp_comp;
{**************** Variable and buffer initialization *******
.init correct_coef: 0x7500, 0x7000, 0x6500, 0x6000, 0x5500, 0x5000, 0x4500, 0x4000;
.init temp_coef:
b#0101010001010101,
                      {a = +0.65884255}
                     (b = +0.32809639)
{c = +0.01390126}
(d = 0)
b#0010100111111111,
b#000000000101110,
b#000000000000000000.
b#00000000000000000;
                     {e = 0}
.init asin_delta_coef:
{ start asin_coef }
ъ#00000000000000000.
b#0111100011001100,
{ start delta_coef }
ь#0101000101111101.
b#0111001101000111;
[********* Interrupt Vector Table *******)
jump start; {Location 0000: reset}
rti; rti; rti;
               (Location 0004: IRQ2)
        rti;
        rti: rti; rti;
        rti; {Location 0008: IRQL1}
               rti; rti;
        rti:
        rti; (Location 000c: IRQL0)
               rti; rti;
        rti;
         rti; {Location 0010: SPORTO tx}
                rti; rti;
         rti;
                (Location 0014: SPORTO rx)
         rti;
               rti; rti;
         rti;
 jump autocalibration; {Location 0018: IRQE}
                       rti;
                rti;
         rti; (Location 001c: BDMA)
         rti; rti; rti;
         rti; (Location 0020: SPORT1 tx or IRQ1)
         rti; rti; rti;
               {Location 0024: SPORT1 rx or IRQ0}
         rti:
         rti; rti;
                        rti;
         ggle_flags; (Location 0028: timer) rti; rti; rti;
  jump toggle_flags;
         rti; (Location 002c: power down)
         rti; rti; rti;
```

```
start:
reset fl0, reset fl2, reset fl1;
                          {F10 - LED/LD driver control}
                          {F12 - current sampling control}
                          {Fl1 - temperature sampling control}
     ax0 = 0;
     dm(stat_togg_flag) = ax0;
     dm(stat_read) = ax0;
     dm(stat_autocalibration) = ax0:
     ax0 = b#0111101100000110;
     dm(PFTYPE) = ax0;
{******************** Serial Port 0 (SPORTO) Set Up ****************************
     ax0 = 0;
     dm(SPORTO_Autobuf) = ax0;
                          {autobuffering disabled}
     dm(SPORTO_Control_Reg) = ax0; {ctrl functions disabled}
ax0 = 0;
     dm(SPORT1_Autobuf) = ax0;
                          {autobuffering disabled}
     {SCLKDIV not used}
     dm(SPORT1_Control_Reg) = ax0; {ctrl functions disabled}
ax0 = 0;
     dm(TSCALE) = ax0;
     dm(TCOUNT) = ax0;
     dm(TPERIOD) = ax0;
     ax0 = 0x0;
     dm(TSCALE) = ax0;
     ax0 = 0xa5;
                    /* -165- a5 -50kHz- */
     dm(TPERIOD) = ax0;
     dm(TCOUNT) = ax0;
     ena timer;
ax0 = b#000000000000100;
     dm(DM_Wait_Reg) = ax0;
     ax0 = b#0111101100000110;
     dm(PFTYPE) = ax0;
     {enable SPORT0}
     dm(System_Control_Reg) = ax0;
     ifc = b#00000011111111;
                              {clear pending interrupt}
     nop;
     icntl = b#00000;
     mstat = b#1100000;
17 = ^asin_delta_coef;
     L7 = 0;
     I1 = ^temp_coef + 1;
     L1 = %temp_coef;
     M1 = 1;
ax0 = b#00000000;
     dm(PFDATA) = ax0;
                          {enable source 1 and source 2}
     imask = b#0000010001;
                          {allow timer and a_calib interrupt}
     ifc = b#000100000000000;
                         {force autocalibration}
     nop;
     imask = b#0000010001;
                         {allow timer and a_calib interrupt}
```

```
wait_interrupt:
       idle;
       jump wait_interrupt;
toggle_flags:
      dis sec_reg;
      ar = dm(stat_togg_flag);
       ar = pass ar;
      if ne jump togg_fl0;
togg_f12:
      toggle fl2, toggle fl1;
                              {current & temperature sampling conrol}
      ax0 = 1;
      dm(stat_togg_flag) = ax0;
togg_f10:
      toggle fl0;
                               {LED driver control}
      ax0 = 0;
      dm(stat_togg_flag) = ax0;
      ar = dm(stat_read);
      ar = pass ar;
      if eq jump read_CH3_and_CH1;
read_CH2:
      my1 = IO(0x01d);
                               {read current: CH2}
      dm(CH2) = my1;
      dm(stat_read) = ax0;
{*********** write to DACs **********
      my1 = dm(output_1);
                               {write to D/A_2}
      IO(0x017) = my1;
      nop; nop;
      my1 = dm(output_2);
      IO(0x00f) = my1;
                              {write to D/A_1}
      rti;
read_CH3_and_CH1:
      imask = b#0000010001;
      nop;
      ax0 = 1;
      dm(stat_read) = ax0;
      ena sec_reg;
{read current: CH3}
      ax0 = IO(0x01b);
      dm(CH3) = ax0;
      ax0 = IO(0x01e);
                              {read temperature: CH1}
      dm(CH1) = ax0;
      ar = dm(stat_autocalibration);
                                   {Come out from calibration?}
      ar = pass ar;
      if eq rti;
{read current: E1 (CH3 on board)}
      ax0 = dm(CH3);
      ay0 = dm(offset_1);
      ar = ax0 - ay0;
                                     {subtract offset from E1}
     my0 = dm(k1);
     mr = ar * my0 (rnd);
                             {normalise gain in E1}
      dm(output_1) = mr1;
                              {____E1 in ax0 register__
     ax0 = mr1;
                              {read current: E2 (CH2 on board)}
     ax1 = dm(CH2);
     ay1 = dm(offset_2);
     ar = ax1 - ay1;
                                    {subtract offset from E2}
     my0 = dm(k2);
     mr = ar * my0 (rnd);
                             {normalise gain in E2}
     ay0 = mr1;
                              {____E2 in ay0 and mr1 register____}
```

nop;

```
{CH1-CH2}
        ar = ax0 - ay0;
        ay1 = ar;
                                                     {CH1+CH2}
        ar = ax0 + ay0;
                                             {(CH1-CH2)/(CH1+CH2)}
        call div:
 This subroutine uses lookup table and linear interpolation to achieve fast and very accurate linearisation of the sensor
        sin(2*theta) response characteristic.
        In fact there are two lookup tables: first-approximation table
        (asin_coef) and interpolation coefficients table (delta_coef);
       each one consists of 256 coefficients.
       Computation Time: 33 cycles maximum
       ar = ay0;
       ar = abs ar;
                                     {absolute value of input}
       sr0 = 0:
                                     {multiply input by 256}
       sr = ashift ar by -7 (hi);
                                     {load M7 of address generator}
       M7 = sr1;
                                     {with multiplied and truncated input}
       sr0 = 0;
                                     {zero the truncated value}
                                     {generate Xn}
       sr = ashift sr1 by 7 (hi);
       ay1 = sr1;
       ar = ar - ay1;
                                     {perform X-Xn}
       mx1 = ar;
       I7 = ^asin_delta_coef;
                                    {pointer at the begining of ASIN table}
      my0 = dm(I7,M7);
                                    {postmodify I7 by M7 register}
      my0 = dm(I7,M7);
                                    {generate Yn}
      I7 = ^asin_delta_coef + 256; {pointer at the begining of DELTA table}
      my1 = dm(I7,M7);
                                    {postmodify I7 by M7 register}
      my1 = dm(I7,M7);
                                    {generate Kn (DELTAn)}
      ax0 = 0x500;
                                    {4% of input signal}
       ar = ax0 - ay1;
                                    {is input < 0.04}
      if GE jump straight; {YES, straight calculation; NO, go further}
       ax0 = 0x6200; {1.15-2.14 format boundary of delta_coef}
                            {2.14-5.11 format boundary of delta_coef}
{is input < = first boundary?}</pre>
      ax1 = 0x7900;
       ar = ax0 - ay1;
       if GE jump delta1;
                                    {YES, perform deltal subrutine}
       ar = ax1 - ay1;
                                    {NO, is input < = second boundary?}
       if GE jump delta2;
                                    {YES, perform delta2 subrutine}
                                    {NO, perform delta5 subrutine}
delta5:
       mr = mx1 * my1 (ss);
                                           {perform: (X-Xn)*Kn }
       sr = ashift mr1 by 4 (hi);
       sr = sr or lshift mr0 by 4 (lo);
                                           {Convert to 1.15 no. format}
       ay1 = my0;
       ar = sr1 + ay1;
                                           {perform: ((X-Xn)*Kn) + Yn}
       af = pass ay0;
       if LT ar = -ar;
                                           {recover sign}
       jump end_response_characteristic;
delta1:
      mr1 = my0;
       mr0 = 0;
       mr = mr + mx1 * my1 (RND);
                                           {perform: (X-Xn)*Kn + Yn }
       af = pass ay0;
       ar = mr1;
       if LT ar = -mr1;
                                           {recover sign}
       jump end_response_characteristic;
delta2:
       mr = mx1 * my1 (ss);
                                           {perform: (X-Xn)*Kn }
       sr = ashift mr1 by 1 (hi);
       sr = sr or lshift mr0 by 1 (lo);
                                           {Convert to 1.15 no. format}
       ay1 = my0;
       ar = sr1 + ay1;
                                           {perform: ((X-Xn)*Kn) + Yn }
       af = pass ay0;
       if LT ar = -ar;
                                           {recover sign}
       jump end_response_characteristic;
straight:
       mx0 = ay0;
       my0 = 0x517d;
       mr = mx0 * my0 (RND);
       ar = mr1;
```

```
end_response_characteristic: nop;
This subroutine uses polynomial approximation of the OCT
       inverted temperature characteristic to calculate the
{
       temperature compensated current output of the OCT.
       The OCT temperature characteristic is measured across the
{
       operating temperature range eg -30C and +80C at a constant
{
       current, e.g., 2000A. Then it is inverted and scaled, and
       polynomial coefficients from 'a' to 'e' are evaluated.
       The subroutine uses these coefficients to calculate y(T)
       function.
       Polynomial function: y(T) = a + bT + cT^2 + dT^3 + eT^4
       Intercept coefficient: f
       Output(I) = Input(I,T) * y(T) * f
       The intercept coefficient is used to set the reference
       temperature eg 23C. At this temperature the compensated
       output is equal to the noncompensated one, ie
       Output(I) = Input(I,Tr) and y(Tr) * f = 1,
       where Tr is reference temperature.
       dm(input_temp_comp) = ar;
                                  {get signal from previous stage}
       ar = dm(CH1);
                                  {enter temperature read}
       mv1 = ar:
       mf = ar * my1 (RND), mx1 = dm(I1,M1); {mf = x^2}
       mr = mx1 * my1 (SS), mx1 = dm(I1,M1); {mr = b*x}
       cntr = 2:
       do approx UNTIL CE;
       mr = mr + mx1 * mf (SS);
approx: mf = ar * mf (RND), mx1 = dm(I1,M1);
mr = mr + mx1 * mf (RND), ar = dm(I1,M1);
       ay0 = mr1;
       ar = ar + ay0;
       my0 = dm(input_temp_comp);
       mr = ar * my0 (RND);
                                        {Input(I,T) * y(T)}
       mx1 = f;
                                        {intersection}
       my1 = mr1;
       mr = mxi * my1 (SS);
                                        {Input(I,T)y(T) * f}
       sr = ashift mr1 by 1 (hi);
       sr = sr or lshift mr0 by 1 (lo); {Convert to 1.15 format}
       ar = sr1:
write:
       dm(output_2) = ar;
autocalibration:
       ax0 = 0:
      dm(stat_autocalibration) = ax0;
      ena sec_reg;
      imask = b#000000001;
      I6 = ^correct_coef;
      L6 = 0;
      M6 = 1;
      ax1 = b#00000000;
      dm(PFDATA) = ax1;
                                 {enable Source_1 and Source_2}
      cntr = 10000;
      do loop_1 until ce;
                                {delay until counter exp.}
loop_1:
```

jump end\_response\_characteristic;

```
nop;
        ay0 = dm(CH3);
                                       {read offset_1 + magnitude_1}
        ay1 = dm(CH2);
                                       {read offset_2 + magnitude_2}
        ax1 = b#00000110:
        dm(PFDATA) = ax1;
                                       {disable Source_1 and Source_2}
        cntr = 10000:
        do loop_2 until ce;
                                     {delay until counter exp.}
loop_2:
        nop:
        ax0 = dm(CH3);
                                       {read offset_1}
        dm(offset_1) = ax0;
        ax1 = dm(CH2);
                                       {read offset_2}
        dm(offset_2) = ax1;
        imask = b#0000000000;
        nop;
        ar = ay0 - ax0;
                                       {magnitude_1}
        dm(magnitude_1) = ar;
        ar = ay1 - ax1;
                                       {magnitude_2}
        dm(magnitude_2) = ar;
        ax0 = dm(magnitude_1);
        ay1 = dm(magnitude_2);
        ar = ax0 - ay1;
                                       {magn_1 - magn_2}
        ar = pass ar;
        if GE jump calculate_k1;
        jump calculate_k2;
calculate_k1:
        ay1 = dm(magnitude_2);
        ar = dm(magnitude_1);
        call div;
        dm(k1) = ay0;
                                      \{k1 = magn_2/magn_1\}
        ay0 = 0x7fff;
        dm(k2) = ay0;
                                       \{k2 = 1\}
        ax0 = dm(magnitude_1);
        ay1 = dm(magnitude_2);
        ar = ax0 + ay1;
        if av jump correct_k1_k2;
        ax0 = 1;
        dm(stat_autocalibration) = ax0;
        ax1 = b#00000000;
        dm(PFDATA) = ax1;
                                     {enable Source_1 and Source_2}
       dis sec_reg;
       rti;
calculate_k2:
       ay1 = dm(magnitude_1);
       ar = dm(magnitude_2);
       divs ay1, ax0;
       call div;
       dm(k2) = ay0;
                                      \{k2 = magn_1/magn_2\}
       ay0 = 0x7fff;
       dm(k1) = ay0;
                                      \{k1 = 1\}
       ax0 = dm(magnitude_1);
       ay1 = dm(magnitude_2);
       ar = ax0 + ay1;
       if av jump correct_k1_k2;
       ax0 = 1;
       dm(stat_autocalibration) = ax0;
       ax1 = b#00000000;
       dm(PFDATA) = ax1;
                                     {enable Source_1 and Source_2}
       dis sec_reg;
       rti;
correct_k1_k2:
```

```
m \times 0 = dm(16, M6):
       my0 = dm(k1);
       mf = mx0 * my0 (SS);
       mx1 = dm(magnitude_1);
       mr = mx1 * mf (RND);
       ay1 = mr1;
       my0 = dm(k2);
       mf = mx0 * my0 (SS);
       mx1 = dm(magnitude_2);
       mr = mx1 * mf (RND);
       ar = mr1 + ay1;
       if av jump correct_k1_k2;
       my0 = dm(k1);
       mr = mx0 * my0 (RND);
       dm(k1) = mr1;
       my0 = dm(k2);
       mr = mx0 * my0 (RND);
       dm(k2) = mr1;
       ax1 = b#00000000;
       dm(PFDATA) = ax1;
                                     {enable Source_1 and Source_2}
       ax0 = 1:
       dm(stat_autocalibration) = ax0;
       rti;
{******************** Divide subroutine (ay0 = ay1/ar) *************************
       divs ay1, ar;
div:
       divq ar; divq ar; divq ar; divq ar;
       divq ar; divq ar; divq ar; divq ar; divq ar;
divq ar; divq ar; divq ar; divq ar; divq ar;
       rts;
.endmod;
```

## **AC-only measurement configuration**

```
.module/RAM/ABS=0
                            Optical_Current_Transducer_ac;
        This program was written by Pawel Niewczas -
                                                            }
        Centre For Electrical Power Engineering,
        University of Strathclyde, Glasgow, UK.
{
        This program is for the use with the DSP
        interrogation system of an Optical Current
        Transducer.
{
       Features:
       - AC current measurement only,
        - autocalibration of the system,
       - digital filtering,
       - vibration compensation of the OCT,
       - sensor response characteristic correction,
        - temperature compensation of the sensor.
{memory mapped ADSP-2181 control registers}
.const IDMA=
                                             0x3fe0:
.const BDMA_BIAD=
                                             0x3fe1:
.const BDMA_BEAD=
                                             0x3fe2;
.const BDMA_BDMA_Ctrl=
                                             0x3fe3;
.const BDMA_BWCOUNT=
                                             0x3fe4:
.const PFDATA=
                                             0x3fe5:
.const PFTYPE=
                                             0x3fe6;
.const SPORT1_Autobuf=
                                             0x3fef;
.const SPORT1_RFSDIV=
.const SPORT1_SCLKDIV=
                                             0x3ff0;
                                             0x3ff1:
.const SPORT1_Control_Reg=
                                             0x3ff2;
.const SPORTO_Autobuf=
                                             0x3ff3;
.const SPORTO_RFSDIV=
                                            0x3ff4;
.const SPORTO_SCLKDIV=
.const SPORTO_Control_Reg=
                                             0x3ff5:
                                             0x3ff6;
```

```
0x3ff7;
 .const SPORTO_TX_Channels0=
                                                    0x3ff8;
 .const SPORTO_TX_Channels1=
 .const SPORTO_RX_Channels0=
                                                    0 \times 3 ff9
                                                   0x3ffa;
 .const SPORTO_RX_Channels1=
 .const TSCALE=
                                                   0x3ffb;
                                                   0x3ffc:
                                                   0x3ffd:
 .const TPERIOD=
                                                   0x3ffe;
 .const DM_WAIT_REG=
                                                   0x3fff:
 .const System_Control_Reg=
                                          {number of fir coefficients}
                 N = 60;
 .const
                                           {number of DC buffers data}
                M = 8 * N;
 .const
                 D = 16;
                                           {decimate by D}
 .const
                                                  \{23C \text{ int, } f = 1.3895 \text{ in } 2.14 \text{ format}\}\
                 f = b#0101100011101101;
 .const
 {******************** Variable and Buffer Declaration **************************
 {sampling control variables:}
            stat_togg_flag;
.var/dm
 .var/dm
                stat_read;
{input/output buffers:}
.var/dm
                CH1;
                CH2;
.var/dm
.var/dm
               CH3:
.var/dm
                output_1;
.var/dm
                output_2;
{autocalibration}
                stat_autocalibration;
.var/dm
.var/dm
                offset_1;
.var/dm
               offset_2;
{OCT response characteristic}
                asin_delta_coef[512];
.var/dm
{DC decimation filter}
.var/pm/circ DC_fir_coef[N];
                data_DC[M];
.var/dm/circ
                buff_1_CH2;
buff_2_CH2;
.var/dm
.var/dm
                buff_3_CH2;
buff_4_CH2;
buff_1_CH3;
.var/dm
.var/dm
.var/dm
                 buff_2_CH3;
buff_3_CH3;
.var/dm
.var/dm
                buff_4_CH3;
.var/dm
                counter_1_dec;
counter_2_dec;
.var/dm
.var/dm
.var/dm
                 counter_3_dec;
.var/dm
                 counter_2_postpone;
.var/dm
                 counter_3_postpone;
                 output_1_CH2;
output_2_CH2;
.var/dm
.var/dm
.var/dm
                 output_3_CH2;
.var/dm
                 output_1_CH3;
.var/dm
                 output_2_CH3;
.var/dm
                 output_3_CH3;
.var/dm
                 DC_CH2;
.var/dm
                 DC_CH3;
.var/dm
                 DC_CH2_temp;
{Temperature compensation}
.var/dm/circ
               temp_coef[5];
.var/dm
                 input_temp_comp;
{************ Variable and buffer initialisation *******************************
.init temp_coef:
b#0101010001010101,
                        {a = +0.65884255}
b#0010100111111111,
                        \{b = +0.32809639\}
b#000000000101110,
                        \{c = +0.01390126\}
b#0000000000000000,
                         \{d = 0\}
b#000000000000000;
                         \{e = 0\}
.init fir_coef:
b#111111111111010100000000,
```

```
b#111111111111010100000000;
 .init asin_delta_coef:
{ start asin_coef }
ь#000000000000000000
b#0111100011001100,
{ start delta_coef }
b#0101000101111101,
b#0111001101000111;
jump start;
            {Location 0000: reset}
       rti;
            rti; rti;
       rti;
             {Location 0004: IRQ2}
       rti;
             rti; rti;
       rti;
             {Location 0008: IRQL1}
       rti:
             rti: rti:
       rti;
              {Location 000c: IRQL0}
       rti:
             rti; rti;
       rti;
             {Location 0010: SPORTO tx}
       rti:
             rti;
                    rti;
       rti:
              {Location 0014: SPORTO rx}
       rti:
             rti:
                    rti:
jump autocalibration; {Location 0018: IRQE}
             rti;
      rti:
                    rti:
      rti:
             {Location 001c: BDMA}
      rti;
             rti;
                   rti;
             {Location 0020: SPORT1 tx or IRQ1}
      rti:
      rti:
             rti:
                    rti;
             {Location 0024: SPORT1 rx or IRQ0}
      rti:
      rti;
             rti;
                    rti;
jump toggle_flags;
                   {Location 0028: timer}
      rti:
             rti:
                   rti;
             {Location 002c: power down}
      rti:
      rti;
             rti;
                   rti;
{******************* ADSP 2181 initialisation **********************************
start:
reset F10, reset F12, reset F11;
                                         {Fl0 - LED driver control}
                                         {F12 - current sampling control}
                                        {Fl1 - temperature sampling control}
      ax0 = 0;
      dm(stat_togg_flag) = ax0;
      dm(stat_read) = ax0;
      dm(stat_autocalibration) = ax0;
      ax0 = b#0111101100000110;
      dm(PFTYPE) = ax0;
{************************* Serial Port 0 (SPORTO) Set Up ************************
      ax0 = 0;
      dm(SPORT0_Autobuf) = ax0;
                                 {autobuffering disabled}
      dm(SPORTO_RFSDIV) = ax0;
                                 {RFSDIV not used}
```

```
{SCLKDIV not used}
       dm(SPORT0\_SCLKDIV) = ax0;
      dm(SPORTO_Control_Reg) = ax0; {ctrl functions disabled}
 ax0 = 0;
                             {autobuffering disabled}
      dm(SPORT1_Autobuf) = ax0;
      dm(SPORT1_RFSDIV) = ax0; {RFSDIV not used}
dm(SPORT1_SCLKDIV) = ax0; {SCLKDIV not used}
      dm(SPORT1_Control_Reg) = ax0; {ctrl functions disabled}
 ax0 = 0;
      dm(TSCALE) = ax0;
      dm(TCOUNT) = ax0;
      dm(TPERIOD) = ax0;
      ax0 = 0x0;
      dm(TSCALE) = ax0;
                       /* -165- a5 -50kHz- */
      ax0 = 0xa5:
      dm(TPERIOD) = ax0;
      dm(TCOUNT) = ax0;
      ena timer;
ax0 = b#000000000000100;
      dm(DM_Wait_Reg) = ax0;
     dm(System_Control_Reg) = ax0;
                                   {clear pending interrupt}
     ifc = b#00000011111111;
     nop;
     icnt1 = b#00000;
     mstat = b#1100000;
I7 = ^asin_delta_coef;
     L7 = 0;
     I1 = ^temp\_coef + 1;
     L1 = %temp_coef;
     M1 = 1;
{****************** wait for interrupt and loop forever ***********************
     ax0 = b#000000000;
     dm(PFDATA) = ax0;
                             {enable source 1 and source 2}
     imask = b#0000010001;
                            {allow timer and a_calib interrupt}
     nop;
     imask = b#0000010001;
                            {allow timer and a_calib interrupt}
     nop;
wait_interrupt:
     idle;
     jump wait_interrupt;
toggle_flags:
     dis sec_reg;
     ar = dm(stat_togg_flag);
     ar = pass ar;
     if ne jump togg_f10;
togg_fl2:
     toggle fl2, toggle fl1;
                            {current & temperature sampling control}
     ax0 = 1;
     dm(stat_togg_flag) = ax0;
     rti;
togg_fl0:
     togale fl0:
                            {LED driver control}
     ax0 = 0;
     dm(stat_togg_flag) = ax0;
     ar = dm(stat_read);
      ar = pass ar;
      if eq jump read_CH3_and_CH1;
```

```
read_CH2:
       my1 = IO(0x01d);
                                  {read current: CH2}
       dm(CH2) = my1;
       dm(stat_read) = ax0;
{******** write to DACs *********}
       my1 = dm(output_1);
       IO(0x017) = my1;
                                  {write to D/A_2}
       nop; nop;
       my1 = dm(output_2);
       IO(0x00f) = my1;
                                 {write to D/A_1}
       rti;
read_CH3_and_CH1:
       imask = b#0000010001;
       nop;
       ax0 = 1;
       dm(stat_read) = ax0;
       ena sec_reg;
ax0 = IO(0x01e);
                                   {read temperature: CH1}
       dm(CH1) = ax0;
       ax0 = IO(0x01b);
                                  {read current: CH3}
       dm(CH3) = ax0;
       ar = dm(stat_autocalibration); {come out from calibration?}
       ar = pass ar;
       if eq rti;
ar = dm(counter_1_dec);
              ar = ar + 1;
                                         {increase counter_1_dec}
              dm(counter_1_dec) = ar;
load_buff_1:
              IO = dm(buff_1_CH2); {pointer at the beginning of buff_1_CH2}
              ax0 = dm(CH2);
              dm(I0,M0) = ax0;
                                   {load data to the buffer}
              dm(buff_1_CH2) = I0; {update pointer}
              IO = dm(buff_1_CH3); {pointer at the beginning of buff_1_CH3}
              ax0 = dm(CH3);
              dm(I0,M0) = ax0;
                                   {load data to the buffer}
              dm(buff_1_CH3) = I0;
                                   {update pointer}
              I0 = dm(buff_1_CH2); {pointer at the beginning of buff_1_CH2}
                                   {perform filtering}
              call fir;
              dm(output_1_CH2) = mr1;
                                      {put filtered data to output_1_CH2}
              IO = dm(buff_1_CH3); {pointer at the beginning of buff_1_CH3}
                                   {perform filtering}
              call fir;
              dm(output_1_CH3) = mr1;
                                         {put filtered data to output_1_CH3}
dec_counter_1: ar = dm(counter_1_dec);
                                         {check cntr1}
              ar = ar - D;
              ar = pass ar;
              if ne jump dec_counter_2; {if cntr1 < D, jump cntr2}
dm(counter_1_dec) = ar; {if cntr1 = D, zero cntr1}
dm(counter_2_postpone) = ar; {if cntr1 = D, zero pstpn2}</pre>
              ar = dm(counter_2_dec);
              ar = ar + 1;
              dm(counter_2_dec) = ar;
                                         {if cntr1 = D, increase cntr2}
                                         {if cntr1 = D, load_buff_2}
              jump load_buff_2;
dec_counter_2: ar = dm(counter_2_postpone);
                                         {check pstpn2}
             ar = pass ar;
              if ne jump end_DC_filter;
                                         {if pstpn2 not = 0, end filter}
             ar = dm(counter_2_dec);
             ar = ar - D;
                                         {if pstpn2 = 0, check cntr2}
             ar = pass ar:
             if ne jump dec_counter_3; {if cntr2 < D, jump cntr3}
             dm(counter_2_dec) = ar;
                                               {if cntr2 = D, zero cntr2}
             dm(counter_3_postpone) = ar; {if cntr2 = D, zero pstpn3}
```

```
ar = 1;
                 dm(counter_2_postpone) = ar; {if cntr2 = D, pstpn2 = 1}
                 ar = dm(counter_3_dec);
                 ar = ar + 1;
                 dm(counter_3_dec) = ar;
                                                          {if cntr2 = D, increase cntr3}
                 jump load_buff_3;
                                                  {if cntr2 = D, load_buff_3}
 dec_counter_3: ar = dm(counter_3_postpone);
                 ar = pass ar;
                                                  {check pstpn3}
                 if ne jump end_DC_filter;
                                                  {if pstpn3 not = 0, end filter}
                 ar = dm(counter_3_dec);
                                                  {if pstpn3 = 0, check cntr3}
                 ar = ar - D;
                 ar = pass ar;
                 if ne jump end_DC_filter;
dm(counter_3_dec) = ar;
                                                  {if cntr3 < D, end filter}
                                                          {if cntr3 = D, zero cntr3}
                 ar = 1;
                                                 {if cntr3 = D, pstpn3 = 1}
{if cntr3 = D, load_buff_4}
                 dm(counter_3_postpone) = ar;
                 jump load_buff_4;
load_buff_2:
                 I0 = dm(buff_2_CH2);
                 ax0 = dm(output_1_CH2);
                 dm(I0,M0) = ax0;
                 dm(buff_2_CH2) = I0;
                 I0 = dm(buff_2_CH3);
                 ax0 = dm(output_1_CH3);
                dm(I0,M0) = ax0;
                dm(buff_2_CH3) = I0;
                I0 = dm(buff_2_CH2);
call fir;
                dm(output_2_CH2) = mr1;
                I0 = dm(buff_2CH3);
                call fir;
                dm(output_2_CH3) = mr1;
                jump end_DC_filter;
load_buff_3:
                I0 = dm(buff_3_CH2);
                ax0 = dm(output_2_CH2);
                dm(I0,M0) = ax0;
               dm(buff_3_CH2) = I0;
               I0 = dm(buff_3_CH3);
               ax0 = dm(output_2_CH3);
               dm(I0,M0) = ax0;
               dm(buff_3_CH3) \approx I0;
               I0 = dm(buff_3_CH2);
call fir;
               dm(output_3_CH2) = mr1;
               I0 = dm(buff_3_CH3);
               call fir;
               dm(output_3_CH3) = mr1;
                jump end_DC_filter;
load_buff_4:
               I0 = dm(buff_4_CH2);
                ax0 = dm(output_3_CH2);
               dm(I0,M0) = ax0;
               dm(buff_4_CH2) = I0;
                I0 = dm(buff_4_CH3);
                ax0 = dm(output_3_CH3);
               dm(I0,M0) = ax0;
               dm(buff_4_CH3) = I0;
                I0 = dm(buff_4_CH2);
                call fir;
               dm(DC_CH2_temp) = mr1;
                I0 = dm(buff_4_CH3);
                call fir;
                dm(DC_CH3) = mr1;
```

```
ax0 = dm(DC_CH2_temp);
            dm(DC_CH2) = ax0;
end_DC_filter: nop;
normalisation:
      ax0 = dm(CH3);
                             {read current: E1 (CH3 on board)}
      ay0 = dm(offset_1);
      ar = ax0 - ay0;
                                   {subtract offset from E1}
      my0 = 0x399a;
      mr = ar * my0 (rnd);
                            {multiply input by 0.45}
      ay1 = mr1;
      ar = dm(DC_CH3);
                             {read DC component of CH3}
      ar = ar - ay0;
                             {subtract offset from it}
      call div;
                             {divide CH3 by DC3}
      ax0 = ay0;
                             {____Elnorm. in ax0 register___}
      ax1 = dm(CH2);
                             {read current: E2 (CH2 on board)}
      ay0 = dm(offset_2);
      ar = ax1 - ay0;
                                   {subtract offset from E2}
      my0 = 0x399a;
      mr = ar * my0 (rnd);
                            {multiply input by 0.45}
      ay1 = mr1;
      ar = dm(DC_CH2);
                             {read DC component of CH2}
      ar = ar - ay0;
                             {subtract offset from it}
      call div;
                             {divide CH2 by DC2}
                             {____E2norm. in ay0 register___}}
ar = ax0 - ay0;
                                        {CH1-CH2}
      ay1 = ar;
      ar = ax0 + ay0;
                                        {CH1+CH2}
      call div:
                                   {(CH1-CH2)/(CH1+CH2)}
The same as in the previous section
The same as in the previous section
write:
      dm(output_2) = ar;
      ar = dm(CH3);
     dm(output_1) = ar;}
     rti;
autocalibration:
     ena sec_reg;
     ay0 = 0;
     dm(stat_autocalibration) = ay0;
imask = b#0000000001;
     ay0 = b#00000110;
     dm(PFDATA) = ay0;
                           {disable Source_1 and Source_2}
     cntr = 10000;
     do loop_1 until ce;
                           {delay until counter exp.}
loop_1:
     nop;
     ay0 = dm(CH3);
                            {read offset_1}
     dm(offset_1) = ay0;
     ay0 = dm(CH2);
                           {read offset_2}
     dm(offset_2) = ay0;
{** DC filter initialisation **}
     L0 = %data_DC;
     M0 = 8;
```

```
I0 = ^data_DC;
        dm(buff_1_CH2) = I0;
I0 = ^data_DC + 1;
        dm(buff_1_CH3) = I0;
         I0 = ^data_DC + 2;
        dm(buff_2_CH2) = I0;
         I0 = ^data_DC + 3;
        dm(buff_2_CH3) = I0;
         I0 = ^data_DC + 4;
        dm(buff_3_CH2) = I0;
I0 = ^data_DC + 5;
        dm(buff_3_CH3) = I0;
        I0 = ^data_DC + 6;
dm(buff_4_CH2) = I0;
I0 = ^data_DC + 7;
        dm(buff_4_CH3) = I0;
         L4 = %DC_fir_coef;
         I4 = ^DC_fir_coef;
         M4 = 1;
        ay0 = 0;
        dm(counter_1_dec) = ay0;
dm(counter_2_dec) = ay0;
dm(counter_3_dec) = ay0;
        ay0 = 1;
        dm(counter_2_postpone) = ay0;
        dm(counter_3_postpone) = ay0;
{** Come out from calibration **}
        ay0 = b#000000000;
        dm(PFDATA) = ay0;
                                          {enable Source_1 and Source_2}
        av0 = 1;
        dm(stat_autocalibration) = ay0;
        rti:
{*********************** calling subroutines ****************************
{******** Finite Input Response (FIR) Filter subroutine ************
        mr = 0, mx0 = dm(I0,M0), my0 = pm(I4,M4);
fir:
        cntr = N - 1;
        do sop until ce;
sop:
        mr = mr + mx0 * my0 (SS), mx0 = dm(I0,M0), my0 = pm(I4,M4);
        mr = mr + mx0 * my0 (RND);
        if mv sat mr;
                                         {output in mr1}
        rts;
div:
        divs ay1, ar;
        divq ar; divq ar; divq ar; divq ar;
        divq ar; divq ar; divq ar; divq ar; divq ar; divq ar; divq ar; divq ar; divq ar; divq ar; divq ar; divq ar;
        rts;
.endmod:
```